Structure-Property Relationships in Sea Urchin Spines and Implications for Technical Materials

Dissertation

der Mathematisch-Naturwissenschaftlichen Fakultät
der Eberhard Karls Universität Tübingen
zur Erlangung des Grades eines
Doktors der Naturwissenschaften
(Dr. rer. nat.)

vorgelegt von
M. Sc. Christoph Lauer
aus Bonn

Tübingen
2019

Gedruckt mit der Genehmigung der Mathematisch-Naturwissenschaftlichen Fakultät der Eberhard Karls Universität Tübingen

Tag der mündlichen Qualifikation:	25.07.2019
Dekan:	Prof. Dr. Wolfgang Rosenstiel
1. Berichterstatter:	Prof. Dr. Klaus G. Nickel
2. Berichterstatter:	Dr. Christoph Berthold

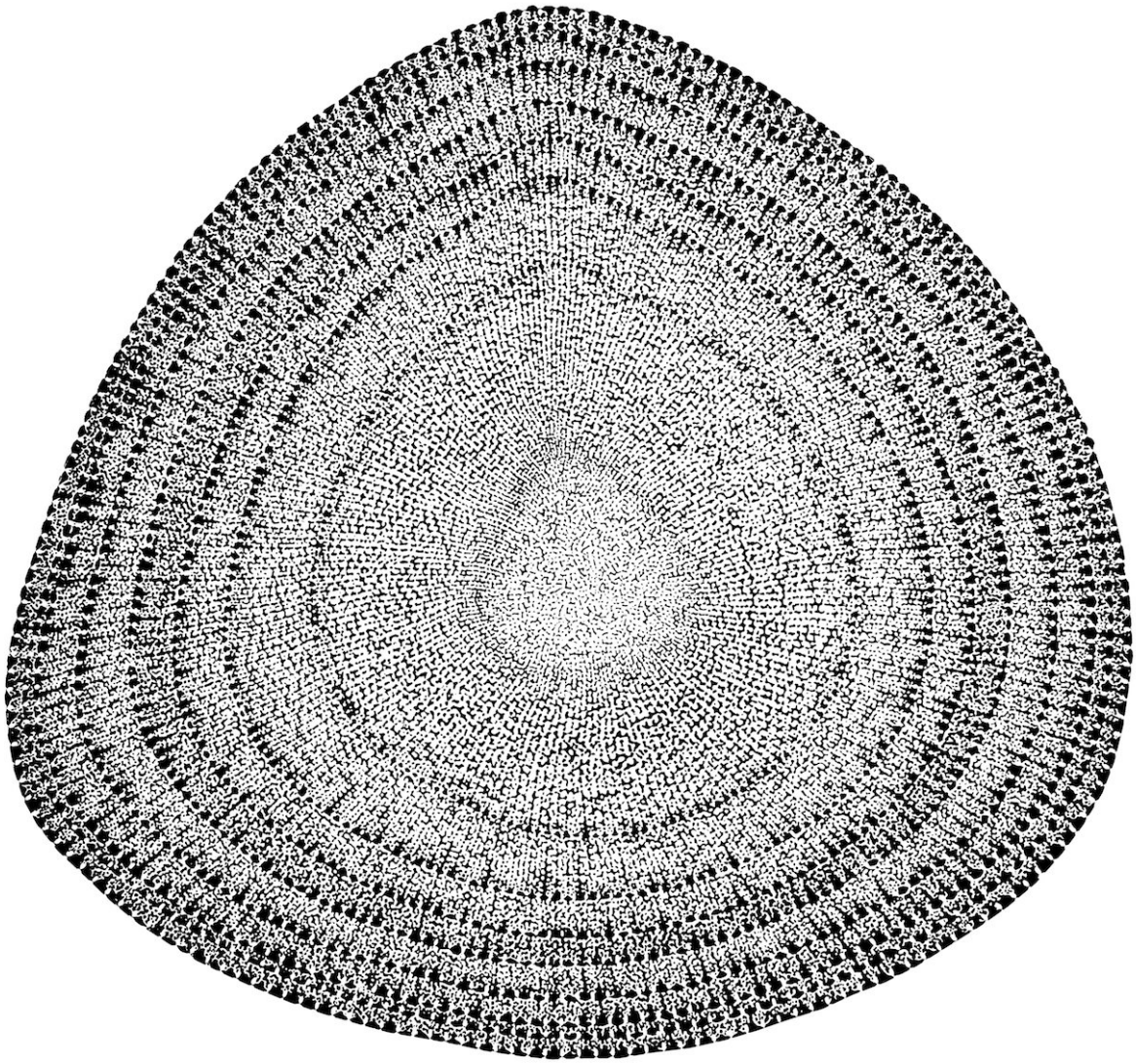

Nature's art: Structure of the dense material in a cross section of a spine of *Heterocentrotus mamillatus*

Acknowledgements

First and foremost, I want to thank Prof. Nickel for giving me the opportunity to conduct my PhD research in such a multidisciplinary and horizons broadening topic, for his supervision and the countless good discussions we had over the years. I also thank him for his always professional and sincere attitude and his commitment for all his PhD students.

Dr. Christoph Berthold taught me to never trust data without questioning them (if own or by others), to revise the approach over and over again and by doing this to gain a deeper understanding and more reliable data. Dr. Patrick Schmidt helped me a lot with IR Spectroscopy and I greatly benefited from his general advice on academic matters.

I am indebted to my colleague and office neighbour Gerald Buck with whom I had many fruitful discussions on preliminary results and a vivid exchange of ideas. I thank Dr. Tobias Kiemle for his always helpful advice and sharing his experience of graduating. I want to thank my other colleagues in the applied mineralogy working group for making my PhD a good time, namely Dr. Melanie Keuper, Dr. Rita Silvia Amicone, Nadja Wichtner, Philippe Charotte, Frieder Lauxmann, Manuel Löber and Dr. Yannick Hemberger. I also thank Katharina Klang.

Special thanks goes to the Bachelor and Master students that worked in close collaboration with me. Sebastian Haußmann and Stefan Mück conducted both their Bachelor and Master Thesis under my supervision and contributed with their data and discussions to the quality and quantity of this PhD thesis. The same can be said about Kilian Sillmann, who wrote his Master Thesis on the mechanical properties of the closely related spines of *H. trigonarious*. I also want to thank Moritz Schwab, for his stamina to finish his Master Thesis under difficult conditions. Isabel Zutterkirch helped me greatly with her work as student assistant and her Bachelor Thesis on the Argonaut shell, a related biological role model.

Without the great help of Simone Schafflick and Barbara Meier in the workshop adequate sample preparation would have been much harder. Their creativity and experience helped to find solutions for preparing these not normed and often challenging samples. I thank Annette Flicker for her advice on IR Spectroscopy.

As the Collaborative Research Center Sonderforschungsbereich Transregio 141 (CRC SFB TRR 141) was a highly interdisciplinary project I had close and fruitful collaborations with Stefanie Schmier from the plant biomimetic group of the University Freiburg. I also thank Dr. Georg Bold and Prof. Dr. Thomas Speck, both showed me how fascinating and diverse the field of biomimetics is. I am grateful to Dr. Tobias Grun and Prof. Dr. James Nebelsick (Palaeontology Group University Tübingen) to share their palaeontological, biological, statistical knowledge and deep understanding of echinoderms with me. Dr. Markus Ströbele and Manuel Löber from the Inorganic Chemistry Group (University Tübingen) helped me a lot with TG and DSC measurements.

Raouf Jemmali (DLR Stuttgart) improved my spatial imagination of the sea urchin stereom with his CT skills greatly. I am indebted to Netzsch Gerätebau GmbH, namely Dr. Carolin Fischer and Doreen Rapp, who conducted free TG-MS and dilatometry measurements for me.

I thank my mother and my father for supporting me in such a great way the entire time of the PhD. I thank all my friends for making my second stay in Tübingen as memorable as the first one for my Bachelor's degree.

And of course, last but not least, I thank my girlfriend Judith, who supported me throughout the long 3.5 years of the PhD in any situation. In the last moths she never failed to point out how cool it is to do a PhD and not to work "properly", which was a great help to take the stressing times of the last phase of the PhD easy. Furthermore, I have never seen a person proof reading so enthusiastically.

I thank the German Research Foundation (DFG – Deutsche Forschungsgemeinschaft) for funding my PhD project in the framework of the SFB TRR 141, project B01. Although, I regret the DFG's decision not extend the SFB TRR 141 to a second funding period.

Table of Contents

List of Abbreviations

3PB	3-point bending
CT	computer tomography
GL	growth layer
GLf	finishing growth layer
GLp	permanent growth layer
IR	infrared spectroscopy
MLE	maximum likelihood estimation
PI	pin indentation
RFDA	resonance frequency damping analysis
RVE	representative volume element
SEM	scanning electron microscopy
SFB TRR 141	Sonderforschungsbereich Transregio 141
TG	thermogravimetry
UC	uniaxial compression
XRD	X-ray diffraction
E	Young's Modulus
EW	Eshelby-Wu coefficient
K_{IC}	fracture toughness (in mode I loading)
m	Weibull modulus
n	sample population
γ	energy dissipation efficiency
ε	strain
σ	stress
σ_0	characteristic strength
σ_{UC}	compressive strength
σ_{3PB}	three point bending strength
σ_{PI}	pin indentation strength
ϕ	porosity

Summary

Sea urchin spines have been studied for numerous reasons including their crystallographic and chemical composition, their aesthetic appearance and their enigmatic growth at ambient conditions. Depending on the species, sea urchins use their spines for protection against predators, for burial in the substrate, for locomotion and for withstanding wave energy by wedging into reef cervices. Hence, sea urchin spines are in most cases optimized for bearing load.

This study deals with the mechanical properties of the unique spines of *Heterocentrotus mamillatus*, a large Indo-Pacific Echinoid. They consist as all skeletal elements of Echinoids of Mg-calcite arranged in a porous meshwork (stereom) with very little organic material incorporated (<0.5 wt%). By the overall porosity of 0.6-0.7 their density is similar to sea water and the large and thick spines are not a burden to carry. These properties make the spines of *H. mamillatus* a promising biomimetic role model for high performance, intelligently structured, lightweight ceramics. Since biological role models are usually a lot smaller than the technical application they inspire, the question of how properties change with an increase in size, is intimately linked to biomimetic research.

In contrast to man-made materials, biological materials gain much of their mechanical performance from the elaborate structuring on many hierarchical levels. Therefore, the relation between structure and property was analysed in depth before addressing the question of scaling. Mechanical properties were tested with uniaxial compression, 3-point bending and resonance frequency damping analysis. The structure was visualized by optical microscopy, secondary scanning microscopy and computer tomography. X-ray diffraction, infrared spectroscopy, thermogravimetry and dilatometry gave insight into the crystallography and chemical composition. For scaling analyses theories of Weibull and Bažant were applied.

The spines generally derive their high strength, high stiffness and exceptional damage tolerance from their construction out of $>10^7$ struts/cm^3. The μm sized struts can be bent elastically, demonstrating that they are practically free of surface flaws. The struts are separated by pores which restrict crack growth and keep damage localised. The porous meshwork is covered irregularly by dense layers, the "growth layers" marking earlier growth stages. They provide the spines with additional stiffness and strength. Spines with many growth layers have a significantly higher strength and stiffness.

The strength of the spines seems not to decrease significantly with increasing size, contradicting scaling theories. To test this unexpected finding, compression tests on samples with and without growth layers were conducted. A novel micro-compression test, the pin indentation was also applied. Despite the uncertainties induced by natural heterogeneities, it seems that spines of *H. mamillatus* counteract the size effect by adding more and denser growth layers to larger (older) spines. By this they work against the decrease in strength with increasing size. This hypothesis was confirmed by segments lacking growth layers that show a size effect.

Zusammenfassung

Seeigelstachel wurden im Laufe der letzten Jahrzehnte u.a. aufgrund ihrer Kristallographie und chemischen Zusammensetzung, ihres ästhetischen Aufbaus und ihrer Bildung bei Raumtemperatur untersucht. Seeigeln dienen ihre Stachel je nach Art als Schutzfunktion gegen Räuber, zur Fortbewegung, als Grabhilfe im Substrat und zum Festklemmen in Riffspalten, um der Wellenenergie zu trotzen. Somit sind die Stacheln in den meisten Fällen darauf optimiert, mechanischer Belastung zu widerstehen.

In der vorliegenden Arbeit wurden die mechanischen Eigenschaften der einzigartigen Stacheln des indopazifischen Echinoiden *Heterocentrotus mamillatus* untersucht. Wie alle Skelettelemente der Echinoidea bestehen sie aus Mg-Calcit, welches in einem porösen Gerüst (Stereom) mit geringen organischen Bestandteilen (<0.5 Gew.%) den gesamten Stachel aufbaut. Die Porosität dieser großen und dicken Stachel beträgt 0.6-0.7, sodass sie kaum schwerer als Meerwasser sind und dem Tier nicht zur Last fallen. Mit diesen Eigenschaften sind die Stacheln von *H. mamillatus* ein vielversprechender biomimetischer Ideengeber für strukturierte und leichte Hochleistungskeramiken. Da biologische Ideengeber häufig deutlich kleiner sind als ihre Anwendungen in der Technik, ist die Frage wie sich die Eigenschaften der Stacheln mit zunehmender Größe verändern, eng mit biomimetischer Forschung verbunden.

Im Gegensatz zu technischen Werkstoffen leiten biologische Materialien ihre mechanischen Eigenschaften aus einer komplexen Strukturierung über mehrere hierarchische Level ab, weshalb der Schwerpunkt der Untersuchungen in dieser Arbeit zuerst auf der Beziehung zwischen Struktur und mechanischen Eigenschaften lag, bevor die Frage der Skalierung aufgegriffen wurde. Die mechanischen Eigenschaften wurden mittels uniaxialer Kompression, Dreipunktbiegung und Impulserregungstechnik untersucht. Zur Verbildlichung der Struktur wurden optische Mikroskopie, Sekundärelektronenmikroskopie und Computertomographie verwandt. Röntgendiffraktion, Infrarotspektroskopie, Thermogravimetrie und Dilatometrie gaben u.a. Auskunft über die chemische Zusammensetzung und Phasenbestandteile. Als Grundlage für die Skalierung dienten die Theorien von Weibull und Bažant.

Die Grundlage für die hohe Festigkeit, Steifigkeit und Fehlertoleranz der Stacheln liegt in ihrer Bauweise aus $>10^7$ Stegen/cm^3. Die μm-großen Stege können elastisch gebogen werden, ein Indiz für das Fehlen nennenswerter Oberflächenfehler. Die Stege sind durch Poren voneinander getrennt, sodass Risswachstum unterbunden und Schaden an der Struktur lokal begrenzt wird. Diese poröse Basisstruktur wird von dichten Wachstumsschichten in unregelmäßigen Abständen eingefasst, welche den Stacheln zusätzliche Festigkeit und Steifigkeit verleihen. Stacheln mit vielen Wachstumsschichten haben eine signifikant höhere Festig- und Steifigkeit.

Die Festigkeit der Stacheln nimmt kaum mit zunehmender Größe ab, was Skalierungstheorien widerspricht. Zur genaueren Charakterisierung wurden uniaxiale Kompressionstests an Proben mit und ohne Wachstumsschichten durchgeführt und es wurde eine eigens entwickelte, lokale Kompressionsmethode angewandt, die Pin Indentation. Trotz der erheblichen natürlichen Schwankungen scheint es so, dass die Wachstumsschichten dem Größeneinflussfaktor entgegentreten. Große Stacheln haben aufgrund ihres Wachstums mehr und dichtere Wachstumsschichten als kleine Stacheln. Diese Theorie unterstützend konnte an Segmenten ohne Wachstumsschichten eine signifikante Abhängigkeit der Festigkeit von der Größe nachgewiesen werden.

List of Publications

Declaration according to § 5 Abs. 2 No. 8 of the PhD regulations of the Faculty of Science of the Eberhard Karls Universität Tübingen

Last Name, First Name: Lauer, Christoph

Published manuscripts

1. S. Schmier, **C. Lauer**, I. Schäfer, K. Klang, G. Bauer, M. Thielen, K. Termin, C. Berthold, S. Schmauder, T. Speck, K.G. Nickel, Developing the Experimental Basis for an Evaluation of Scaling Properties of Brittle and 'Quasi-Brittle' Biological Materials, in: J. Knippers, K.G. Nickel, T. Speck (Eds.), Biomimetic Research for Architecture and Building Constructions, Springer International Publishing, Switzerland, 2016, pp. 277-294.
2. **C. Lauer**, T.B. Grun, I. Zutterkirch, R. Jemmali, J.H. Nebelsick, K.G. Nickel, Morphology and porosity of the spines of the sea urchin *Heterocentrotus mamillatus* and their implications on the mechanical performance, Zoomorphology 137 (2017) 137-154.
3. **C. Lauer**, S. Schmier, T. Speck, K.G. Nickel, Strength-size relationships in two porous biological materials, Acta Biomater 77 (2018) 322-332.
4. **C. Lauer**, K. Sillmann, S. Haußmann, K.G. Nickel, Strength, elasticity and the limits of energy dissipation in two related sea urchin spines with biomimetic potential, Bioinspir Biomim 14(1) (2018) 016018.

Prepared manuscripts

5. **C. Lauer**, S. Mück, T. Grun, I. Zutterkirch, K.G. Nickel, Individual growth of the spines of *Heterocentrotus mamillatus*
6. **C. Lauer**, S. Haußmann, P. Schmidt, C. Fischer, D. Rapp, C. Berthold, K.G. Nickel, On the relationship of amorphous calcium carbonate and the macromechanical properties of sea urchin spines, *planned to submit to: Advanced functional materials*
7. **C. Lauer**, G. Buck, S. Mück, R. Jemmali, C. Berthold, K. G. Nickel, Pin indentation: a method for local testing mechanical properties of ceramic foams, *planned to submit to: Ceramics, special issue: Ceramics for biomedical applications*
8. **C. Lauer**, G. Buck, S. Mück, K.G. Nickel, Hierarchical construction of spines of *Heterocentrotus mamillatus* weakens the size effect on structural strength

Personal contribution to publications

Declaration according to § 5 Abs. 2 No. 8 of the PhD regulations of the Faculty of Science of the Eberhard Karls Universität Tübingen

*Table I: All percentages refer to the amount of work done by candidate of this PhD thesis. * denotes shared first authorship.*

Nr.	Accepted publication yes/no	Nr. of all authours	Position of candidate in list of authors	scientific ideas by the candidate [%]	Data generation by the candidate [%]	Analysis and interpretation by the candidate [%]	Paper writing done by the candidate [%]	Nr. in reference list
1	yes	11	2	30	30	30	20	[126]
2	yes	6	1	80	60	60	60	[41]
3	yes	4	1*	40	50	40	50	[59]
4	yes	4	1	90	50	80	80	[28]
5	no	5	1	90	20	50	80	[65]
6	no	8	1	80	50	60	70	[57]
7	no	6	1	50	20	50	50	[127]
8	no	4	1*	50	20	30	90	[128]

I confirm that the above-stated is correct

_____

Date, signature of the candidate

I/We certify that the above-stated is correct.

_____

Date, signature of the doctoral committee or at least of one of the supervisors

1. Introduction

1.1 Biomimetics and the SFB TRR 141

Nature takes a very different approach to design materials. Unlike man-made materials, biological materials are hierarchically structured from nano- to macroscale and are synthesized via self-assembly at ambient conditions from a very limited pool of raw materials (e.g. [1-4]). The resulting materials are often superior to man-made materials [5], even more so when taking the specific properties (i.e. property/density of material) into account.

Although human technology has come up with high performance materials with e.g. exceptional stiffness outperforming biological materials clearly, these materials are usually optimised for a single purpose, e.g. being stiff. Biological materials, however, are always multifunctional, performing well in many fields [2], such as toughness and stiffness [6]. This - from an engineering point of view - contradicting combination is achieved by a complex structural arrangement of soft and hard materials over many hierarchical levels. Good examples are bone and nacre [7] (Table 1).

As the living world has populated nearly any niche on earth, it is likely that nature has already found a solution in over 3.8 Ga of successful evolution to many technical problems. Notable examples of these solutions of immense technological potential are listed in Table 1. For some of these problems technology has not found any feasible solution to date such as underwater adhesion [8]. It is therefore a good starting point to look for inspiration in nature when addressing technical problems.

This approach was termed “biomimetics” by Otto Schmitt in 1957 [9]. Since then, many synonyms such as bioinspiration, bionics and biomimicry have arisen [9]. In this work only biomimetics is used. Biomimetics is by far not a novel approach. Leonardo da Vinci was inspired back in the 15th century by birds for the sketches of his flying machine [1], however, only in recent times biomimetics got a boost. This is not only caused by the ever growing demand for high-tech materials that repeatedly outperform their predecessor, but also by the highly economic use of raw materials in nature and their general 100 % recyclability [1]. Especially resource efficiency and recyclability are fields were humans are still stuck in a Stone Age state.

*Table 1: Well-known biological role models alongside with some lesser known role models investigated in the SFB TRR 141 (e.g. [4]). All of these materials are hierarchically structured and built via self-assembly. * denotes technical implementation on lab scale and +denotes commercially available bionic product. References only give an overview, there is a vast literature available on these topics.*

biological role model	technically desired property	principle	possible technical break-through /implementation
lotus leaf	superhydrophobicity [10], self-cleaning [11]	ultra-rough structured and repellent surface [11]	self-cleaning wall paint and fabrics [12]*, Lotusan wall paint+
nacre	tough and stiff at the same time [6, 13, 14]	composed of aragonite and proteins in brick and mortar structure [6]	toughening mechanisms for ceramics [13], [15]*
shark skin	drag reduction [16]	micro-enameloid scales with fine channels to direct flow and reduce turbulence [8]	reducing drag of ship's hull and thus fuel saving [17, 18]*
gecko foot	ultra-high and reversible adhesion [19]	hierarchically, finely structured hairs increase surface immensely [20]	reusable, strong tape [21]*
some of the biomimetic studies in the SFB TRR 141			
snap trap of carnivorous plants [22]	fast and hinge-less movements [23]	kinematic amplification of the bending deformation of the midrib [22]	replacing error-prone hinges, Flectofold* [24], Flectofin* [23]
sea urchin shells [25]	segmented shell construction, interconnection of plates [25]	polygonal plates arrange spherical body without collagenous support [25]	connection of segments with reduced load peaks,
sea urchin spines	combination of lightweight and stiffness [26] and energy dissipation [27]	structural, lightweight arrangement of porous Mg-calcite [28]	structurally graded lightweight concrete [29, 30]*

The SFB TRR 141 (Sonderforschungsbereich Transregio 141) tackles this problem with a multidisciplinary approach. Biologists, Geologists and Mechanical Engineers collaborate in analysing the potential of biological structures in order to improve architecture and building constructions in respect to property-structure-functionality relations and thus sustainability. For example, modern concrete consumes vast amount of resources [31]. Large quantities of raw materials could be saved, if full wall elements would only be used where maximum load occurs, and in all other parts the wall would be porous or considerably thinner. Such a functionally graded concrete based on the abstracted structure of the sea urchin spines of *Heterocentrotus mamillatus* was developed in project A02 and outperforms regular concrete in many aspects [29].

Project B01, where this doctoral research is located in, had close connections to A01 and investigated and analysed the structural layout of *H. mamillatus* with the following questions in mind (see also section 2):

(1) How does structure relate to mechanical properties in the lightweight spines of *Heterocentrotus mamillatus*?
(2) Can these properties of the few cm large sea urchin spines be scaled up to concrete dimensions (meter scale) and how can we predict the effect of upscaling on properties such as strength?

In the following paragraph a brief background of the biology, morphology and mechanical properties of *H. mamillatus* is given (1.2) and it is elucidated, why upscaling is not a simple task and why an increase in size usually comes with a decrease in strength (1.3).

1.2 The biomimetic role model: The aboral spines of *Heterocentrotus mamillatus*

1.2.1 Echinoids

The Indo-Pacific *Heterocentrotus mamillatus* (LINNAEUS, 1758) belongs to the echinoids, family Echinometridae, and lives nocturnal [32] in coral reefs of the tropical oceans. Its fossil record dates back at least to the Miocene [33]. It is evolutionarily spoken a quite recent species of the highly successful echinoids, which populate nearly all marine habitats from deep sea to shallow waters and from tropical to arctic oceans since 450 Ma [33]. Echinoids are classified in regular and irregular sea urchins. As *H. mamillatus* belongs to the former, only the basic body plan of the regular sea urchins is sketched further.

Regular echinoids have a rigid, often spherical body (also named test) out of Mg-calcite. For detailed sketches of the sea urchin test see ref. [34]. The spherical body shape is achieved by an intricate arrangement of polygonal plates organized in five ambulacral and interambulacral columns (two plates per column) running from the oral side, where the mouth is located, to the aboral side, where the anus is located. This body plan constitutes the characteristic pentamerous symmetry of regular echinoids. Each of the polygonal plates possesses tubercles, with the largest tubercle featuring a primary spine, surrounded by smaller secondary spines. Ambulacral plates possess also pores, where the tube feet for attachment, locomotion and respiration can penetrate through. All hard parts of the echinoids are composed out of Mg-calcite ($(Ca_{1-x}Mg_x)CO_3$), with varying amounts of Mg. Sea urchin teeth have with $x>0.2$ the highest amount of Mg [35, 36] and the content of test and spines ranges between $x=0.02$-0.12 (spines have generally a slightly lower content [36]). The Mg content can be correlated with the water temperature: The higher the temperature the more Mg incorporated [37]. Sea urchins are comparably well studied out of a number of reasons:

1. **Biology**: They exhibit (as outlined above) a very different body plan compared to mammals, birds or insects. Just to name a few other peculiarities: Echinoids generally have no eyes, no ears, no brain and do not mate physically.
2. **Morphology**: The highly aesthetic and symmetrical structure of the test itself, of the test elements and especially of the spines has attracted attention. The porous meshwork, called stereom, which is

the basic building unit of all skeletal parts, has often elaborate structures that can be classified in more ordered and disordered types (e.g. [38-41]).

3. **Crystallography**: Under polarized light and by means of X-ray diffraction sea urchin spines and mostly all other skeletal elements appear as single crystal [42-44], despite their complicated stereom construction, pores and rounded surfaces. Most intriguingly, the perfect cleavage planes of calcite are absent and the echinoid calcite shows conchoidal fracture (e.g. [44, 45]). Seto et al. [46] could show that a sea urchin spines are mesocrystals composed of calcite nanocrystallites (~100 nm [46, 47]), as hypothesized already by [42, 48-50], all well-aligned and embedded in an amorphous carbonate and protein matrix.
4. **Thermodynamics**: The sea urchin Mg-calcite is thermodynamically metastable at room temperature (e.g. [48-51]). Its diverse compositions fall in the miscibility gap of the phase diagram of calcite ($CaCO_3$) and dolomite ($CaMg(CO_3)_2$). These mixtures should not exist, however, nature has found a way to form these minerals at ambient conditions and to stabilize them.
5. **Formation**: It was found in the last three decades that biogenic calcite forms at ambient conditions via transient amorphous carbonate (ACC) under mediation of proteins [52-55] and subsequently crystallizes into calcite. Remnants of this formation can still be found in mature sea urchin spines [46, 56, 57] see Appendix II, Manuscript 6).
6. **Biomimetics**: The test has been used as inspiration for domes and plate interconnections [58]. The spines of *H. mamillatus* have been investigated as role model for lightweight materials [28, 59] (Appendix I, Manuscripts 4 and 3) such as lightweight ceramics [30] and lightweight, structurally graded concrete [29]. It was also proposed to use the stereom of these spines as bone tissue scaffold template [60] and was implemented in femoral bone of rats [61] and of rabbits [62]. The ribbed surface of *H. mamillatus* spines might serve to reduce drag [32] and a patent proposal (DE20314342U1) of the same author was submitted in 2003.

The last point illustrates that *H. mamillatus* alone is an abundant source for biomimetic inspiration. Before going into more detail, the morphology of this sea urchin will be described in the next paragraph (1.2.2), as it is the foundation for the remarkable mechanical properties reported in 1.2.3 and investigated in this doctoral research.

1.2.2 Morphology and hierarchical structure of the spines of *H. mamillatus*

For Echinometridae *H. mamillatus* has rather large and heavy spines in relation to its test, which is more typical for the family of Cidaridae [63]. The spines of *H. mamillatus* and of congeneric *H. trigonarius* belong surely to the largest, heaviest and thickest spines among echinoids. The mass of a single spine can exceed 6 g and it reaches lengths above 9 cm and thicknesses up to 1.7 cm ([64, 65]). These dimensions give the spines of *H. mamillatus* a rather clumsy appearance (Fig. 1). A pointed tip is lacking and the spines are not poisonous. The spine's appearance changes from blade shaped, spatula-

like on the oral side to nearly round at the aboral side [66] (Fig. 1A, C). The flat oral spines are probably optimized for locomotion as in other sea urchins [67] and the thick and large aboral spines are used to wedge into reef cervices for protection against predators [63]. It is hypothesized that these spines also protect against strong wave forces in *H. mamillatus*' shallow water, high wave energy habitat [68].

In sections the spines show conspicuous growth layers (GL). Synonyms for these structures are: growth rings [69], growth bands [64] and growth lines [70, 71]. Due to their three-dimensional structure the term "growth layer" is used here [41] (Appendix I, Manuscript 2). These GLs are outlines of past growth stages and mark growth cycles (e.g. [64, 66, 69]). It is widely accepted, that GLs - unlike growth lines of trees - cannot be used for absolute age determination [64, 71], since the time resolved between two GLs is not clear. Weber et al. [64] estimated it to be of a lunar cycle, Dotan and Fishelson [66] favoured a year and Ebert [71, 72] declared growth to be completely irregular. Indeed, the influence of nutrient availability, gonad growth and local sea temperatures are known to influence sea urchin growth strongly [73, 74]. Own results highlight that GLs cannot be used to determine the age of *H. mamillatus* [65] (Appendix II, Manuscript 5).

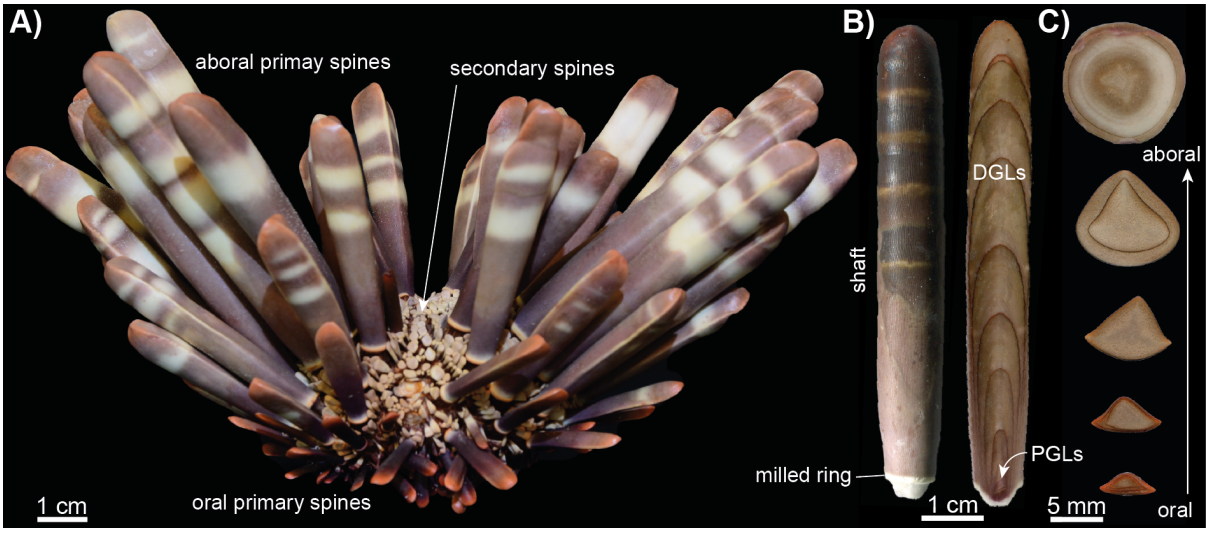

Figure 1: Heterocentrotus mamillatus and the distribution of its clumsy spines (a). In longitudinal (b) and horizontal (c) sections growth layers can be seen as downscaled versions of the spine. It can be distinguished in distal growth layers (DGLs) and proximal growth layers (PGLs). Blade and spatula-like spine shape changes from oral side to nearly round at aboral side (c). Adapted from [65].

Leaving the macroscopic observations behind and zooming into microscale, the elaborate, fenestrated stereom structure becomes apparent (Fig. 2). Excluding the milled ring, there are three stereom types constituting aboral and oral spines alike: (1) the central, most porous part, the medulla, (2) the densest parts, the growth layers intercepting the (3) radiating layer (RL) with intermediate porosity (Fig. 2). After the classification of Smith [40], Grossmann and Nebelsick [69] identified the medulla to be laminar and the RL to be labyrinthic. Smith [40] himself claimed, that the central region (medulla) of all Non-cidaridae (i.e. *H. mamillatus*) is labyrinthic.

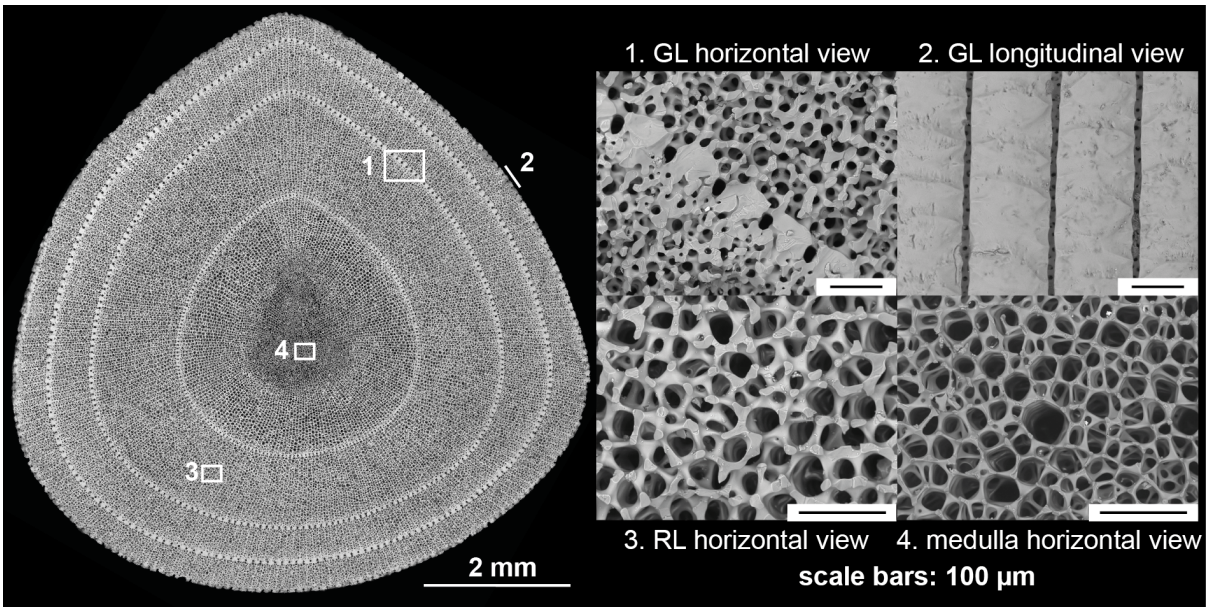

Figure 2: SEM picture of a horizontal section of an aboral H. mamillatus spine at 25 % of the spine length (measured from base) with detail shots of growth layer (GL), radiating layer (RL) and medulla.

Sea urchin spines generally bear a rather simple hierarchical structure compared to other biological materials. On the nanoscale Seto et al. [46] describe the structure as a mesocrystalline arrangement of Mg-calcite nanocrystals embedded in an ACC matrix (8-10 mol% [46, 56]) with occluded organic macromolecules (~0.02 mol%). The next hierarchical level can be found on the microscale and is composed of the porous stereom structure [46]. The basic building block of this hierarchical level can be abstracted as a pore surrounded by dense struts which is repeated innumerably. Large aboral spines of *H. mamillatus* ($V = 7\ cm^3$) can contain $>10^8$ of these building blocks! The next hierarchical level is the general stereom differentiation in medulla, radiating layer and GLs. The confining GLs and their arrangement in spines of *H. mamillatus* was identified as the highest hierarchical element, giving the spine its final shape [27]. This sums up to three hierarchical levels, which is the same amount as in nacre [7] and considerably less than in bone [7] or plant seeds [75].

Despite in depth morphological analyses of the spines of *H. mamillatus* [69, 76] a central information for linking structure and mechanical properties is ill addressed: porosity. It affects mechanical properties immensely (e.g. [77-80]). Surprisingly many studies on the mechanical properties of *H. mamillatus* have been performed (Table 2) without taking the porosity adequately into account [27, 45, 61, 62, 69]. Therefore, key question of the morphological characterization of this PhD thesis was an analysis of the porosity distribution in the spines of *H. mamillatus* for a better understanding of the mechanical properties [41].

1.2.3 Mechanical background and review of data from *H. mamillatus*' spines

From the point of view of a mechanical engineer, the spines of *H. mamillatus* are an irregularly structured, brittle, open-cell foam ceramic. To describe these, models are available and the starting point is usually the open cell model by Gibson and Ashby [81] derived by dimensional analysis which equals the semi-empirical Coble-Kingery [78] approach refined by Pabst and Gregorová [82]:

$$E_\phi = E_d * (1-\phi)^2 \quad \text{(Eq. 1)}$$

with the porosity ϕ, the Young's modulus of the dense strut wall material E_d and the porous bulk material E_ϕ. Pabst and Grégorova [83], extended Eq.1 by incorporating the pore shape with the Eshelby-Wu coefficient (*EW*), which is dependent on the aspect ratio of the pores, the Poisson's ratio ν of the material and the direction of load. For prolate pores *EW* approaches 2.3 asymptotically (only for materials with $\nu \approx \nu_{calcite}$ = 0.322 [84]) and for oblate pores *EW* approaches infinity, illustrating the severe effect of oblate pore shape (Eq. 2).

$$E_\phi = E_d * (1-\phi)^{EW} \quad \text{(Eq. 2)}$$

For the dependence of strength σ on porosity the Gibson-Ashby framework (e.g. [77, 81, 85]) gives also a solution. However, for brittle foams the data basis was not solid as noted by the authors themselves [85]. Therefore, the applicability of Eq. 3 for all kinds of brittle foams is not proven:

$$\sigma_\phi = \sigma_d * C * (1-\phi)^{1.5} \quad \text{(Eq. 3)}$$

σ_ϕ gives the strength of the porous material, σ_d the strength of the dense strut wall material. *C* is a constant the authors determined on basis of their limited data to be 0.65. Later studies showed, that Eq. 3 can only be seen as an approximation. Dam et al. [86] give 2.2 for the exponent and 0.3 for *C*, Brezny and Green [87] give 2.1 for the exponent and show that *C* may be dependent on cell size [88]. Seuba et al. [89] fit Eq. 3 with *C* = 0.2 to a data set of freeze-casted alumina ceramics. However, the scatter in this data set is considerable even in a double logarithmic diagram. Nearly any model could have been fitted to the data. This is an inherent problem of brittle foams. Strength scatters considerably because it is governed by flaw size, which is statistically distributed in the material (see 1.3.1) and testing in uniaxial compression (UC) brings problems with coplanarity as loading is often not uniform [86] leading to premature failure.

Furthermore, it needs to be considered that equations from the Gibson-Ashby framework apply to a limited range of porosities. For strength of flexible and plastic foams the equations given in the Gibson-Ashby framework only apply to materials with $\phi > 0.7$ (e.g. [81, 85]). Unfortunately, the authors do not give such a limit of applicability for Eq. 3, possibly because of their small data set. However, from the formulation of Eq. 3 it is obvious that it can only be valid to comparably porous materials. The strength of a dense material with no porosity would calculate to only 65 % of its actual strength according to Eq. 3 (because of *C*). Therefore, Eq. 3 applies only to a limited range of porosities. Spines

of *H. mamillatus* usually have a lower porosity than 0.7 (the limit of applicability for strength of plastic and flexible foams) so it might be that they are not well described by Eq. 3.

Ji et al [90] give a more generalized formalism valid for all porosities (Eq. 4):

$$M_\phi = M_d * (1-\phi)^{1/J} \quad \text{(Eq. 4)}$$

with M being a specific property such as e.g. Young's Modulus or strength [90] of the dense strut wall material (M_d) and the porous bulk material (M_ϕ). The parameter J has a similar function as the EW coefficient: it describes the pore shape. Spherical pores have $J = 0.5$ [90], so for this special case Eq. 1, Eq. 2 with $EW = 2$ and Eq. 4 with $J = 0.5$ coincide. Eq. 5 is derived from Eq. 4 and replaces the $1/J$ exponent by the EW coefficient. By this the more meaningful EW coefficient replaces the J parameter.

$$\sigma_\phi = \sigma_d * (1-\phi)^{EW} \quad \text{(Eq. 5)}$$

Commonly, brittle foams are tested in uniaxial compression (UC) and the literature covering this is vast (e.g. [85, 89, 91-103]). All kinds of foams (brittle, elastic and flexible) show, in theory, three distinct regions in their UC stress-strain cures: Linear elastic region, plateau region and densification (Fig. 3A) [85]. The onset of densification depends on ϕ [85] and thus the length and strength of the plateau is also governed by ϕ. Foams are particularly well in absorbing energy and are hence used in the packaging industry [104]. Most of this energy is absorbed in the plateau [79]. Therefore, the higher the plateau strength, the more energy can be absorbed. Brittle materials have a large potential in energy absorbing purposes, since they are generally stronger than elastic or flexible foams and could protect against impact situations [105]. To quantify energy absorption or dissipation, the concept of energy dissipation efficiency, γ was applied. It is the ratio of dissipated energy and the theoretical maximum of dissipated energy, which is achieved by a constant plateau that equals linear elastic limit until the onset of densification (e.g. [106, 107]) (Fig. 3A). The approach by Miltz and Gruenbaum [106] was simplified in this work to [28] (Appendix I, Manuscript 4):

$$\gamma = \frac{\sigma_{pl}}{\sigma_{el}} \quad \text{(Eq. 6)}$$

with the measured average plateau strength σ_{pl} and the strength at elastic limit σ_{el} (Fig. 3B). However, the term "plateau" is misleading for brittle materials. It is rarely a plateau and even rarer smooth (Fig. 3B). Spines of *H. mamillatus* show a cascading graceful failure behaviour when loaded parallel to their long axis [27] in the strain range of the plateau. Sudden load drops caused by brittle fracture can recover quickly and strength of the elastic limit can be reached again (Fig. 3B). According to Presser [27] this striking behaviour is caused by the succession of dense GLs and porous radiating layers and is one reason why these spines where chosen as role model. The extend of the graceful failure was also quantified with Eq. 6 [28].

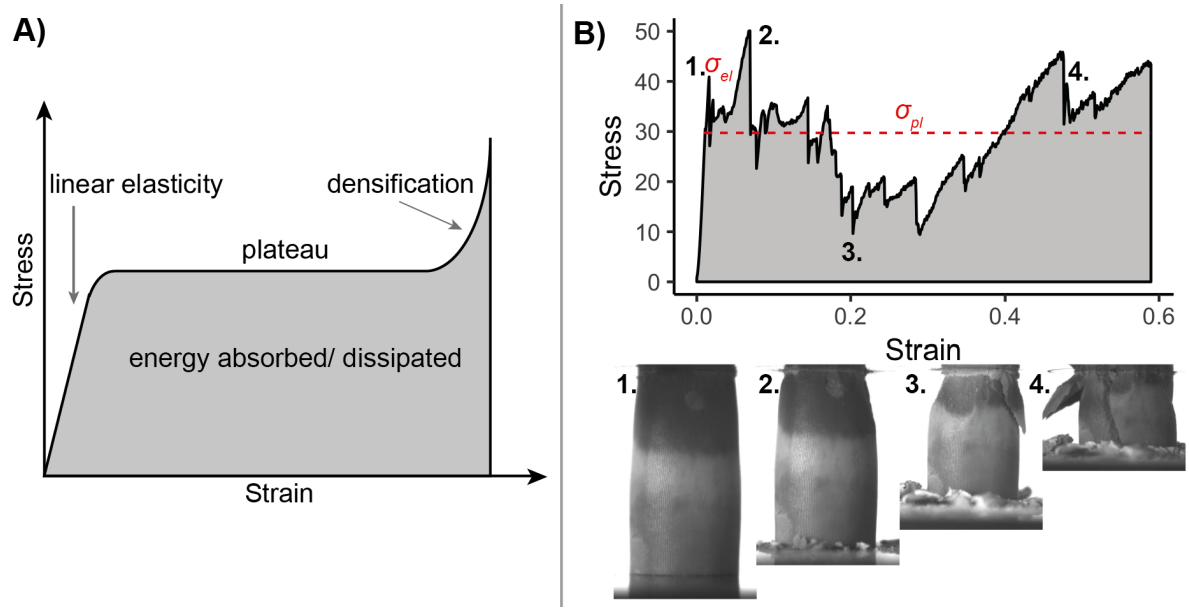

Figure 3: Idealized stress-strain cure of an elastic foam (A) compared to crushing behaviour of H. mamillatus spine segment with the rugged "plateau" (B). Numbers in B) correspond to pictures (1-4). Average plateau strength (σ_{pl}) and strength at elastic limit (σ_{el}) for calculating energy dissipating efficiency (Eq. 6) are indicated (here: $\gamma = 0.72$). Note that although this segment has a very pronounced cascading graceful failure behaviour [27], it has no growth layer but the one at the rim.

Presser et al. [27] were not the only ones who studied the mechanical properties of *H. mamillatus'* aboral primary spines. The authors in Table 2 conducted UC, 3-point (3PB), 4-point bending (4PB) and nanodindentation, however, the quality of the measurements is often difficult to assess. Only Presser et al. [108] related the mechanical data to porosity and they are also the only ones who took microstructure in both of their studies into account. None of the studies except Weber et al. [26] give the precision of sample manufacturing, and Weber et al. [26] and Vecchio et al. [61] do not report the sample population of their investigations. 3PB and 4PB were conducted with whole spines [45, 69], increasing the error of the measurement due to non-ideal geometry [109]. Because in most studies, neither porosity nor microstructure or macrostructure are reported and the quality of sample geometry is unknown, comparing these data with own measurements remains a difficult task. Nevertheless, it is attempted in section 4.1.3. Table 2 lists also the Weibull modulus m and characteristic strength σ_0, which leads directly to the last section of the introduction (1.3), the scalability of mechanical properties, namely the strength.

Table 2: Mechanical studies on aboral primary spines of H. mamillatus and H. trigonarius (*). UC = uniaxial compression, 3PB = 3 point bending, 4PB = 4 point bending, l/d = length/diameter, σ_{av} = average strength, E = Young's Modulus, σ_0 = characteristic strength (see 1.3.1), m = Weibull modulus (see 1.3.1).

Study	Mechanical test	sample shape	sample population (*n*)	Results
Weber et al. 1969 [26]	**UC** (confined)	machined cylinders, l/d = 3	not known, very few	confined compressive strength: 48 MPa
Su et al. 2000 [45]*	**4PB** (30 / 15 mm configuration) with Weibull Analysis	whole spines	17	4 pb strength: σ_{av} = 26 MPa, σ_0 = 29 MPa, m = 3.2
Vecchio et al. 2007 [61]	**UC** (unconfined)	whole spine cylinders l/d ≈0.6	not known	compressive strength: σ_{av} = 42 MPa
Presser et al. 2009 [27]	**UC** (unconfined) with Weibull Analysis	whole spine cylinders l/d ≈2	38	compressive strength: σ_0 = 58 MPa, m = 3.4
Presser et al. 2010 [108]	**nanoindentation** (Berkovich indenter)	indentations in all stereom parts	85	*E* = 39.8±6.1 (medulla) 62.6±3.7 GPa (GL)
Grossmann and Nebelsick 2013 [69]	**3PB** (small and large spines), 3 pb configuration not specified	whole spines (large and small ones)	27 (large) 10 (small)	σ_{av} = 29.1 MPa, *E* = 2,5 GPa (large) σ_{av} = 50 MPa, *E* = 2,8 GPa (small)
Cao et al. 2017 [62]	**UC** (not confined) with Weibull Analysis	whole spine cylinders, l/d ≈1.3	33	compressive strength: σ_{av} = 43.4 MPa, σ_0 = 49 MPa, m = 3.1

1.3 The problem with becoming big

1.3.1 Weibull Theory

Biological role models are often magnitudes smaller than the technical application they inspire, so the question of upscaling is closely linked to biomimetic research. For many properties, however, up scaling would destroy the function, as e.g. the superhydrophobicity of lotus leaves or the adhesion of gecko feet (Table 1) is caused because of the structural layout and size [21]. These properties can only be transferred to technical surfaces, if they are structured in the same size as in the biological role model.

For mechanical properties such as strength, there is also a clear dependency on size. It was already noted by da Vinci and Galileo [110] and proven by Griffith [111] in 1921: strength decreases with increasing size (volume) when considering the same material.

Weibull [112] was the first who described the strength of materials probabilistically, as a function of the volume *V* and the applied stress σ. In its simplest form it can be done by only two variables, the Weibull modulus *m* (also: shape parameter) and the characteristic strength σ_0 (also: scale parameter):

$$P(V,\sigma) = 1 - \exp\left(-\frac{V_i}{V_0}\left(\frac{\sigma_i}{\sigma_0}\right)^m\right) \quad \text{(Eq. 7)}$$

with the failure probability P, the sample i, the applied stress σ_i, and the Volume V_i, and the referencing volume V_0, which is for convenience mostly set to equal the volume of the sample population [113]. In the specific case of strength of brittle materials the Weibull distribution has also a physical meaning [110]. Starting point is the weakest link theory, often illustrated with a chain that only bears the load its weakest link is capable of. Only by the failure of this single link, the whole chain loses its function. Coming back to brittle materials, they all contain weakest links in form of flaws, which are impurities, little pores or cracks. They govern the failure of the whole material. The flaw size is statistically distributed with the critical large flaws being rare. The tail of the flaw size distribution, where the large flaws are located, is well described by the Weibull distribution [113, 114]. It is more likely to find such a rare large flaw in a large volume than in a small volume (e.g. [110, 113]). Therefore, the reason why larger samples exhibit a lower average strength than smaller samples of the same material is of pure statistical nature. This phenomenon is called size effect and illustrated in Fig. 4.

Eq. 7 is often rearranged in such a way, that the Weibull distribution can be displayed as a straight line in a double logarithmic diagram (Fig. 4). m is the slope of this distribution and can be obtained by many methods (e.g. [115, 116]), commonly by linear regression (LR) or maximum likelihood estimation (MLE). m is ideally a material constant and independent of the sample volume. It is a measure for the reliability of the material: The higher m, the narrower the range of failure stresses and thus the more reliable and predictable is material failure. For technical ceramics m = 5-20 [117] and non-brittle materials have considerably higher Weibull moduli (e.g. Mg alloys: m > 90, [118]).

The characteristic strength σ_0, is the strength where ~63.2 % of all samples failed (y = 0) and depends on the sample volume (Fig. 4). The size effect of two samples with volume V_{01} *and* V_{021}, and characteristic strength σ_{01} and σ_{02} respectively, can be calculated with by modifying Eq. 7 to:

$$\left(\frac{\sigma_{01}}{\sigma_{02}}\right) = \left(\frac{V_{02}}{V_{01}}\right)^{\frac{1}{m}} \quad \text{(Eq. 8)}$$

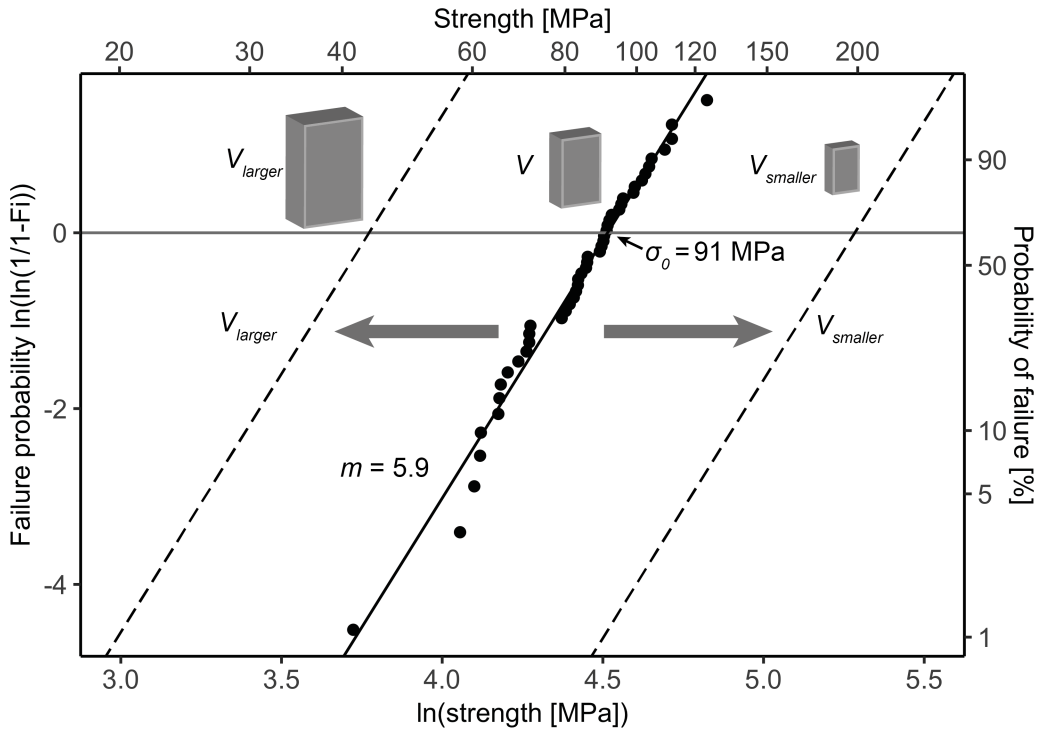

Figure 4: Schematic expression of the size effect from spines of a single animal (data from [28], Appendix I, Manuscript 4). With increasing sample volume, the strength of the samples should shift left to lower strengths and with decreasing sample volume it should shift right to higher strengths (dotted lines). The Weibull modulus m, is ideally independent of the size in contrast to the characteristic strength σ_0.

1.3.2 Size effect

It was long assumed, that if a size effect occurs, it is of statistical nature and can be explained by Weibull theory [110] (Eq. 8). However, Weibull theory applies only to samples with uniformly distributed and non-interacting flaws [110, 119] and also requires immediate failure of the sample after crack activation and no redistribution of stresses. This requirement seems trivial, but many nominal brittle materials exist, where it is not met. Concrete beams do not fail after crack initiation in bending. Before final failure an zone of large and stable growing cracks develops, the fracture process zone (FPZ) [110, 114]. In it, considerable stress redistribution occurs. Materials with these properties were coined "quasi-brittle" and include besides concrete, many brittle foams and also many biological materials (e.g. wood and shells) [110]. Quasi brittle materials experience a notably stronger size effect than brittle materials (e.g. [120]) and this size effect type was termed energetic-statistical.

Instead of the critical crack size of the brittle materials (i.e. the Griffith crack size), quasi-brittle materials have a the representative volume element (RVE) as failure criterion. This is the volume that needs to fail in order for the whole material to fail [114]. The RVE and FPZ are usually of the same size and approximately 3 times the dominant inhomogeneity size of the material [114, 120]. When quasi-brittle materials become large enough, their size effect becomes purely Weibullian again and the statistical component overpowers the energetic component [110, 114, 120-122] as the FPZ becomes

one of many (statistical) weaknesses. Therefore, the type of fracture (quasi-brittle or brittle) depends on the volume of the material tested and, thus the encountered size effect is also a function of the tested volume. For example concrete beams behave quasi-brittle in lab scale but brittle on dam wall scale and fine grained ceramics are quasi-brittle on a μm-mm scale but brittle in most applications [120]. This means vice versa, that all "brittle" materials behave quasi-brittle on a sufficiently small scale and only become brittle at larger scales.

As outlined above, natural materials and foam ceramics often behave quasi-brittle in common sizes. Spines of *H. mamillatus* are a biologically formed foam ceramic, yet brittle failure is encountered. In bending they fail catastrophically after the linear elastic increase in a single crack event, with no visible stress redistribution from stress-strain curves [28, 69]. Setbacks in stress-strain curves derive from imprinting of the loading rollers in the compliant stereom (compressive forces) and do not originate from bending failure[28]. In UC, however, failure was described as "graceful" [27] (Fig. 3b) and might be indicative for stress redistribution in quasi-brittle failure. As this is an issue with any foam ceramic, Seeber et al. [123] concluded that bending is the only reliable failure mechanism as catastrophic failure occurs. Therefore, the stress redistribution in the spines of *H. mamillatus* is attributed to the testing method and not to the quasi-brittleness of the material. Additionally, it needs to be underlined, that in UC stress redistribution was not due to the growth of large stable cracks, but to the localized failure of single struts in contact with the loading pads. As soon as large cracks emerged (horizontally or vertically), sudden and smooth stress drops were visible in the stress-strain curves. They showed no signs of softening, as concrete does.

Keeping in mind the delicate foam structure of *H. mamillatus* spines, it is very likely that the size encountered in the mechanical tests, surpasses the threshold from quasi-brittle to brittle with 1000 RVEs per material [114]. Although the exact size of a RVE is unknown, the dominant heterogeneity in the structure can be seen as the building block of the second hierarchical level (a cell of struts surrounding a pore), hence, even a conservative estimation yields more than 10^6 RVEs in a medium spine. Therefore, a size effect according to Eq. 8 is expected.

The size effect in biological materials was not investigated by many researchers, although the few findings published point towards a deviation from the size effect predicted by Eq. 8 or Bažant. It was stated by Vincent [1] that the size of the smallest building unit (i.e. the nanocrystals for biological ceramics such as nacre or echinoderm calcite) is below the critical crack size and are thus crack free constituting to high strength and stiffness. Hence, critical cracks are restricted to higher hierarchical levels, where the composite structure of natural materials makes fracture much harder [1]. Taylor [124] noted, that the fatigue strength of mammalian bone does not scale with size. In bones of larger mammals the hydroxyapatite crystal orientation is optimised and with secondary osteons a new hierarchical level is introduced, both mechanisms increase the fatigue strength and counteract the size effect [124]. Lei [119] evaluated the size effect in tensile strength of wood in longitudinal direction and could show that it is less pronounced than proposed by Eq. 8 and that Weibull size effect can also be applied to non-

uniformly distributed flaws. Trujillo et al [125] tested bamboo fibres and could also show that their dependence on size (in this particular case length) is lower than predicted by Eq. 8.

In terms of spines of *H. mamillatus* the size effect was not investigated yet, though it could be shown that the strength distribution can be well fitted with Weibull statistics [27, 45, 61, 62]. This is the starting point for the size effect investigations in this study, which leads directly to the objectives (2).

2. Objectives

This study sets out to answer two **key questions**:

1. **How does structure relate to property in the spines of *Heterocentrotus mamillatus*?** As outlined in 1.2.3 prior studies concerned with this topic often failed to report exact measurement conditions or did not take the microstructure and/or porosity into account. This shortcoming is addressed in micro- and macrostructural analysis tailored for mechanical properties [41, 65] (Appendix I, Manuscript 2 and Appendix II, Manuscript 5), followed by an in depth analysis of the mechanical properties with means of uniaxial compression, 3-point bending and resonance frequency damping analysis [28] (Appendix 1, Manuscript 4). Furthermore, the first time it was attempted to reveal the influence of amorphous calcium carbonate on the mechanical properties [57] (Appendix II, Manuscript 6).
2. **Of what nature is the size effect in spines of *H. mamillatus*?** Many biological materials seem not to follow Weibull's size effect predictions (1.3.2). A joint study of the two biological role models in project B01 was conducted [59] (Appendix I, Manuscript 3) and due to large biological heterogeneities in the spines of *H. mamillatus*, the assessment of the size effect underlies uncertainties. A local testing method was developed to overcome them [126, 127] (Appendix I, Manuscript 1 and Appendix II, Manuscript 7) and was then applied [128]. (Appendix II, Manuscript 8)

During the work concerned with the two key questions, also other observations were made as well that are not reported and discussed in the cumulative PhD Thesis. Lauer et al. [65] contributed to the ongoing debate of the way sea urchin spines grow. Lauer et al. [57] investigated how the minor constituents of the composite material sea urchin spine contribute to the macro-mechanical ("bulk") properties. In order to do so, plentiful analytical methods were applied to identify and quantify all relevant phases in the system. The analytical procedure is not reported here, details are found in [57]. Section 3.1.4 concentrates on the mechanical tests conducted with the knowledge obtained in [57].

The reader is generally pointed to the publications and manuscripts, as this introduction to the cumulative PhD Thesis is only a brief report of the more detailed investigations. In the results section the morphological investigations are reported first (3.1.1, 3.1.2) contributing to key question 1, followed by the mechanical properties influenced by the morphology (3.1.3). Then the strength size relationship (key question 2) is investigated (3.2.1), which required the development of a new method (3.2.2) and finally more refined measurements were possible (3.2.3).

Please note that if not mentioned otherwise, the term "spine" in this study relates to the large aboral primary spines only (Fig. 1A) and that growth layer refer to distal growth layers only (Fig. 5A).

3. Results

3.1 Key Question 1: Structure-property relationships

3.1.1 Morphology

GLs were described by Presser et al. [27] as the most relevant structural feature for mechanical properties. Several GL types were identified in this study (Fig. 5A) [41], with only the distal capping layers and the regular GLs exhibiting the characteristic cap, which is important for graceful failure [27]. Distal capping layers were only found in the largest aboral spines [41] and they were absent in the majority of the aboral spines.

GL spacing and number is unique for each spine [65]. It is impossible be deduce these from other spines of the same animal, even if the spines are of the same size and plate position (Fig. 5C). GL structure needs to be characterised for each spine individually.

On the same hierarchical level as the GLs another structuring entity was found. Numerous (often >200) thin, wedge-like features organise the spine in a radiating manner [41]. The idealized layout of such a wedge is sketched in Fig. 5D. By this alternating succession of porous stereom interspace and radiating trabeculae, longitudinal structural weaknesses are introduced into the spine. This building principle is best visible when many GLs are present (i.e. in basal cross sections) but is difficult to discern when they are absent (i.e. at the tip) [41]. In the spines of the congeneric *H. trigonarius* this radiating building principle is much more evident [28].

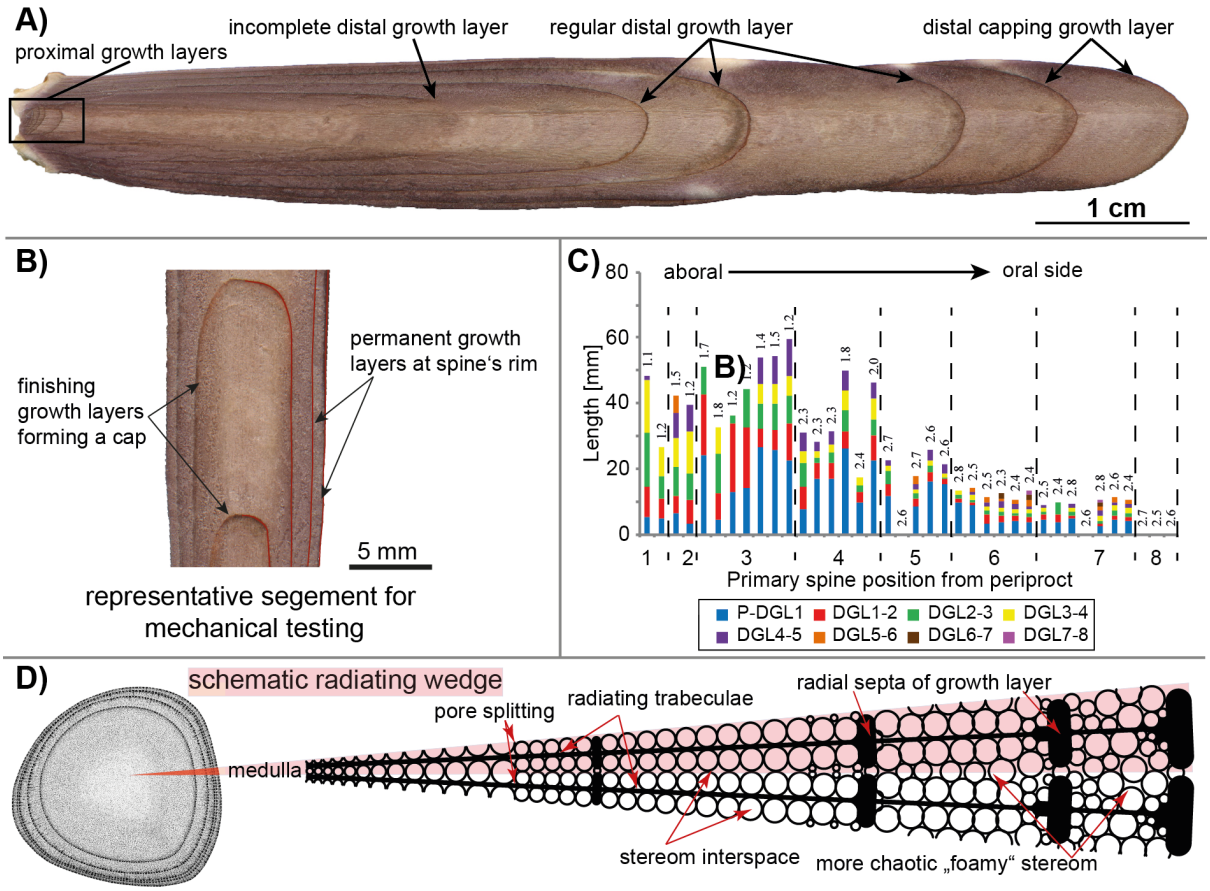

Figure 5: Summary of the morphology of H. mamillatus' spines. Growth layer type classification (A) and their characterisation for mechanical testing (B). Growth layer spacing of spines from the same animal in relation to position on test (C). Colours indicate extent of a growth cycle measured from tip to tip of each growth layer (P = proximal growth layer, DGL = distal growth layer). D) displays a schematic wedge representation. Modified after [41, 65].

3.1.2 Porosity

Local porosity determination was performed as described in [41]. Porosity varies strongly in a single aboral spine of *H. mamillatus* and two porosity gradients became apparent:

1. The porosity increases from the bottom to the tip of the spine. This porosity increase can be as high as 0.15 in a large aboral spine (Fig. 6A) [41].
2. The porosity decreases from the centre (medulla) towards the rim of the spine, where the dense GLs are located. Peak porosities in the medulla can reach 0.9, while GLs are comparably dense with porosities of 0.2-0.4 (Fig. 6B) [41], depending on spine type (Fig. 6D) and (relative) age (Fig. 6E) [128].

Small aboral spines, located on the youngest plates of the test, show the same porosity trends as large aboral spines (Fig. 6A), although generally on a slightly lower porosity level [65]. Oral spines show a different porosity trend [65] (Fig. 6A) and are unsuitable for mechanical testing due to their flattened shape and small size.

H. trigonarius' large aboral spines also display these two porosity trends, although on a significantly denser level (approx. 0.1 denser (Fig. 6B, C)) [28].

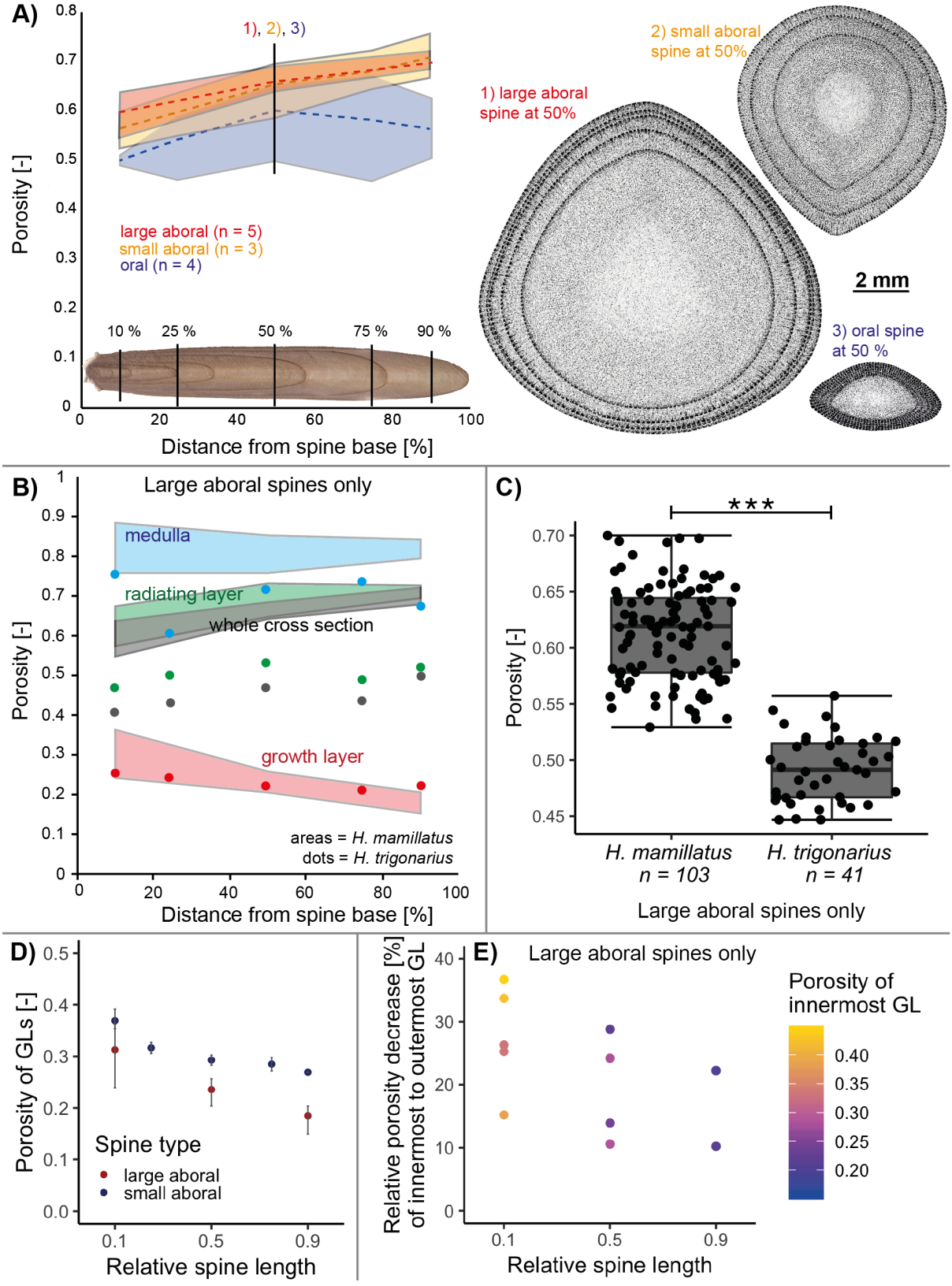

Figure 6: Summary of the porosity of spines of H. mamillatus. A) shows the porosity variations in spine length of oral, small and large aboral spines alongside representative cross sections. Porosity of the different stereom types for H. mamillatus (n=5 spines, areas) and for a representative H. trigonarius spine (data dots) (B). Porosity data

*in A), B), D), E) was obtained by image analysis (for methodology: [41]) and in C) by gravimetry for bulk porosity of segments used for UC. H. trigonarius is significantly denser (Welch t-test, ***p ≪ 0.001). Growth layers (GLs) are denser in large than in small aboral spines (D) and the porosity of growth layers decreases towards the outermost GL at the rim of the spine (E). Adapted after [28, 65, 128].*

Porosity of the dense GLs of *H. mamillatus* was investigated in more detail (Fig. 6D, E). They are considerably denser in large aboral spines than in their smaller counterparts (Fig. 6D). Porosity of GLs decreases from innermost to outermost GL systematically in all large aboral spines investigated (Fig. 6E) meaning that the youngest and outermost GL has the lowest porosity.

The morphological and porosity investigations stressed that each spine needs to be characterised thoroughly before mechanical testing. Both, structure and porosity, scatter considerably and it is not possible to extrapolate from one spine to another. Therefore, bulk porosity was gravimetrically determined before each measurement and local porosity analyses were conducted for local testing. GLs were counted on the top and bottom side of each testing sample and high resolution optical scans of the two cross sections were taken. The difference in GL quantities on those two sides was assigned to "finishing growth layers" (GLf) in the testing specimen and the remaining GLs were assigned to "permanent growth layers" (GLp) (Fig. 5B). They are constantly present as a "shell" protecting the porous "core". As prior to testing the course of GL is difficult to assess (only by CT) this rather unprecise characterisation was the best at hand. After testing and fracturing the course of the GLs could be analysed, if necessary.

3.1.3 Mechanical Investigations

All mechanical tests are summarised briefly in Table 3 and references for more detailed information are given. The paragraphs and figures below describe the most important findings.

Strength of *H. mamillatus* spine segments measured in UC is largely influenced by porosity and the amount of permanent GLp [28]. Samples with more GLp are more likely to have a high strength, than samples with only one GLp (Fig. 7A). For example, at the same porosity those samples with many GLp are stronger than samples with few GLp (Fig. 7A). Increasing porosity clearly reduces the strength (Fig. 7A). Porosity and the quantity of GLp are loosely linked to each other, as more dense GLs decrease the porosity. However, as Fig. 7A shows, also porous spines with many GLp and dense spines with few GLp exist. The strength of the denser *H. trigonarius* spines is significantly higher than those from *H. mamillatus* (Fig. 7B) [28].

The porosity dependence of the spines' Young's Modulus (E) can be well modelled with Eq. 2 [28] with EW = 2-2.3, which indicates spherical to longitudinal pore shape for the mechanically relevant pores [83] (Fig. 7C). E depends strongly on porosity and ranges for *H. mamillatus* between 8-16 GPa. Resonance frequency damping analysis (RFDA) is best suited for measuring E of these biological samples. In 3PB issues with imprinting of the loading rollers into the samples occurred, complicating

correct calculation of the strain. Imperfect coplanarity in UC leads to a heterogeneous load distribution in the sample and erroneous strain calculation ([28], also 4.1.2).

Table 3: Brief summary of all mechanical tests of H. mamillatus (H. trigonarius: HT) published or in prepared manuscripts. Results depend on porosity and internal structure and are listed to give an overview only. Strength (σ) is given in MPa, Young's Modulus (E) in GPa and energy dissipation efficiency (γ) is dimensionless.

Testing method	Cumulated sample population (n)	Used to answer which questions?	Where to find more detailed information?	Mechanical key data
Uniaxial compression	Unconfined spine segments: >173 (HT: 59) Confined spine segments: 3 Drilled cores: 40	- Strength of spines, σ - Size effect - Energy dissipation efficiency, γ - Young's Modulus, E	Lauer et al. 2018a [59] Lauer et al. 2018b [28] Lauer et al. [57] Lauer et al. [127]	σ = 20-124 (HT: 37-169) E = 5.1-16.1 (HT: 6.4-18.8) γ = 0-0.72 (HT 0-0.19) (data for unconfined spines only)
3-point bending	Full spines: 10 Drilled cores: 32	- Bending strength, σ - Young's Modulus, E	Lauer et al. 2018b [28] Lauer et al. [57]	σ = 22-33 (cores: 17-65) E = 6.6-16.6 (cores: /)
Resonance frequency damping analysis	Full spines (fs): 18 (HT: 8) Drilled cores (c): 12 (HT: 8)	- Young's Modulus, E	Lauer et al. 2018b [28] Lauer et al. [57]	E (fs) = 10.5-15.9 (HT: 16-24.4), E (c) : 2.7-8.6, (HT: 15-23.3)
Pin indentation	Shallow indentations: >108 Deep indentations: >50	- Strength, σ - Energy dissipation efficiency, γ - Size effect	Schmier et al. 2016 [126] Lauer et al. [127] Lauer et al. [128]	σ = 18-183 γ = usually >1

Microstructure was found to have a large influence on crack propagation. The wedge-like superstructure often resulted often in "piece of cake" shaped flakes fracturing during testing (4.1.2, Fig. 13B). Cracking alongside GLs, as reported by [27] was less observed and comparably rare (4.1.2).

Energy dissipation efficiency (γ) is influenced by porosity and the simplicity of the spine structure. Generally, a threshold porosity of 0.55-0.6 needs to be exceeded for showing γ (Fig. 7D). This is the reason why the denser spines of *H. trigonarius* are less good in dissipating energy (Fig. 7D). All 5 spines with the highest energy dissipation had the same structural layout: only one permanent GL and, if any, only few finishing GLs. A possible explanation is given in 4.1.2. γ levels < 0.2 should not be considered for energy dissipation. These low values are obtained when large parts of the spine were spalled and only remnants carried the load.

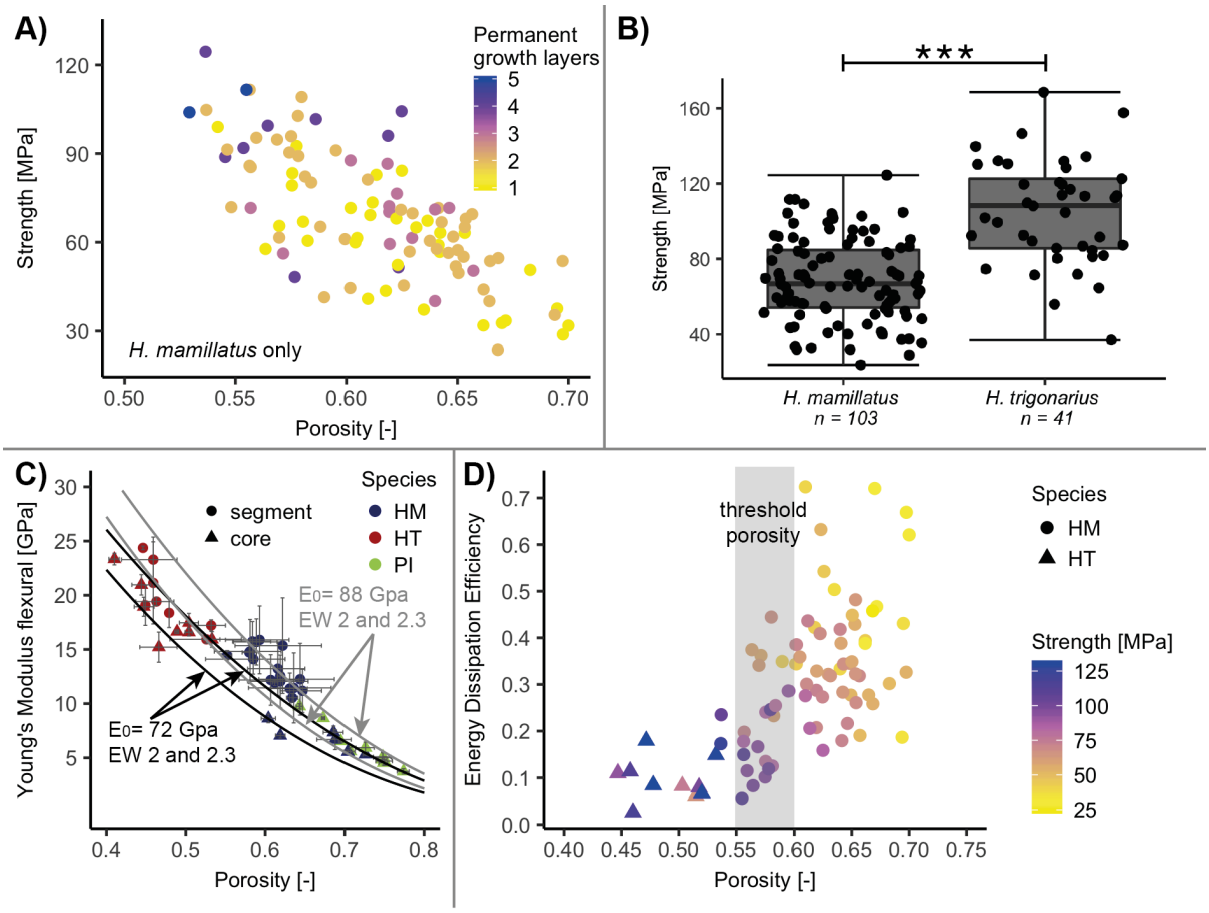

*Figure 7: Summary of the mechanical testing. A) shows the strength range of large aboral spines of H. mamillatus (HM) and how it is influenced by porosity and growth layers. Spines of H. trigonarius (HT) are significantly stronger than spines of H. mamillatus (Wilcoxon rank-sum test, ***$p \ll 0.001$) (B). Young's Modulus was measured with Resonance frequency damping analysis (C) and values follow predictions of the model (Eq. 2)[83]. Energy dissipation efficiency of HM and HT spines is shown in (D). A threshold porosity of 0.55-0.6 needs to be exceeded (grey shaded area). Modified after [28].*

3.1.4 Influence of amorphous calcium carbonate on mechanical properties

The influence of amorphous calcium carbonate (ACC) on mechanical properties of the spines of *H. mamillatus* was revealed by heating spines to 250 °C in order to crystallize ACC. This temperature was determined by a multi-method approach including XRD, IR, TG-MS, DSC and microstructural observations in SEM [57]. By combining the results of these methods the temperature intervals of the Mg-calcite decomposition, dewatering and organic decomposition, all processes also taking place when heating echinoderm calcite (Fig. 8), could be narrowed down, so that their influence on mechanical properties can be excluded [57]. When heating the spines with a ramp of 1 °C/min to 250 °C followed by immediate cooling with the same speed, complete ACC crystallization is the only process that takes place.

A prolonged dwelling time would start Mg-calcite decomposition into dolomite and brucite (Fig. 8). These processes would induce microporosity and crack formation, by which pathways for dewatering would be created. A slight irreversible dilatation of 0.1 % at 250 °C was found and is

possibly due to crack formation induced by ACC crystallization. These cracks need to be considered for assessing changes of mechanical properties of heated spines. The water content of the spines could be estimated to ~2.5 wt% by TG-MS, the ACC content to ~ 5.5 wt% by DSC and the organic content to <0.5 wt% [57]. For a more detailed description of the analytical procedure the reader is guided to [57] (Appendix II, Manuscript 6) and [129].

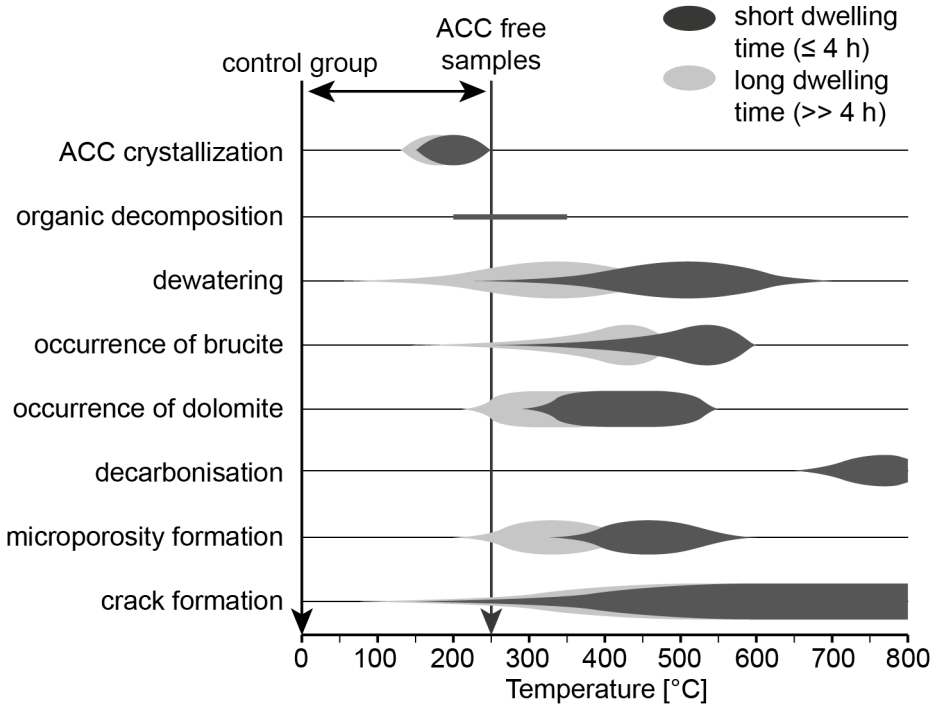

Figure 8: Schematic summary of all processes taking place when heating spines of H. mamillatus. At 250 °C ACC crystallization is terminated and with no dwelling time other processes have not started. Modified after [57].

For 3PB and UC respectively, samples were split into two groups with statistical undistinguishable sample distribution in respect to volume, porosity and number of GLs [57]. UC revealed no difference between those two groups (Fig. 9A) (median strength: 55 MPa heated, 53 MPa unheated, Wilcoxon test: $p = 0.7$). In 3PB differences are also statistically not significant (median strength: 33 MPa unheated, 28 MPa heated, Wilcoxon test: $p = 0.24$), but Weibull analysis reveals a considerable change in failure reliability (Fig. 9B). Heated samples' m is reduced from 4.5 to 2.8. Generally the Weibull distribution does not describe the 3PB data as well as the UC data. Whether this is due to the small sample population compared to UC or because in 3PB testing a bimodal flaw size distribution is present [113] could not be resolved here.

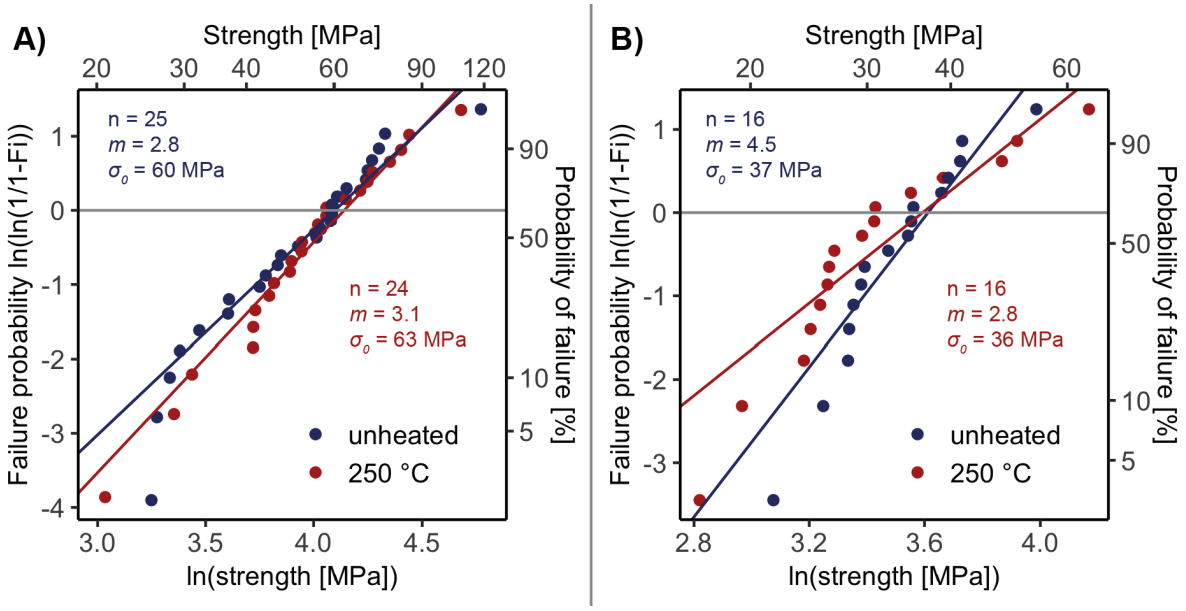

Figure 9: Strength distribution in uniaxial compression (A) and 3-point bending (B), modified after [57].

E changes were measured with non-destructive RFDA on the same samples upon heating. *E* decreased consistently for all samples (n = 7) in the range of 2-8 % when heated to 250 °C, which is statistically not significant as it lies in the range of measurement error [57]. However, these samples were kept for 4 h at 250 °C and it is likely that without dwelling time (as for UC and 3PB) the drop would have been even smaller. RFDA samples were subsequently heated to higher temperatures and even at 500 °C with 4 h dwelling time the porosity adjusted changes in *E* (as microporosity and irreversible dilatation increase porosity) were as little as 0-16 %. Considering the amount of micropores and cracks that are present at 500 °C [57] this is an intriguing finding.

3.2 Key Question 2: Strength-size relationship

3.2.1 Strength-size relationship in uniaxial compression experiments

UC experiments conducted with spine segments of different sizes displayed no significant relation between size and strength (Kruskal-Wallis test, p = 0.14), however, the scatter in data is considerable (Fig. 10A) [59]. The highest strengths were measured in the sample group with the second largest volume. Due to the apparent independence of size and strength, we felt justified to plot all data in a single Weibull plot (Fig. 10B). The colour code indicates that the porosity, in contrast to volume, influences the failure probability. Samples with higher porosity are more likely to fail than samples with low porosity [59]. Both, σ_0 (65 MPa) and m (5), are considerably higher than previously reported [27, 45, 62].

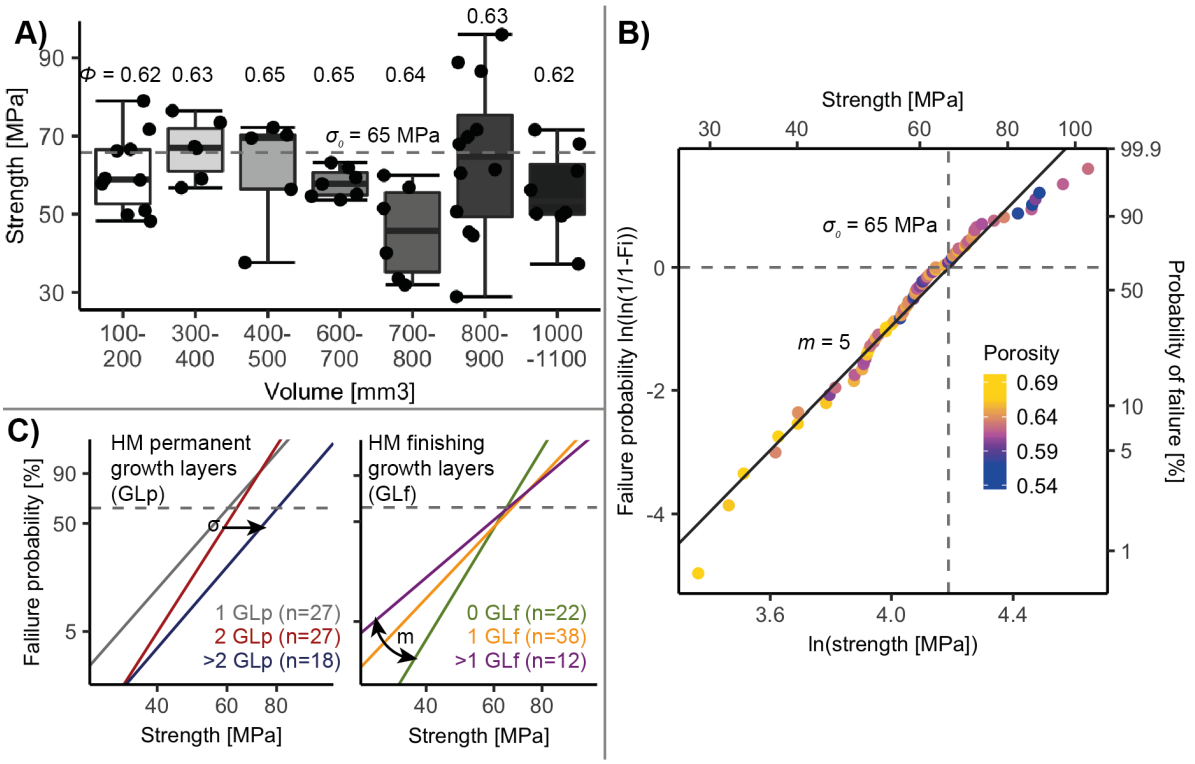

Figure 10: Summary of the strength-size relationship in uniaxial compression of H. mamillatus' spines. No such dependency as described by Eq. 8 was found and the volume of samples seems not to affect strength (A). Numbers above boxes display average porosity of each group (A). In contrast, the influence of porosity is evident in the Weibull plot (B). Growth layers affect σ_0 and m (C). Data dots are not shown for clarity but the number of samples (n) is given in the plots. Modified after [59].

The internal structure in form of GLs profoundly influences σ_0 and m. Samples were split according to the quantity of GLp and GLf (Fig. 10C). Samples with a more developed core-shell structure due to many GLp exhibited a significantly higher strength (81 MPa vs. 60 and 64 MPa, One-way Analysis of Variance, $p < 0.001$, Tukey HSD post-hoc test), whereas m decreases with the number of GLf from 7.2 for segments with no GLf to 3.7 of segments with more than 1 GLf.

The influence of porosity and internal structure might overprint the size-strength relationship. A method that circumvents these obstacles is needed to evaluate the exact nature of the strength-size relationship. From the bulk UC data it can only be deduced that the correlation of strength and sample size is probably weaker than predicted by Weibull theory (Eq. 8), because for a magnitude of size difference no size effect was found [59]. For this purpose the pin indentation (PI) method was developed (3.2.2) and applied (3.2.3.1). Furthermore, cores of two different sizes with defined geometry drilled out of the spines were measured (3.2.3.2).

3.2.2 Development of pin indentation method

PI is a downscaled UC test with the loading plate (i.e. the pin) being much smaller than the sample [126]. The method originates from metal foams (e.g. [130, 131]) and was refined for ceramic foams during this PhD. A pin is pushed with constant speed into the sample and produces a sharp and

deep impression (Fig. 11A, B) [126, 127]. PI can be used for two purposes: (1) Measurement of the pin indentation strength (σ_{PI}) and (2) measurement of the energy dissipated during the indentation (Fig. 11C). σ_{PI} is defined as the strength terminating the linear elastic increase, ideally the high elastic limit (Fig. 11E). For this parameter shallow measurements just exceeding the first major load drop are sufficient. The measurement of energy dissipation requires deeper pin indentations [127]. By variation of the indenter diameter (i.e. 0.6, 1 and 3 mm) and the selection of appropriate testing locations, different volumes of the material can be tested. Hence, the size effect is investigated without the influence of GLs, other structural heterogeneities and the issue of coplanarity.

σ_{PI} is not equal to the strength measured in UC (σ_{UC}) (Fig. 11D) as the force field induced by the pin is larger than the area of the pin [127] (Fig. 11C). An elastic stress field with the approximate shape and extent after simulations of [132] arises. Therefore, σ_{PI} represents an engineering stress that derives from a larger area than the pin, which increases the measured strength. In the case of the spines of *H. mamillatus*, σ_{PI} is 45 % higher than σ_{UC} fitted by Eq. 3 and 56 % higher fitted by Eq. 5 (Fig. 11D) [127].

In the moment where the pin cuts into the material, the upper part of the elastic stress field surrounding the indenter relaxes again and the whole stress field moves together with the pin deeper into the material. Failure occurs beneath the pin indenter only. At the indenter rim the material does not fail by compression but by shearing or bending forces. These forces might be considerable for metallic foams, where the method is derived from, but they are negligible for ceramic foams, as ceramics are much weaker in bending than in compression [77].

When penetrating deeper into the material for measuring the energy dissipation properties, crushed material accumulates in front of the pin and densifies (Fig. 11C). By this process, the stress after σ_{PI} increases until a plateau is reached (denoted by * in Fig. 11E). As only tapered indenters were used to reduce the friction between indenter wall and material [127], crushed material “flows” around the pin into the tapering. When this process and the densification in front of the pin reach an equilibrium, the stable plateau develops (Fig. 11E) [127].

Deep PI can also be used to uncover structural heterogeneities hidden in the structure as they are expressed by stress changes in the plateau. Growth layers lead to a spike in the recorded stress [27, 126]. For other applications of PI the reader is recommended to reference [127] (Appendix II, Manuscript 7).

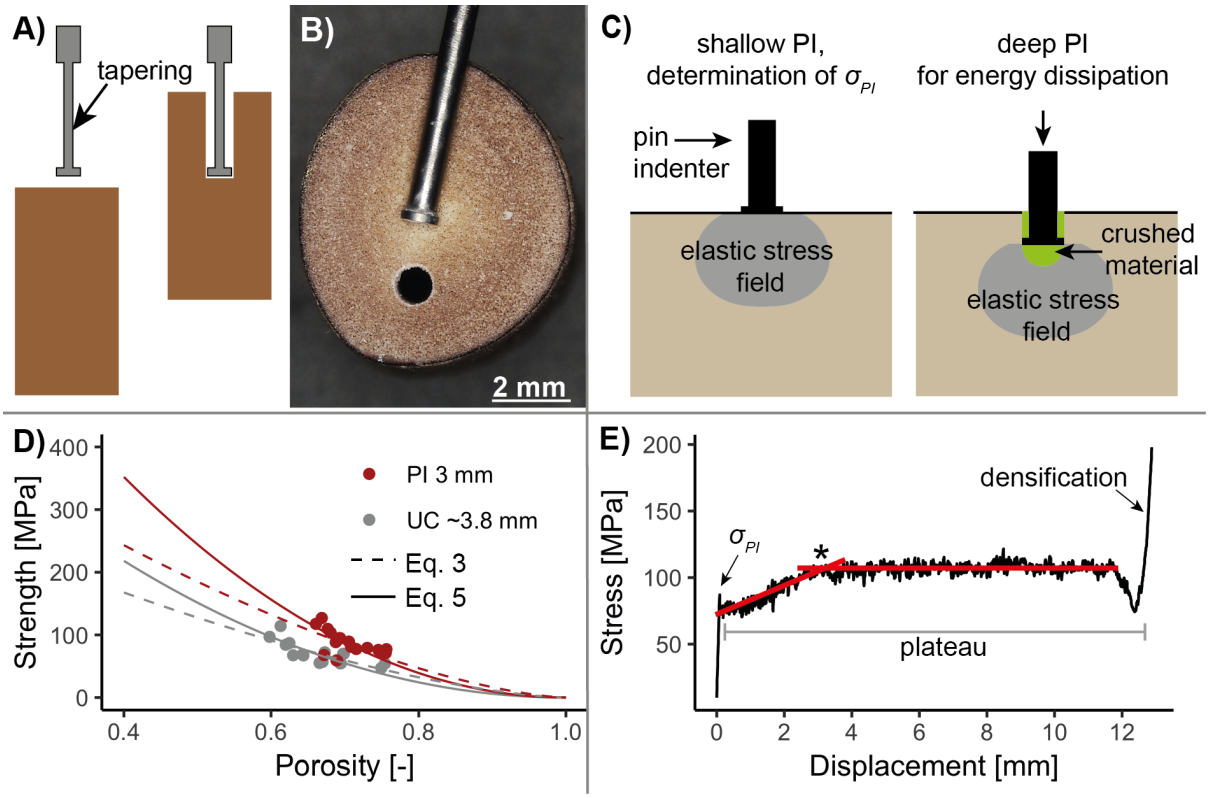

Figure 11: Principle of pin indentation (PI) (A) and the sharp impression of the pin after testing (B). The pin indentation strength σ_{PI} is obtained by shallow PI (C) and is determined by the elastic stress field being larger than the indenter. Due to this stress field σ_{PI} is higher than σ_{UC} (D). Data were fitted with Eq. 3 (dashed lines) with C = 0.65, σ_0 of 805 MPa (3 mm PI) and 555 MPa (UC, ~3 mm cores). Full lines represent fits with Eq. 5 with σ_0 of 946 MPa (3 mm PI) and 606 MPa (UC, ~3 mm cores) and EW = 2 for spherical pores. Deep PI can determine energy dissipation and produces a smooth plateau (E). Additionally the accumulation of crushed material arises (C) increasing the strength until an equilibrium between the material accumulating in front of the pin and the material flowing around in the tapering is reached (in E). Modified after [127].*

3.2.3 Overcoming heterogeneities to evaluate the size effect

3.2.3.1 Pin indentation

For investigation of the size effect, σ_{PI} was measured with three different pin indenter sizes (0.6, 1, 3 mm). Fig. 12A includes all measurements and Fig. 12B shows PI with a local porosity of 0.64-0.7 only. Porosity was determined locally by a method developed in [41] and further refined for the PI experiments [127]. Independently of the pin indenter diameter, dense PIs tend to have a higher σ_{PI} than the porous PIs (Fig. 12A). No difference was found in σ_{PI} measured with 0.6 and 1 mm (Fig. 12A, Table 4). Their σ_0 and m are comparable. 3 mm PI revealed a lower σ_0, although much less so than predicted by Eq. 8 (Fig. 12A). For this prediction the area of the PIs were used as V_1 and V_2, which is a simplification and is discussed in 4.2.1. If considering the higher mean porosity of the 3 mm PIs (Table 4) compared to the 1 and 0.6 PIs, the gap of the respective σ_0 narrows down to ~10 MPa (Fig. 12A, Table 4). However, as porosity correction always underlies uncertainties, Fig. 12B shows for better comparability PIs of the porosity interval between 0.64-0.7 only. In this representation, PIs including

GLs were omitted as well, which was especially an issue for 3 mm PIs. 4 of 19 contained a GL and they all except one had $\sigma_{PI} > 100$ MPa, showing the severe influence of GLs [128, 133]. Unfortunately, the population size of the 3 mm PIs is small, but exhibits clearly lower σ_0, coming closer to the predictions of Eq. 7 (Table 4). This may be indicative for a weak size effect.

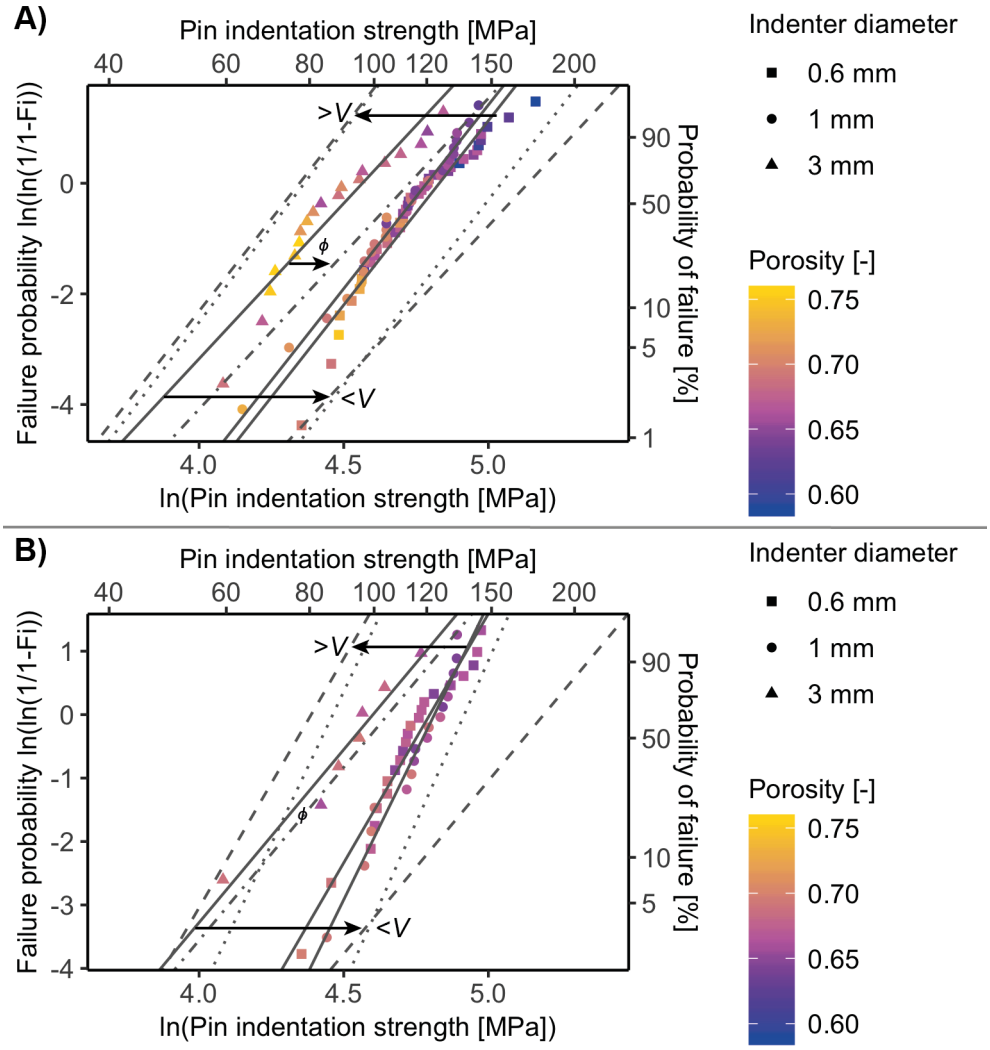

Figure 12: Pin indentation strength of H. mamillatus spines tested in the radiating layer including all measurements (A) and only those with porosity of 0.64-0.7 and no growth layer (B). Doubly dashed line illustrates strength shift of 3 mm indentations due to mean porosity adjustment with Eq. 5 (Table 4), single dashed lines show size effect predicted by Eq. 8 and dotted lines by highest m within the confidence interval (Table 4). Weibull modulus displayed is obtained by LR. Data from [133] modified after [128].

The determination of *m* has some uncertainties highlighted by the different fitting results with LR and MLE and by the 95 % confidence intervals of MLE (Table 4) and affects the extrapolation with Eq. 8 [128]. However, even when applying the upper limit of the 95 % confidence interval for extrapolation, the size effect in spines of *H. mamillatus* is still weaker than predicted [128, 133]. Please note, that except for 3 mm PI, *m* increases significantly (exceeding 95 % confidence interval) when considering a narrower porosity interval and decreasing heterogeneity (Table 4) [128].

Table 4: Data to Fig. 12. Areas of pin indentation were used as volume for interpolation (Eq. 8). Porosity correction was done with Eq. 5 and σ_d = 1002 MPa for Fig. 12A and 946 MPa for Fig. 12B [133]. Weibull modulus was fitted by linear regression and by maximum likelihood method (MLE, in brackets). Italics give 95 % confidence interval of m determined by MLE in GNU R open source environment.

	Pin indenter diameter [mm]	sample size *n*	Indenter area [mm^2]	Mean porosity [-]	Weibull modulus *m*	Characteristic strength σ_0 [MPa]	σ_0 [MPa] porosity corrected	σ_0 [MPa] extrapolated (Eq. 8)
Figure 12A	0.6	40	0.283	0.666	6.7 (5.6) *4.4-6.9*	125 (126)	-	169 (155)
	1	30	0.785	0.674	6.6 (7.1) *5.1-9.2*	120 (120)	-	-
	3	19	7.069	0.698	5.6 (5.0) *3.3-6.7*	96 (97)	113 (at ϕ = 0.67)	77 (79)
Figure 12B	0.6	22	0.283	0.669	7.9 (7.3) *5.0-9.6*	121 (121)	-	180 (137)
	1	17	0.785	0.668	9.3 (11.0) *6.6-15.3*	123 (123)	-	-
	3	7	7.069	0.677	5.5 (6.5) *2.7-10.2*	100 (99)	105 (at ϕ = 0.668)	80 (87)

3.2.3.2 Cores with defined geometry

Geometrically well-defined cores of two different sizes (Fig 13A) with comparable mean porosities (Table 5) were drilled out of spines of *H. mamillatus*. Exceptional coplanarity (<10 μm) was achieved by a method described in [128] (Appendix II, Manuscript 8) involving infiltration with wax and subsequently cleaning with acetone for 5 h. The core drilling destroys the hierarchy of the spines as GLs confining the spine at the rim are removed. Despite the missing dense shell, the cores show a surprisingly high strength, with small cores being significantly stronger than the large cores (Welch t-test, $p < 0.01$) (Fig. 13B) also reflected in the corresponding Weibull plot (Fig. 13C). Failing (shearing) along a GL layers was observed in 3 samples, which are highlighted by a black circle (Fig. 13C). These samples failed below average strength.

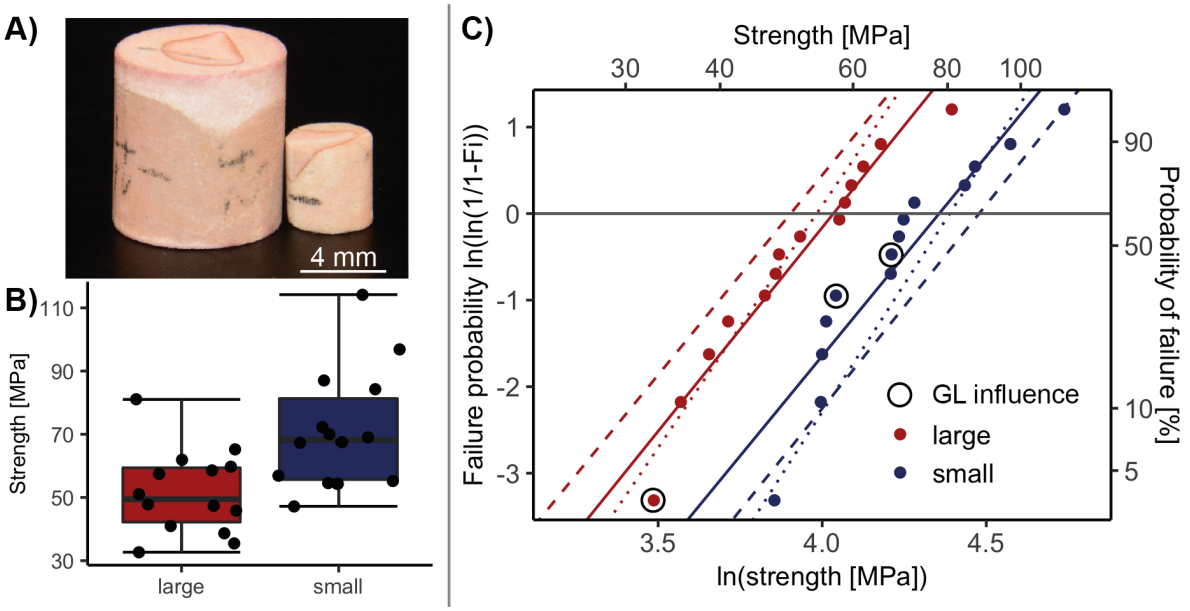

Figure 13: Uniaxial compression experiments of geometrically well-defined small and large cores (A). Small cores have a significantly higher strength (B) (Welch t-test, $p < 0.01$) and the population shows a size effect, although slightly less than predicted by Eq. 8 (dashed lines, C). If considering the upper boundary of the confidence interval, extrapolations fall within measured data (dotted lines, C, Table 5. Modified after [128].

m of both sample sizes is nearly identically determined by LR and MLE method (Table 5). The size effect is weaker than predicted by Eq. 8 (Fig. 13C, Table 5). However considering the small sample size and if setting m = 5.6 and 5.9, the upper limit of confidence intervals, respectively, predictions come close to measured data (dotted lines Fig. 13C).

Table 5: Data to Fig. 13C. Weibull modulus and characteristic strength were obtained with linear regression and maximum likelihood method (MLE, in brackets). Italics give 95 % confidence interval of m determined by MLE in GNU R freeware.

	sample population *n*	Mean volume [mm^3] and (range)	Mean porosity and (range)	Weibull modulus *m*	Characteristic strength σ_0 [MPa]	σ_0 [MPa] extrapolated (Eq. 8)
small	14	46 (41-48)	0.663 (0.598-0.754)	4.6 (4) *2.5-5.6*	78 (78)	88 *81*
large	14	372 (365-379)	0.664 (0.600-0.703)	4.7 (4.3) *2.6-5.9*	56 (57)	50 *53*

4. Discussion

4.1 Key Question 1: Structure-property relationships

4.1.1 Porosity

Porosity is the crucial property governing the mechanical properties of spines of *H. mamillatus* [28]. Although this relationship is well known (e.g. [77, 83]), it helps to explain the great scatter in data observed in this study [28, 41, 59], and also in other studies dealing with biological materials. Taking the porosity into account, *E* was successfully modelled with the power-law relation by [83] and an *EW* coefficient of 2-2.3. In the observed porosity range of segments used for UC experiments, this model predicts an increase in *E* of 245 % (*EW* = 2) from the max. porosity of 0.7 to the min. porosity of 0.53, underlining the importance of always reporting the porosity with the measured mechanical property. Hence, it is surprising that this was not done in many of the previous studies concerning spines of *H. mamillatus* [27, 45, 61, 62, 69].

The *EW* of 2-2.3 means that either spherical (2) or columnar pores (2.3) are dominating the mechanical response of the spines [83]. As the structure of the spines is an open pore network, the exact nature of the pores is difficult to discern and fitting of these pores always underlies an abstraction of the structure. However, it is evident that both pore shapes can be found in the stereom. The wedge structure dominates in the basal region of the spines where channel-like pores run parallel to the loading direction. The stereom becomes more foamy towards the distal parts of the spine and spherical pores dominate. As the difference of 2 and 2.3 is rather small (Fig. 7C), the scatter of data does not allow to safely distinguish between these cases, since not only porosity and pore shape are relevant, but also the distribution of porosity. It became apparent in the data of UC experiments, that permanent GLs affect the strength and *E* significantly, even if the porosity of the concerning groups is comparable [59].

When many GLp are located at the rim of the spine, which was often observed for more basal segments, then the porosity distribution can be approximated with a core-shell construction, which is abundant in biological materials [134]. These structures have superior stiffness and strength compared to the same material with a homogeneous porosity distribution. The outer spine serves as a very stiff shell, and the porous, compliant interior reduces the weight of the structure crucially and increases resistance against buckling [135]. This construction increases bending strength and *E*.

4.1.2 Structure and failure

As also seen in the last two paragraphs of 4.1.1, porosity and structure are intimately connected and a clear distinction is not possible. This section deals with the influence of the structure on the failure mechanism in UC, as its influence on *E* and strength is described above (4.1.1).

The failure behaviour of *H. mamillatus* spines in UC was investigated by Presser et al. [27, 30] and they reported a "cascading graceful failure behaviour", caused by the succession of dense, dome-shaped growth layer caps (GLf) and the porous radiating layer in between. As *H. trigonarius* has significantly more GLs than *H. mamillatus*, we expected to find this failure behaviour there in an enhanced form [28]. However, results show the contrary. *H. trigonarius* spines are too dense to fail in a foam-like manner as spines of *H. mamillatus* do. The threshold porosity for foam like failure is reported to be ~0.6 [89, 94, 136] and is in good agreement with our measurements [28]. *H. trigonarius* spines fall below this threshold. This means structure alone does not cause the "cascading graceful failure", a porosity above ~0.6 is mandatory.

Linking structure and failure for the more porous *H. mamillatus* spines did also display no causality between finishing GLf and foam like failure as detailed by [27, 30]. The energy dissipation efficiency is not improved by many GLf in the structure, only the reliability of failure is reduced as the structure is more heterogeneous [59]. Our analyses expose finishing GLs as heterogeneities in the structure, along which failure is more likely. The most likely fracture involving GLs was along capping GLs, as they directly end on the spine's shaft and not as regular layers in the milled ring (Fig. 14A). The density contrast between GLs and the surrounding stereom is often as much as 0.4. This is a structural weakness facilitating failure and resulting in spallation of large segments (Fig. 14A), leaving a damaged spine segment behind and reducing the cross sectional area in contact with the compression plate and thus the engineering stress. Both lead to a considerable drop in energy dissipation efficiency. The "cascading failure" may be caused by GLf (Fig. 14A) as found by Presser et al. [27, 30], but more often it occurs with no obvious link to structure. Fig. 3B shows a textbook example of cascading failure, yet the spine segment has not a single GLf to explain this. It is caused by constant size changes of the area in contact with the loading plate (Fig. 3B).

The other and by far more frequently observed cracking mechanism, especially in the basal segments, was along the wedge structure. These flakes often had a "piece of cake" shape, as the wedges run radially from the centre towards the rim (Fig. 14B). They are also structural weaknesses, as the stereom interspace is less dense than the radiating trabeculae, which can even be seen in the bulk measurement of a CT scan (300*300 μm) [41]. By this fracture, like in the case of finishing GLs, longitudinal cracks are induced in the structure and large flakes are spalled, reducing γ.

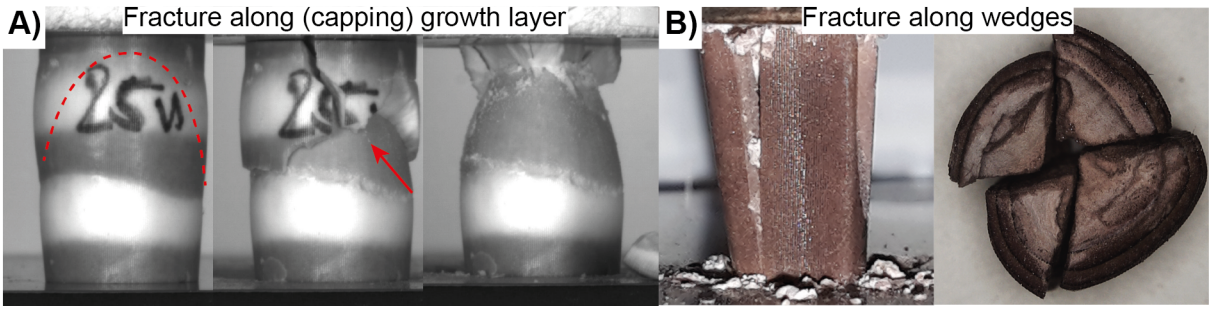

Figure 14: Structurally induced fracture along growth layers (A) and wedges (B). The capping growth layer providing the fracture face is outlined in the first picture of A. Wedge induced fracture is far more common (B).

The spine segments with the highest γ ($\gamma > 0.6$) all had a very simple layout. They were from the upper part of the spine, close to the tip, where the wedge structure is less pronounced and a more homogeneous, foamy stereom is encountered. Furthermore, GLs are sparse, with only a single GLp and, if at all, only one GLf. This reduces the structure to a homogeneous foam with a dense shell. Structural weaknesses are rare in this layout and fracturing of large flakes is impeded [28].

Our results show that energy dissipation has, in contrast to stiffness, no relevance for the living animal. Stiff and strong spines are useful for defence against predators and for wedging into reef cervices and withstanding wave energy. These load situations make clear that spines of *H. mamillatus* rarely fail in pure compression in nature but by a mixture of load situations with bending being presumably the most dominant [41]. γ is only a side effect of the porous structure [28] and our analyses show, that the spines are by no means optimised for it, as only a few show a suitable layout for this purpose.

4.1.3 Comparison with other studies

As porosity and structure were often not reported with the mechanical data published in previous studies, differences can principally be explained with dissimilar porosity and structure. However, the mechanical measurements obtained in this doctoral research are always higher than in the other studies (samples are stronger, stiffer and fail more reliably, compare Table 2 to 3). It might be, that spines in this study were generally denser, however, this is very unlikely given the many spines tested: In this study alone more tests were conducted than in all previously published studies. Reasons must be found otherwise.

E of spines was for the first time determined with RFDA [28] and ranges for full spines between 8-16 GPa. This is considerably higher than the 2.5 GPa reported by Grossmann and Nebelsick [69] obtained by 3PB. Our own bending tests revealed the difficulty of imprinting of the loading rollers in the compliant stereom of the spines [28]. If not measuring the depth of these imprints accurately and subtracting it from the recorded displacement, a far too low *E* is obtained. No such procedure is reported in [34, 69]. As these low *E* are very similar to those obtained in our measurements without imprint correction [28] it is likely, that no such correction was conducted in these studies.

Su et al. [45] conducted 4-point bending tests with complete spines of *H. trigonarius* and found an average strength of 26 MPa and a *m* of 3.2. These data are not directly comparable to the 3PB tests of complete *H. mamillatus*' spines conducted in this study ($n = 10$, $m = 7.9$, $\sigma_{average} = 29$ MPa), however, a uniform force inducement of 4 loading rollers into the irregular shaped spines is a challenging task and might explain why the here reported *m* is so much higher than by Sue et al. [45]. Concluding from the own measurements and these two studies [45, 69], bending tests are not reliable for testing these biological materials, unless a defined sample geometry can be assured.

If a precise sample geometry can be obtained (as by core drilling or using especially round spines), RFDA is by far the simplest method to obtain accurate *E* measurements that are in accordance with theory [78, 81, 83]. The method is non-destructive and measurements can be repeated *ad libitum*. UC yields generally slightly lower *E* with the difference becoming larger with lower porosity. UC requires a very coplanar sample geometry, especially for foam materials [86]. If this criteria is not met, some parts of the specimen experience high stresses when others are still stress-free, resulting in different strains. This error becomes larger, the stiffer (~less porous) tested spines are [28]. For samples tested in UC a coplanarity of ±15 μm was required in this study which is a time consuming procedure to achieve and still it is not precise enough for measuring *E* of stiff spines [28].

The importance of coplanarity for meaningful data was investigated using drilled cores with a deliberately bad coplanarity (100-200 μm), but otherwise identical geometry as the small cores (3.2.3.2). Their average strength (n = 10, σ_{av} = 26 MPa, $\phi_{av} = 0.68$) is only 36 % of the coplanar small cores and their *m* is 2.6 (compared to 4.6). Therefore, insufficient coplanarity helps to explain, why the values reported by [61, 62] of full spine segments with intact hierarchy are counterintuitively lower than those of the more porous drilled cores reported in 3.2.3.2 [128], in which the confining and stiffening GLs as hierarchical element are missing. In this PhD much effort was put in the preparation of coplanar samples and this likely accounts for the generally higher strength reported here than in any other study.

Differences in *m* can, besides insufficient coplanarity, also be explained by natural heterogeneity. The spines used in [59] originated from only 5 different animals. Spines (n=47) of a single animal had an even higher *m* of ~6 (Fig. 4). The origin of the spines of [27, 61, 62] is not reported, but it is likely that they were purchased loosely and originate from many animals [32]. For experiments conducted in [57] loose spines were used, too (coplanarity: ± 15 μm), and the *m* of 3-3.3 matches the data of [27, 61, 62] well. This illustrates that despite insufficient coplanarity a low *m* can also be obtained due to natural heterogeneities. Furthermore, it is possible that the spines still attached to the animals (they were dead for at least two years) were in a somehow "fresher" condition, with the organic matter less deteriorated leading to a higher *m*.

4.2 Key Question 2: Strength-size relationship

The size effect in spines of *H. mamillatus* was determined in three ways: UC of full segments, PI in full segments and UC of drilled cores. Only the latter displays a clear size effect. Reasons for this lay are either in the heterogeneity of the biological samples, the testing methods (4.2.1) and/or in the structuring of the spines (4.2.2). So 4.2.1 deals with the question why a size effect may have been overlooked due to methodological constraints and 4.2.2 why an extenuation of the size effect may be caused by the hierarchical structure of the spines of *H. mamillatus*.

4.2.1 Uncertainties in determination of the size effect

Uncertainties arise from the inherent natural heterogeneity of biological materials and the testing methods. Strictly speaking, each spine of *H. mamillatus* is unique [65] and thus testing specimen are not "geometrically similar" as required by Weibull theory. As the spines of *H. mamillatus* all share a common RVE, Weibull theory was successfully applied to many biological materials (e.g. [27, 59, 125, 137]) and other problems (e.g. [138, 139]), we feel justified to also apply it to the spines of *H. mamillatus* despite their natural heterogeneity.

The natural heterogeneity is expressed by the generally low *m* compared to technical ceramics, the dependency of *m* on GLs (Fig. 10C) [59] and on the range of the porosity interval (Fig. 12). Furthermore, the uncertainty in determination of *m* is expressed by the large range of the 95 % confidence interval, which is caused by the small sample population and by outliers. The poor determination of *m* has severe implications for the extrapolation of strength as it enters in the denominator of the exponent in Eq. 8. This means that all extrapolations (i.e. Fig. 12, 13C) only show the approximate range of expected strength distributions and not the exact location. This was underlined in Fig. 13 where the upper limit of the confidence interval of *m* agrees reasonably well with the predictions of Eq. 8. However, these uncertainties cannot account for the weak size effect in PI experiments (Fig. 12) and UC testing of full segments alone (Fig. 10).

Usually, the size effect is investigated by tensile testing for non-ceramic materials and bending for ceramic materials as fracture is well defined in this methods. For mechanical testing brittle cellular materials, however, there is not a single testing norm that could guide mechanical tests [95]. The classical applications of cellular ceramics are filtering, catalysis, high-temperature resistance and thermal insulation [140], however, load bearing applications gain in importance such as bone scaffolds. The need for tailored testing cellular ceramics is also expressed in [127] (Appendix II, Manuscript 7). Bending, however, was not chosen for size effect investigations in this study, as additionally to the difficulties concerning the sample geometry (4.1.3) it was noted by [141] that *m* in bending of cellular materials depends on the ratio of sample height divided by the number of cells in height. Hence, *m* is in bending not a material constant as required by Weibull theory. Furthermore, the effectively tested volume is generally much smaller than in UC, which would make it more challenging to obtain large differences in volume to evaluate the size effect.

However, UC has shortcomings, too. Insufficient coplanarity reduces strength and influences failure behaviour (e.g. [28, 86]). To minimize this problem, in this study only samples with a coplanarity of $\leq$30 μm were used. Furthermore, small samples had a comparable relative coplanarity (coplanarity/diameter) to large samples to ensure that smaller samples were not affected stronger by imperfect coplanarity. This margin of <30 μm assures that the whole sample is loaded before fracture, though it is not necessarily loaded homogeneously. This is an inherent problem of UC. Hence, scatter of strength is also caused by imperfect coplanarity and in in the case of *H. mamillatus* spines, also by

porosity and GLs (natural heterogeneity) [59] and not only due to randomly distributed flaws as assumed by Weibull. As the drilled cores of *H. mamillatus* spines (3.2.3.2) and the coconut endocarp [59] show, UC can reveal a size effect, if present, even for very heterogeneous samples. This might indicate that despite large heterogeneity and small sample populations, full segments with intact hierarchy only have a weak size effect that is covered by natural heterogeneity (Fig. 11A).

In PI experiments the locations of the PIs can be chosen to be as homogeneous as possible (i.e. free of GLs and of similar porosity), which reduces the influence of natural heterogeneities considerably [128]. This is expressed by the high *m* in PI compared to UC. Unconfined UC testing of full segments (Fig. 10C) and 1 mm PI (Fig. 12A) span a range of 0.15 of porosity, yet *m* is a third higher in PI, possibly due to the elimination of heterogeneities such as GLf. Full spine segments with no GLf show a very similar *m* in UC [59]. The reliability of the material further increases when considering a close porosity interval only (Fig. 12B), approaching the reliability of technical ceramics. As the porosity still scatters by 0.06 (Fig. 12B), it can be assumed that *m* further increases when narrowing down the porosity range to <0.01 (the range of technical ceramics), which was experimentally not feasible [128]. This highlights how "well-made" this biological ceramic is (see also 4.3.2).

However, calculating the size effect with PI underlies difficulties [128]. The extent of the stress field under the indenter is unknown and potentially requires modelling for a better understanding [132, 142]. Without this knowledge, the stressed volume to calculate the size effect (Eq. 8) can only be approximated under the assumption that the indenter area is linear to the stressed volume (Fig. 15A). This is a simplification. It omits the extent of the elastic stress field surpassing the pin diameter carrying load without fracturing and it does not take into account the increase of strain depth with increasing indenter diameter. A schematically, more realistic elastic stress field is shown in Fig. 15B, modified after simulations of [132] for the elastic region of metals. Especially for 3 mm PIs it can exceed sample dimensions (Fig. 13C). However, as long as failure is restricted to the area underneath the indenter, the simplifications made in Fig. 13A are likely valid, although only for size effect calculations and not for the shape and extent of the whole stress field. Only few measurements showed damage exceeding the location of the measurement (3 of 89). In this cases a large fault located in the elastic stress field next to the pin lead to failure. These measurements were excluded as the failure did not occur in the assumed volume [128]. In extreme cases, PI can lead to a catastrophic failure of the sample. This was not observed for spines of *H. mamillatus*.

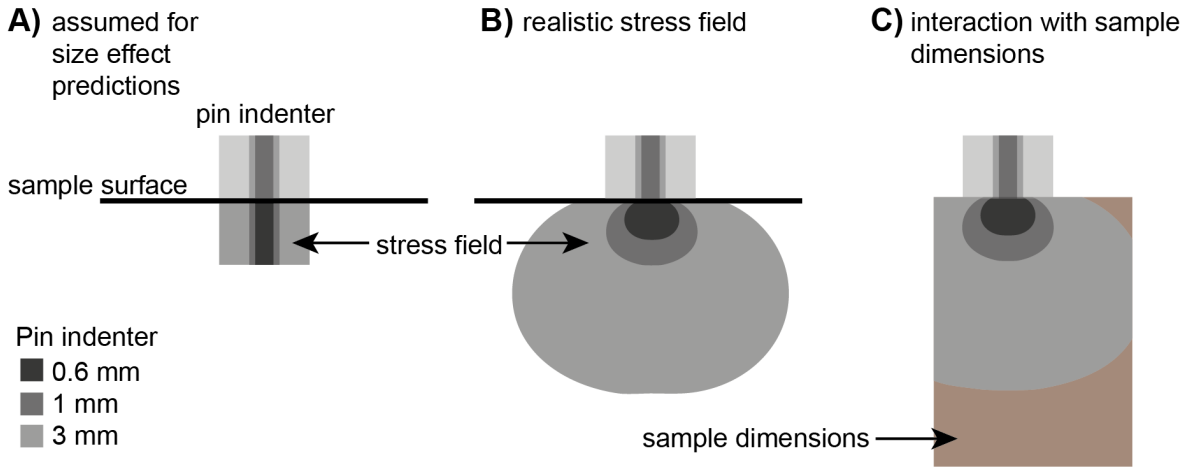

Figure 15: Schematic stress field assumed in size effect calculations (A), more realistic, schematic stress field after [132] (B) and interaction of stress field with sample dimensions (C). Grey scales refer to different pin diameters and their outlines sketch extents of equal stresses. Modified after [128].

These considerations highlight that the extrapolation in PI underlies some difficulties that could not all be resolved in this research. However, PI is principally able to detect a size effect as data of porous unidirectional ceramics produced by ionotropic gelation show [128] (Appendix II, Manuscript 8). Hence, the weaker nature of the size effect in spines of *H. mamillatus* cannot be caused by the method.

4.2.2 Possible explanations for extenuation of the size effect

UC of full segments with intact hierarchy shows no size effect that is distinguishable from the natural heterogeneities (Fig. 10, 12) and is thus arguably weaker than predicted by Eq. 8. PI shows a discernible, but weak size effect after eliminating heterogeneities. In contrast, UC tests of drilled cores showed a clear size effect (Fig. 13). As this inconsistency cannot be explained by natural heterogeneity, small sample populations and uncertainties in testing methods alone (4.2.1), the reason must be found to some extent in the structure of the spines of *H. mamillatus*.

Lauer et al. [59] explained the extenuation of the size effect in UC of full segments with the hypothesis that the critical crack size (the size from which the energy released by a crack surpasses the energy consumed to create new surfaces) and strut size are of the same order. This would effectively eliminate the statistical size effect on the strut level, as strut size does not increase with spine size [69]. The pivotal assumption of Weibull theory that larger volumes can accommodate larger flaws is not met, as all spines - no matter their size - are composed out of the same tiny struts. Later results [128] question this hypothesis. As full segments and drilled cores both are composed out of the same small struts, drilled cores should also show no size effect according to the theory of [59]. The only difference between drilled cores and full segments is that from the former the highest hierarchical level was removed, i.e. the confining GLs at the spine rim. Moreover, the calculation of the critical crack size a by applying Griffith facture criterion (Eq. 9) with the engineering stress of UC experiments, the fracture

toughness of geological calcite (K_{IC} = 0.39 MPa m$^{-1/2}$ [143]) and the geometrical configuration $Y = \pi$ is based on flawed assumptions.

$$K_{IC} = \sigma_f Y \sqrt{a} \qquad \text{Eq. 9}$$

Instead of engineering stress, the flexural strength of the strut material σ_f needs to be applied. It corresponds to mode I loading and was approximated with the bending strength of spines (data from Fig. 9B) to be ~360 MPa at ϕ = 0 (Eq. 5). A more realistic value of K_{IC} for biological calcite was obtained with the estimation given by [144] for cellular brittle materials derived from the same framework as Eq. 1 [77]. K_{IC} calculates to 0.5 MPa m$^{-1/2}$. With these improved values a falls below 1 μm, which is larger than the nanocrystals constituting the mesocrystalline structure (see 4.3.2). However, even when taking uncertainties in a determination into account, as e.g. K_{IC} of biological materials is difficult to determine [145], a stays likely below strut size (20 ± 7 μm [69]). The refined calculation of a is corroborated by twist hackles in fracture faces of struts that are indicative for instable and fast crack growth exceeding a [146] (Fig. 16A).

As outlined above, the only difference in UC experiments of drilled cores and full spine segments is the removal of the highest hierarchical level, the confining GLs at the rim, by drilling the geometrically well-defined cores. While the former show a clear size effect, the latter do not. This would imply, that GLs provide the spine not only with stiffness and strength, but also weaken the size effect to such an extent that it is indistinguishable the natural heterogeneity. In any load situation GLs, the densest and stiffest parts of the spines [41], carry the largest part of the applied load, as also finite element simulations by Cao et al. [62] show. This means, the porous radiating layer and medulla are of minor importance in carrying load, and might fulfil the purpose of a compliant core to further enhance the stiffness against bending compared to a hollow spine, as described for many biological structures by [134, 135].

Still, RL and medulla are able to carry high loads, as the experiments of the hollow drilled cores lacking GLs show (Fig. 13). The reason for this ability lies in the elastic properties of the struts constituting the material. A spine section of ~200 μm thickness could be bent >3 mm elastically before fracture (Fig. 16B). At this thickness, the section is composed out of 4 pores surrounded by struts in cross section and several thick GL septa are present (Fig. 16C), implying that the elastic properties of a single strut of the RL or medulla exceeds those of the section by far. Although the elastic properties might be exaggerated by the geometric shape of the thick section, this experiment highlights how well-built the material is. The high elasticity of a single strut is caused by its thinness and smooth surface (even on μm to sub-μm magnifications [47]) and indicates that they are nearly free of cracks and surface flaws. This provides the spines of *H. mamillatus* with a very high basic strength, which is further enhanced by GLs, the highest hierarchical level.

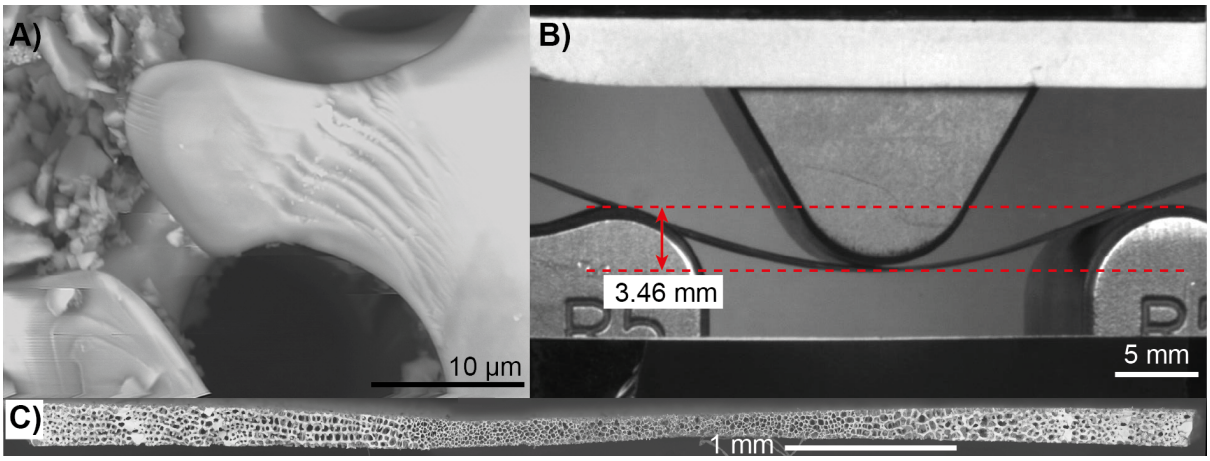

Figure 16: A strut showing twist hackles typical for instable crack growth (A). B) shows maximum elastic deflection of a ~200 µm thick spine section containing several dense growth layer trabeculae as can be seen on fracture surface (C). The span width in C) is 30 mm. Bending stresses were too low to be recorded

Spine segments with many GLp at the rim are significantly stiffer and stronger than spines with only one GLp [59]. Due to the growth mechanism of spines of *H. mamillatus*, small aboral spines tend to have fewer proximal GLs in general [65], and thus fewer GLp per segment in specific. Small aboral spines originate from the youngest ambulacral and interambulacral plate bearing primary spines [65]. Hence, they have less time to grow, experienced fewer growth cycles and thus have fewer of the mechanically relevant distal GLs Fig. 17A [65]. Therefore, the growth mechanism implies, that large aboral spines contain more GLs increasing their strength and stiffness. Furthermore, in contrast to struts of RL and medulla, the GL septa (Fig. 5D, 3.1.1) scale with increasing diameter (~spine volume) as their number remains approximately constant in all distal GLs of aboral spines [41]. The increase in size of the GL septa implies that they experience a lower true stress compared to the thinner GL septa of small aboral spines. Moreover, by the size increase of the GL septa it is geometrically given that the porosity decreases, which increases their strength. This means that small spines generally have more porous GLs, which was confirmed (Fig. 6D, 3.1.2). As the growth stage of a small aboral spine can still be found in large aboral spines (the innermost GLs), this relation can be even shown in a single spine: The innermost (oldest) GLs always have a higher porosity than the outermost (youngest) GLs (Fig. 6E, 3.1.2). This mechanism also works against the size effect. Whether it is a side effect of spine growth of *H. mamillatus* or a structural mechanism to weaken the size effect is currently unknown [128].

Figure 17B summarises the size effect in *H. mamillatus* spines in uniaxial compression. Despite the considerable scatter in data, it is visible that the drilled cores follow the size effect predictions of Eq. 8, whereas the full segments with intact hierarchy show no clear size effect. Although the difference in volume between the smallest and largest segments is 1250 %, the strength of the largest segments is in average only 8 MPa lower, which is statistically not significant (Welch t-test, $p > 0.1$). For the cores an 8 times larger volume leads to a mean strength decrease of 20 MPa which is statistically significant (3.2.3.2, [128]).

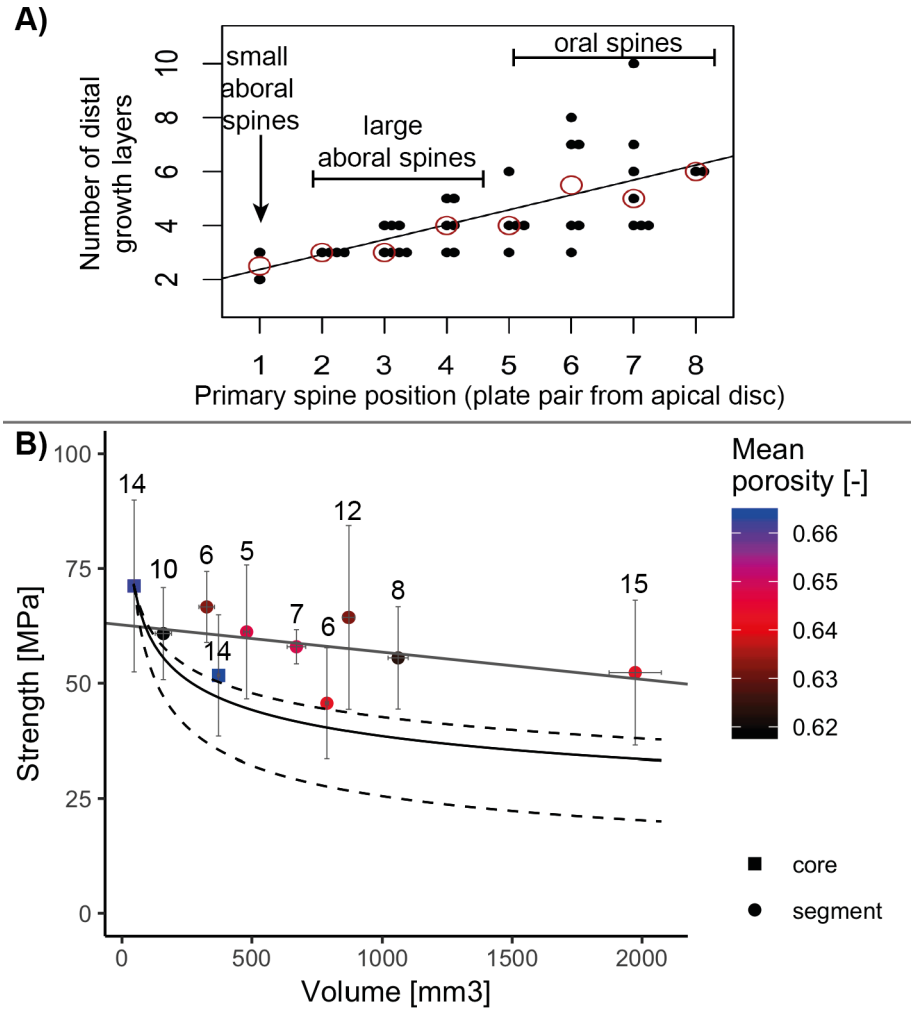

Figure 17: Number of distal growth layers in respect to spine position from oral to aboral side of a single animal (A). Coefficient of determination of linear fit: R^2=0.42, red circles show the median. Modified after [65]. B) displays a summary of mean σ_{UC} of distinct volume groups. Numbers give size of sample population, error bars are ± standard deviation. Curved lines are strength predictions (Eq. 8) with σ_{mean} and V_{mean} from the small cores and m = 5 [59]. Dotted lines are highest (m=6, Fig. 4) and lowest Weibull modulus (m=3, Fig. 9) obtained for larger sample populations of full H. mamillatus segments. Straight line is a linear fit for mean strength data of full segments only (R^2 = 0.12). Data from [57, 59, 128].

However, data from PI experiments do not fit into the theory of the hierarchical construction mitigating the size effect at the first glance. As location for PI were chosen to be GL free, these experiments should reveal a size effect comparable to the drilled cores, yet the size effect is weaker and could even be masked on a large proportion by the natural heterogeneities, i.e. porosity differences between sample groups. A closer look reveals that it was not possible to position the 3 mm pin solely in the radiating layer due to their comparably large size. 3 mm PI locations were always close to a GL. This likely increases the strength of the 3 mm PI by two mechanisms [128]. (1) The proximity to a GL could have a confining effect on the indentation. (2) The RL generally has a porosity gradient from high values close to the medulla to low values adjacent to the GL, implying that a 3 mm PI covers a wider range of porosity than a 0.6 and 1 mm PI. The strength of the 3 mm indentation is likely determined by the densest parts of the RL close to the GL and not by the average porosity that is assumed for

correlation of the 3 mm σ_{PI}. Removing both effects, the proximity to GLs and the local higher density in the RL, would likely decrease the σ_{PI} of 3 mm PI and thereby increase the size effect measured by PI in the spines of *H. mamillatus* [128].

According to this theory, the hierarchy of the spines of *H. mamillatus* weakens the size effect. A similar finding was made by Taylor for mammalian bone [124]. He argued that in bones of large animals secondary osteons were introduced as new hierarchical level to increase the fatigue strength and counteract the size effect. This way bones of mice and bovine have a comparable fatigue strength [124]. It seems that many biological materials have found a way to weaken the size effect as shown in Table 1 of [59], possibly due to their hierarchical structure which is uncommon for technical materials.

4.3 Biomimetic implications of this research

4.3.1 Key Question 1: Structure-property relationships

Unlike many other biological role models such as nacre, bone, antler and sponge spicules, the spines of *H. mamillatus* can be regarded as an "all ceramic composite material", achieving superior strength, stiffness, beneficial local failure behaviour and high damage tolerance without the incorporation of a significant amount of organic material. Whether their minor organic content influences the mechanical properties is debated. Although Berman [54, 147] found evidence for an alternation of the fracture properties by attachment of proteins oblique to calcite's [104] cleavage plane, Seto et al. [46] argued that the intricate arrangement of ACC and Mg-calcite on the nanoscale is responsible for the very same. Hozmann [148] even explained the change in fracture properties from well-cleaving to conchoidal with lattice distortions by the incorporation of Mg into the calcite. However, it should be noted that Hozmann's research predates the discovery of ACC in adult sea urchin spines and therefore does not cover the whole complexity of the spines.

We found low organic content in the spines, not resolvable in IR spectroscopy and likely below 0.5 wt%, which is in agreement with literature [149]. Keeping this in mind, it does not come by surprise that we identified the sophisticated structural arrangement being responsible for the outstanding macromechanical performance of *H. mamillatus*' spines. Their damage tolerance, high strength, high stiffness, local failure behaviour in PI and weakening of the size effect can all be explained by the structure. We indeed found that the crystallization of ACC has no effect on macromechanical properties [57]. This means, by elaborate structuring of Mg-calcite, an "actually rather poor building material" [150] transforms into a high performance ceramic. This highlights that appropriate structuring can improve materials impressively and that this field bears a lot of potential for human technology. Furthermore, the all-ceramic composite material sea urchin spine is easy and 100 % recyclable due to the restriction to a single constituent in amorphous and crystalline form: Mg-calcite.

The hypothesis of Presser et al. [27, 30], that the alternation of dense GLs and porous radiating layers is responsible for the graceful failure behaviour of the spines of *H. mamillatus* could not be confirmed [28]. Although Presser et al. [30] and Toader et al. [29] demonstrated that an alternation of highly porous and dense layers is beneficial for the energy dissipation of brittle materials, the layout of their structures differed from the spines of *H. mamillatus*. Whereas the spines have this alternation mainly vertically (excluding the few caps of GLs), the porosity gradient in the materials inspired by *H. mamillatus*' spines [29, 30] is mainly horizontal.

Energy dissipation is not a crucial property for the spines of *H. mamillatus*. They rather fail in bending or shearing than in purely compressive forces and the energy dissipation ability is likely a side effect of the high porosity [28]. For bending they are optimised by their core shell construction, a common building principle for biological materials [134] and often implemented in technological applications. However, for energy dissipation, spines of *H. mamillatus* can also serve as role model for abstraction. In contrast to the cascading graceful failure behaviour identified by Presser [27], good energy absorbers or dissipaters used in packaging industry or as impact protection, are characterised by a long, constantly high plateau [104]. A homogeneous foam structure of a uniform porosity of > 0.6 serves best for this purpose and can be found in the top part of large aboral spines of *H. mamillatus*.

The biomimetic relevance of the core shell principle and the construction principle of a good energy dissipater is limited, as these concepts are already implemented in numerous applications. This study could only show that nature applied the same strategies in its materials long before mankind did.

4.3.2 Key Question 2: Strength-size relationship

The likely weakening of the size effect by hierarchical structuring in the aboral spines of *H. mamillatus* is an important finding and a similar mechanism was also observed in mammalian bones by Taylor [124, 151]. However, large natural heterogeneities in porosity and structure of the sea urchin spines, deviations from coplanarity in sample preparation for UC and the inherent problem of exact determination of *m* of small sample populations [152] complicate interpretation. As outlined above, there are good reasons that besides these uncertainties a extenuation of the size effect in the spines of *H. mamillatus* is likely, although it cannot be deduced to which exact extent the size effect is mitigated.

With the current understanding of the hierarchy of *H. mamillatus*' spines, the lowermost hierarchical level on the nanoscale inhibits conchoidal fracture by the arrangement of Mg-calcite nanocrystallites and amorphous calcium carbonate (Fig. 18). The size of the calcite nanocrystallites is with <100 nm [47] surely below critical crack size which creates a flaw-free material on the nanoscale in agreement with Vincent's hypothesis [1]. The next hierarchical level on the microscale, the dense sea urchin calcite is structured in thin, μm-sized struts to constitute the porous stereom (Fig. 18). These thin struts have smooth surfaces and can be bent elastically, which highlights the practically flaw-free nature of the basic building block of the spines of *H. mamillatus*. The basic building block (pore

surrounded by struts) is repeated innumerable times, resulting in the high damage tolerance of the material. Failure of single struts or even strut clusters can be compensated by stress redistribution [57]. The interplay of the different stereom types medulla, radiating layer and GLs in the highest hierarchical level increases the strength and stiffness of the spines and possibly works against the size effect (Fig. 18). As large (older) aboral spines have more GLs than small (young) aboral spines and the youngest GLs (formed in latest growth cycles) are denser than the older GLs of earlier growth cycles, there is a foundation for the mitigation of the size effect solely explained by the growth mechanism. This means, by adding small quantities of dense material at the right spots, the size effect of this biological foam ceramic is weakened. Full spine segments being 50 times larger than cores drilled out of the spine, have an only somewhat lower strength as they have a "new" hierarchical level that the cores lack. This interplay of structure and property has undergone millions of years of evolution and it can be concluded in the way Jackson describes nacre [145] that the spines of *H. mamillatus* are "simply well made". Keeping in mind their "actually rather poor building material" [150], they are indeed better made than human technology is currently capable of.

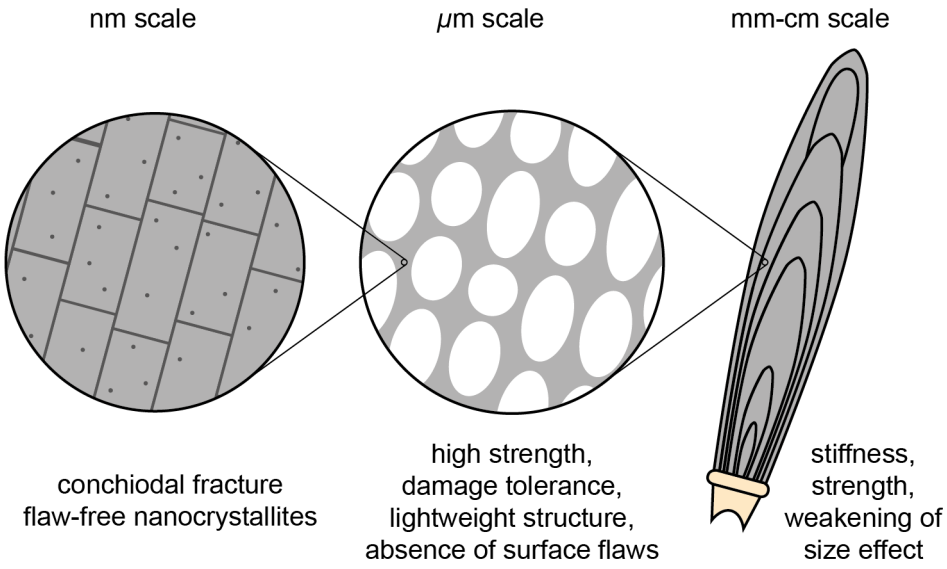

Figure 17: Relation between hierarchical levels and mechanical properties of the spines of H. mamillatus.

This principle of counteracting the size effect could be incorporated in any foam ceramic by adding appropriate dense structures (i.e. small pillars or a thin dense shell) aligned in the prevailing load direction. It important to note that by the new hierarchical element the function of the foam ceramic (e.g. filtering, insulation or impact protection) is not affected. However, this requires experimental validation and leads directly to the perspectives of this research.

5. Perspectives

The mechanical analyses of the spines of *H. mamillatus* in this doctoral research have been detailed, yet questions remain to be answered. The focus in this work laid on the structure-property and the strength-size relationship of the spines from a biomimetic background.

For a less biomimetic and more biological approach, the variation of the spine's mechanical properties depending on their position on the sea urchin test would be of interest, e.g. is there a systematic strength or stiffness variation? For σ_{UC} and E the spines of a single animal were investigated in this respect, but these preliminary results showed no systematic variation (Fig. 19A,B).

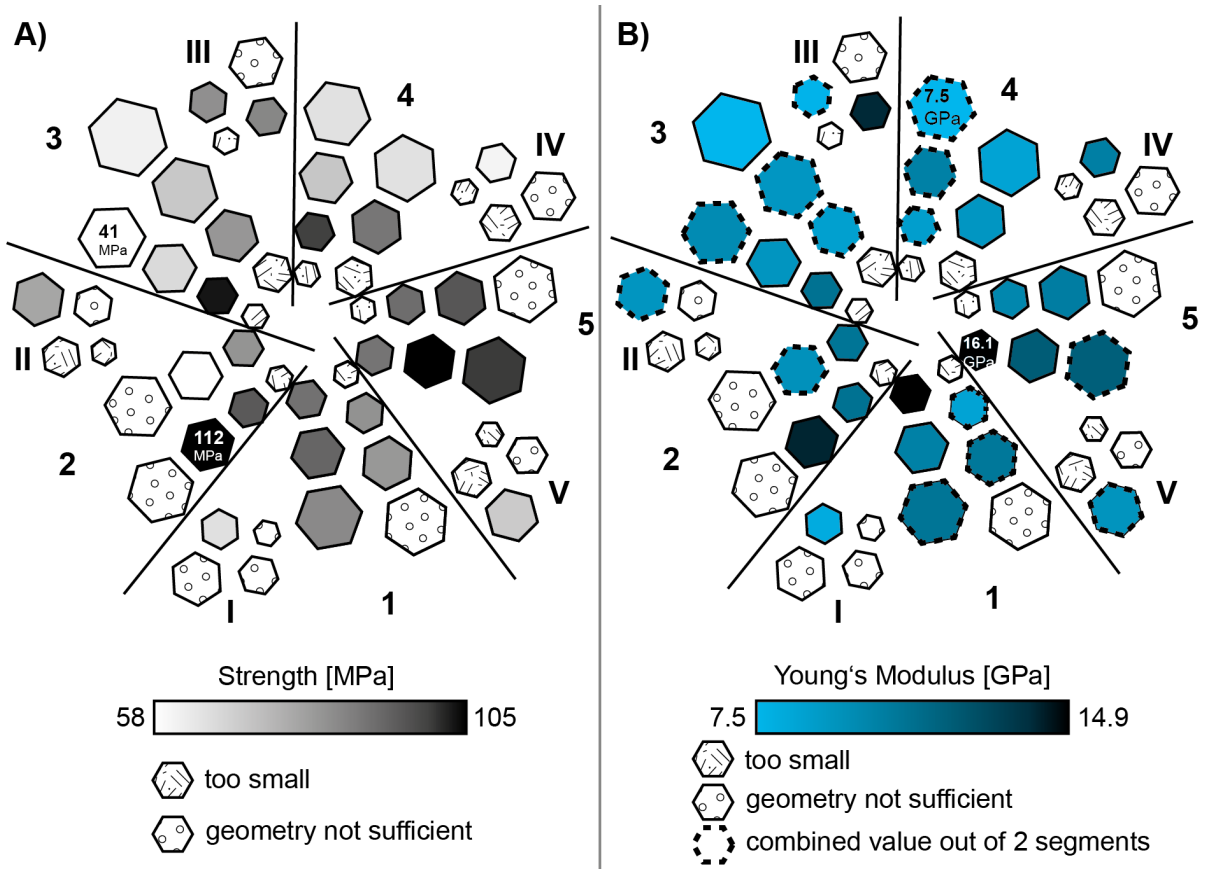

Figure 18: Hexagons display schematically the ambulacral and interambulacral plots of a sea urchin test in top view. Nomenclature of plate columns is after [153]. Pentamerous symmetry is outlined by black straight lines. Colour-coded are strength (A) and Young's Modulus (B) variations measured with uniaxial compression in relation to the spine position on the test. No systematic variation was found.

Unquestionably, the next step of the biomimetic research would be to abstract the principle of counteracting the size effect of a spine of *H. mamillatus* and implement it into a technical material such as a foam ceramic or lightweight concrete material. Probably additive manufacturing would be a promising approach (i.e. [154]), as practically any structure can be tailored with this method. Ionotropic gelation and freeze casting, two methods investigated in project C03 of the SFB TRR 141, are able to produce very porous and finely structured ceramics, yet their outcome is often difficult to control and relies on many parameters, so that additive manufacturing might be more suitable for this purpose.

Also interesting for biomimetic research would be to investigate the damage tolerant structure of the spines of *H. mamillatus* in more detail. This would entail a reliable determination of the K_{IC} of the material with micro or nanoindentation and of the hierarchical, porous structure with notched beams in 3PB. By comparison of these values, the influence of the porous structure on the K_{IC} could be revealed and the hypothesis of Lauer et al. [59] that the critical crack size is on the same order than strut size, could be finally disproved. Furthermore it could be tested, whether the general implication of the hypothesis by [59] is correct, i.e. foam materials where the strut size is of critical crack size exhibit no size effect. Therefore brittle foams out of silica glass would be a promising candidate, as due to their low strength their strut size would not become too small to manufacture (~40 μm according to Eq. 8).

Weiner and Addadi [150] suggested that many biological ceramic materials "strive for isotropy". Following this thought, mechanical properties could be tested directional. E was tested longitudinal and flexural in RFDA (parallel and perpendicular crystallographic c-axis, respectively). Tested cylinders revealed no difference between these two directions [28], although E is anisotropic in geological calcite. This finding could be used as starting point for a more detailed investigation of the direction dependence of mechanical properties.

6. References

[1] J.F. Vincent, Biomimetics--a review, Proc Inst Mech Eng H 223(8) (2009) 919-39.
[2] M.A. Meyers, P.Y. Chen, M.I. Lopez, Y. Seki, A.Y. Lin, Biological materials: a materials science approach, J Mech Behav Biomed Mater 4(5) (2011) 626-57.
[3] U.G. Wegst, H. Bai, E. Saiz, A.P. Tomsia, R.O. Ritchie, Bioinspired structural materials, Nature materials 14(1) (2015) 23-36.
[4] J. Knippers, K.G. Nickel, T. Speck, Biomimetic Research for Architecture and Building Construction: Biological Design and Integrative Structures, Springer International Publishing, Switzerland, 2016.
[5] M.A. Meyers, P.-Y. Chen, A.Y.-M. Lin, Y. Seki, Biological materials: Structure and mechanical properties, Progress in Materials Science 53(1) (2008) 1-206.
[6] R. Menig, M.H. Meyers, M.A. Meyers, K.S. Vecchio, Quasi-static and dynamic mechanical response of Haliotis rufescens (abalone) shells, Acta Materialia 48 (2000) 6.
[7] R. Wang, H.S. Gupta, Deformation and Fracture Mechanisms of Bone and Nacre, Annual Review of Materials Research 41(1) (2011) 41-73.
[8] B. Bhushan, Biomimetics: lessons from nature - an overview, Philosophical Transactions of the Royal Society A 367(1893) (2009) 1445-1486.
[9] O. Speck, D. Speck, R. Horn, J. Gantner, K.P. Sedlbauer, Biomimetic bio-inspired biomorph sustainable? An attempt to classify and clarify biology-derived technical developments, Bioinspir Biomim 12(1) (2017) 011004.
[10] Y.-T. Cheng, D.E. Rodak, Is the lotus leaf superhydrophobic?, Applied Physics Letters 86 (2005) 144101.
[11] W. Barthlott, C. Neinhuis, Purity of the sacred lotus, or escape from contamination in biological surfaces, Planta 202 (1997) 1-8.
[12] B. Bhushan, Y.C. Jung, K. Koch, Micro-, nano- and hierarchical structures for superhydrophobicity, self-cleaning and low adhesion, Philos Trans A Math Phys Eng Sci 367(1894) (2009) 1631-72.
[13] G. Mayer, Rigid biological systems as models of synthetic composites, SCience 310 (2005) 4.
[14] A.Y. Lin, M.A. Meyers, Interfacial shear strength in abalone nacre, J Mech Behav Biomed Mater 2(6) (2009) 607-12.
[15] F. Bouville, E. Maire, S. Meille, B. Van de Moortele, A.J. Stevenson, S. Deville, Strong, tough and stiff bioinspired ceramics from brittle constituents, Nature materials 13(5) (2014) 508-14.
[16] D.W. Bechert, W. Reif, On the Drag Reduction of the Shark Skin, (1985).
[17] D.W. Bechert, M. Bruse, W. Hage, R. Meyer, Fluid Mechanics of Biological Surfaces and their Technological Application, Naturwissenschaften 87 (2000) 157-171.
[18] L. Wen, J.C. Weaver, G.V. Lauder, Biomimetic shark skin: design, fabrication and hydrodynamic function, J Exp Biol 217(Pt 10) (2014) 1656-66.
[19] K. Autumn, Y.A. Liang, T.S. Hsieh, W. Zesch, W.P. Chan, W.K. Kenny, R. Earing, R.J. Full, Adhesive force of a single gecko foot-hair, Nature 405 (2000) 681-685.
[20] R. Ruibal, V. Ernst, The Structure of the Digital Setae of Lizards, J Morphol 117 (1965) 271-293.
[21] A.K. Geim, S.V. Dubonos, I.V. Grigorieva, K.S. Novoselov, A.A. Zhukov, S.Y. Shapoval, Microfabricated adhesive mimicking gecko foot-hair, Nature materials 2(7) (2003) 461-3.
[22] S. Poppinga, M. Joyeux, Different mechanics of snap-trapping in the two closely related carnivorous plants Dionaea muscipula and Aldrovanda vesiculosa, Phys Rev E Stat Nonlin Soft Matter Phys 84(4 Pt 1) (2011) 041928.
[23] J. Lienhard, S. Schleicher, S. Poppinga, T. Masselter, M. Milwich, T. Speck, J. Knippers, Flectofin: a hingeless flapping mechanism inspired by nature, Bioinspir Biomim 6(4) (2011) 045001.
[24] A. Körner, L. Born, A. Mader, R. Sachse, S. Saffarian, A.S. Westermeier, S. Poppinga, M. Bischoff, G.T. Gresser, M. Milwich, T. Speck, J. Knippers, Flectofold—a biomimetic compliant shading device for complex free form facades, Smart Materials and Structures 27(1) (2018) 017001.

[25] T.B. Grun, M. von Scheven, M. Bischoff, J.H. Nebelsick, Structural stress response of segmented natural shells: a numerical case study on the clypeasteroid echinoid Echinocyamus pusillus, J R Soc Interface 15(143) (2018).
[26] J. Weber, R. Greer, B. Voight, E. White, R. Roy, Unusual strength properties of echinoderm calcite related to structure, Journal of Ultrastructure Research 26 (1969) 355-366.
[27] V. Presser, S. Schultheiß, C. Berthold, K.G. Nickel, Sea Urchin Spines as a Model-System for Permeable, Light-Weight Ceramics with Graceful Failure Behavior. Part I. Mechanical Behavior of Sea Urchin Spines under Compression, Journal of Bionic Engineering 6(3) (2009) 203-213.
[28] C. Lauer, K. Sillmann, S. Haussmann, K.G. Nickel, Strength, elasticity and the limits of energy dissipation in two related sea urchin spines with biomimetic potential, Bioinspir Biomim 14(1) (2018) 016018.
[29] N. Toader, W. Sobek, K.G. Nickel, Energy Absorption in Functionally Graded Concrete Bioinspired by Sea Urchin Spines, Journal of Bionic Engineering 14(2) (2017) 369-378.
[30] V. Presser, C. Kohler, Z. Zivcova, C. Berthold, K.G. Nickel, S. Schultheiß, E. Gregorova, W. Pabst, Sea Urchin Spines as a Model-System for Permeable, Light-Weight Ceramics with Graceful Failure Behavior. Part II. Mechanical Behavior of Sea Urchin Spine Inspired Porous Aluminum Oxide Ceramics under Compression, Journal of Bionic Engineering 6(4) (2009) 357-364.
[31] S. Schmier, G. Bauer, G. Buck, K. Klang, C. Lauer, N. Toader, O. Gericke, W. Haase, I. Schäfer, S. Schmauder, W. Sobek, K.G. Nickel, T. Speck, Hohe Belastungen sicher überstehen, in: J. Knippers, U. Schmid, T. Speck (Eds.), Stuttgarter Beiträge zur Naturkunde, Naturkunde Museum Stuttgart, Stuttgart, 2017.
[32] W. Hasenpusch, Die Stachel der Griffelseeigel, Mikrokosmos 89(1) (2000) 23-27.
[33] A.B. Smith, A.e. Kroh, The Echionoid Directory. World Wide Web electronic publication, http://www.nhm.ac.uk/research-curation/projects/echinoid-directory [accessed 25/03/19], 2011.
[34] N. Grossmann, Stereom differentiation in sea urchin spines under special consideration as a model for a new impact protective system, Paleontology, Institute for Geosciences, University Tübingen, Tübingen, 2010, p. 160.
[35] J.S. Robach, S.R. Stock, A. Veis, Mapping of magnesium and of different protein fragments in sea urchin teeth via secondary ion mass spectroscopy, Journal of Structural Biology 155(1) (2006) 87-95.
[36] A.M. Smith, D.E. Clark, M.D. Lamare, D.J. Winter, M. Byrne, Risk and resilience: variations in magnesium in echinoid skeletal calcite, Marine Ecology Progress Series 561 (2016) 1-16.
[37] U. Magdans, H. Gies, Single crystal structure analysis of sea urchin spine calcites: Systematic investigations of the Ca/Mg distribution as a function of habitat of the sea urchin and the sample location in the spine, European Journal of Mineralogy 16(2) (2004) 261-268.
[38] E. Hesse, Die Mikrostruktur der fossilen Echinoidenstacheln und deren systematische Bedeutung, E. Schweizertbart'sche Verlagshandlung, Suttgart, 1900.
[39] S. Becher, Über statische Strukturen und kristallograohische Eigentümlichkeiten des Echinodermenskeletts, in: A. Bauer (Ed.) Verh. dtsch. zool. Ges. 24, Berlin, 1914.
[40] A. Smith, Stereom microstructures of the echinoid test, Special Papers in Palaeontology 25 (1980) 1-81.
[41] C. Lauer, T.B. Grun, I. Zutterkirch, R. Jemmali, J.H. Nebelsick, K.G. Nickel, Morphology and porosity of the spines of the sea urchin Heterocentrotus mamillatus and their implications on the mechanical performance, Zoomorphology 137 (2017) 137-154.
[42] H.U. Nissen, Crystal Orientation and Plate Structure in Echinoid Skeletal Units, Science 166 (1969) 1150-1152.
[43] D.M. Raup, Crystallography of echinoid calcite, Journal of Geology 67(1) (1959) 661 - 674.
[44] K.M. Towe, Echinoderm calcite: single crystal or polycrystalline aggregate, Science 157 (1967) 1048-1050.
[45] X. Su, S. Kamat, A.H. Heuer, The structure of sea urchin spines, large biogenic single crystals of calcite, Journal of Materials Science 35(22) (2000) 5545-5551.
[46] J. Seto, Y. Ma, S.A. Davis, F. Meldrum, A. Gourrier, Y.Y. Kim, U. Schilde, M. Sztucki, M. Burghammer, S. Maltsev, C. Jager, H. Colfen, Structure-property relationships of a biological mesocrystal in the adult sea urchin spine, Proceedings of the National Academy of Sciences of the United States of America 109(10) (2012) 3699-704.

[47] Y. Oaki, H. Imai, Nanoengineering in Echinoderms: The Emergence of Morphology from Nanobricks, Small 2(1) (2006) 66 - 70.
[48] F.W. Clarke, W.C. Wheeler, The inorganic constituents of echinoderms, United States Geological Survey Professional paper 90(L) (1915) 191 - 196.
[49] J.A.D. Dickson, Transformation of echinoid Mg calcite skeletons by heating, Geochimica et Cosmochimica Acta 65(3) (2001) 443-454.
[50] J.R. Goldsmith, D.L. Graf, O.I. Joensuu, The occurence of magnesian calcies in nature, Geochimica et Cosmochimica Acta 7 (1955) 212-230.
[51] J.N. Weber, The incorporation of magnesium into the skeletal calcites of echinoderms, American Journal of Science 267(5) (1969) 537-566.
[52] J. Aizenberg, G. Lambert, S. Weiner, L. Addadi, Factors involved in the formation of amorphous and crystalline calcium carbonate: A study of an ascidian skeleton, Journal of the American Chemical Society 124(1) (2002) 32-39.
[53] E. Beniash, J. Aizenberg, L. Addadi, S. Weiner, Amorphous calcium carbonate transforms into calcite during sea urchin larval spicule growth, Proceedings of the Royal Society of London, Series B: Biological Sciences 264 (1997) 461 - 465.
[54] A. Berman, L. Addadi, S. Weiner, Interaction of sea-urchin skeleton macromolecules with growing calcite crystals - a study of intracrystalline proteins, Nature 331 (1988) 3.
[55] Y. Politi, T. Arad, E. Klein, S. Weiner, L. Addadi, Sea Urchin Spine Calcite Forms via a Transient Amorphous Calcium Carbonate Phase, Science 306 (2004) 1161-1164.
[56] M. Albéric, E.N. Caspi, M. Bennet, W. Ajili, N. Nassif, T. Azaïs, A. Berner, P. Fratzl, E. Zolotoyabko, L. Bertinetti, Y. Politi, Interplay between Calcite, Amorphous Calcium Carbonate, and Intracrystalline Organics in Sea Urchin Skeletal Elements, Crystal Growth & Design 18(4) (2018) 2189-2201.
[57] C. Lauer, S. Haußmann, P. Schmidt, C. Fisher, D. Rapp, C. Berthold, K.G. Nickel, On the relation of amorphous calcium carbonate and the macromechanical properties of sea urchin spines, prepared for submission to: Advanced functional materials.
[58] T.B. Grun, J.H. Nebelsick, Structural design of the minute clypeasteroid echinoid Echinocyamus pusillus, R Soc Open Sci 5(5) (2018) 171323.
[59] C. Lauer, S. Schmier, T. Speck, K.G. Nickel, Strength-size relationships in two porous biological materials, Acta Biomater 77 (2018) 322-332.
[60] J.N. Weber, E.W. White, J. Lebiedzik, New porous biomaterials by replication of echinoderm skeletal microstructures, Nature 233(5318) (1971) 337 - 339.
[61] K.S. Vecchio, X. Zhang, J.B. Massie, M. Wang, C.W. Kim, Conversion of sea urchin spines to Mg-substituted tricalcium phosphate for bone implants, Acta Biomater 3(5) (2007) 785-93.
[62] L. Cao, X. Li, X. Zhou, Y. Li, K.S. Vecchio, L. Yang, W. Cui, R. Yang, Y. Zhu, Z. Guo, X. Zhang, Lightweight Open-Cell Scaffolds from Sea Urchin Spines with Superior Material Properties for Bone Defect Repair, ACS Appl Mater Interfaces 9(11) (2017) 9862-9870.
[63] L.S. Lewis, J.E. Smith, Y. Eynaud, Comparative metabolic ecology of tropical herbivorous echinoids on a coral reef, PLoS One 13(1) (2018) e0190470.
[64] J.N. Weber, Origin of Concentric Banding in the Spines of the Tropical Echinoid Heterocentrotus, Pacific Science 23 (1969) 452-466.
[65] C. Lauer, S. Mück, T.B. Grun, I. Zutterkirch, K.G. Nickel, Individual growth and morphology of the spines of Heterocentrotus mamillatus, prepared for submission.
[66] A. Dotan, L. Fishelson, Morphology of spines of Heterocentrotus mammillatus (Echinodermata, Echinoidae) and its ecological significance, in: B.F. Keegan, B.D.S. O'Connor (Eds.) Fifith International Echinoderm Conference, A.A.Balkema, Galway, 1984, pp. 253-260.
[67] N. Schlüter, F. Wiese, M. Reich, Systematic assessment of the Atelostomata (Spatangoida and Holasteroida; irregular echinoids) based on spine microstructure, Zoological Journal of the Linnean Society 175(3) (2015) 510-524.
[68] A. Dotan, Population structure of the echinoid Heterocentrotus mammillatus (L.) along the littoral zone of the south-estern Sinai, Coral Reefs 9 (1990) 75-80.
[69] J.N. Grossmann, J.H. Nebelsick, Comparative morphological and structural analysis of selected cidaroid and camarodont sea urchin spines, Zoomorphology 132(3) (2013) 301-315.

[70] T.A. Ebert, A new theory to explain the origin of growth lines in sea urchin spines, Marine Ecology 34(1) (1986) 197 - 199.
[71] T.A. Ebert, Growth, Regeneration, and Damage Repair of Spines of the Slate-Pencil Sea Urchin Heterocentrotus mammillatus, Pacific Science 42(3 - 4) (1988) 160 - 172.
[72] T.A. Ebert, Growth and repair of spines in the sea urchin strongylocentrotus purpuratus (stimpson), Biological Bulletin 133(1) (1967) 141 - 149.
[73] J.D. Gage, Skeletal growth zones as age-markers in the sea urchin Psammechinus miliaris Marine Biology 110 (1991) 217-228.
[74] M.P. Russell, M. R.W., Natural growth lines in echinoid ossicles are not reliable indicators of age: a test using Strongylocentrotus droebachiensis, Invertebrate Biology 199(4) (2000) 410-420.
[75] P. Schuler, T. Speck, A. Buhrig-Polaczek, C. Fleck, Structure-function relationships in Macadamia integrifolia seed coats--fundamentals of the hierarchical microstructure, PLoS One 9(8) (2014) e102913.
[76] J.N. Grossmann, J. Nebelsick, Stereom Differentiation in spines of Plococidaris verticillata, Heterocentrotus mammillatus and other regular sea urchins, Taylor & Francis Group, London, 2013.
[77] M.F. Ashby, The Mechanical Properties of Cellular Solids, Metallurgical Transactions A 14(A) (1983) 1755-1769.
[78] R. Coble, W. Kingery, Effect of porosity on physical properties of sintered alumina, Journal of the American Ceramic Society 39(11) (1956) 377-385.
[79] L.J. Gibson, M.F. Ashby, Cellular Solids: Structure and Properties, 2nd ed., Cambridge University Press, Cambridge, UK, 1997.
[80] W. Pabst, E. Gregoroá, G. Tichá, Elasticity of porous ceramics--A critical study of modulus-porosity relations, Journal of the European Ceramic Society 26(7) (2006) 1085-1097.
[81] L.J. Gibson, M.F. Ashby, The mechanics of three-dimensional cellular materials, Proceedings of the Royal Society of London A: Mathematical, Physical and Engineering Sciences 382 (1982) 43-59.
[82] W. Pabst, E. Gregoroá, Derivation of the simplest exponential and power-law relations for the effective tensile modulus of porous ceramics via functional equations, Journal of Material Science Letters 22 (2003) 1673-1675.
[83] W. Pabst, E. Gregorová, Young's modulus of isotropic porous materials with spheroidal pores, Journal of the European Ceramic Society 34(13) (2014) 3195-3207.
[84] J. Ito, Y. Matsushima, H. Unuma, N. Horiuchi, K. Yamashita, M. Tajika, Preparation and properties of pressureless-sintered dense calcite ceramics, Materials Chemistry and Physics 192 (2017) 304-310.
[85] S.K. Maiti, L.J. Gibson, M.F. Ashby, Deformation and energy absorption diagrams for cellular solids, Acta Metallurgica 32(11) (1984) 1963-1975.
[86] C.Q. Dam, R. Brezny, D.J. Green, Compressive behavior and deformation-mode map of an open cell alumina, Journal of Material Research 5 (1990) 163-171.
[87] R. Brezny, D.J. Green, Uniaxial Strength Behavior of Birttle Cellular Materials, J Am Ceram Soc 76(9) (1993) 2185-92.
[88] R. Brezny, D.J. Green, The effect of cell size on the mechanical behavior of cellular materials, Acta metall. mater. 38 (1990) 2517-2526.
[89] J. Seuba, S. Deville, C. Guizard, A.J. Stevenson, Mechanical properties and failure behavior of unidirectional porous ceramics, Sci Rep 6 (2016) 24326.
[90] S. Ji, Q. Gu, B. Xia, Porosity dependence of mechanical properties of solid materials, Journal of Materials Science 41(6) (2006) 1757-1768.
[91] P. Colombo, A. Arcaro, A. Francesconi, D. Pavarin, D. Rondini, S. Debei, Effect of Hypervelocity Impact on Microcellular Ceramic Foams from a Preceramic Polymer, Advanced Engineering Materials 5(11) (2003) 802-805.
[92] P. Colombo, E. Bernardo, Macro- and micro-cellular porous ceramics from preceramic polymers, Composites Science and Technology 63(16) (2003) 2353-2359.
[93] P. Colombo, E. Bernardo, L. Biasetto, Novel Microcellular Ceramics from a Silicon Resin, J Am Ceram Soc 87(1) (2004) 152-154.
[94] S. Meille, M. Lombardi, J. Chevalier, L. Montanaro, Mechanical properties of porous ceramics in compression: On the transition between elastic, brittle, and cellular behavior, Journal of the European Ceramic Society 32(15) (2012) 3959-3967.

[95] C. Voigt, J. Storm, M. Abendroth, C.G. Aneziris, M. Kuna, J. Hubálková, The influence of the measurement parameters on the crushing strength of reticulated ceramic foams, Journal of Materials Research 28(17) (2013) 2288-2299.
[96] N.A. Fleck, An overview of the mechanical properties of foams and periodic lattice materials, in: R.F. Singer, C. Körner, V. Altstädt (Eds.), Cellular Metals and Polymers, Fragezeichenverlag, Fürth, 2004.
[97] P. Greil, T. Lifka, A. Kaindl, Biomorphic Cellular Silicon Carbide Ceramics from Wood: II. MEchanical Properties, J Eur Ceram Soc 18(14) (1998) 1975-1983.
[98] P. Ramavath, P. Biswas, N. Ravi, R. Johnson, Prediction and validation of bukling stress of the ceramic honeycomb cell walls under quasi-static copression, congent engineering 3 (2016) 1168068.
[99] W. Xue, Y. Huang, Z. Xie, W. Liu, Al2O3 ceramics with well-oriented and hexagonally ordered pores: The formation of microstructures and the control of properties, Journal of the European Ceramic Society 32(12) (2012) 3151-3159.
[100] B.-H. Yoon, C.-S. Park, H.-E. Kim, Y.-H. Koh, In-situ fabrication of porous hydroxyapatite (HA) scaffolds with dense shells by freezing HA/camphene slurry, Materials Letters 62(10-11) (2008) 1700-1703.
[101] I. Sabree, J.E. Gough, B. Derby, Mechanical properties of porous ceramic scaffolds: Influence of internal dimensions, Ceramics International 41(7) (2015) 8425-8432.
[102] J. Seuba, S. Deville, C. Guizard, A.J. Stevenson, The effect of wall thickness distribution on mechanical reliability and strength in unidirectional porous ceramics, Sci Technol Adv Mater 17(1) (2016) 128-135.
[103] D. Ghosh, A. Wiest, R.D. Conner, Uniaxial quasistatic and dynamic compressive response of foams made from hollow glass microspheres, Journal of the European Ceramic Society 36(3) (2016) 781-789.
[104] M.F. Ashby, A.G. Evans, N.A. Fleck, L.J. Gibson, J.W. Hutchinson, H.N.G. Wadley, Metal Foams - A Design Guide Butterworth-Heinemann, Woburn, 2000.
[105] M. Scheffler, P. Colombo, Cellular Ceramics: Structure, Manufacturing, Properties and Applications, Wiley-VCH Weinheim, 2005, p. 645.
[106] J. Miltz, G. Gruenbaum, Evaluation of Cushioning Properties of Plasitc Foams From Compressive Measureents, Polymer Engineering and Science 21(15) (1981) 1010-1014.
[107] M. Alizadeh, M. Mirzaei-Aliabadi, Compressive properties and energy absorption behavior of Al–Al2O3 composite foam synthesized by space-holder technique, Materials & Design 35 (2012) 419-424.
[108] V. Presser, K. Gerlach, A. Vohrer, K. Nickel, W. Dreher, Determination of the elastic modulus of highly porous samples by nanoindentation: a case study on sea urchin spines, Journal of Materials Science 45 (2010) 2408-2418.
[109] G.D. Quinn, B.T. Sparenberg, P. Kosky, J.K. Ives, S. Jahanmir, D.D. Arola, Flexural Strength of Ceramic and Glass Rods, Journal of Testing and Evaluation 37(3) (2009).
[110] Z.P. Bazant, Size effect, International Journal of Solids and Structures 37 (2000).
[111] A.A. Griffith, The Phenomena of Rupture and Flow in Solids, Philosophical Transactions of the Royal Society A 221 (1921) 163-198.
[112] W. Weibull, A Statistical theoroy of the strength of materials, Ingeniörsvetenskapsakademiens Handlingar 151 (1939) 1-45.
[113] R. Danzer, On the relationship between ceramic strength and the requirements for mechanical design, Journal of the European Ceramic Society 34(15) (2014) 3435-3460.
[114] Z.P. Bažant, S.-D. Pang, Activation energy based extreme value statistics and size effect in brittle and quasibrittle fracture, Journal of the Mechanics and Physics of Solids 55(1) (2007) 91-131.
[115] M. Ambrožič, L. Gorjan, Reliability of a Weibull analysis using the maximum-likelihood method, Journal of Materials Science 46(6) (2010) 1862-1869.
[116] D. Wu, J. Zhou, Y. Li, Methods for estimating Weibull parameters for brittle materials, Journal of Materials Science 41(17) (2006) 5630-5638.
[117] H. Salmang, H. Scholze, Keramik, Springer Verlag, Berlin Heidelberg, 2007.
[118] S. Guo, R. Liu, X. Jiang, H. Zhang, D. Zhang, J. Wang, F. Pan, Statistical Analysis on the Mechanical Properties of Magnesium Alloys, Materials (Basel) 10(11) (2017).

[119] W.-S. Lei, A generalized weakest-link model for size effect on strength of quasi-brittle materials, Journal of Materials Science 53(2) (2018) 1227-1245.
[120] Z.P. Bazant, Scaling theory for quasibrittle structural failure, Proceedings of the National Academy of Sciences of the United States of America 101 (2004) 13400-13407.
[121] Z.P. Bazant, M. Vorechovsky, D. Novák, Role of deterministic and statistical length scales in size effect for quasibrittle failure at crack initiation, in: G. Augusti, G.I. Schueller, M. Ciampoli (Eds.) 9th Int. Conf. on Structural Safety and Reliability, Millpress, Rome, 2005, pp. 411-415.
[122] Z.P. Bazant, M. Vorechovsky, D. Novák, Asymptotic Prediction of Energetic-Statistical Size Effect from Deterministic Finite-Element Solutions, J Eng Mech 133 (2007) 153-162.
[123] B.S.M. Seeber, U.T. Gonzenbach, L.J. Gauckler, Mechanical properties of highly porous alumina foams, J Mater Res 28(17) (2013) 2281-2287.
[124] D. Taylor, Scaling effects in the fatigue strength of bones from different animals, J Theor Biol 206(2) (2000) 299-306.
[125] E. Trujillo, M. Moesen, L. Osorio, A.W. Van Vuure, J. Ivens, I. Verpoest, Bamboo fibres for reinforcement in composite materials: Strength Weibull analysis, Composites Part A: Applied Science and Manufacturing 61 (2014) 115-125.
[126] S. Schmier, C. Lauer, I. Schäfer, K. Klang, G. Bauer, M. Thielen, K. Termin, C. Berthold, S. Schmauder, T. Speck, K.G. Nickel, Developing the Experimental Basis for an Evaluation of Scaling Properties of Brittle and 'Quasi-Brittle' Biological Materials, in: J. Knippers, K.G. Nickel, T. Speck (Eds.), Biomimetic Research for Architecture and Building Constructions, Springer International Publishing, Switzerland, 2016, pp. 277-294.
[127] C. Lauer, G. Buck, S. Mück, R. Jemmali, C. Berthold, K.G. Nickel, Pin indentation: a method for local testing mechanical properties of ceramic foams, prepared for submission to: Ceramics.
[128] C. Lauer, S. Mück, G. Buck, K.G. Nickel, Hierarchical construction of spines of Heterocentrotus mamillatus weakens size effect on structural strength, prepared for submission.
[129] S. Haußmann, Amorphous calcium carbonate in sea urchin spines, Naturwissenschaftlich Fakultät, Fachbereich Geowissenschaften, Eberhard Karls Universität Tübingen, 2019.
[130] E.W. Andrews, G. Gioux, P. Onck, L.J. Gibson, Size effects in ductile cellular solids. Part II: experimental results, International Journal of Material Sciences 43 (2001) 13.
[131] O.B. Olurin, N.A. Fleck, S. M.F., Indentation resistance of an aluminium foam, Scripta Materialia 43 (2000) 7.
[132] B. Riccardi, R. Montanari, Indentation of metals by a flat-ended cylindrical punch, Materials Science and Engineering: A 381(1-2) (2004) 281-291.
[133] S. Mück, Mechanical Properties of Highly Porous Biological and Ceramic Materials, Naturwissenschaftliche Fakultät, Fachbereich Geowissenschaften, Eberhard Karls Univeristät Tübingen, 2019.
[134] M.A. Dawson, L.J. Gibson, Optimization of cylindrical shells with compliant cores, International Journal of Solids and Structures 44(3-4) (2007) 1145-1160.
[135] G.N. Karam, L.J. Gibson, Elastic buckling of cylindrical shells with elastic cores—II. Experiments, International Journal of Solids and Structures 32(8-9) (1995) 1285-1306.
[136] G. Jiang, Q. Li, C. Wang, J. Dong, G. He, Characterization and investigation of the deformation behavior of porous magnesium scaffolds with entangled architectured pore channels, J Mech Behav Biomed Mater 64 (2016) 139-50.
[137] G. Dill-Langer, R.C. Hidalgo, F. Kun, Y. Moreno, S. Aicher, H.J. Herrmann, Size dependency of tension strength in natural fiber composites, Physica A: Statistical Mechanics and its Applications 325(3-4) (2003) 547-560.
[138] S.H. Pishgar-Komleh, A. Keyhani, P. Sefeedpari, Wind speed and power density analysis based on Weibull and Rayleigh distributions (a case study: Firouzkooh county of Iran), Renewable and Sustainable Energy Reviews 42 (2015) 313-322.
[139] W. Weibull, A Statistical Distribution of Wide Applicability, ASME Journal of Applied Mechanics (1951) 293-297.
[140] A.R. Studart, U.T. Gonzenbach, E. Tervoort, L.J. Gauckler, Processing Routes to Macroporous Ceramics: A Review, Journal of the American Ceramic Society 89(6) (2006) 1771-1789.
[141] R. Brezny, D.J. Green, Characterization of edge effects in cellular materials, J Mater Sci 25 (1990) 4571-4578.

[142] Z. Chen, X. Wang, A. Atkinson, N. Brandon, Spherical indentation of porous ceramics: Elasticity and hardness, Journal of the European Ceramic Society 36(6) (2016) 1435-1445.
[143] B.E. Broz, R.F. Cook, W. D.L., Microhardness, toughness, and modulus of Mohs scale minerals, The American Mineralogist 91 (2006) 135-142.
[144] R. Wang, Fracture Toughness and Interfacial Design of a Biological Fiber-Matrix Ceramic Composite in Sea Urchin Teeth, J Am Ceram Soc 81(4) (1998) 1037-40.
[145] A.P. Jackson, J.F. Vincent, R.M. Turner, The mechanical design of nacre, Proc R Soc Lond B 234 (1988) 415-440.
[146] S.S. Scherrer, G.D. Quinn, J.B. Quinn, Fractographic failure analysis of a Procera AllCeram crown using stereo and scanning electron microscopy, Dent Mater 24(8) (2008) 1107-13.
[147] A. Berman, L. Addadi, A. Kvick, L. Leiserowitz, M. Nelson, S. Weiner, Intercalation of sea urchin proteins in calcite: study of a crystalline composite material, Science 250(4981) (1990) 664 - 667.
[148] P. Hozmann, Das unterschiedliche Härteverhalten biogener und anorganischer Calcitkristalle, Bochumer geologische und geotechnische Arbeiten 10 (1983) 100.
[149] J.D. Currey, D. Nichols, Absence of Organic Phase in Echinoderm Calcite, Nature 214(4) (1967) 81-83.
[150] S. Weiner, L. Addadi, Design strategies in mineralized biological materials, Journal of Materials Chemistry 7(5) (1997) 689-702.
[151] D. Taylor, Fatigue of Bone and Bones: An Analysis Based on Stressed Volume, Journal of Orthopaedic Research 16 (1998) 163-169.
[152] A. Khalili, K. Kromp, Statistical properties of Weibull estimators, J Mater Res 26 (1991) 6741-6752.
[153] S. Lovén, Études sur les éch*i*noidées, P. A. Norstedt & Söner, Stockholm, 1874.
[154] H. Cui, R. Hensleigh, H. Chen, X. Zheng, Addative Manufacturing and size-dependent mechanical properties of three-dimensional microarchitectured, high-temperature ceramic metamaterials, Journal of Materials Research 33(3) (2017) 360-371.

7. Further contributions

Publications also associated with the SFB TRR 141

K.G. Nickel, K. Klang, **C. Lauer**, G. Buck, Sea urchin spines as role models for biological design and integrative structures, in: S. Heuss-Aßbichler, G. Amthauer, G. John (Eds.), Highlights in applied mineralogy, De Gruyter 2017.

K. Klang, G. Bauer, N. Toader, **C. Lauer**, K. Termin, S. Schmier, D. Kovaleva, W. Haase, C. Berthold, K.G. Nickel, T. Speck, W. Sobek, Plants and Animals as Source of Inspiration for Energy Dissipation in Load Bearing Systems and Facades, in: J. Knippers, K.G. Nickel, T. Speck (Eds.), Biomimetic research for Architecture and Building Constructions, Springer International Publishing, Switzerland, 2016, pp. 109-133.

S. Schmier, G. Bauer, G. Buck, K. Klang, **C. Lauer**, N. Toader, O. Gericke, W. Haase, I. Schäfer, S. Schmauder, W. Sobek, K.G. Nickel, T. Speck, Hohe Belastungen sicher überstehen, in: J. Knippers, U. Schmid, T. Speck (Eds.), Stuttgarter Beiträge zur Naturkunde, Naturkunde Museum Stuttgart, Stuttgart, 2017.

Publications with no link to this PhD Thesis

P. Schmidt, **C. Lauer**, G. Buck, C.E. Miller, K.G. Nickel, Detailed near-infrared study of the 'water'-related transformations in silcrete upon heat treatment, Physics and Chemistry of Minerals 44(1) (2016) 21-31.

Conference Contributions as speaker

C. Lauer, K. Klang, G. Buck, C. Berthold, K.G. Nickel, Energy Dissipation Measurement of Brittle Porous Materials by Blunt Indentation, 91st DKG Annual Conference, Freiberg, Germany (2016)

C. Lauer, K. Klang, G. Buck, P. Schmidt, N. Wichtner, C. Berthold, K.G. Nickel, Structure Mechanical Property Relations of Sea Urchin Spines: A Highly Porous Composite Material. 4th CellMat, Dresden, Germany (2016)

C. Lauer, S. Schmier, G. Buck, I. Zutterkirch, N. Wichtner, T. Speck, K.G. Nickel, Scaling Sea Urchin Spines: Is there a way to overcome the size effect? 4th Euro Bio-Inspired, Potsdam, Germany (2018)

C. Lauer, S. Mück, G. Buck, Berthold, K.G. Nickel, Size effect in brittle sea urchin spines on structural strength: Is there a way to outsmart Weibull theory? MSE Dramstadt, Germany (2018)

Supervision of Bachelor and Master Theses

I. Zutterkirch, Untersuchung der Schalen von Argonauta argo und Argonauta hians hinsichtlich Struktur und mechanischen Eigenschaften, Bachelorarbeit, Universität Tübingen, 2016

S. Haußmann, Strukturveränderung kalzitischer Seeigelstacheln durch Wärmebehandlung, Bachelorarbeit, Universität Tübingen, 2016

S. Mück, Penetrationsfestigkeiten hochporöser biologischer und keramischer Materialien, Bachelorarbeit, Universität Tübingen, 2016

K. Sillmann, Heterocentrotus trigonarius: eine mechanische und strukturelle Analyse von Seeigelstacheln, Masterarbeit, Universität Tübingen, 2018

M. Schwab, Eine Fallstudie über die Magnesiumverteilung der biogenen Calciten von Seeigelstacheln, Masterarbeit, Universität Tübingen, 2018

S. Haußmann, Amorphous Calcium Carbonate in Sea Urchin Spines (preliminary title), Masterarbeit, Universität Tübingen, 2019

S. Mück, Mechanical Properties of Highly Porous Biological and Ceramic Materials (preliminary title), Masterarbeit, Universität Tübingen, 2019

8. Appendix I: Published manuscripts

Manuscript 1

Developing the Experimental Basis for an Evaluation of Scaling Properties of Brittle and 'Quasi-Brittle' Biological Materials

(20 pages)

DOI: https://doi.org/10.1007/978-3-319-46374-2_14

Chapter 14

DEVELOPING THE EXPERIMENTAL BASIS FOR AN EVALUATION OF SCALING PROPERTIES OF BRITTLE AND "QUASI-BRITTLE" BIOLOGICAL MATERIALS

Stefanie Schmier[1,2], Christoph Lauer[3], Immanuel Schäfer[4], Katharina Klang[3], Georg Bauer[1,2], Marc Thielen[1], Kathrin Termin[3], Christoph Berthold[3], Siegfried Schmauder[4], Thomas Speck[1,2], Klaus G. Nickel[3]

[1]Plant Biomechanics Group, Botanic Garden, University of Freiburg, Schänzlestr. 1, D-79104 Freiburg, Germany

[2]Freiburg Centre for Interactive Materials and Bioinspired Technologies (FIT), Georges-Köhler-Allee 105, D-79110 Freiburg, Germany

[3]Applied Mineralogy, University of Tübingen, Wilhelmstr. 56, D-72074 Tübingen, Germany

[4]Institute for Materials Testing, Materials Science and Strength of Materials (IMWF), University of Stuttgart, Pfaffenwaldring 32, D-70569 Stuttgart, Germany

Corresponding author: stefanie.schmier@biologie.uni-freiburg.de

ABSTRACT

The development of lightweight structures exhibiting a high energy dissipation capacity and a locally adapted puncture resistance is of increasing interest in building construction. As discussed in Chapter 7, inspiration can be found in biology, as numerous examples exist that have evolved one or even several of these properties. Major challenges in this interdisciplinary approach, i.e. the transfer of biological principles to building constructional elements, are scaling (different dimensions) and (at least for the botanic examples) the fact that different material classes constitute the structural basis for the functions of interest. Therefore, a mathematical description of the mechanical properties and the scalability is required that is applicable for both biological and technical materials. A

basic requisite for the establishment of mathematical descriptions are well-defined test setups rendering a reliable data basis. In the following, two biological role models from the animal and plant kingdoms are presented, namely, sea urchin spines and coconut endocarp, and two experimental setups for quasi-static and dynamic testing of biological and bio-inspired technical materials are discussed.

1. INTRODUCTION

Intuitively, problems are bound to arise in the transfer of the principles and characteristics of natural materials, which come in millimetre or centimetre sizes, to architectural objects, which may span many metres. However, the analysis of this scaling problem is far from being trivial and is of particular importance in the realm of brittle materials, to which at least the matrix of common building materials such as cement and concrete belongs. A theoretical and experimental evaluation requires proper data sets. In the following, we describe our efforts to develop the methods by which to obtain such data.

In 1921, Griffith reported that the experimentally determined strength of homogeneous, isotropic and brittle solids is several times lower than can be expected from calculations based on their intrinsic properties such as elastic moduli and surface energies (Griffith 1921). Weibull characterised this phenomenon statistically, stating that the probability of failure depends on two factors: a given distribution of stresses (e.g. according to the test method) and, in particular, the volume of the tested specimen. Weibull was the first who took into account the volume of the tested specimen as a reason for the large scatter of experimentally obtained ultimate strength data (Weibull 1939, Bažant 2000).

Weibull's theory is based on the weakest link hypothesis, which assumes that a specimen fails at its weakest point (e.g. an internal flaw or imperfection). In a homogeneous, isotropic and brittle material, in which the failure events are independent of each other, the size of the flaws controlling the strength follows a statistical distribution function for a given volume. If the size of flaws in a volume is a matter of probability, then it is tantamount that the stress needed to break the material of a given volume is statistically distributed. The probability of failure $P_{i,V0}$ for a specimen i within a given volume V_0 is then, in its simplest form, defined by the two-parameter Weibull formula:

$$P_{i,V_0} = 1 - e^{-\left(\frac{\sigma_i}{\sigma_0}\right)^m}, \qquad (1)$$

where σ_i is the critical stress at failure for specimen i, σ_0 is the characteristic strength and m the Weibull modulus. The Weibull modulus m is therefore a measure of the reliability of the material: the lower the Weibull modulus, the higher the scatter of critical stresses in a material and the lower the material's reliability. For this reason, technical ceramics are desired to have high Weibull moduli ($m = 10 – 20$) (Danzer 2014). The characteristic strength is the critical stress at which 63.2% of the tested specimens with volume V_0 fail. Unlike the Weibull modulus m, the characteristic strength σ_0 is not a material constant as it depends on the volume of the investigated specimen and, therefore, the corresponding material constant is $\sigma_0 V_0^{1/m}$. The Weibull modulus and characteristic strength can be determined experimentally by using the empirical distribution function F for P_{V0}. By fitting a regression line to $ln\ (ln\ (1/(1-F_i)))$ versus $ln\ (\sigma_i)$, the Weibull modulus m can be identified as the slope and $\sigma_0 = exp(-c/m)$ with c being the intercept of the regression line (Fig. 14-1). Materials to which this method can be applied are said to show "Weibull behaviour" (Weibull 1939, Weibull 1951, Danzer et al. 2007, Danzer 2014).

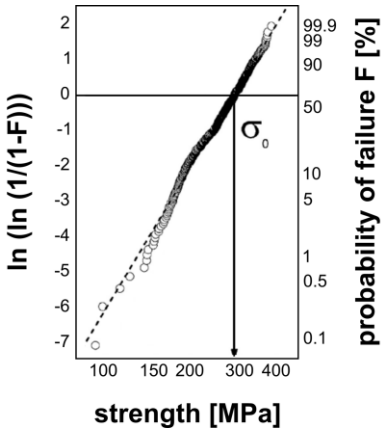

Figure 14-1. Determination of characteristic strength σ_0 and Weibull modulus m of a set of 600 tested varistor ceramics (σ_0=284 MPa, m=5.8). The regression line represents the related Weibull distribution. The distribution fits the data very well and the material is said to show "Weibull behaviour" (adapted from Danzer 2014, p. 3437, Copyright (2016), with permission from Elsevier).

Weibull defined the characteristic strength as depending on the respective volume of the specimen. This is because it is more likely to find a critical flaw in a large specimen than in a small one. Thus, a large specimen will statistically fail at lower stresses (i.e. at lower σ_0) than small ones. This effect is called the "size effect" and is expressed for specimens of the same material having the same probability of failure by:

$$\left(\frac{\sigma_1}{\sigma_2}\right) = \left(\frac{V_2}{V_1}\right)^{\frac{1}{m}}, \quad (2)$$

where σ_1 is the strength at failure of the object with volume V_1, σ_2 is the strength at failure of the object with volume V_2 ($F_{1,V1} = F_{2,V2}$), and m is the Weibull modulus of the material (Danzer et al. 2007).

For brittle components (e.g. ceramics), the procedure of defining the Weibull modulus as a material constant is well established (e.g. Lawn 1993). Since samples at their final volume often cannot be tested because of costs and testing procedures, Eq. (2) can be applied for scaling up to the size used under realistic operational conditions of the respective material. This automatically leads to a strong decrease in characteristic strength.

Extending this theory to biological samples and role models (e.g. sea urchin spines and coconut shells) is fairly difficult. As biological samples rarely constitute homogeneous or isotropic materials, verification of Weibull´s theory is not easy. Weibull himself proposed empirical tests for whether his distribution function could be applied to mechanical properties of other materials than the standard homogeneous, isotropic and brittle solids, as demanded as preconditions for the theory of the weakest link. Therefore, an application of the Weibull approach to biological samples with their specific material properties seems to be justified. For some biological materials, "Weibull behaviour" has previously been proposed, e.g. for the determination of failure strength of sea urchin spines (Presser et al. 2009), abalone shells (Menig et al. 2000), pea seeds (Łysiak 2007), teeth (Chan et al. 2009) or bone (Wagermaier et al. 2015). Many other distributions in nature have recently been identified as being Weibull-distributed (Krumbholz et al. 2014).

For the bones of various animals, Taylor (2000) could prove a fatigue strength behaviour according to Eq. (1). However, interestingly, bones from larger animals failed at similar stresses compared with bones of smaller animals. This seems to contradict the scaling effect (Eq. (2)) and Taylor assumed that an improvement in the bone structure counteracted it. Detecting, analysing and understanding such structural features influencing the scaling effect would be of great interest for the development of building construction involving scaling problems and would also help us to comprehend the specific failure behaviour of the biological role models used as concept generators for biomimetic materials in greater detail (reverse biomimetics).

2. SEA URCHIN SPINES – BIOLOGICAL ROLE MODEL FROM THE ANIMAL KINGDOM

A more detailed description of the spines of *Heterocentrotus mammilatus* (HM) and *Phyllacanthus imperialis* (PI) is given in Chapter 7 "Plants and animals as source of inspiration for energy dissipation in load bearing systems and facades" and elsewhere (Grossmann and Nebelsick 2013, Presser et al. 2009). However, the most relevant properties for scaling purposes will be briefly described here: Sea urchin spines

- are lightweight constructions because of their highly porous microstructure.
- have a hierarchical structure (Seto et al. 2012).
- are composed of a highly sophisticated composite material comprising calcite (>99 wt.%) and organic macromolecules (<1 wt.%, e.g. Seto et al. 2012, Sue et al. 2000) that overcome the brittleness of calcite and make it a good building material for undertaking the tasks of such a spine (Moureaux et al. 2010, Presser et al. 2009).
- of PI and especially of HM show a "graceful failure" behaviour (Presser et al. 2009), which is a quasi-ductile partial failure under uniaxial compression without losing the capacity to withstand the load.
- have a remarkable capability to absorb energy (cp. 14-2c).

All these characteristics make the sea urchin spine an object of great scientific interest and of even more interest for biomimetics. In order to scale these properties, the exact figures of merit of the sea urchin spines need to be measured.

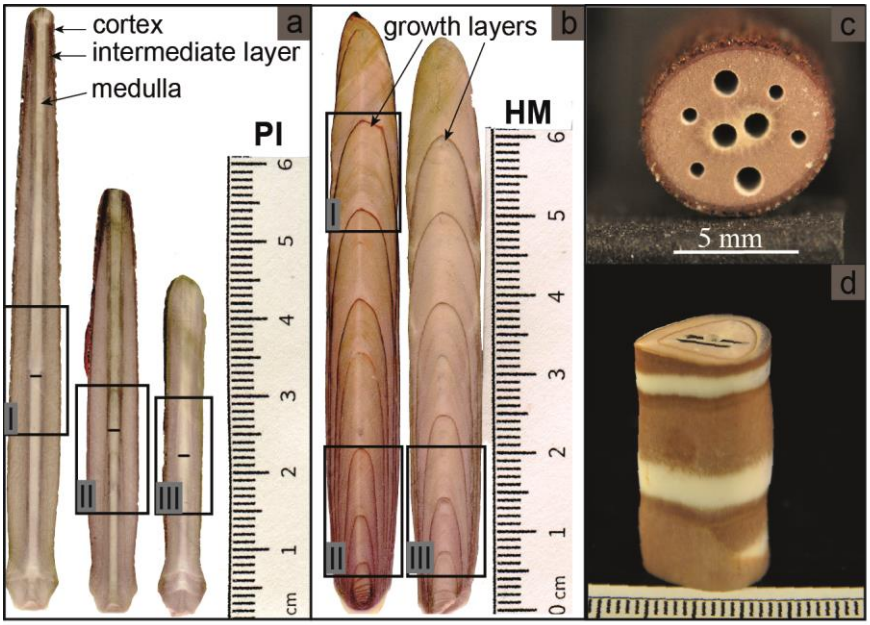

Figure 14-2. Photographs of longitudinal spine sections of (a) PI (*Phyllacanthus imperialis*) and (b) HM (*Heterocentrotus mammilatus*). Black boxes represent sample dimensions for uniaxial compression tests. (c) Detailed view of a spine segment of PI after 8 longitudinal indentation tests (5 – 10 mm deep). Although the spine is locally damaged, the whole spine is still intact highlighting its capacity to absorb energy. (d) Detailed view of a spine segment of HM typically used in the indentation tests.

Presser et al. (2009) determined the Weibull modulus *m* by uniaxial compression tests for HM and PI. Su et al. (2000) determined *m* with 4-point bending tests for *Heterocentrotus trigonarius* (HT), which belongs to the same genus as HM.

PI exhibits the highest Weibull modulus ($m = 6.0$), whereas HM and HT show a significantly lower reliability with $m = 3.4$ and $m = 3.2$, respectively. Presser et al. (2009) attributed the higher reliability of PI to its regular structure (Fig. 14-2a), compared with the fairly heterogeneous structure of HM. PI is characterised by dense dome-shaped growth layers, which induce crack deflection (Presser et al. 2009). Although the strength in PI is more reliable, considerable variations exist in the spine structure depending on spine size (Fig. 14-2a). The highly porous medulla has, in all three spines of Fig.14-2a, a comparable size (as indicated by the black bar in the boxes I-III, length = 1.5 mm), so that the highest proportion of very porous and low-strength material occurs in the smallest spine, presumably resulting in lower strength.

In addition to the above-mentioned heterogeneities in the structure leading to a lower reliability, the determination of *m* itself is challenging

with regard to all these biological samples. A good estimate of the critical stress (σ_c, MPa) can only be found with precise geometric information of the spine. The spines of HM and PI are not perfectly cylindrical (Fig. 14-2c/d), as is assumed for the quantitative assessment of uniaxial compression experiments, and the spines of HT do not have two perfectly parallel surfaces as assumed by Su et al. (2000) for the 4-point bending tests.

Hence, the geometry of the spines and the heterogeneity of their structure challenge the determination of the Weibull modulus with uniaxial compression or 4-point bending tests. A method is thus needed that does not depend on the geometry of the spine and that has a high spatial resolution for an easier determination of the Weibull modulus and for easier scaling.

3. COCONUT ENDOCARP – BIOLOGICAL ROLE MODEL FROM THE PLANT KINGDOM

The coconut (*Cocos nucifera*) is a tropical palm that grows in coastal regions and riverbanks and can reach heights of up to 30 m. The ripe fruits, which have the ability to float, remain able to germinate even after several months in seawater and, therefore, the palm is widely distributed in the tropics. The fruits reaching weights of 3.7 kg have to withstand severe impacts of up to 1 kJ when they drop from the crown of the palm onto the ground. To assure the germination of the embryo inside, they have to absorb the impact energy and remain closed to protect the embryo from fungal and bacterial infection. All of these properties are ensured by the triple-layered fruit wall of the drupe consisting of a leathery exocarp, a fibrous mesocarp and a tough endocarp (Chan and Elevitch 2006, Franke et al. 2012, Bauer et al. 2015) (Fig. 14-3).

The tough endocarp is currently under investigation. Its shape varies from elongated and egg-shaped to almost spherical (Chan and Elevitch 2006). The tricarpelary structure of the ovary is still visible in the mature fruit, as three longitudinal ridges exist representing the fusion marks of the three carpels. Furthermore, three micropyles or "germinating eyes" are present in the endocarp. These are regions in which the endocarp is thinner and the tissue is much softer, allowing the embryo to "escape" the endocarp during sprouting (Winton 1901).

Figure 14-3. Cut open ripe fruit of the coconut palm (*Cocos nucifera*). *Left*. Exterior view. *Right*. Interior view: The pericarp consisting of exocarp, mesocarp and endocarp lies over the endosperm, in which the embryo is embedded. The embryo is located under one of the three micropyles at the side at which the fruit is attached to the palm via the floral axis. Not visible is the testa or seed wall surrounding the endosperm. Scale bar: 5 cm.

The endocarp consists predominantly of red to brownish-coloured, isodiametric or strongly elongated stone cells (Fig. 14-4a), comprising several layers of secondary cell walls (Fig. 14-4d/e). Dark channels can be observed that serve as a connection between the still young and living cells and can be interpreted as lignified plasmodesmata (Fig. 14-4e). The elongated cells are mostly oriented with their long axis parallel to the outer surface of the endocarp (Fig. 14-4b/c). The vascular bundles mainly consist of spiral and pitted tracheids or vessels (Fig. 14-4f/g). In close vicinity to the vascular bundles, elongated stone cells are found arranged with their longitudinal axis parallel to the bundles, an arrangement that we interpret as ensuring a smooth structural and mechanical transition between the stone cells and vascular bundles in the endocarp (Fig. 14-4c/f) (Winton 1901).

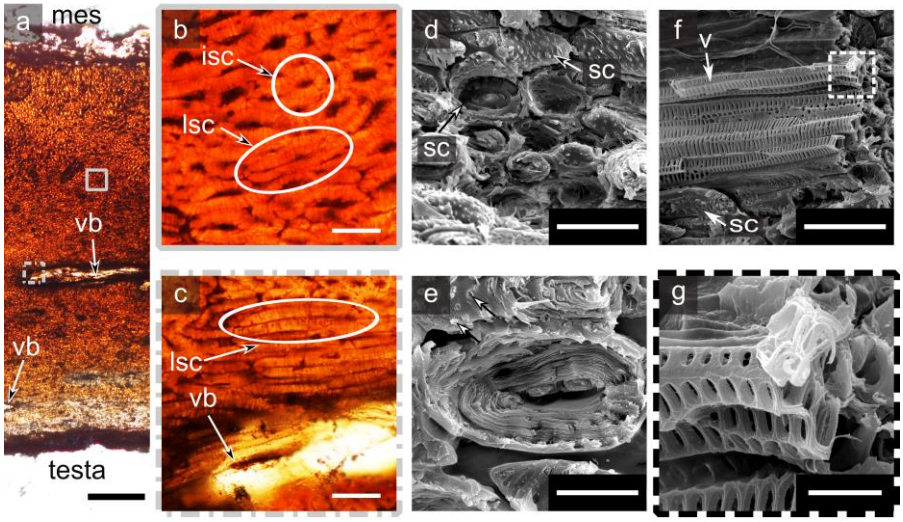

Figure 14-4. (a-c) Light micrographs of a polished cross section and (d-g) SEM micrographs of a fracture surface through the coconut endocarp. (a) The structure mainly consists of densely packed, thick walled stone cells and embedded vascular bundles (vb). The diameter of the stone cells becomes gradually smaller in the direction from the outer side of the endocarp facing the mesocarp (mes) towards the inner side adjacent to the testa. (b) Detailed view of stone cells, which can be either (nearly) isodiametric (isc) or elongated (lsc). (c) Detailed view of a vascular bundle surrounded by longitudinally elongated stone cells. (d) Image of the fracture surface showing individual stone cells (sc). Whereas some cells are still intact, others are fractured, revealing the layered inner structure of the cell walls. (e) Detailed view of a fractured stone cell showing the multi-layered cell wall. The roundish structures (arrows) within the cell walls are plasmodesmata. (f) Pulled out vascular bundle with several rigid tracheids/vessels (v) surrounded by densely packed aligned stone cells (sc). (g) Detailed view of some tracheids/vessels from c. The rigidity of the scalariform tracheids/vessels is caused by the ladder-like design and lignin deposition in the cell walls.
Scale bars: a: 500 µm, b, c, d, f: 50 µm, e: 20 µm, g: 9 µm.

The endocarp represents a hierarchically structured material comprising various types of densely packed, typically highly lignified cells in an inhomogeneous agglomeration, resulting in its anisotropic mechanical behaviour. Since botanical materials are rarely purely brittle, we consider the endocarp as a "quasi-brittle" material. This term was introduced by Bažant (2004) for materials such as concrete, bone and biological shells. In the fracture process zone of quasi-brittle materials, microcracks occur that lead to a softening of the material (in brittle materials this zone is negligible). The coconut endocarp was chosen as the botanical role model for quasi-brittle materials.

Once the mechanical tests are well established, comparative studies with coconut dwarf varieties are planned. These varieties have smaller fruits with

thinner fruit walls, features that will enable us to test smaller sample sizes of the endocarp and therewith to contribute to the question of the size dependency of fracture behaviour.

4. MECHANICAL TESTS

To assure reliable results within this project, two different test setups have been developed. Since the behaviour of materials differs in static and dynamic loading situations, both situations have been taken into account. For the quasi-static loading situation (penetration tests), a constant feed motion has been applied to the samples, whereas in the dynamic situation (impact tests), the sudden impact is caused by an impact pendulum. With the mechanical tests, we aim to identify the Weibull behaviour of the biological materials. Combined with detailed information about the inner structure of the materials, we hope to identify structural parameters (such as cell arrangement or porosity gradients) which have an impact on $\sigma_0 V_0^{1/m}$.

4.1 Penetration tests on sea urchin spines

The method of choice is known to metallurgists as the "impression test" (Yang and Li 2013). This test is used, for example, to characterise highly porous ductile metallic foams (e.g. Olurin et al. 2000, Kumar et al. 2003). A cylindrical indenter penetrates with a constant velocity several millimetres into the sample. Various geometries of the indenter tip have been reported in the literature, such as a flat-ended cylindrical indenter tip (FEI) or a spherical-ended indenter tip (SEI) (Olurin et al. 2000, Kumar et al. 2003) (Fig. 14-5a). Based on the first measurements by Presser et al. (2009), this method has been transferred to brittle porous materials and is called the "penetration test" to avoid any possibility of confusion with the "impression test". Hereby, we eliminate some difficulties of the uniaxial compression tests (Chapter 7) and provide:

- Simple and low cost sample preparation: a highly precise geometric sample is not required
- High spatial resolution, which is of special interest for the growth layers of HM and characterisation of the individual intrinsic material properties of the substructures medulla, intermediate layer and cortex.
- The specimens are not destroyed entirely after measurements (Fig. 14-2c/d), which is advantageous for further investigations.
- Multiple measurements can be made on a single specimen (Fig. 14-2c).

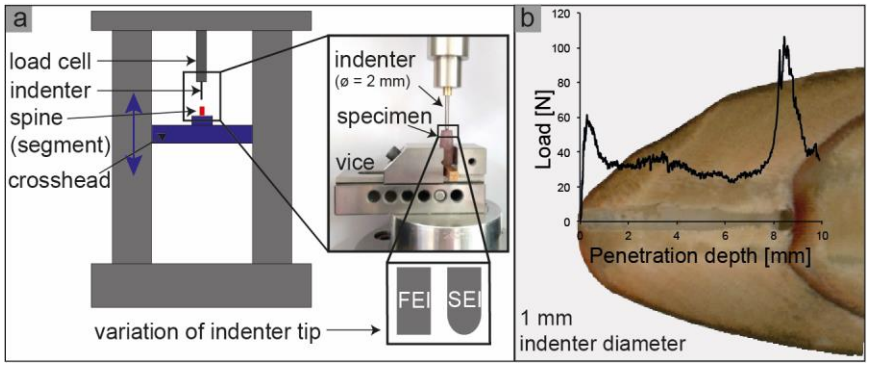

Figure 14-5. (a) Representation of the universal testing machine Instron 4502. The first magnification is a photograph of a fixed spine on the crosshead and the second magnification sketches the shape of a flat-ended and a spherical-ended indenter tip, FEI and SEI, respectively. (b) Correlation of the load penetration curve of HM with its internal structure. The spine was cut longitudinally afterwards. The force is highest when penetrating through the dense growth layers.

Nevertheless, the overall principles of indentation are still similar to uniaxial compression tests (Kumar et al. 2003, Yu et al. 1985, Olurin et al. 2000, Andrews et al. 2001).

For our measurements, cylindrical tungsten carbide indenters (d = 0.6, 1, 2 mm) were used with flat-ended indenter tips and spherical-ended indenter tips (Fig. 14-5a). Sea urchin spines were cut into segments (Fig. 14-2c/d) and indented from the top of the spine (= crystallographic c-axis). The indentations were performed with an Instron 4502 universal testing machine (Instron Deutschland GmbH, Pfungstadt, Germany) with a constant cross head speed of 0.5 mm/min. The indentation depth varied from 5 to 20 mm and was mostly chosen to be 10 mm.

4.1.1 Spatial resolution of the penetration test

Fig. 14-5b highlights the spatial resolution of this method by showing the load/penetration depth curve of an SEI (ø =1 mm) in a HM spine section compared with its interior structure (the spine was cut longitudinally afterwards). The force required to penetrate through the outer growth cap into the spine is about 60 N, drops after penetration below 40 N and increases to more than 100 N just shortly before penetrating the next growth cap after 8 mm. This initial load increase might in part be attributable to the accumulation of debris (crushed calcite) in front of the indenter (Presser et al. 2009); this requires further investigation.

In a later stage of this work, the results of the penetration test will be compared with uniaxial compression tests of sea urchin spines. Since

markedly different volumes will be used in the two tests, the size effect in sea urchin spines can be evaluated. Of interest will be to determine whether this follows the predictions of Eq. (2) or whether the sea urchin spines manage to overcome the size effect as observed in the bones of animals (Taylor 2000).

4.1.2 Influence of indenter geometry

Figure 14-6a shows the influence of the shape of the indenter tip on the measurements. Representative measurements for FEI (d = 0.6 mm, solid grey line) and SEI (d = 0.6 mm, black dotted line) are given. These measurements were conducted in the intermediate layer of the same spine segment of PI (Fig. 14-2c). For FEI, the load increases sharply right after the touchdown of the indenter on the spine, whereas for SEI, the load increases gradually. This is attributable to the shape of the SEI tip, whereby the cross sectional area increases in the first 0.3 mm of penetration (Fig. 14-6a on the top left: shape of SEI tip). The load/penetration depth curves of the FEI and SEI intersect after 0.3 mm of penetration, exactly at the point at which the cross sectional areas of these indenters are identical (indicated by the black line in Fig. 14-6a). Subsequently, similar curves highlight the independence of the indentation response and indenter geometry. These observations agree with Kumar et al. (2002) who have found the same results for the impression of metallic foams. Because calculations with the FEI are simpler and because the deformation zone is less complicated (Mouginot and Maugis 1985), future measurements will be conducted with an FEI.

The effect of the indenter diameter on penetration stress (strength) is demonstrated in Fig. 14-6b. Indenter diameters of 0.6, 1 and 2 mm) were used for the intermediate layer (blue colours) and medulla (red colours) of PI. The shaded background colours highlight the range of stresses obtained in the 31 experiments. For clarity, only six stress/penetration depth curves are included in Fig. 14-6b. The strength of the intermediate layer ranges between 100 – 200 MPa and is generally higher than the strength of the highly porous medulla with 30 – 100 MPa, concentrating around 40 – 80 MPa. The scatter in both structural units of the PI spine is attributable to the heterogeneity of biological materials. Although the statistic is not exhaustive, the 31 measurements suggest that the strength data obtained with various indenter sizes do not vary systematically with indenter sizes.

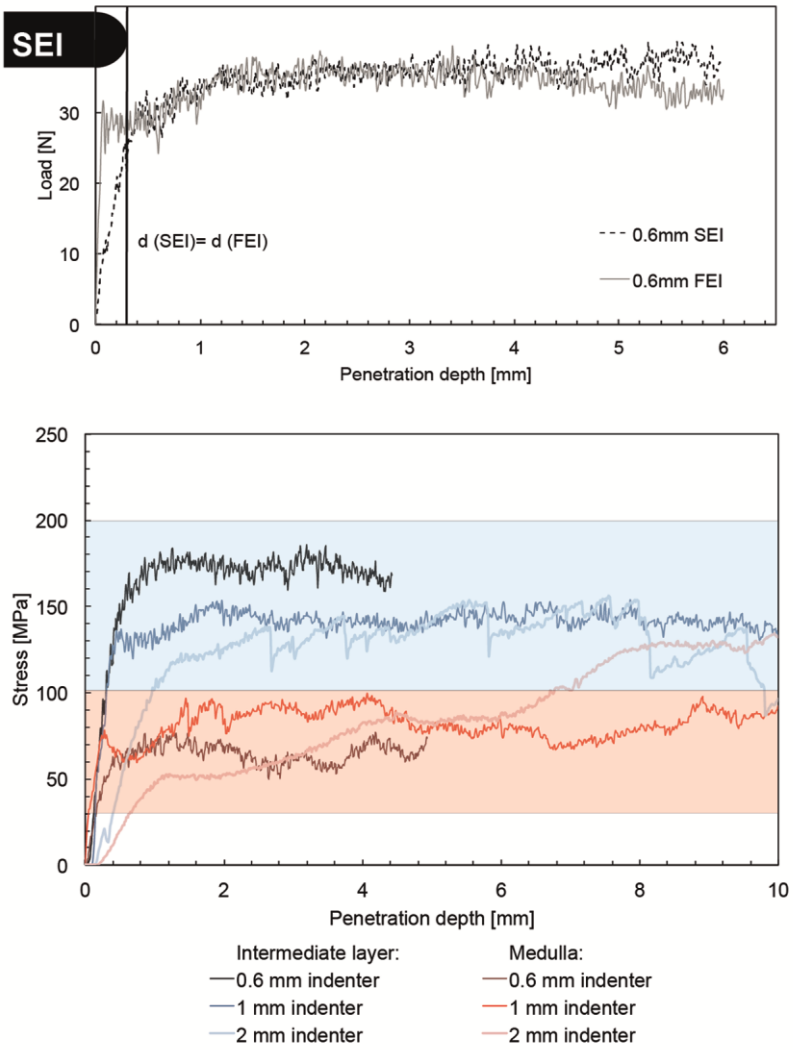

Figure 14-6. (a) Load/penetration depth curve for SEI and FEI of PI. (b) Stress/penetration depth curves for various indenter diameters conducted on 31 PI spine segments; for clarity, only six representative measurements are shown.

4.2 Impact pendulum tests with coconut endocarp

In order to determine the mechanical parameters in a dynamic loading situation, a test setup with an instrumented impact pendulum (B5113.303, Zwick GmbH & Co. KG, Ulm, Germany) was developed. The setup is based on the norm for instrumented Charpy impact tests (DIN EN ISO 179-2) of

unnotched and straight polymer samples. Our setup differs from that norm because the curvature of the coconut endocarp makes it impossible to obtain the required cuboid and straight sample geometry, as our samples were unnotched but arch-shaped (Fig. 14-7a). The height of the samples was approximately 10 mm; the curvature and sample width, however, varied depending on the geometric and anatomical parameters of the individual fruits (Fig. 14-7c). We tested two sample groups differing in their respective orientation within the endocarp: termed equatorial and meridional. The end of the coconut with the micropyles was defined as the north pole, the opposite end as the south pole. The equator lay centrally between the north pole and south pole, with the meridians running through the two poles (Fig. 14-7b).

The described tests were performed with an instrumented pendulum hammer of 7.5 J work capacity (BRA5113.3145, Zwick GmbH & Co. KG, Ulm, Germany). The span between the abutments was set to 50 mm and was determined to assure that the pendulum hammer did not become immobilised during the test, together with the broken sample fragments between the base of the pendulum. However, for this adapted setup, the exact span of the abutments was of minor interest, as the inner ends of the arch-shaped samples constituted the load-bearing points. The inner sample length is essential for evaluating the comparability of the biological samples, which inevitably differ (slightly) as to their size and shape (Fig. 14-7c). The samples were centred, so that the force transducer hit the sample in its vertex. This was also the point at which the width and height of the samples was measured (Fig. 14-7c).

The tests were performed with 41 equatorial and 58 meridional samples. The equatorial samples had a smaller radius of curvature (median: 43.69 mm) than the meridional samples (median: 63.48 mm), because of the ovoid shape of the endocarp. Moreover, the radius of curvature of the meridional samples had a larger scatter. The radius of curvature showed no significant influence on the impact resistance ($r_s = -0.098$). For all other parameters, no significant differences between the equatorial and meridional samples were found (Tab. 14-1) and no significant relationship could be observed between the sample dimensions and the impact resistance.

Table 14-1. Dimensions of the 99 tested coconut endocarp samples. Abbreviations: n: number of samples, IQR: interquartile range.

sample orientation	n	height [mm]		radius of curvature [mm]		width [mm]		inner length [mm]	
		median	IQR	median	IQR	median	IQR	median	IQR
equatorial	41	10.22	0.76	43.69	3.02	3.64	0.60	72.18	17.18
meridional	58	10.09	0.20	63.48	20.78	3.82	0.48	75.08	14.05

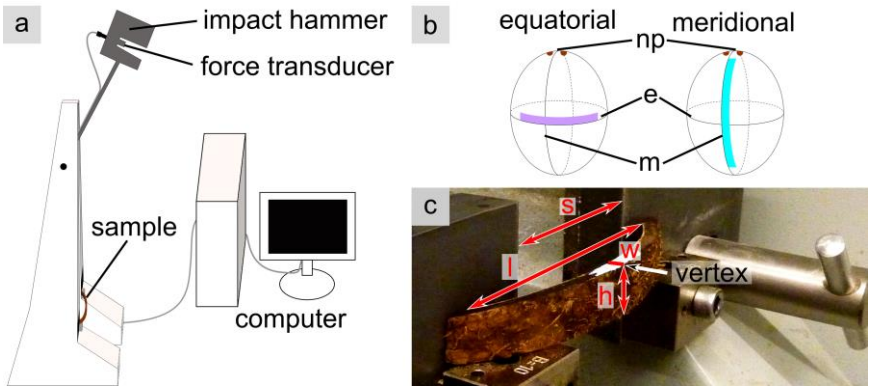

Figure 14-7. Instrumented impact pendulum tests. (a) Sketch of the test setup. (b) Orientation of the test specimen as cut from the coconut endocarp. Abbreviations: np: north pole, e: equator, m: meridian. (c) Detailed view of the mounted sample with geometric sample parameters. The sample geometry is arch-shaped because of the fruit morphology. The impacting hammer hits the sample at the vertex. Abbreviations: s: span between abutments, l: inner length = distance between the inner edges of contact areas of the sample with the abutments, w: specimen width at sample centre, h: specimen height at sample centre.

The impact resistance of the equatorial samples (median = 4.46 kJ/m) was significantly higher than the impact resistance of meridional samples (median = 2.36 kJ/m) (Fig. 14-8). This reveals the anisotropy of the biological material, reflected by structural differences within the endocarp, such as the different course of the vascular bundles or the variable cell orientation and cell distribution. A detailed analysis of the structural variations at various hierarchical levels is of special interest not only for a transfer to biomimetic products, but also for characterising quasi-brittle biological materials and is currently being performed.

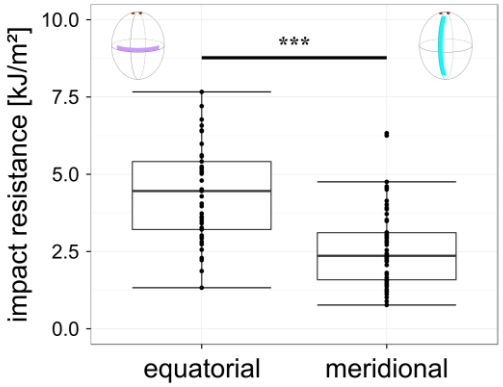

Figure 14-8. Comparison of the impact resistance (absorbed energy per crossectional area) of equatorial (41 specimens) and meridional samples (58 specimens). The equatorial samples

had a significantly higher impact resistance (median = 4.46 kJ/m) than the meridional samples (median = 2.36 kJ/m) (Mann-Whitney-U test; $W = 434$, $p < 0.001$).

5. SIMULATION: SUPPORT FOR MEASUREMENT AND SCALING CHALLENGES

The description and analysis of the material properties of biological materials is a great challenge. Natural materials show non-uniform directed properties because they often consist of an aggregation of various cell types (such as stone cells and vascular bundles within the coconut endocarp) or have other microstructures, for example, pores of various sizes (such as in the sea urchin spines), which result in inhomogeneous properties. Finite Element (FE) simulations of the materials and of the experiments might support the measurements and reveal the influence of specimen geometry and microstructure on the results of the experiments.

The failure behaviour during the impact of the coconut endocarp in the revised Charpy impact tests is highly complex, being the result of the inhomogeneous and anisotropic structure of the material and the arch shape of the sample. To generate comparable results and to analyse the influence of the shape of the coconut endocarp (and artefacts connected with it), we have used flat and arch-shaped PVC samples to determine the influence of the geometry of the probe. When the influence is known, a comparison of the properties of the natural arch-shaped samples with samples of other materials tested by Charpy impact tests can be performed. Variations not only of the shape, but also of the material itself can be easily taken into account in the simulation and can help to provide a better understanding of the influence of the geometries.

Simulations can only be as realistic as the input data and boundary conditions. Important input parameters in the case of the PVC samples are the density, elastic modulus and plastic behaviour. All these data can be found in the data sheet provided by the producer, except for the plastic material behaviour. For a first simulation (Fig. 14-9), literature values of the plastic behaviour of common PVC materials are used, but tensile tests will be performed in the near future to obtain the required information directly from the real tested specimens. The explicit linear elastic/plastic simulation with the FE-software Abaqus includes 5747 elements of type C3D8R, whereas the hammer and the abutment are modelled as 3D analytic rigid shells. The simulation includes so-called "cohesive surfaces" to simulate the crack opening behaviour of the sample. Defining these cohesive surface properties is one of the greatest challenges in the modelling of material behaviour. Only with inverse methods will it be possible to find suitable

material parameters requiring additional simulations that have to be compared with the experiments. Initial results show good agreement with the experimental data.

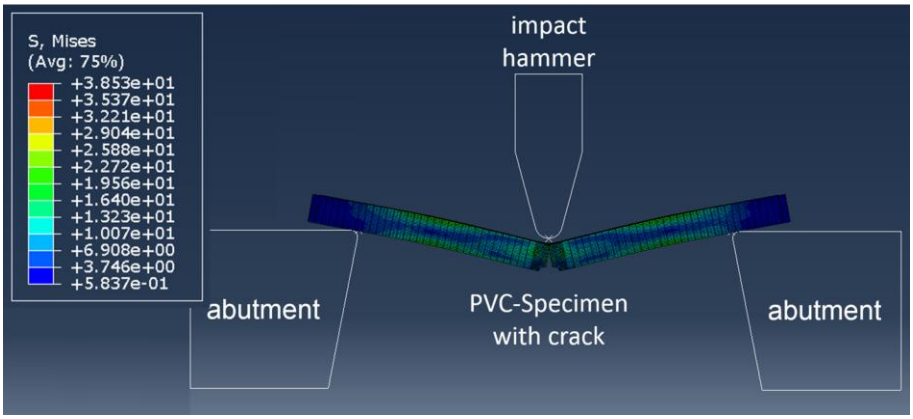

Figure 14-9. Von Mises stress distribution in the simulation of a Charpy impact test of a flat 7 cm long PVC specimen.

The simulation with flat PVC specimen is the first step; the second step is the analysis of arch-shaped PVC samples differing only in their shape from the flat ones in the Charpy impact tests. Thus, reliable information about shape is necessary (the shape dependency is discussed in more detail at the end of this paragraph).

The third step includes the natural material, which shows not only an arch-shaped form, but also inhomogeneous material properties (compare section 3). Therefore, structural information, such as cell forms and dimensions, plus the number and dimensions of embedded vascular bundles need to be included in the simulation. Moreover, the cohesive surface properties will be of special interest here and need to be determined by inverse methods. The results of each experiment will differ in detail, because the tests are performed on a natural material with structural and mechanical variations that are, for example, attributable to differentially distributed vascular bundles. Hence, this step needs to include information about the geometric artefacts found in the first steps of simulation and the relevant structural information in order to estimate the quality of the results obtained with the natural material. A comparison with artificial materials such as PVC specimens is needed and will help to provide an improved interpretation of the features of the natural material.

As already mentioned the shape needs to be defined exactly. This can be obtained by scanning or exact measuring of the samples or by computer tomography (CT). Revealing the exact shape from the CT-images through a

defined process was previously carried out in the group of the IMWF. One example is shown in Fig. 14-10 in which a sample of a PI sea urchin spine was analysed in a CT and converted into a 3D representation of the surface, which was then meshed and used in FE simulations. In this case, the resolution of the scan was high enough to reveal the macrostructure and the outer surface but not the microstructure such as the porous stereom.

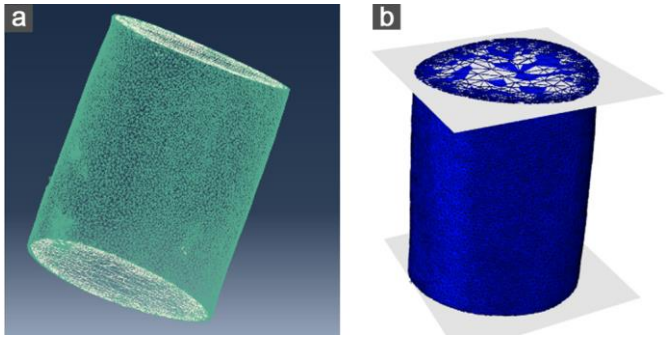

Figure 14-10. Simulations of a PI sea urchin spine test specimen. (a) Mesh reconstructed from a CT scan and (b) screenshot of the FE simulation of the compression test with added pressure plates and filled with a bulk material with isotropic elastic properties as a first approximation.

6. DISCUSSION

The challenge of scaling up natural constructions to sizes relevant for building construction is complicated for several reasons: natural biological materials show complex mechanical behaviour because of their complex hierarchical internal structure. This often creates a failure mode, which is neither ideally brittle nor ductile making it difficult to predict an upscaling based on classic reliability evaluation treatments such as Weibull algorithms.

In order to evaluate such theories, the main obstacle is the uniqueness of individual natural samples. A first step therefore involves the development of methods suitable for these unique materials in order to build up a reliable data base.

In our studies, promising model candidates are spines from large sea urchins, because they have an internal structure that can be characterised by quantitative parameters such as local densities, pore size and shape, while still being made of a single material (calcium carbonate) with little additions. This also makes them attractive for simulation treatment, which should be of great help in the evaluation of properties.

An unusual experimental treatment, namely the penetration of the quasi-brittle highly porous stereom of sea urchins, was chosen to yield quantitative strength and energy dissipation values. We have shown that the treatment

represents a local probing method that allows structural evaluation before tests by computer tomography and/or by sectioning the partially destroyed samples after testing and that gives easily understood numbers for materials engineering.

Another, but structurally much more complex, candidate is the tough coconut endocarp. Here, we have also tried to adapt a conventional material testing procedure, namely the impact pendulum (Charpy) test, to evaluate dynamic behaviour in terms of energy consumption. Again, we have the chance to investigate the structures both before and after treatment. The non-ideality of samples cut from fruits is still a challenge but, with the aid of computer simulations, we are confident that we can obtain values suitable for use in a scaling up evaluation. If this methodological approach can be evaluated for coconut endocarp, it will be transferred to even more challenging botanical materials such as highly energy dissipating tree barks, which are another role model for bio-inspired construction materials (Chapter 7).

ACKNOWLEDGEMENTS

This work has been funded by the German Research Foundation (DFG) as part of the Transregional Collaborative Research Centre (SFB/Transregio) 141 'Biological Design and Integrative Structures' / project B01 'Scaling of Properties of Highly Porous Biological and Biomimetic Constructions'. The Plant Biomechanics Group Freiburg also thanks E. Heizmann and UNIVEG Freiburg, Germany, for providing the coconuts.

REFERENCES

Andrews E W, Gioux G, Onck, P, Gibson L J (2001) Size effects in ductile cellular solids. Part II: experimental results. Int J Mech Sci 43(3): 701-713

Bauer G, Schmier S, Thielen M, Speck T (2015) Energy dissipation in plants – from puncture resistant seed coats to impact resistant tree barks. In: Yamamoto H, Morita M, Gril J (eds.) Proceedings of the 8th Plant Biomechanics Conference, Nagoya, Japan, pp 190-195

Bažant Z P (2000) Size effect. Int J Solids Struct 37(1): 69-80

Bažant Z P (2004) Scaling theory for quasibrittle structural failure. P Natl Acad Sci USA 101(37): 13400-13407

Burkhardt A, Hansmann W, Märkel K, Niemann H J (1983) Mechanical design in spines of diadematoid echinoids (Echinodermata, Echinoidea). Zoomorphology 102(3): 189-203

Chan E, Elevitch C R (2006) *Cocos nucifera* (coconut). Species Profiles for Pacific Island Agroforestry 2: 1-27

Chan Y L, Ngan A H W, King N M (2009) Use of focused ion beam milling for investigating the mechanical properties of biological tissues: a study of human primary molars. J Mech Behav Biomed 2(4): 375-383
Danzer R (2014) On the relationship between ceramic strength and the requirements for mechanical design. J Eur Ceram Soc 34(15): 3435-3460
Danzer R, Supancic P, Pascual J, Lube T (2007) Fracture statistics of ceramics–Weibull statistics and deviations from Weibull statistics. Eng Fract Mech 74(18): 2919-2932
Franke E, Lieberei R, Reisdorff C (2012) Nutzpflanzen. Georg Thieme Verlag, Stuttgart
Griffith A A (1921) The phenomena of rupture and flow in solids. Phil Trans R Soc A 221: 163-198
Grossmann J N, Nebelsick J H (2013) Comparative morphological and structural analysis of selected cidaroid and camarodont sea urchin spines. Zoomorphology 132(3): 301-315
Krumbholz M, Hieronymus C F, Burchardt S, Troll V R, Tanner D C, Friese N (2014) Weibull-distributed dyke thickness reflects probabilistic character of host-rock strength. Nat Commun 5:3272
Kumar P S, Ramachandra S, Ramamurty U (2003) Effect of displacement-rate on the indentation behavior of an aluminum foam. Mater Sci Eng A 347(1): 330-337
Lawn B (1993) Fracture of brittle solids. Cambridge university press
Lawrence J M (ed) (2013) Sea urchins: biology and ecology, vol 38. Academic Press
Łysiak G (2007) Fracture toughness of pea: Weibull analysis. J Food Eng 83(3): 436-443
Menig R, Meyers M H, Meyers M A, Vecchio K S (2000) Quasi-static and dynamic mechanical response of *Haliotis rufescens* (abalone) shells. Acta Mater 48(9): 2383-2398
Mouginot R, Maugis D (1985) Fracture indentation beneath flat and spherical punches. J Mater Sci 20(12): 4354-4376
Moureaux C, Pérez-Huerta A, Compère P, Zhu W, Leloup T, Cusack M, Dubois P (2010) Structure, composition and mechanical relations to function in sea urchin spine. J Struct Biol 170(1): 41-49
Olurin O B, Fleck N A, Ashby M F (2000) Indentation resistance of an aluminium foam. Scripta Mater 43(11): 983-989
Presser V, Schultheiß S, Berthold C, Nickel K G (2009) Sea urchin spines as a model-system for permeable, light-weight ceramics with graceful failure behavior. Part I. Mechanical behavior of sea urchin spines under compression. J Bionic Eng 6(3): 203-213
Seto J, Ma Y, Davis S A, Meldrum F, Gourrier A, Kim Y Y, Schilde U, Sztucki M, Burghammer M, Maltsev S, Jäger C, Cölfen H (2012) Structure-property relationships of a biological mesocrystal in the adult sea urchin spine. P Natl Acad Sci USA 109(10): 3699-3704
Su X, Kamat S, Heuer A H (2000) The structure of sea urchin spines, large biogenic single crystals of calcite. J Mater Sci 35(22): 5545-5551
Taylor D (2000) Scaling effects in the fatigue strength of bones from different animals. J Theor Biol 206(2): 299-306
Wagermaier W, Klaushofer K, Fratzl P (2015) Fragility of bone material controlled by internal interfaces. Calcif Tissue Int 97(3): 201-212
Weibull W (1939) A statistical theory of the strength of materials. Generalstabens litografiska anstalts förlag, Stockholm
Weibull W (1951) A Statistical Distribution Function of Wide Applicability. J Appl Mech 18: 293-297
Winton A L (1901) Anatomy of the fruit of *Cocos nucifera*. Am J Sci 70: 265-280
Yang F, Li J C (2013) Impression test—A review. Mat Sci Eng R 74(8): 233-253
Yu H Y, Imam M A, Rath B B (1985) Study of the deformation behaviour of homogeneous materials by impression tests. J Mater Sci 20(2): 636-642

Manuscript 2

Morphology and porosity of the spines of the sea urchin *Heterocentrotus mamillatus* and their implications on the mechanical performance

(16 pages)

Zoomorphology
DOI 10.1007/s00435-017-0385-4

ORIGINAL PAPER

Morphology and porosity of the spines of the sea urchin *Heterocentrotus mamillatus* and their implications on the mechanical performance

Christoph Lauer[1] · Tobias B. Grun[2] · Isabel Zutterkirch[1] · Raouf Jemmali[3] · James H. Nebelsick[2] · Klaus G. Nickel[1]

Received: 22 July 2017 / Revised: 16 October 2017 / Accepted: 19 October 2017

Abstract Spines of the slate pencil sea urchin *Heterocentrotus mamillatus* Linnaeus, 1758, are in focus of biomimetic research as they feature a "graceful" failure behaviour under uniaxial compression dissipating energy and resisting high loads even after high strain. This study elucidates and quantifies the organization of calcitic trabeculae and pores in large primary spines of the slate pencil urchin *H. mamillatus* by image analysis from scanning electron microscopy, X-ray micro-computed tomography (µCT) and gravimetry. This study delivers a detailed distribution of porosities within the whole spine and shows that parts of the spines have a much higher porosity then hitherto thought. The central part (medulla) of the high-magnesium calcitic stereom of *H. mamillatus* spines has a porosity range of 75% to nearly 90%. From this innermost structure, more than 200 radially aligned, but often sinuous trabeculae extend to the spine rim. The structure of this complicated meshwork (radiating layer) is best seen in basal cross sections and was confirmed by µCT scans. The radiating layer has a porosity range from 40–70% and is irregularly separated by the dense growth layers (15–35% porosity). Growth layers were classified in proximal and distal growth layers with numbers ranging within a single animal between 3–14 and 2–7, respectively. These growth layers are characteristic for *H. mamillatus* spines and play a major role in their remarkable mechanical properties. The porosity of the spine increases from base to tip. Biological and mechanical implications of the variations are discussed.

Keywords Morphology · Echinoids · Sea urchin spines · Porosity · µCT scans

Introduction

Sea urchin spines consist of magnesium calcite ($(Mg_{(1-x)}Ca_x)CO_3$) (Clarke and Wheeler 1915; Weber 1969a) forming a lattice-like 3d meshwork, called stereom (e.g. Smith 1980). Spines of sea urchins show a wide variety of shapes with respect to size, internal morphology and surface sculpturing (e.g. Durham 1955; Kroh and Smith 2010). Hesse (1900) distinguished six spine types by the architecture of the radial septa and showed that the different spine types can be common in a specific echinoid group, though are not necessarily restricted to these groups. Spines of various taxa have been investigated focusing on the microstructure and functional morphology alike (Nichols 1962; Dotan and Fishelson 1985; Lawrence 1987; Moureaux et al. 2010; Tsafnat et al. 2012; Grossmann and Nebelsick 2013a, b; Nebelsick et al. 2015). The various forms of the spines have been correlated to environmental interactions such as predator defence, sediment penetration or feeding (e.g. Telford 1982; Mooi 1986; Lawrence 1987). The lightweight architecture of the stereom reflects an economic way of constructing skeletons which has been discussed as an important factor for the evolutionary success of the echinoderms in general (e.g. Emson 1985;

✉ Christoph Lauer
christoph.lauer@uni-tuebingen.de

[1] Division of Applied Mineralogy, Department of Geosciences, University of Tübingen, Wilhelmstraße 56, 72074 Tübingen, Germany

[2] Division of Invertebrate Paleontology and Paleoclimatology, Department of Geosciences, University of Tübingen, Hölderlinstraße 12, 72074 Tübingen, Germany

[3] German Aerospace Institute (DLR), Institute for Structure and Design, Pfaffenwaldring 38, 70569 Stuttgart, Germany

Published online: 04 November 2017

Simkiss and Wilbur 1989). Smith (1980) distinguished ten stereom types within the echinoids and described their occurrence in the skeleton along with functional interpretations.

More recently, the spines of *H. mamillatus* have come into the focus of biomimetic research as they exhibit an outstanding crushing behaviour under uniaxial compression recognized as "graceful" failure (Presser et al. 2009a, b; Klang et al. 2016; Toader et al. 2017). The failure is based on a brittle foam type behaviour, which allows a layer-by-layer breakdown and the porosity changes within the stereom where cracks become deflected at the densest parts (growth layers) resulting in a successive crushing. Due to this construction, the spine can resist high loads even after a considerable strain (> 0.2) and a "graceful" failure has been observed (Presser et al. 2009a; Klang et al. 2016).

It should be emphasized, that in this context, strength is always structural strength caused by structural behaviour. Strength in brittle materials is never a material property as such. The strength of the building material calcite depends on its orientation towards stress, the distribution of inner defects and therefore, the stressed volume (e.g. Danzer et al. 2007; Danzer 2014). The structural features making the construction of a spine a strong component are exactly those, which can potentially improve constructions in civil engineering with respect to exceptional high impacts (Weber et al. 1969; Presser et al. 2011; Klang et al. 2016; Toader et al. 2017).

Morphology

The *H. mamillatus* spines belong to the thickest, largest and heaviest among sea urchins. The primary spines of this species vary in shape and size from the oral side, where they are flat and blade-shaped and comparatively small, to the aboral side, where they are large and almost round in cross section (Dotan and Fishelson 1985). The large and robust aboral spines (Fig. 1) can protect the echinoid against predators and serve as mechanical fixation structure in reef cavities and fissures where the nocturnal *H. mamillatus* is found during the day (Grossmann and Nebelsick 2013b). Besides the large primary spines, the test is also covered by blunt secondary spines (Deutler 1926; Dotan and Fishelson 1985), which are only a few millimetres in length.

In sections, the most prominent features of the primary spines of *H. mamillatus* are the conspicuously brownish-red coloured growth layers (Fig. 1a). They resemble smaller versions of the spine and separate growth cycles from one other with the oldest part of the spine in the centre (e.g. Weber 1969b; Dotan 1990). The colouration is caused by naphthaquinones (Vevers 1966), embedded in the fairly thin (usually < 50 µm) structure. The structures termed as growth layers have been synonymously named "growth rings" (Grossmann and Nebelsick 2013b), "growth bands" (Weber 1969b) or "growth lines" (Ebert 1986, 1988). In the present paper, the term "growth layer" is preferred in order to reflect the three-dimensional character of this structural entity.

On the microscale, the growth layers are composed of a relatively dense microperforate stereom (Fig. 1b, c) (Grossmann and Nebelsick 2013b) following Smith's classification (1980). A single growth layer is composed out of numerous radial septa giving the growth layers a radiating appearance (Hesse 1900). The radial septa are separated by channels, seen as large pores in cross sections (Fig. 1c). Growth layers belong to the densest parts of the spine (Presser et al. 2010). As the spine surface is equivalent to the youngest growth layer of the spine, the radial septa give the spine a corrugated surface seen as ribs in SEM micrographs (Fig. 1d) (e.g. Hasenpusch 2000; Grossmann and Nebelsick 2013a). Furthermore, the surface is covered by an epithelium.

Besides the conspicuous growth layers, the spine's architecture consists of the central medulla (Fig. 1a) with a laminar stereom type (Grossmann and Nebelsick 2013b). The stereom in between the medulla and the growth layers, the radiating layer, was reported to consist of labyrinthic stereom (Grossmann and Nebelsick 2013b). The seemingly random stereom distribution in the radiating layer was already noted by Hesse (1900). He described the radiating nature of *H. mamillatus* spines being restricted to the growth layers only and is lost in foam-like meshwork in between. In contrast, spines of other species exhibit a radiating microstructure resembling wedges (Kroh and Nebelsick 2010) with the number and shape of radiating units even being used as a species diagnostic feature (e.g. Coppard and Campbell 2004). The present study investigates the stereom distribution in *H. mamillatus* spines in detail adding to the description of Hesse (1900) and Grossmann and Nebelsick (2013b). The occurrence, shape and distribution of growth layers is discussed also with respect to mechanical performance of the spines as investigated by Presser et al. (2009a).

Porosity

Porosity is one of the most important factors influencing mechanical properties of porous materials, such as sea urchin spines, where the elastic properties as for example the Young's modulus are directly dependent on porosity (e.g. Coble and Kingery 1956; Gibson and Ashby 1982; Lu et al. 1999; Pabst et al. 2006; Ji et al. 2006). Despite being mechanically tested extensively (Su et al. 2000; Presser

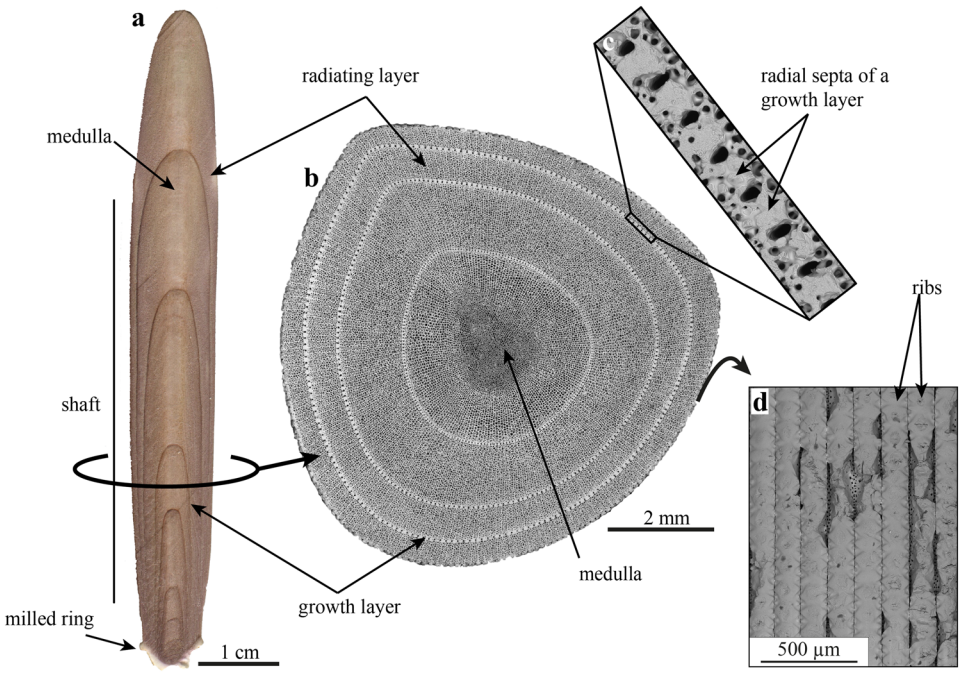

Fig. 1 Morphology and terminology of spines of *H. mamillatus*. In longitudinal sections (**a**) the growth layers are highlighted by their brownish-red colour. In SEM pictures of cross sections, the three different stereom types (medulla, radiating layer and growth layers) are best seen (**b**). Growth layers are composed out of numerous radial septa (**c**) that are ribs (**d**) giving the spine a corrugated surface. The surface of the spine is usually equivalent with the youngest growth layer

et al. 2009a; Grossmann and Nebelsick 2013a; Klang et al. 2016; Schmier et al. 2016), the porosity of sea urchin spines in general, and of *H. mamillatus* in particular, has not attracted much attention to date. Most studies state that the stereom structure is highly porous, without providing exact measures of the porosity (Burkhardt et al. 1983; Su et al. 2000; Presser et al. 2009a; Tsafnat et al. 2012; Grossmann and Nebelsick 2013b). Presser et al. (2010) determined porosity highly locally around nanoindentations in the stereom structure of *H. mamillatus* and reported values of 16 ± 1.9–19 ± 2.4% for the growth layers, 38 ± 3.8% for the radiating layer and 61 ± 4.8% for the medulla. The present study aims to provide a more global porosity distribution across the spine length and from the interior to the exterior of the spine. Implications for mechanical properties are discussed with respect to biological implications and mechanical tests performed by Presser et al. (2009a), Grossmann and Nebelsick (2013b) and Schmier et al. (2016). The data presented in these studies are characterized by a considerable scatter that is usually referred to "biological heterogeneity".

Materials and methods

Material

Eight adult individuals of *H. mamillatus* (HMf1-HMf8) were obtained from a material supplier (Mineralien- und Fossilienhandlung Peter Gensel, Weimar, Germany). In addition, an assortment of disarticulated *H. mamillatus* primary spines was obtained (Fischhaus Zepkow, Zepkow, Germany).

Methods

Growth layers and primary spine morphology

The specimen with the largest spines (HMf1) was selected for studying the shape and variation of growth layers within the spines. All primary spines larger than 15 mm (n = 69) were removed and sectioned longitudinally along the *z*-axis (crystallographic *c*-axis) with a Buehler med 1000 diamond saw (blade thickness: 500 µm). To assure that all growth layers were encountered, the section was not cut exactly along the middle of the spine, as the smallest layers can be somewhat off-centred after growth of the following layers. The spines were subsequently ground using carborundum abrasive paper with a grain size of 10 µm to the point where the growth layers close to the base were best visible. Spines smaller than 3 cm were polished only, as they were too thin for sectioning. Despite this careful procedure, not all growth layers at the base were exposed in some spines, thus their numbers are reported as "minimum values".

Spines were scanned by an Epson V370 high-resolution scanner to a resolution of 1200 dpi. Growth layers were then identified and counted from the scanned images. The growth layers were statistically analysed for a potential relationship between different growth layer types using a major axis regression in R (R Core Team 2016) with the

smatr extension (Warton et al. 2012). The length and mass variation along the oral spines and aboral spines was analysed by non-parametric Kruskal–Wallis *H* tests followed by pairwise Benjamini, Hochberg and Yekutieli *p*-adjusted Wilcoxon post hoc analyses to determine possible length and mass differences between groups.

Complete specimens of *H. mamillatus* were used to determine the shape of the primary spines with respect to their position on the test. Length (maximum distance from base to tip), diameter (maximum thickness perpendicular to the spine's longitudinal axis) and mass of the spines were measured on the same primary spines that were used for growth layer description prior to sectioning. Length was determined by a calliper with an accuracy of ± 0.05 mm. The spines were weighed on a Sartorius BP 211D scale with a precision of ± 0.0001 g.

Microstructural description

Microstructural analyses are based on micrographs obtained from a Hitachi TM 3030 Tabletop scanning electron microscope (SEM). SEM samples were prepared as cross sections and longitudinal sections of numerous spines from both complete individuals and spines from the spine assortment. After dissection, the samples were cleansed for 15 min in an ultrasonic bath with deionized water. The samples were then dried for at least 30 min at 110 °C in a drying cabinet. Dried and cleaned samples were analysed uncoated in the SEM.

The number of radial septa per growth layer was determined from SEM micrographs at six aboral spines. Therefore, cross sections at 10, 25, 50, 75 and 90% of the spine length measured from the base were used. The consistency of the number of radiating septa in cross section of a single spine and along different spines was analysed.

2d porosity determination and gravimetry

The porosity was determined based on SEM micrographs of five specimens in cross sections used for counting the radial septa. The samples were prepared for SEM analyses by infiltrating the stereom with epoxy resin Araldite 2020/A for 15 min at 0.05–0.15 bar. The samples were then polished. A full infiltration and a smooth surface is necessary for 2d porosity determination, otherwise struts or pores not lying in the analysed plane are mistakenly included in the analysis and would result in false porosities.

The porosity was calculated using the ImageJ software environment Fiji 2.0.0. The images were binarized using the iterative "default" threshold based on Ridler and Calvard (1978) which is accurate as the stereom is pale grey to white and can be distinguished by binarization from the dark grey or black epoxy resin that fills the pores. Pixel-clusters larger than 8 connected pixels were counted in the "analyse particles" function for porosity determination. Pixel-clusters smaller than 8 connected pixels can result from impurities in the Araldite 2020/A epoxy resin and were thus not analysed. The spine segment porosity was also determined gravimetrically prior to infiltration by assuming a density of 2.711 g/cm^3 for calcite (DeFoe and Compton 1925). Therefore, the volume of the spines was calculated by measuring the area of the cross section (A) on the SEM picture and by multiplying it with the mean thickness (d) of ten measurements of the segment that were carried out prior to infiltration. Together with the mass (m) that was also measured before the infiltration the porosity (ϕ) could be estimated with Eq. 1. Error bars were calculated with the standard deviation of the thickness.

$$\phi[\%] = \left(1 - \left(\frac{m[\mathrm{g}]}{A[\mathrm{cm}^2] \times h[\mathrm{cm}] \times 2.711[\mathrm{g} \times \mathrm{cm}^{-3}]}\right)\right) \times 100. \quad (1)$$

In 2d analysis, the porosity was analysed for the whole cross section, the growth layer(s), the radiating layer(s) and the medulla. Growth layers were numbered in an ascending order from old to young (interior to exterior). The radiating layer is separated by the growth layers in as many ring-shaped sections of radiating layer as there are growth layers. These radiating layers were numbered in the same ascending order from old to young.

3d porosity determination

For 3d porosity determination, two X-ray micro-computed tomography (µCT) scans were performed, one in the medulla and one in the radiating layer. In both cases, the scanned volume was a cube with an edge length of 1.278 mm within a thin bar extracted at 50% of the spine length of a large aboral spine from the articulated spine collection. The spine was prepared in the same way as described above for the microstructural analysis. The µCT scans were conducted using a Nanotom (GE Sensing & Inspection Technologies GmbH, Wunstorf) equipped with a microfocus X-ray tube. The samples were scanned at 80 kV/180 µA with an exposure time of 800 ms to a resolution of 1.27 µm per voxel. The acquired 2d X-ray images were reconstructed with a Filtered Back Projection reconstruction algorithm (datos|*x*). The µCT data were visualized and analysed with the commercially available software packages VGStudioMax 3.0 (Volume Graphics GmbH, Heidelberg), Avizo 9.3 (FEI SAS, Mérignac) and MAVI 1.5.2 (Fraunhofer IWTM, Kaiserslautern).

An anisotropic diffusion filter was applied to the µCT scans reducing the noise while preserving edges of the structures. The reconstructed objects were than binarized

by Otsu's threshold method (Otsu 1979) as it is suitable for data sets with bimodal grey value distributions and is user independent. In the µCT scans, porosity was determined in x_1, x_2 and z-direction (crystallographic c-axis) meaning the porosity in the z-direction is the porosity measured on the plane perpendicular to the z-axis (x_1, x_2 plane), etc. The mean porosity is composed out of the porosity in x_1, x_2, and z-direction. The porosities of the medulla and the radiating layers are compared to the porosities obtained by gravimetric porosity determination, 2d SEM analysis and to porosities reported in the literature.

Results

Growth layer description

Growth layers in primary and secondary *H. mamillatus* spines in both, cross- and longitudinal section, are recognized as thin, often brownish-red lines (Figs. 1, 2). Two different types of growth layers were found: Proximal growth layers (1) are present as densely packed loops near the base (Fig. 2b, c). They merge into each other and rarely exceed a few millimetres in size. These layers resemble growth layers found on secondary spines (Fig. 2d). Secondary spines possess proximal growth layers only. Distal growth layers (2) are more widely spaced and the regular distal type extends from the milled ring to the tip of the spine where they form the typical blunt tip (Fig. 2a). A succession of these regular distal growth layers provide the spine a matryoshka-doll-like appearance (Fig. 2a). Two sub-types of distal growth layers beside the regular ones were encountered: capping growth layers (1) are characterized by an isolated growth cap (Fig. 2a) separated from its disjunct basal layer emanating from the milled ring towards the cap (Fig. 2e). Incomplete distal growth layers (2) lack the characteristic cap (Fig. 2g). Whether or not such an incomplete distal growth layer can be present at the surface of the spine or occurs due to later resorption is unclear.

A sequence of all distal growth layer types can develop in a single spine and may form a complex growth pattern as present in the spine shown in Fig. 2a. Here, the incomplete distal growth layer is the oldest distal growth layer followed by three regular distal growth layers. This construction is topped by two capping growth layers. The disjunct basal layer of growth cap 1 is already overgrown by the younger disjunct basal layer of growth cap 2 (Fig. 2f). Distal growth layers are usually not evenly spaced (Fig. 2a).

Primary spines

Primary spines show a wide variety of sizes and shapes within a single individual. In cross section, oral primary spines are flat and blade-shaped, where aboral primary spines are triangular to round. A graded transition of the spine morphology can be found from the oral to the aboral side of the test (Fig. 3). Nearly perfect circular spine cross sections are not found on every individual. Oral spines are the smallest (median: 26.1 mm) and lightest (median: 0.340 g) spines (Fig. 4a, b, Table 1). The aboral primary spines are the largest spines of this echinoid. Two groups of aboral primary spines were distinguished: aboral spines without capping growth layer and with capping growth layer. Capping growth layers were only found on aboral spines longer than 44 mm and are always present on spines longer than 73 mm (Fig. 4a, c, Table 1). Aboral spines lacking these capping growth layers are lighter and shorter than aboral spines with capping growth layers, but still heavier and longer than the oral spines (Table 1, Fig. 4a–c). All three groups show a considerable scatter in their masses, maximal diameters and lengths. Only for oral spines and aboral spines with capping growth layer the group distinction is statistically significant with $p < 0.05$ (Fig. 4a, b, Table 2). An increasing spine length is correlated by an increase of the spine mass (Fig. 4c). These correlations are statistically significant for all three spine groups (Table 2).

There are slight differences in the distribution of growth layers in oral and aboral spines. Oral spines appear to have an approximately equal distribution of proximal and distal growth layers, as they scatter around the bisecting line (Fig. 4d). There is only weak correlation between the number of proximal and distal growth layers for oral spines, although it is significant (Table 2). Aboral spines without capping growth layers tend to have a higher number of proximal than distal growth layers (Fig. 4e) with again a weak, though significant correlation (Table 2). The highest number of proximal and least number of distal growth layers are found in the aboral spines closest to the apical disc (Fig. 4e). Aboral spines with capping growth layers show no correlation in number of distal and proximal growth layers (Fig. 4f, Table 2). They usually have less proximal growth layers than distal growth layers (Fig. 4f).

Microstructure description

On the microscale and best seen in cross sections, growth layers are composed of numerous radial septa as pointed out by previous authors (Hesse 1900; Grossmann and Nebelsick 2013a) and is confirmed by this study (Fig. 1b–

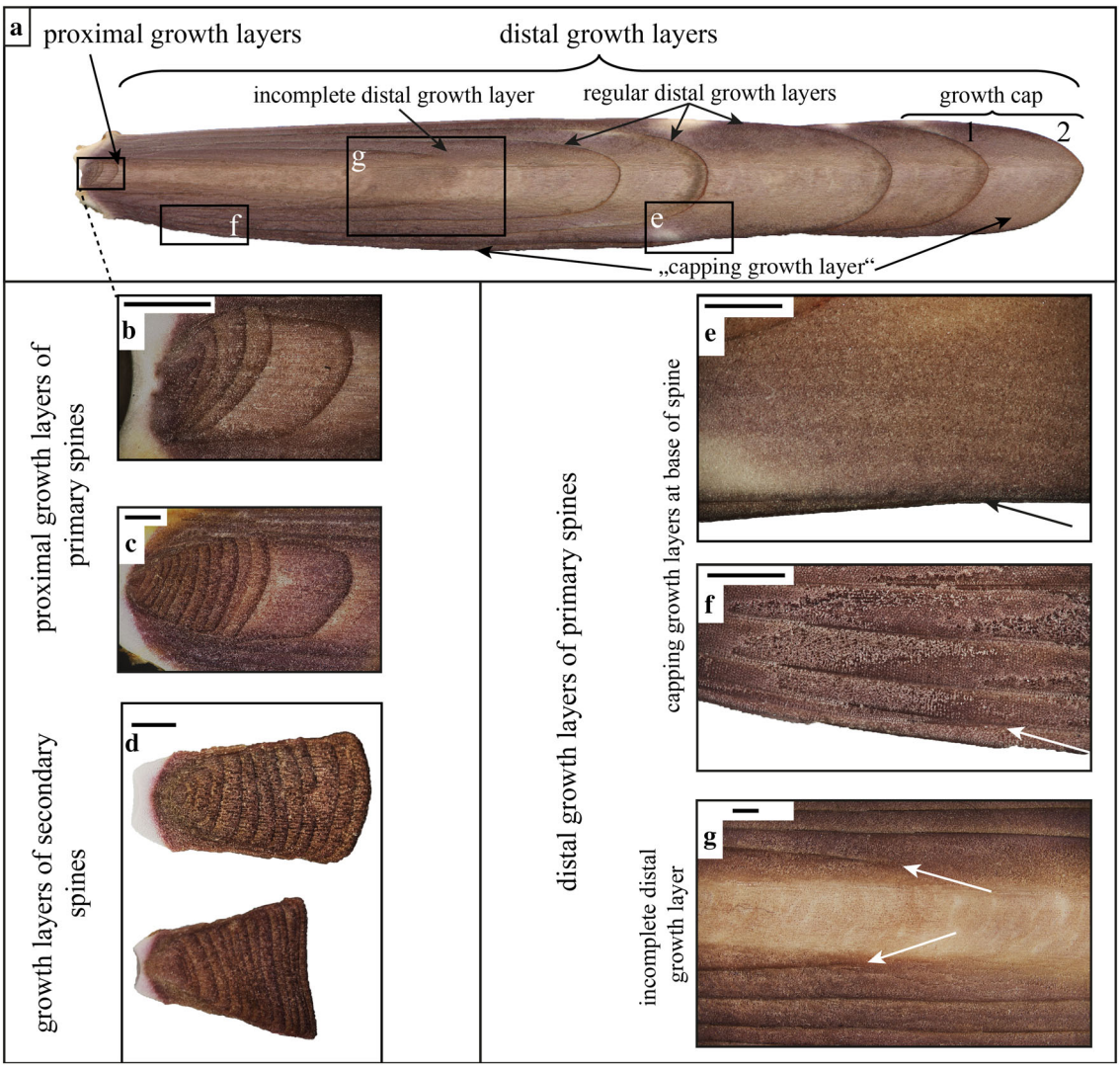

Fig. 2 The different types of growth layers in longitudinal sections in a primary spine (**a**) with magnifications (**b**, **e**, **f**, **g**). **b**, **c** show the closely packed proximal growth layers in the base of primary spines which resemble the growth layers found in secondary spines (**d**). Regular distal growth layers usually extend from the base to the tip of the spine (**a**), but two variations were found: (1) capping growth layers (**a**), that top the regular distal growth layers with caps, but also have a corresponding succession at base (**d**, **e**) and (2) incomplete distal growth layers lacking the dome shaped cap (**a**, **g**). Scale bars = 1 mm

Fig. 3 Cross section series of spines from the oral towards the aboral side. All spines taken from HMf3. The brownish-red lines within the cross sections represent growth layers, which appear as bands or lines in 2d sections. The largest spine on the right shows healed wounds indicated by arrows. Possible reasons for this damage is a predator attack or exposure to high-energy marine environment

d). The number of radial septa was counted in all growth layers of six aboral spines (Table 3).

The number of radial septa per growth layers is remarkably constant (Table 3), considering the shape and variations and increasing circumference of the spines with age. The fewest radial septa per spine were observed in HMf4 (196-214), the most in HMf2 (260-272). The largest increase of radial septa within a single growth layer is 15, the largest decrease found is 27 (Table 3). Nevertheless, for the majority of growth layers, the number of radial septa is nearly constant throughout the spine and all growth layers.

In cross sections close to the milled ring, the radial septa of the growth layers are interconnected by radiating trabeculae which extend from the middle of one radial septa to the next (Fig. 5a–c). These radiating trabeculae start

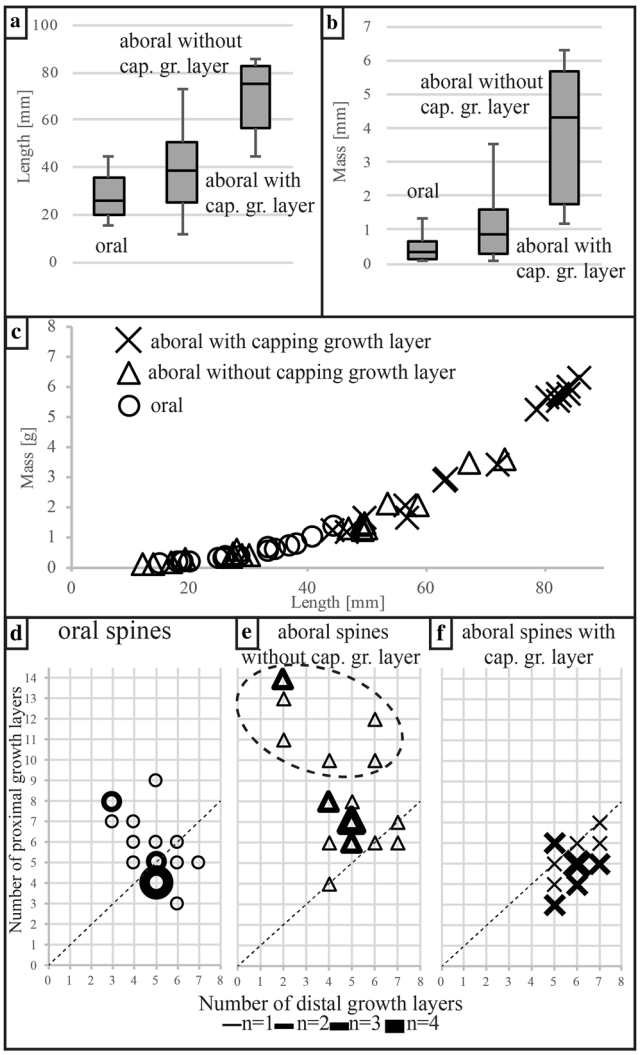

Fig. 4 Correlations of different spine types of HMf1 to mass (**a**, **b**), length (**a**, **c**) and number of growth layer type (**d**–**f**). All correlations are listed in Table 2. Dashed lines in d–f represent an equal distribution of proximal and distal growth layers. "cap. gr. layer" refers to capping growth layer

right after the medulla (Fig. 5b) and connect the growth layer's radial septa until the spines rim. The radiating trabeculae are not always straight, but can be slightly sinuous (Fig. 5c). In longitudinal sections, the interconnecting radiating trabeculae appear as a perforated wall with a more regular structure and a smaller pore size than the stereom filling the interspace between the radiating trabeculae (Fig. 5d). In cross section, this stereom interspace has the width of a single pore right after the radiating trabeculae emanate from the medulla (Fig. 5b). In later stages, two pores are situated between the radiating trabeculae (Fig. 5c). The transition from one to two pores is highlighted by the line in Fig. 5a and occurs in a similar distance to the medulla between all radiating trabeculae. This overall radiating structure is best seen close to the milled ring and generally in smaller aboral spines (Fig. 5) of *H. mamillatus*.

The radiating structure is also traceable in large spines (Fig. 6). A radiating trabecula is highlighted by the white line in Fig. 6a–d and a schematic representation of the whole radiating structure with a shaded background for the basic radiating unit is given (Fig. 6e). Numerous repetitions of this radiating unit consisting of radiating trabeculae, radial septa and stereom interspace are present. The radiating trabeculae arise from the medulla, where laminar stereom meets the ordered radiating trabeculae (Fig. 6b). By placing the radiating trabeculae in the centre of the basic radiating unit (Fig. 6a, e), it is then framed by the width of half a pore of the stereom interspace on each side (Fig. 6b, e). At a critical pore diameter, the single pore between two radiating trabeculae splits up into two smaller pores with a thin strut in between, such that the radiating trabeculae is now framed by the width of a full pore on each side (Fig. 6c, e). Close to the spine edge, at least two pores to each side of the radiating trabeculae make the overall stereom appear more chaotically arranged (Fig. 6d, e). Nevertheless, the radiating trabeculae are still visible, as they are thicker than the ordinary struts of the stereom interspace (Fig. 6a, d). Although the whole stereom seems to merge into a chaotic structure at some parts, the radiating trabeculae can still be recognized (white box, Fig. 6a).

Porosity distributions

Gravimetric porosities and the porosity determined by 2d image analysis of the 15 segments show good accordance. The 2d porosity coincides within the error range of the gravimetric porosity (Fig. 7a). In the 15 segments, the overall porosity ranges from 54.3 to 71.6%. The medulla has the highest porosity (average of 75.4–88.3%) and the growth layers the lowest porosity (14.9–36.2%) with the radiating layer ranging in between. This means the densest part of the spine is close to the spine surface, the lightest stereom is in the centre (medulla) and the radiating layer is filled with stereom of intermediate porosity. The resulting porosity gradient is occasionally interrupted by older growth layers. This porosity gradient is, on the one hand, stepwise between the morphological distinct stereom types of medulla, radiating layers and growth layers, but on the other hand gradual in the radiating layer as seen in Fig. 7b, c. The radiating layer (RL1) between medulla and the oldest growth layer (GL1) has a porosity of 67.4% while the radiating layer (RL3) between the youngest growth layer (GL3) and the second growth layer (GL2) has a porosity of 56.3% which is a reduction of 11.1% points. Porosities of the radiating layer in cross sections at 50 and 90% of the spine length are generally higher, but still

Table 1 Measurements of oral and aboral *H. mamillatus* spines from HMf1

Position on test	*n*	Length (mm)			Mass (g)			Max. diameter (mm)		
		Range	Median	Mad	Range	Mean	Mad	Range	Median	Mad
Aboral (without capping growth layer)	18	11.7–73.1	38.4	11.5	0.090–3.546	0.892	0.565	2.5–10.6	8.0	2.0
Aboral (with capping growth layer)	16	44.2–85.8	75.2	9.7	1.173–6.295	4.298	1.458	7.9–12.3	11.0	0.8
Oral	17	15.0–44.4	26.1	7.3	0.080–1.325	0.340	0.213	4.3–10.5	6.5	1.4

Only spines where the number of proximal growth layers could be determined are listed. *n* sample size, *mad* median absolute deviation

Table 2 Pairwise Benjamini, Hochberg and Yekutieli *p*-adjusted Wilcoxon post hoc analyses to determine possible length and mass differences between groups (Fig. 3a, b)

		n	*p*	R^2
Figure 3a	Oral spines with capping growth layers vs. aboral spines without capping growth layers	17	0.0513	
	Oral vs. aboral with capping growth layers	18	< 0.001	
	Aboral without vs. with capping growth layers	16	< 0.001	
Figure 3b	Oral vs. aboral without capping growth layers	17	0.07	
	Oral vs. aboral with capping growth layers	18	< 0.001	
	Aboral without vs. with capping growth layers	16	0.029	
Figure 3c	Oral	17	< 0.001	0.992
	Aboral without capping growth layers	18	< 0.001	0.975
	Aboral with capping growth layers	16	< 0.001	0.981
Figure 3d	Oral	17	0.015	0.315
Figure 3e	Aboral without capping growth layers	18	< 0.001	0.362
Figure 3f	Aboral with capping growth layers	16	0.094	0.18

Major axis regressions of proximal and distal growth layers (see Fig. 3c–f). *n* sample size, *p* *p* value, R^2 regression coefficient

decreasing from interior to exterior (Fig. 7c, Table 4). Porosity changes within the radiating layer alongside with the values for growth layers and medulla are listed for all analysed segments in Table 4.

Over the spine length from the bottom cross section at 10% to the cross section close to the tip at 90%, the porosity consistently increases for all five analysed spines (Fig. 7d). The porosity of the medulla remains constant at around 80% and the porosity of the growth layers decreases from around 30% to below 20% along the spine length. The radiating layer exhibits the same increasing porosity trend at similar values as the whole cross sections showing that it contributes most to the overall porosity (Fig. 7d). The number of growth layers present in the cross section influences the overall porosity of the cross section as well (Fig. 7e). It correlates linearly with the porosity ($R^2 = 0.7878$). The higher the porosity, the fewer growth layers were encountered. No significant correlation was found between the number of basic radiating units that constitute the spine and the overall porosity of the cross section ($R^2 = 0.0025$, Fig. 7f).

The porosity obtained by µCT scans (Fig. 8) reflects the 2d porosity determination in the cross sections. The radiating layer has an average porosity of 63.2% and the medulla of 79.7% (straight lines in Fig. 8). The porosities in *x*1, *x*2 and *z*-direction coincide closely with the average porosity, however, there are two exceptions. (1) In the *z*-direction (crystallographic *c*-axis) the porosity of the medulla is first higher than 79.7% peaking at 84.7% and after 0.6 mm it is lower than the average. (2) In the x_1-direction of the radiating layer, periodic oscillations with a wavelength of 30–70 µm are present with decreasing amplitude.

Discussion

Basic radiating units as building principle of spines of *H. mamillatus*

On a micrometre scale the stereom of the radiating layer might appear chaotic (Fig. 6) as described in Grossmann

Table 3 Number of radial septa counted per growth layer (GL) in cross sections taken at 10, 25, 50, 75 and 90% of the spine length measured from the base, respectively

Sample	Length [mm]	Mass [g]	Number of radial septa per GL at length of spine measured from base				
			At 10%	At 25%	At 50%	At 75%	At 90%
HMf2	65	3.83					
GL 1			266	274	273		
GL 2			265	268	272	271	
GL 3			262	266	270	272	272
GL 4			260	263	268		272
HMf4	69	3.67					
GL 1			202				
GL 2			202	202			
GL 3			202	202			
GL 4			202	202	202		
GL 5			202	202	202		
GL 6			202	202	204	204	
GL 7			202	202	204	203	196
GL 8			202	202	204	203	214
HMf5	70	4.04					
GL 1			208				
GL 2			218	213			
GL 3			218	218	218		
GL 4			218	218	218	204	
GL 5			218	218	218	218	221
HMf7	67	2.97					
GL 1			231	225			
GL 2			232	230	225	215	
GL 3			232	232	230	226	225
HMf8	72	3.9					
GL 1			213				
GL 2			237	210			
GL 3			240	235	225		
GL 4			240	238	232	224	
GL 5			240	240	236	231	230
HMrs1	93	7.04					
GL1			231	–	–	–	–
GL2			249	–	–	–	–
GL3			249	249	–	–	–
GL4			249	249	257	–	–
GL5			249	249	256	263	265
GL6			249	–	–	–	–
GL7			249	249	–	–	264

Spines were sampled form six different animals

and Nebelsick (2013a, b); however, when zooming out to the mm scale, it becomes obvious that the stereom is ordered in a radiating manner. This order has been reported for spines of *Heterocentrotus trigonarius* (Hesse 1900; Weber 1969b), the closest relative of *H. mamillatus*, where it is much more obvious due to an overall lower porosity of the spines and more growth layers with their radial septa present in cross sections. Both facilitates tracking the radiating unit. This is probably the reason why the radiating structure is more clearly seen in *H. mamillatus* basal cross sections where the porosity is lower and more growth layers are present than in distal cross sections close to the

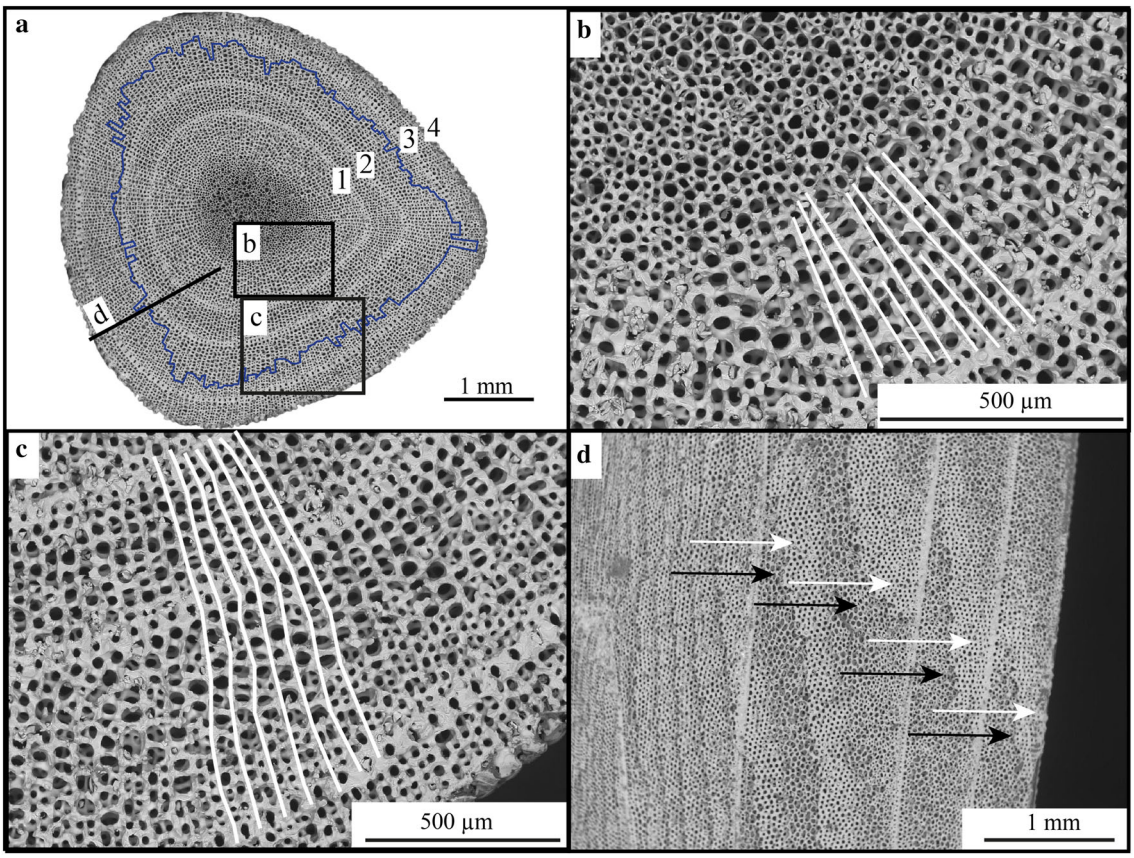

Fig. 5 A small aboral spine with 4 growth layers (1–4) displays radiating trabeculae well traceable from the medulla to the outside of the spine (**a**). The line marks the transition from 1 to 2 pores between the radiating trabeculae (**a**). The detail pictures **b** and **c** are enlargements of the frames in **a**, showing the radiating structure in higher detail. In longitudinal sections (**d**) the radiating trabeculae (in 3d a wall-like structure) stand out with smaller pore sizes and visually higher pore order (white arrows) compared to the stereom interspace filling the space in between the radiating trabeculae (black arrows)

tip. Hesse (1900) described the radiating nature of *H. mamillatus* spines being restricted to the growth layers only and is lost in foam-like meshwork in between. The SEM micrographs presented here show that radiating trabeculae connecting the radiating septa of the growth layers, although sometimes sinuous, and give the spine an overall radiating arrangement as typical for many sea urchin spines (e.g. Hesse 1900; Coppard and Campbell 2004; Kroh and Nebelsick 2010). Strong evidence for the presence of this radiating structure comes also from the µCT analysis, where perpendicular to the direction of the radiating structure porosity oscillations with the wavelength typical for the width of a radiating unit ranging between 30 and 70 µm (Fig. 8). Lower porosities reflect denser radiating trabeculae and higher porosities reflect the stereom interspace.

The basic radiating unit occurs in numerous repetitions and at least 200 per spine were found. In contrast to *H. trigonarius*, where new radiating units are frequently added in new growth cycles in order to keep geometry with the increasing spine diameter (Weber 1969b), their number is nearly constant in aboral spines of *H. mamillatus*. This implicates a growth mechanism by a subsequently widening of the radiating unit. Furthermore, the number of radiating units is not diagnostic for *H. mamillatus* as has been found for other species (e.g. Coppard and Campbell 2004) since their number differs largely among spines. In contrast to other species, where few but dense and thick wedges make up the basic radiating unit (e.g. *Paracentrotus lividus*, see i.e. Kroh and Nebelsick 2010), *H. mamillatus* has a delicate radiating structure which serves the overall lightweight construction. In this manner, the advantages of a lightweight construction as a compromise between functional aspects and energetic costs are achieved.

Porosity distributions

Presser et al. (2010) determined gravimetrically the porosity of a cuboid segment of a *H. mamillatus* spine for 4-point bending tests. In this sample, medulla and radiating layer were present and they detected a porosity of 59%,

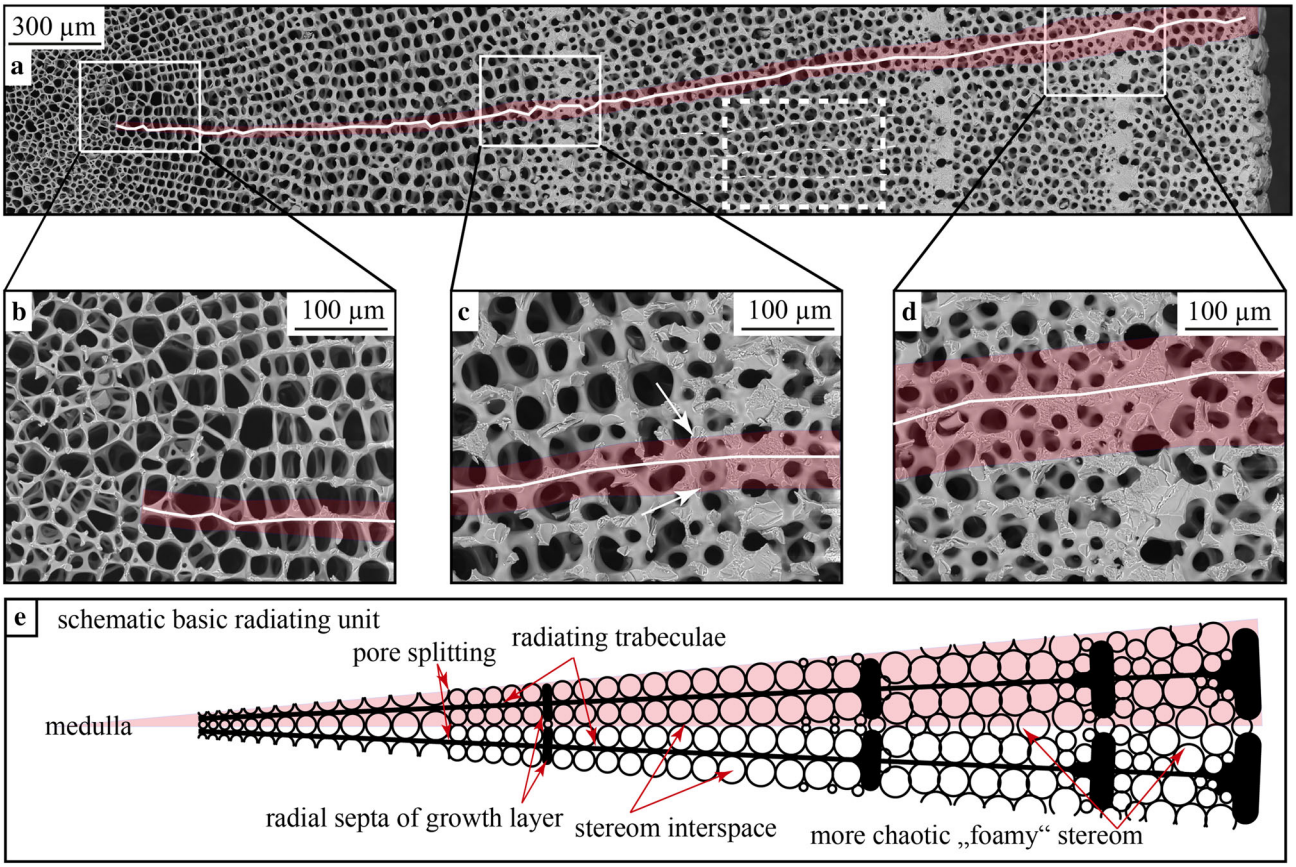

Fig. 6 Tracking a shaded basic radiating unit in a large aboral spine (**a**). The radiating trabeculae initiates right after the medulla (**b**), the first "pore-splitting" occurs right before the oldest growth layer (**c**). Close to the surface of the spine, the basic radiating unit reaches a width of four pores (**d**). The white dashed box in **a** shows an example region, were the radiating structure is difficult to discern. A schematic representation of a radiating unit is given in **e** to highlight the main observations and facilitate orientation

which is slightly lower than the porosity reported here. In the same study, porosity around nanoindentations was determined and gave systematically lower porosities (61 ± 4.8% for the medulla and 38 ± 3.1% for the radiating layer) than in this study. These differences in porosity determination may be due to sample size and location of the measurements within the stereom.

The two major porosity trends found in this study have an important implication for the mechanical performance of *H. mamillatus* spines. A spine with the most porous part (medulla) in the centre and the densest part (growth layers) at or closely beneath the surface may be abstracted as a cylinder with a porous, hence more compliant filling, a structure, which is quite common in nature (Dawson and Gibson 2007). From simple beam theory, it is clear that the change in geometrical moment of inertia results in an increase in stiffness for a given weight and, for the same reason, an increase in bending strength. This is a straight forward case of how to maintain the strength of an enlarged spine structure without becoming a burden by weight.

The further here identified porosity increase from spine base to its tip has other consequences. Because of the simple inverse relation of porosity and strength (e.g. Ji et al. 2006) the spine will be weaker in compression at the distal region, i.e. it will start to fracture at the tip. If this would be true in a bending case depends on the geometrical boundary conditions of the bearing. One may assume, however, that on average the failure of the spine is more likely to occur in the distal tip region. This effect might be beneficial for the regeneration of truncated spines, which is a slow process (Dotan and Fishelson 1985; Ebert 1988). The extent of extra costs incurred by regeneration for the living animal would be reduced by more distally located failure sites.

Distal growth layers and their implications on mechanical performance

The growth layers in *H. mamillatus* are crucial structural elements for a cascading manner within a graceful failure behaviour by deflecting cracks along the interface of the

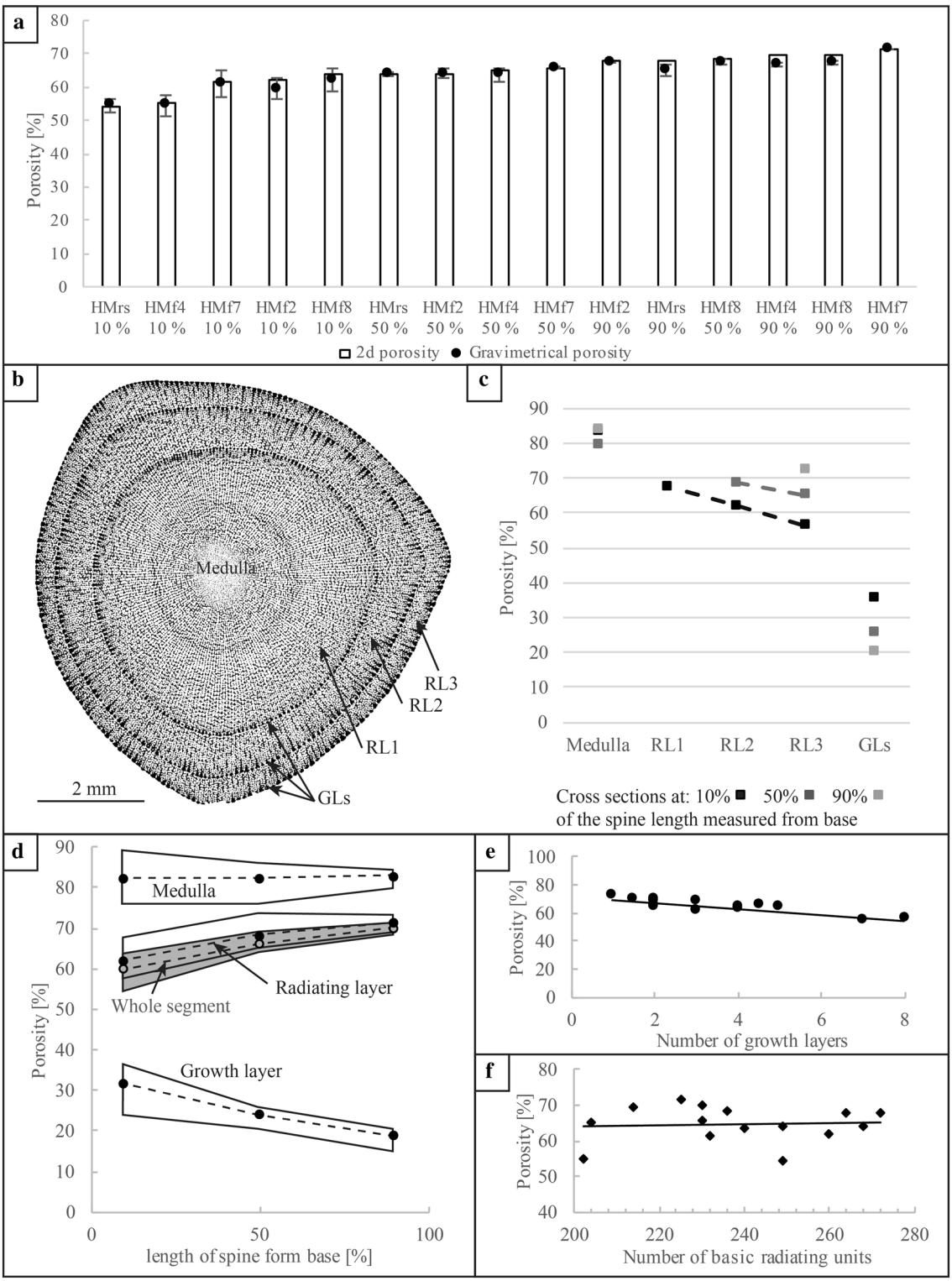

Fig. 7 Porosity of *H. mamillatus* spines. There is a good accordance between gravimetrically determined porosity and by 2d analysis (**a**). Porosity generally decreases within a cross section (**b**) from interior to exterior with a gradient also present in the radiating layer (**c**). Over the spine length the bulk porosity (grey shaded area) increases considerably (**d**). Interpolated areas correspond to all 5 measured spines and data dots represent the mean of all 5 porosities. The porosity of the growth layer shows an opposing trend to the overall porosity, while the porosity of the medulla remains constant over the whole spine length. Radiating layer and overall porosity show the same trend and similar values (**d**). The porosity of the cross sections correlates linearly with the number of growth layers (**e**, $R^2 = 0.7878$). There was no correlation found between the number of basic radiating units overall porosity of the cross section (**f**, $R^2 = 0.0025$)

Table 4 Porosities of all cross sections analysed for medulla, radiating layer and growth layers

Specimen	Segment at (%)	Porosities [%] of:				
		Medulla	Radiating layer (range)	Radiating layer (mean)	Growth layers	Whole cross section
HMf2	10	88.3	46.9–64.1	60.1	28.7	62.0
	50	85.2	51.3–71.6	66.8	23.5	64.1
	90	80.8	66.1–73.2	69.7	14.9	67.7
HMf4	10	76.7	42.3–65.5	58.5	32.1	55.0
	50	84.3	42.4–72.4	66.6	23.6	65.0
	90	84.1	62.8–73.1	69.5	20.4	69.6
HMf7	10	83.3	56.3–67.4	63.5	35.5	61.4
	50	79.5	65.0–68.5	67.2	25.7	65.6
	90	83.8	61.0–78.0[a]	72.5	20.3	71.6
HMf8	10	84.0	61.1–70.9	67.1	36.2	63.6
	50	84.3	60.4–70.8	68.6	24.6	68.4
	90	–[b]	–[b]	72.0	18.7	69.8
HMrs1	10	75.6	39.9–64.6	57.3	23.9	54.3
	50	75.4	61.9–65.2	64.4	20.4	63.8
	90	79.4	66.3–71.4	69.1	18.2	67.9

For radiating layer a range of porosities is given. The highest value corresponds to the radiating layer between medulla and oldest growth layer, the lowest value to the radiating layer situated between youngest and 2nd youngest growth layer

[a]As there was only one growth layer present the radiating layer and the radiating layer was not separated naturally, max value was obtained in a 0.4-mm band around the medulla and min value in a 0.4-mm band adjacent to the growth layer

[b]The stereom structure was overall unclear because of the termination of a growth layer exactly in this cross section. The medulla was replaced by the terminating growth layer and could not be measured

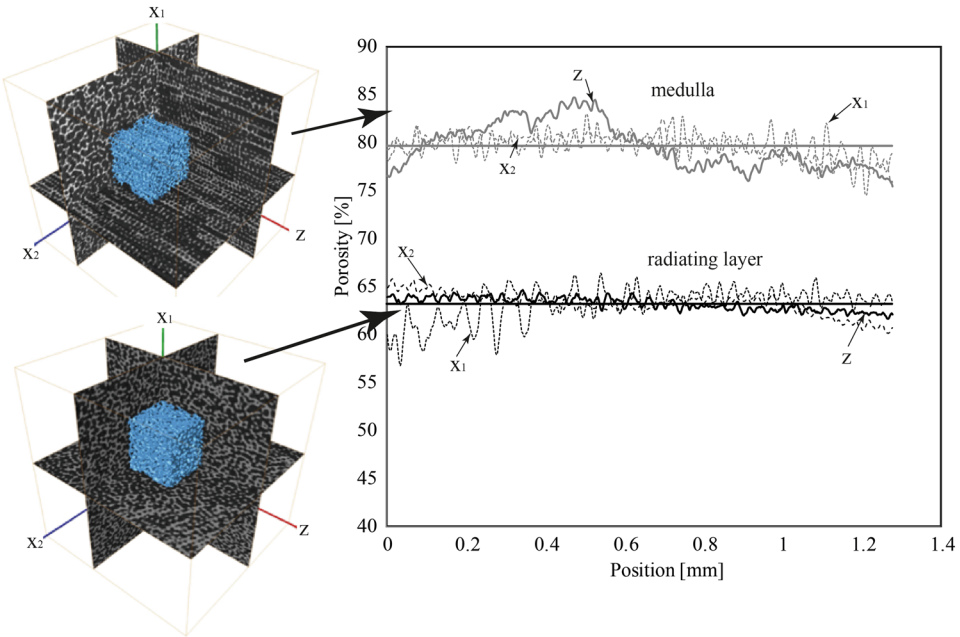

Fig. 8 Porosity determined by µCT. Areas of analysis are shown on the left (upper: medulla, lower: radiating layer). The *z*-direction corresponds to the crystallographic *c*-axis, *x*1 and *x*2-directions are in the plane perpendicular to the *z*-direction. Porosities are given in *x*1-direction (thin dotted line), *x*2-direction (dashed line) and *z*-direction (full line). The straight lines correspond to the overall porosity in the analysed cube obtained from the porosities in *x*1, *x*2 and *z*-direction

denser growth layers and the more porous radiating layer (Presser et al. 2009a). The present study found that the number of growth layers is highly variable (2–7) in aboral primary spines of a single individual, that they are unevenly spaced over the spine length and that there are 3 different types of distal growth layers. All these observations in addition to the porosity gradient help to explain the large variations found for mechanical properties of the

spines of this species (Presser et al. 2009a; Grossmann and Nebelsick 2013b; Schmier et al. 2016). More growth layers within the tested segment will lead to a pronounced cascaded graceful failure under uniaxial compression. In contrast to regular distal growth layers, the growth caps of capping growth layers can deflect the crack directly to the surface of the spine, which will lead to a direct spallation of parts of the stereom reducing the compressive strength. Incomplete distal growth layers have no growth cap and hence do not have the ability to deflect cracks in the same way as regular distal and capping growth layers.

Depending on whether the tested segment has been extracted from the base or the tip, the overall porosity can differ by more than 10% (Fig. 8d, Table 4). This has a significant influence on the Young's modulus of the segment and thus the mechanical properties such as compressive and bending strength or stiffness. Modelling the porosity–Young's modulus relationship according to Pabst et al. (2006), a porosity of 58% for the basal segment and of 70% for the tip segment yields Young's moduli of 12.8 and 6.5 GPa, respectively.

Brittle materials do show a natural scatter of data in terms of strengths, because of the statistical nature of defect distribution (e.g. Danzer 2014). By adding the structural variations like the amounts of growth layers and growth layer types, the structural mechanical performance of two segments out of the same spine can be entirely different. Both effects will contribute to the large scatter of data in compression tests of Presser et al. (2009a), 3-point bending tests of Grossmann and Nebelsick (2013b) and indentation experiments of Schmier et al. (2016). Quantifying the porosity and the number and type of growth layers prior to mechanical experiments is thus paramount to distinguish the differing influences and to help to understand the mechanical data in light of their material, their basic construction and the heterogeneity of biological individuals.

Conclusions

1. In the large primary spines of the sea urchin *H. mamillatus*, proximal and distal growth layers have been identified. The latter can be subdivided in (1) the regular distal growth layers spanning from the shaft to the base, (2) incomplete distal growth layers, and (3) capping growth layers. The number of proximal and distal growth layers is variable in primary spines and may be diagnostic for oral, aboral spines without capping growth layer and aboral spines with capping growth layer.
2. Besides the striking growth layers, a basic radiating structure is recognized. The number of radiating units is not diagnostic for this species, but is approximately constant throughout a single large aboral primary spine and can be obtained by counting the ribs of the corrugated surface.
3. The porosity of the spines found here is higher than previously reported. Values obtained by 2d image analysis and 3d analysis with μCT range from more than 80% in the central medulla to 20–30% in the comparably dense growth layers and the radiating layer laying somewhere in between. The overall porosity of a whole spine is around 60% as confirmed by gravimetry and 2d analysis.
4. Two major porosity trends have been recognized: (1) an increase in porosity from milled ring to the tip of up to 15% and (2) a decrease from interior to exterior, which can exceed 60%.
5. The variations in porosity and structural units all contribute to the structural strength of the spines in compression and bending. This opens the possibility to learn which feature has a positive effect for which property under which stressing mode, which in turn can potentially inspire new building construction materials. The advantage for the animal from those features remains somewhat speculative, but can certainly inspire further structural and behavioural research.

Acknowledgements The authors gratefully thank the German Research Foundation (DFG—Deutsche Forschungsgemeinschaft) for funding this work within the framework of the Collaborative Research Centre (SFB/Transregio) 141 "Biological Design and Integrative Structures" project B01. We also thank Barbara Maier and Simone Schafflick in the workshop for their support. The work of an anonymous reviewer is kindly appreciated.

Compliance with ethical standards

Conflict of interest The authors declare that they have no conflict of interest.

Statements on the welfare of animals The sea urchins were purchased dead from a fossils collector, were not killed for the purpose of this study and are not listed as endangered species.

Informed consent This article does not contain any studies with human participants performed by any of the authors.

References

Burkhardt A, Hansmann W, Märkel K, Nieman HJ (1983) Mechanical design in spines of diadematoid echinoids (Echinodermata, Echinoidea). Zoomorphology 102:189–203

Clarke FW, Wheeler WC (1915) The inorganic constituents of echinoderms. US Geol Surv Prof Pap 90:191–196

Coble R, Kingery W (1956) Effect of porosity on physical properties of sintered alumina. J Am Ceram Soc 39:377–385

Coppard SE, Campbell AC (2004) Taxonomic significance of spine morphology in the echinoid genera diadema and echinothrix. Invertebr Biol 123:357–371

Danzer R (2014) On the relationship between ceramic strength and the requirements for mechanical design. J Eur Ceram Soc 34:3435–3460

Danzer R, Supancic J, Pascual T, Lube T (2007) Fracture statistics of ceramics—Weibull statistics and deviations from Weibull statistics. Eng Fract Mech 74:2912–2932

Dawson MA, Gibson LJ (2007) Optimization of cylindrical shells with compliant cores. Int J Solids Struct 44:1145–1160

DeFoe OK, Compton AH (1925) The density of rock salt and calcite. Phys Rev 25:618–620. https://doi.org/10.1103/PhysRev.25.618

Deutler F (1926) Das Wachstum des Seeigelskeletts. In: Hartmann M, Hesse R (eds) Zoologische Jahrbücher Abteilung für Anatomie und Ontogenie der Tiere. Verlag von Gustav Fischer, Jena, pp 119–200

Dotan A (1990) Population structure of the echinoid *Heterocentrotus mammillatus* (L.) along the littoral zone of the south-eastern Sinai. Coral Reefs 9:75–80

Dotan A, Fishelson L (1985) Morphology of spines of *Heterocentrotus mammillatus* (Echinodermata: Echinoidae) and its ecological significance. In: Keegan BF, O'Connor BDS (eds) Echinodermata: Proceedings of the international echinoderm conference, Galway 24–29 Sept 1984. A.A. Balkema, Rotterdam, pp 253–260

Durham JW (1955) Classification of clypeasteroid echinoids. Univ Calif Press Geol Sci 31:73–198

Ebert TA (1986) A new theory to explain the origin of growth lines in sea urchin spines. Mar Ecol 34:197–199

Ebert TA (1988) Growth, regeneration, and damage repair of spines of the slate-pencil sea urchin *Heterocentrotus mammillatus*. Pac Sci 42:160–172

Emson RH (1985) Bone idle—a recipe for success? In: Keegan BF, O'Connor BDS (eds) Echinodermata. Balkema, Rotterdam, pp 25–30

Gibson LJ, Ashby MF (1982) The mechanics of three-dimensional cellular materials. Proc R Soc Lon 382:43–59

Grossmann JN, Nebelsick J (2013a) Stereom Differentiation in spines of Plococidaris verticillata, *Heterocentrotus mammillatus* and other regular sea urchins. In: Johnson C (ed) Echinoderms in a changing world. Taylor & Francis, London, pp 97–104

Grossmann JN, Nebelsick JH (2013b) Comparative morphological and structural analysis of selected cidaroid and camarodont sea urchin spines. Zoomorphology 132:301–315. https://doi.org/10.1007/s00435-013-0192-5

Hasenpusch W (2000) Die Stachel der Griffelseeigel. Mikrokosmos 89:23–27

Hesse E (1900) Die Mikrostruktur der fossilen Echinoidenstacheln und deren systematische Bedeutung. In: Bauer M, Koken E, Liebisch T (eds) Neues Jahrbuch für Mineralogie, Geologie und Paläontologie, E. Schweizertbart'sche Verlagshandlung, Stuttgart, pp 185–264

Ji S, Gu Q, Xia B (2006) Porosity dependence of mechanical properties of solid materials. J Mater Sci 41:1757–1768

Klang K, Bauer G, Toader N, Lauer C, Termin K, Schmier S, Kovaleva D, Haase W, Berthold C, Nickel KG, Speck T, Sobek W (2016) Plants and animals as source of inspiration for energy dissipation in load bearing systems and facades. In: Knippers J, Nickel KG, Speck T (eds) Biomimetic research for architecture and building construction. Springer, Switzerland, pp 109–133. https://doi.org/10.1007/978-3-319-46374-2_7

Kroh A, Nebelsick JH (2010) Echinoderms and Oligo-Miocene Carbonate Systems: potential applications in sedimentology and environmental reconstruction. Int Assoc Sedimentol Spec Publ 42:201–228

Kroh A, Smith AB (2010) The phylogeny and classification of post-Palaeozoic echinoids. J Syst Palaeontol 8:147–212

Lawrence JM (1987) A functional biology of echinoderms. The Johns Hopkins University Press, Baltimore

Lu G, Lu GQ, Xiao ZM (1999) Mechanical properties of porous materials. J Porous Mater 6:359–368

Mooi R (1986) Structure and function of clypeasteroid miliary spines (Echinodermata, Echinoides). Zoomorphology 106:212–223. https://doi.org/10.1007/bf00312042

Moureaux C, Perez-Huerta A, Compere P, Zhu W, Leloup T, Cusack M, Dubois P (2010) Structure, composition and mechanical relations to function in sea urchin spine. J Struct Biol 170:41–49. https://doi.org/10.1016/j.jsb.2010.01.003

Nebelsick JH, Dynowski JF, Grossmann JN, Tötzke C (2015) Echinoderms: hierarchically organized light weight skeletons. In: Hamm C (ed) Evolution of light weight structures. Analyses and technical applications. Springer, Dordrecht, pp 141–154

Nichols D (1962) Echinoderms. Anchor Press, Essex, p 200

Otsu N (1979) A threshold selection method from grey-level histograms. IEEE Trans Syst Man Cybern SMC 9:62–66

Pabst W, Gregorová E, Tichá G (2006) Elasticity of porous ceramics—a critical study of modulus-porosity relations. J Eur Ceram Soc 26:1085–1097

Presser V, Schultheiß S, Berthold C, Nickel KG (2009a) Sea urchin spines as a model-system for permeable, light-weight ceramics with graceful failure behavior. Part I. Mechanical behavior of sea urchin spines under compression. J Bionic Eng 6:203–213

Presser V, Kohler C, Zivcová Z, Berthold C, Nickel KG, Schultheiß S, Gregorová E, Pabst W (2009b) Sea urchin spines as a model-system for permeable, light-weight ceramics with graceful failure behavior. Part II. Mechanical behavior of sea urchin spine inspired porous aluminum oxide ceramics under compression. J Bionic Eng 6:357–364

Presser V, Gerlach K, Vohrer A, Nickel KG, Dreher W (2010) Determination of the elastic modulus of highly porous samples by nanoindentation: a case study on sea urchin spines. J Mater Sci 45:2408–2418

Presser V, Schultheiß S, Kohler C, Berthold C, Nickel KG, Vohrer A, Finckh H, Stegmaier T (2011) Lessons from nature for the construction of ceramic cellular materials for superior energy absorption. Adv Eng Mater 13:1043–1049. https://doi.org/10.1002/adem.201100066

R Core Team (2016) R: A language and environment for statistical computing. R Foundation for Statistical Computing, Vienna, Austria

Ridler TW, Calvard S (1978) Picture thresholding using an iterative selection method. IEEE Trans Syst Man Cybern 8:630–632

Schmier S, Lauer C, Schäfer I, Klang K, Bauer G, Thielen M, Termin K, Berthold C, Schmauder S, Speck T, Nickel KG (2016) Developing the experimental basis for an evaluation of scaling properties of brittle and 'Quasi-Brittle' biological materials. In: Knippers J, Nickel KG, Speck T (eds) Biomimetic research for architecture and building construction. Springer, Switzerland, pp 277–294. https://doi.org/10.1007/978-3-319-46374-2_14

Simkiss K, Wilbur KM (1989) Echinoderms - cells and syncytia. Biomineralization: cell biology and mineral deposition. Harcourt Brace Jovanovich, San Diego, pp 146–149

Smith A (1980) Stereom microstructures of the echinoid test. Spec Pap Palaeontol 25:1–81

Su X, Kamat S, Heuer AH (2000) The structure of sea urchin spines, large biogenic single crystals of calcite. J Mater Sci 35:5545–5551

Telford M (1982) Echinoderm spine structure, feeding and host relationships of four species of dissodactylus (Brachyura: Pinnotheridae). Bull Mar Sci 32:584–594

Toader N, Sobek W, Nickel KG (2017) Energy absorption in functionally graded concrete bioinspired by sea urchin spines. J Bionic Eng 14:369–378. https://doi.org/10.1016/s1672-6529(16)60405-5

Tsafnat N, Fitz Gerald JD, Le HN, Stachurski ZH (2012) Micromechanics of sea urchin spines. PLoS One 7(9):e44140. https://doi.org/10.1371/journal.pone.0044140

Vevers HG (1966) Pigmentation. In: Boolootian RA (ed) Physiology of Echinodermata. Interscience Publishers, New York, pp 265–267

Warton DI, Duursma RA, Falster DS, Taskinen S (2012) smatr 3- an R package for estimation and inference about allometric lines. Methods Ecol Evol 3:257–259. https://doi.org/10.1111/j.2041-210X.2011.00153.x

Weber JN (1969a) The incorporation of magnesium into the skeletal calcites of echinoderms. Am J Sci 267:537–566

Weber JN (1969b) Origin of concentric banding in the spines of the tropical Echinoid *Heterocentrotus*. Pac Sci 23:452–466

Weber J, Greer R, Voight B, White E, Roy R (1969) Unusual strength properties of echinoderm calcite related to structure. J Ultrastruct Res 26:355–366

Manuscript 3 with Supplementary Material

Strength-size relationships in two porous biological materials

(11+9 pages)

Acta Biomaterialia 77 (2018) 322–332

Contents lists available at ScienceDirect

Acta Biomaterialia

journal homepage: www.elsevier.com/locate/actabiomat

Full length article

Strength-size relationships in two porous biological materials

Christoph Lauer [a,*,1], Stefanie Schmier [b,c,1], Thomas Speck [b,c], Klaus G. Nickel [a]

[a] University of Tübingen, Department of Geosciences, Division of Applied Mineralogy, Wilhelmstraße 56, D-72074 Tübingen, Germany
[b] University of Freiburg, Faculty of Biology, Botanic Garden, Plant Biomechanics Group, Schänzlestraße 1, D-79104 Freiburg, Germany
[c] Freiburg Center for Interactive Materials and Bioinspired Technologies (FIT), Georges-Köhler-Allee 105, D-79110 Freiburg, Germany

ARTICLE INFO

Article history:
Received 28 February 2018
Received in revised form 24 May 2018
Accepted 3 July 2018
Available online 5 July 2018

Keywords:
Biomimetics
Weibull analysis
Size effect
Sea urchin spine
Coconut endocarp

ABSTRACT

According to the Weibull theory for brittle materials, the mean experimental strength decreases with test specimen size. For the brittle parts of an organism this would mean that becoming larger in size results automatically in reducing strength. This unfavorable relationship was investigated for two porous, biological materials that are promising concept generators for crack deflective and energy dissipative applications in compressive overloading: the quasi-brittle coconut endocarp and the brittle spines of the sea urchin *Heterocentrotus mamillatus*. Segments in different volumes were prepared and tested in uniaxial compression experiments. Failure of both materials is Weibull distributed underlining that it is caused by statistically distributed flaws in the structure. However, the coconut endocarp has a much higher Weibull modulus (m = 14.1–16.5) than the spines (m = 5). The more predictable failure of the endocarp is probably attributed to a rather homogeneous microstructural design and water bound in the structure. In terms of the spines it was found that the Weibull modulus is structure dependent: More homogeneous spines feature a higher Weibull modulus than spines with a heterogeneous structure.

Whereas the nearly dense endocarp exhibited, although less pronounced, the expected decrease in strength with increase in size, the spines showed a failure independently of size. This remarkable behavior may be explained with their highly porous internal structure. Small and large spines consist of struts of similar size, which constitute the porous internal structure, potentially limiting the flaw size to the size of the strut regardless of the spine size.

Statement of Significance

Scaling is an important aspect of the biomimetic work process, since biological role models and structures have rarely the same size as their technical implementations. The algorithms of Weibull are a standard tool in material sciences to describe scaling effects in materials whose critical strength depends on statistically distributed flaws. The challenge is to apply this theory (developed for homogeneous, isotropic technical materials) to brittle and quasi-brittle biological materials with hierarchical structuring.

This study is a first approach to verify whether the Weibull theory can be applied to the coconut endocarp and to sea urchin spines in order to model their size/volume/property-relations.

1. Introduction

1.1. Background

In biomimetics scaling is an important topic to deal with. Often the biological role models are much smaller than the components of technical applications they will be transferred to. In this context a central question is whether the probability of failure scales with size and in which way it scales. This question is crucial if one uses biological role models showing an overall size of several centimeters and a hierarchical structuring down to the sub-micrometer level as inspirations for improving energy dissipation and puncture resistance in large concrete based structural components for building construction and architecture. In the framework of the CRC "Biological Design and Integrative Structures" we identified the endocarp of the coconut and the spines of some sea urchins as promising role models for this goal. The coconut endocarp (*Cocos nucifera*) and the aboral primary spines of the Indo-Pacific sea urchin *Heterocentrotus mamillatus* both show elaborate ways to

* Corresponding author.
E-mail address: christoph.lauer@uni-tuebingen.de (C. Lauer).
[1] Authors contributed equally to this paper.

https://doi.org/10.1016/j.actbio.2018.07.010
1742-7061/

deflect cracks and protect the seed (coconut) and the body (sea urchin). Although having different mechanisms to deflect cracks, both biological materials can dissipate comparably high amounts of energy by crack path extension (coconut) and multiple cracking in the porous sea urchin spine [1,2]. Furthermore, the spines of *H. mamillatus* are a lightweight construction with a high strength despite a high porosity. This is why they have already been used as precursors for generating bone implants [3,4]. With these properties the two biological materials can serve as role models for improving everyday materials such as concrete [5], impact protectors [6] and porous ceramics [7]. Here, the question arises in which way the desired mechanical properties, like the high strength despite the lightweight construction or the high energy dissipation capacity, are affected by scaling to much larger dimensions.

In the following we will test experimentally, whether the classical Weibull theory for brittle materials can be used to describe the failure under compression of both porous biological materials. A proof for the basically brittle nature of the spine material of *H. mamillatus* comes from bending tests of complete specimen [8,9], where a complete catastrophic failure during a linear elastic stressing occurs at nominal stresses in the order of 30–60 MPa. However, it should be noted that many natural materials such as the spines of *H. mamillatus* (of porous magnesium calcite [10–12]) and the coconut endocarp (of highly lignified cells [13,14]) strictly speaking belong to the class of quasi-brittle materials [15,16]. Cracking in these materials in compression does not lead to immediate failure [16] and failure can be triggered by a significant number of local events [17]. Nevertheless, the Weibull theory for brittle materials is often applied to quasi-brittle materials due to its simplicity and ability to model the failure of these materials satisfactorily [15,17]. Weibull [18] modelled the strength of brittle materials as a function of their flaw size distribution. Flaws can be impurities, little cracks or pores. At a certain load, one of these flaws becomes critical and leads to the failure of the whole structure (weakest link theory). The probability of failure ($P_{V0}(i)$) is thus function of the flaw size distribution and therefore of the volume:

$$P_{V_0}(i) = 1 - \exp\left(-\frac{V_i}{V_0}\cdot\left(\frac{\sigma_i}{\sigma_0}\right)^m\right), \quad (1)$$

where V_i is the effective tested volume of the sample i, V_0 the reference volume, σ_i the stress at failure ("critical strength"), σ_0 the scaling value ("characteristic strength" at which 63.2% of all samples of a population with V_0 have already failed) and the Weibull modulus m (measure for reliability). The narrower the range of critical strength in which the samples fail, the higher their reliability. For high performance ceramics Weibull moduli above 20 can be reached [19], for biological materials with their high natural heterogeneity the Weibull modulus is usually below or even far below 10 (Table 1).

As can be seen in Eq. (1) failure probability is volume dependent. In a larger volume it is more likely to find a large crack leading to failure than in a smaller volume and therefore, it is more likely that the specimen fails at lower stresses. As the Weibull modulus is a material constant, Eq. (1) can be reformulated for sample sets of the same material but different volumes:

$$\left(\frac{\sigma_{01}}{\sigma_{02}}\right) = \left(\frac{V_{02}}{V_{01}}\right)^{\frac{1}{m}}, \quad (2)$$

with reference volume V_{01} and corresponding characteristic strength σ_{01} and reference volume V_{02} with corresponding characteristic strength σ_{02}. Just recently Lei [20] generalized Weibull's formula (Eq. (1)) to account for non-uniform distributed flaw populations with a correction constant β ($\beta\epsilon\mathbb{R}|\beta > 0$):

$$P_{\beta,V_0}(i) = 1 - \exp\left(-\beta\cdot\left(\frac{V_i}{V_0}\right)^{\beta}\cdot\left(\frac{\sigma_i}{\sigma_0}\right)^m\right) \quad (3)$$

For $\beta = 1$ Eq. (3) reduces to Eq. (1) for uniform distributed flaws, for $0 < \beta < 1$ the spatial distribution is less dense and for $\beta > 1$ the spatial distribution is denser than the uniform distribution. For $0 < \beta < 1$ the scaling effect is reduced compared to the scaling effect predicted by Weibull and for $\beta > 1$ the scaling effect is even aggravated. Lei [20] demonstrated the applicability of his model amongst others for spruce wood and aluminum foams.

For our role models, this size effect is a problem since the mechanical properties as the high strength and the high energy dissipation capacity would suffer when scaling the material up to e.g. concrete slab dimensions. However, a $\beta < 1$ would at least retard the size effect. For example, for the strength of Norwegian spruce wood in longitudinal fiber direction the size effect is less than a quarter ($\beta = 0.22$) than expected from Weibull theory ([20], data from [21], see also Table 1 for other examples). Lu et al. [22] reported that the strength of porous ZnO ceramics is

Table 1
Studies on biological materials with regard to Weibull distributed critical strength and size effect. Abbreviations: HM = *Heterocentrotus mamillatus*, PI = *Phyllacanthus imperialis*.

Study	Material	Test method	Weibull modulus m	sample size n	size effect investigated?
Menig et al. [23]	shell of Abalone (*Haliotis rufensis*)	Static and dynamic compression	2.5–5.1 (depending on direction measured)	7–14 per group	No
Łysiak [24]	Pea seeds wet and dried	Static compression	1.3–16.2 (depending on moisture)	16–20 per moisture group	No
Presser et al. [1]	Sea urchin spines (HM and PI)	Static compression	3.4 (HM) 6.0 (PI)	38 (HM) 33 (PI)	No
Chan et al. [25]	Enamel (human teeth)	Microcantilever, nanoindentation and 3-point bending	not given	4 (6 tests per sample)	Yes, found[a]
Trujillo et al. [26][b]	Bamboo fibre (*Guadua angustifolia*)	Tensile strength	6.7–7.6	34–159	Yes, found[c,e]
Dill-Langer et al. [21]	spruce wood (*Picea abies*)	Tensile test (parallel to grain)	8.3 (small samples) 10.3 (large samples)	23 per group	Yes, found[e]
Pedersen et al. [27]	Spruce wood (*Picea abies*)	Tensile test (perpendicular to grain)	2[d]	9 per group (4 volumes tested)	Yes, found[f]
Moshtaghin et al. [28]	Spruce wood (*Picea abies*)	Tensile test (parallel to grain)	7.85	37–45 per group (4 lengths tested)	Yes, found[e]

[a] Covered with their test methods volumes incorporating different hierarchical levels of the enamel structure, strictly speaking not Weibull conform.
[b] Exhaustive references for Weibull investigations concerning natural fibers given.
[c] Related the size effect not on volume but on length as commonly done for fibers.
[d] Argue that stresses are not distributed homogeneously and Weibull modulus cannot be given reliably.
[e] Size effect less pronounced as predicted by Eq. (2) with $\beta < 1$ in Eq. (3).
[f] Size effect more pronounced as predicted by Eq. (2) with $\beta > 1$ in Eq. (3).

independent of size and they attributed this to a homogenization of critical crack sizes by pore/grain size interactions.

1.2. Endocarp of the coconut

The fruit of *Cocos nucifera* is a drupe, whose fruit wall consists of three layers: the leathery exocarp, the fibrous mesocarp and the hard and tough endocarp. To ensure comparability in this study only the innermost fruit wall layer, the endocarp (Fig. 1A), has been investigated due to its quasi-brittle failure behavior. The ripe endocarp is a structure build up by a matrix material, consisting of sclereid cells, traversed by an interconnected three-dimensional network of vascular bundles [13,14]. The lumen of the sclereid cells is nearly entirely filled with lignified cell wall layers and the sclereid cells are connected with each other via lignified pits, resulting in a very dense matrix material [13]. The cells of the former phloem are mostly ruptured and therefore the vascular bundles can be seen as a system of air-filled tubes running through the endocarp. Only the lignified cell walls of the hollow tracheids in the vascular bundles have a comparable density as the sclereid cell walls [13,29].

1.3. Spines of H. mamillatus

The aboral primary spines of the Indo-Pacific sea urchin *H. mamillatus* (Fig. 1B) are used for locomotion, fixation in reef cavities and as protection against predators [9,30]. Despite their size, the spines are very light due to the elaborate porous internal structure called "stereom" (e.g. [31]) resulting in an overall density only slightly above that of sea water [32]. Three structural different stereom types are present in the spine with the medulla in the center (highest porosity) surrounded by the radiating layer (intermediate porosity). The nearly dense characteristic growth layers form the third stereom type and interrupt the two other stereom types irregularly (Fig. 1B). This way the porosity distribution in the spine is not uniform [32]. In this study, we distinguish between growth layers that finish in the segment used for uniaxial compression tests and form a cap ("finishing growth layers") and growth layers that are constantly present close to the rim ("permanent growth layers") (Fig. 1B).

Presser et al. [1] found that the finishing growth layers affect the failure behavior of the spines under uniaxial compression. They act as crack deflector and support a layer-by-layer breakdown resulting in a "cascading failure" behavior with no catastrophic failure and load-bearing capacity even after high strain (>0.2). The same authors conducted a Weibull study on sea urchin spines (Table 1). However, the large natural variation in the spines like the porosity and the number of permanent and finishing growth layers was not taken into account.

This paper addresses two questions: Firstly, whether our role models show a Weibull distributed critical strength and secondly, whether they show the hypothesized size effect. This will be done by comparing the critical strength of small to large test specimen. In order to answer these questions we need to characterize the influence of the natural heterogeneity on the strength. Finally, the model of Lei [20] is applied to our data.

2. Materials and methods

2.1. Sample preparation

10 coconut fruits with removed exo- and mesocarp have been purchased from a local supplier (Greenyard Fresh Germany GmbH, Freiburg, Germany). Four fruits were selected, which had an endocarp thickness ranging at least from 2.5 to 5 mm. Cylindrical samples of the coconut endocarp were prepared using a lathe (Leinen DLZ 140, Boley & Leinen, Esslingen, Germany). Afterwards the samples were stored at ambient conditions, resulting in an average water content of 13.4 wt% (±3.7 wt% SD), determined gravimetrically for 10 samples using the method described by [33]. Small samples were cut to diameters of 4 mm and large samples to a diameter of 8 mm. Subsequently, the outer and inner sides of the endocarp were manually sanded coplanar to remove the curvature and any remaining parts of the mesocarp and the testa. The natural variation of the endocarp thickness was used to prepare samples with volumes of 30 ± 5 mm^3 and 210 ± 30 mm^3 of the same fruit. Mass was determined with a Kern ABT-220-5DM scale (Kern&Sohn GmbH, Bahlingen-Frommern, Germany) with a precision of 0.1 mg and length was measured with a digital caliper (SMT023, AGT™) with an accuracy of 10 μm. By this preparation method it was

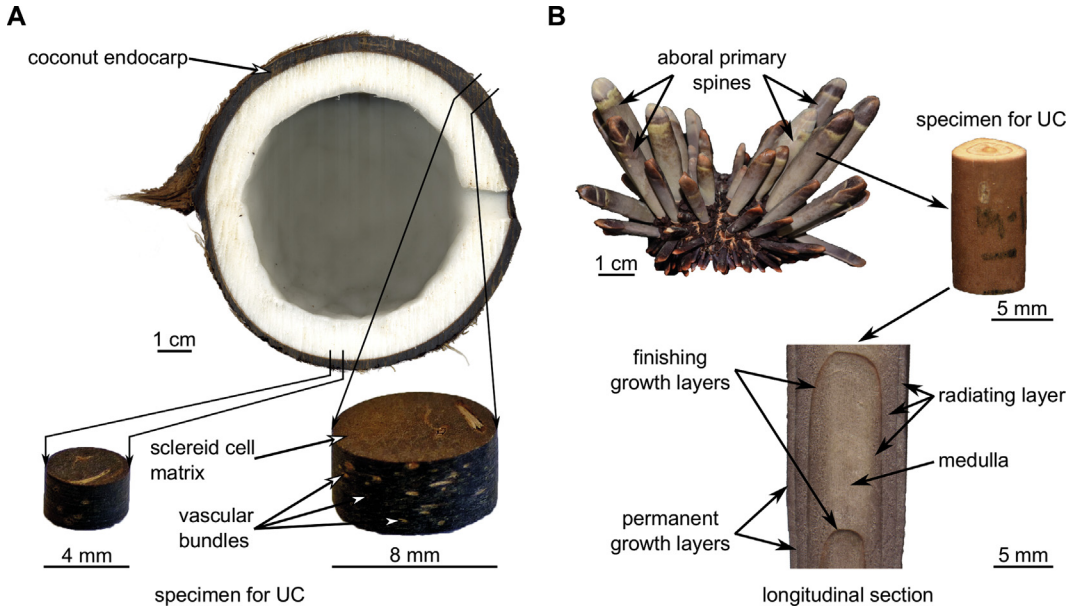

Fig. 1. Role models of this study: Coconut endocarp (A) and *H. mamillatus* with its aboral primary spines (B). Segments used for uniaxial compression (UC) experiments are shown as well as micrographs with the most relevant structural features.

ensured to have geometrical similar samples per group (n_{large} = 24, n_{small} = 25) and a minimum scaling factor of 5 (largest volume for small specimens: 35.3 mm^3, smallest volume for large specimens: 187.5 mm^3) (Fig. 1A). The average porosity, as well as medium and largest diameter of vascular bundles of the coconut endocarp were determined for small (n = 10) and large (n = 10) specimens using a μ-CT (Skyscan 1272, Bruker microCT, Kontich, Belgium) and CT-Analyser (V. 1.16.4.1, Bruker microCT, Kontich, Belgium).

Five complete animals of *Heterocentrotus mamillatus* have been purchased from a supplier (Mineralien- und Fossilienhandlung Peter Gensel, Weimar, Germany). They were tested three years after collection, so it is possible that the here reported mechanical properties deviate from those of fresh spines, although the organic content of sea urchin spines is generally low [34,35] and thus deterioration, if occurring in this period of time, is most probably negligible. The aboral spines most suitable for uniaxial compression tests were removed and cut in coplanar (±15 μm) segments with a Buehler med 3000 saw (Buehler-Met Deutschland, Esslingen, Germany). The obtained segments (n = 72) ranged from 33 to 1395 mm^3 in size, which corresponds to a maximum scaling factor of 42. To prevent buckling in uniaxial compression, all spine segments had a length to diameter ratio of 2(±0.3):1 [36]. The porosity was determined gravimetrically by using the volume and the bulk density (the structural density, including voids) and the material density (using 2.711 g/cm^3, the literature density of pure calcite [37]). The incorporation of heavier magnesium (up to 10 mol % $MgCO_3$ [12]), lighter organic matter (0.1–1.6 wt% [34,35]) and lighter amorphous calcium carbonate (8–10 mol% [34,35]) in the biogenic calcite surely alters the density, but likely balances each other, so the literature value for calcite is still a valid estimation. Mass of the segments was determined with a Sartorius BP 211D scale (Sartorius AG, Göttingen, Germany) with a precision of 0.01 mg. Length was measured with an micrometer gage (Mitutoyo IP65, Mitutoyo Deutschland GmbH, Germany) with an accuracy of 1 μm. As the coplanar segments do not have a constant cross section over their length, averaging the upper and lower cross section and multiplying it by the height yields only an approximation of their volume. Error calculations are described in detail in Supplementary 1 and a conservative approach yields an error of ±0.3–13.1% (median: ±5%) for volume and ±0.1–6 percent points (median: ±2 percent points) for porosity.

2.2. Uniaxial compression tests

The spine segments and the small coconut samples were tested with a 10 kN Instron 4502 universal testing machine (Instron Deutschland GmbH, Pfungstadt, Germany). The large coconut samples were tested with a modified Instron 1380-1001 universal testing machine with a 25 kN force transducer (AEP Transducers, Modena, Italy). The cross head speed was constant with 0.5 mm/min in all experiments. As both biological materials do not fail catastrophically, the critical strength was defined as the first stress maximum (engineering stress, calculated by dividing the force by the initial cross-sectional area) terminating the linear elastic force increase. In most cases the length decrease during compression was recorded with a Videoextensometer for the sea urchin spines (Limess RTSS_C02, Limess Software und Messtechnik GmbH, Krefeld, Germany). Stress was divided by strain in the range of the linear increase to obtain the Young's modulus (see Fig. S2).

2.3. Scaling analysis

For the Weibull analysis the empirical probability of failure for each specimen $F_{V0}(i)$ was calculated for each group (with reference Volume V_0) by assigning ranks to the samples in ascending order according to their critical strength and using Eq. (4):

$$F_{V_0}(i) = \left(\frac{n_i - 0.5}{n}\right) \tag{4}$$

where n_i is the assigned rank of specimen i and n the sample size of the group.

To determine the respective Weibull modulus m and the characteristic strength σ_0 with the empirical failure probability, Eq. (1) has been converted into the following equation (see also Supplementary 3):

$$\ln\left(\ln\left(\frac{1}{(1-F_{V_0})^{\left(\frac{V_0}{V_i}\right)}}\right)\right) = m\cdot\ln(\sigma_i) - m\cdot\ln(\sigma_0) \tag{5}$$

A linear regression was performed on the data with $\ln(\sigma_i)$ forming the x-values and the left side of Eq. (5) forming the y-values. The slope of the regression line returns m and the x-intercept returns σ_0 after conversion. Unlike for technical materials, where specimen can be manufactured to the desired sample geometry, the hierarchical structuring and the shape of the biological samples constrain the sample geometry. The height of the coconut samples is defined by the endocarp thickness and size of sea urchin spine samples by the external shape of the spine. Therefore, the scatter in volume tested is quite high and the volume factor (V_0/V_i) in Eq. (5) does not simplify to 1 as for technical materials, where $V_i \approx V_0$.

For the analysis after [20], Eq. (4) was also used to determine the empirical failure probability F_{V0}. Similar to the transformation of the Weibull equation, Eq. (4) is converted into Eq. (6) and β is determined in order to get the best R^2-value for the regression line. The shape parameter m_{Lei} is the slope of the corresponding regression line and the characteristic strengths σ_0 were determined solving Eq. (6) for σ_i with F_{V0} = 0.632 (being the strength at which 63.2% of all samples failed) for the respective volume groups:

$$\ln\left(\ln\left(\frac{1}{(1-F_{V_0})^{\left(\frac{1}{\beta}\left(\frac{V_0}{V_i}\right)^{\beta}\right)}}\right)\right) = m_{Lei}\cdot\ln(\sigma_i) - m_{Lei}\cdot\ln(\sigma_0) \tag{6}$$

2.4. Statistics

Data processing has been done with the free software GNU R (V. 3.4.0), statistical testing and plotting of the data have been done with GNU R including the additional package *ggplot2* and *car* [38–40]. The data were checked for normal distribution (Shapiro-Wilk test) and variance homogeneity (Levene test). Afterwards a non-parametric Wilcoxon rank sum test was used to test for differences between two groups of data with no normal distribution (Shapiro-Wilk test) and no variance homogeneity (Levene test). To test for differences between more than two groups a one-way Analysis of Variance followed by a Tukey HSD post hoc test was used for data with normal distribution (Shapiro-Wilk test) and variance homogeneity (Levene test), whereas a Kruskal-Wallis test was performed on data with normal distribution (Shapiro-Wilk test) and no variance homogeneity (Levene test). The tests used for the different porous biological materials are indicated in the results section.

3. Results

3.1. Coconut endocarp

As shown by the analysis of the μCT-data the most frequently found diameter range for the vascular bundles (defined as occupying the highest pore space fraction) did not vary between large and

small samples, while the maximum diameter range of the vascular bundles were markedly larger in the larger samples (for more details on the analysis of the μCT-data see Supplementary 4). Therefore, larger samples show a significantly higher porosity (Wilcoxon rank-sum test, W = 17, p < 0.05) (Table 2).

The recorded videos of the uniaxial compression tests revealed that water was pressed out of the material during the elastic deformation of the endocarp prior to failure. This expelled water was re-entering the material, when cracks were formed after the critical strength was exceeded (Point 5, Fig. 2). The occurrence of cracks prior to failure (Point 4 Fig. 2) is typical for quasi-brittle materials under compression.

To get a better access to the data and for reasons of comparability with sea urchin data, in a first step all samples are combined in one group according to Eq. (5) using the mean volume as reference volume ($V_0 = V_{mean} = 117$ mm^3). The samples scatter according to their volume in two distinct populations (Fig. 3A), with the smaller samples clustering at higher strengths than the larger samples, demonstrating a size effect. Fig. 3B emphasizes the significantly higher critical strength for small samples (median: 222 MPa) compared to large ones (median: 196 MPa, Wilcoxon rank-sum test, W = 493, p < 0.001). In a classical Weibull plot (Fig. 3C), where the samples are grouped to their respective reference volumes ($V_{0,small} = 30$ mm^3, $V_{0,large} = 205$ mm^3) with their corresponding failure probabilities and where the volume factor is omitted (Eq. (5) with $V_0/V_i = 1$) both populations show similar Weibull moduli ($m_{small} = 16.5$, $m_{large} = 14.1$) (Table 2). Despite the scatter in volume, the neglect of the volume term (V_0/V_i) in Fig. 3C is justified in first order approximation, since the Weibull moduli only slightly change and the characteristic strength data do not change at all (Fig. S5, volume term included). Predicting the characteristic strength of the respective other group by Eq. (2) yielded 236 MPa for small specimen and 200 MPa for large specimen and is illustrated by the dotted lines in Fig. 3C.

The model by Lei [20] (Eq. (6)) was applied to the strength data of the coconut endocarp with its two different volumes (Fig. 4). All measurements lie roughly on a single master curve when $\beta = 0.84$ ($R^2 = 0.955$), which was determined manually yielding the best R^2-value after power law fitting [20]. The resulting shape parameter m_{Lei} yields 15.8, which is between the Weibull moduli of small and large specimen, and the characteristic strength for small samples yields 226 MPa and for large samples 204 MPa (Table 2). This is in good accordance to the observed ones (Table 2).

Table 2
Overview of the scaling analysis of coconut endocarp samples. Abbreviations: IQR: interquartile range, m: Weibull modulus, n: sample size, σ_0: characteristic strength, m_{Lei}: shape parameter of Lei model, $\sigma_{0,Lei}$: characteristic strength calculated with Lei model [20].

Group	n	Volume [mm^3]		Porosity [/]	m	σ_0 [MPa]	m_{Lei}	$\sigma_{0,Lei}$ [MPa]
		Median	IQR					
Small	25	30	28–31	0.015	16.5	225	15.8	226
Large	24	205	194–222	0.027	14.1	205	15.8	204

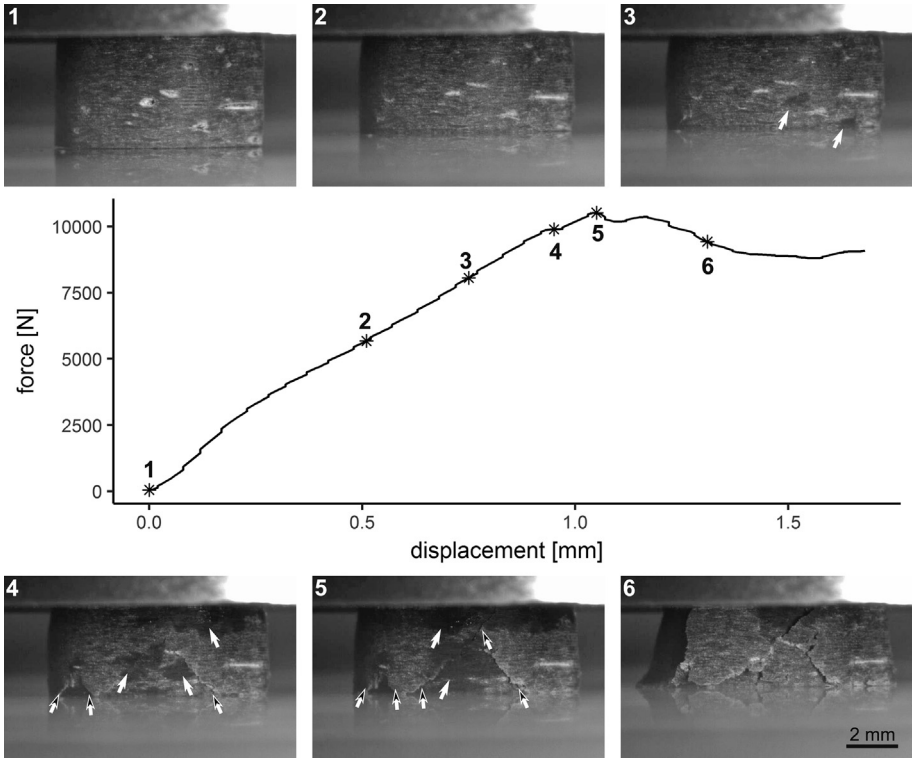

Fig. 2. Representative force-displacement curve of a big coconut endocarp sample. The images are taken from the recorded video of the test and show (1) the sample at the start of the compression test, (2) the elastic deformation of the sample, (3) the water pressed out of the sample (white arrows) and the developing cracks (4, 5 black and white arrows) which identifies the material as quasi-brittle, as an immediate failure was not observed after crack initiation. The first delaminations become visible and all the water has disappeared (6). Point (5) marks the force used to calculate the critical strength of the sample.

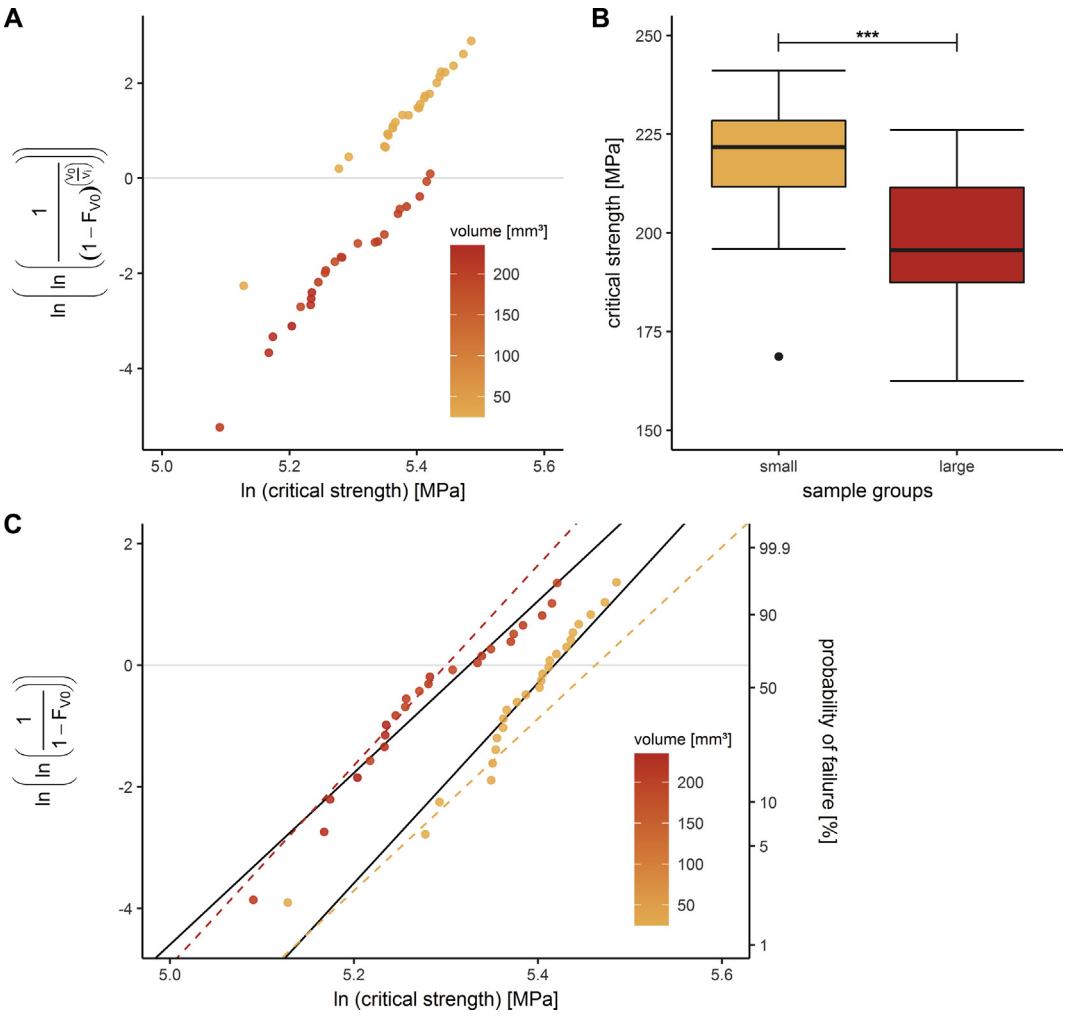

Fig. 3. Weibull plot according to Eq. (5) taking the volume factor (V_0/V_i) into account and considering all samples as representatives of a single volume group (A). The data group according to their respective volume along the y-axis. Furthermore a shift to lower critical strengths is observed for the large samples (A). The critical strength of coconut endocarp samples is significantly higher for small samples than for large ones (Wilcoxon rank-sum test, W = 493, $^{***}p < 0.001$) (B). Weibull plot according to Eq. (5) neglecting the volume factor (C). The regression lines prove a good approximation of the data ($R^2_{small} = 0.935$, $R^2_{large} = 0.949$) and the calculated Weibull modulus m and characteristic strength σ_0 are independent of the volume factor (Fig. S5). The dashed lines in C indicate expected probability distributions for each group, predicted by Eq. (2) from the respective other group.

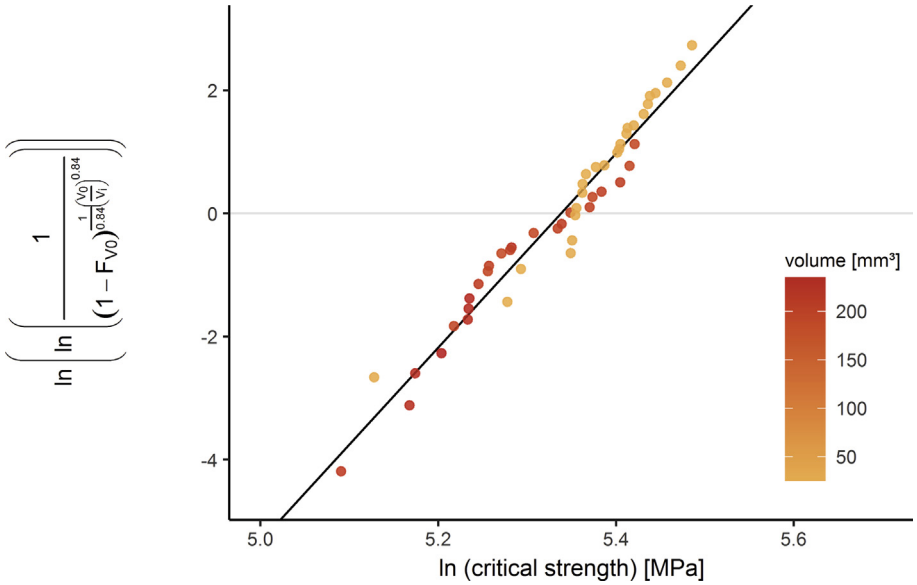

Fig. 4. Data of coconut endocarp plotted according to Lei's model [20] (Eq. (6)) with $\beta = 0.84$ and $V_0 = 117\ mm^3$ (mean of coconut volumes). The corresponding shape parameter m_{Lei} and the characteristic strengths are calculated from the regression line ($R^2 = 0.955$) and are shown in Table 2.

3.2. Spines of H. mamillatus

The failure of spines of *H. mamillatus* is described in detail elsewhere [1,2]. Fig. 5A shows the strength distribution of all samples when $V_0 = 643$ mm^3 (mean sea urchin spine volume) (Eq. (5)). This representation has two implications: Firstly, it illustrates that in contrast to the coconut endocarp no distinct volume groups could be manufactured from the population, as all samples differ in their sizes and this leads to a considerable scatter. Secondly, no size effect is apparent. Small samples have comparable strengths to large samples. This hypothesis is tested for different volume groups extracted from the whole population (Fig. 5B). No significant differences between these groups (Kruskal-Wallis test, $X^2(6) = 9.74$, $p > 0.05$) and no trend for a decreasing critical strength with increasing volume is observed. This means the data can be treated as a population of a single volume where $V_0 = V_i$, which simplifies the representation to the classical Weibull distribution (Fig. 5C). It fits the data reasonably well ($R^2 = 0.97$) although the 72 segments are highly heterogeneous in volume, porosity, elasticity (Table 3) and internal stereom distribution. The characteristic strength is 66 MPa and the Weibull modulus calculates to 5.0. Using $m = 5$ and assuming a volume effect, the theoretical characteristic strengths of the volume groups in Fig. 5B have been predicted with Eq. (2). No matter whether the small volume or the

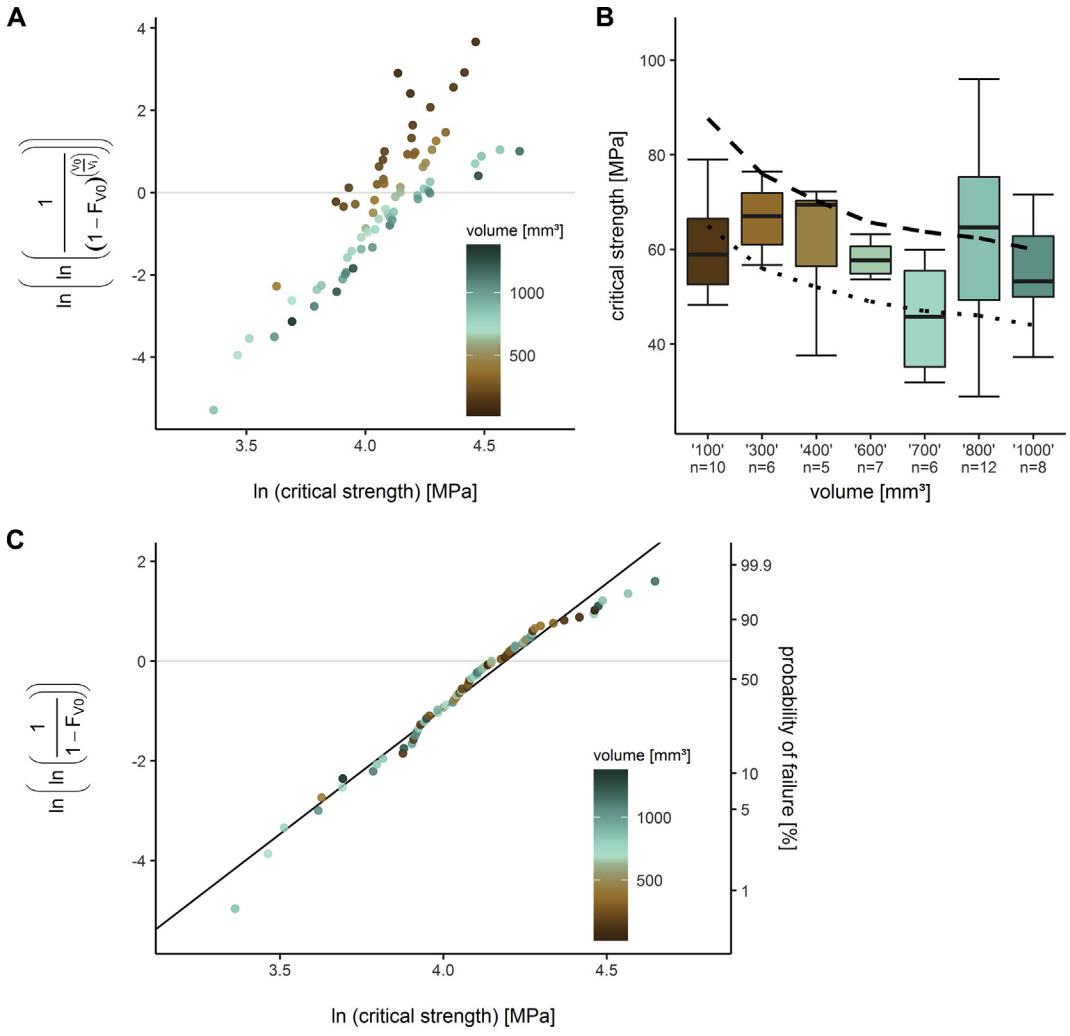

Fig. 5. No size effect can be found in the volume corrected plot (Eq. (5)) and samples scatter significantly due to no distinct group sizes (A). Volume groups in intervals of 100 mm^3 (100–199: '100', 200–299: '200', etc.; minimum number of specimen $n = 5$) have been extracted from the whole population. A Kruskal-Wallis test revealed no significant differences between the groups. Strengths of the volume groups was predicted with Eq. (2) with $V_{\cdot 100 \cdot}$ (thin dotted line) and $V_{\cdot 1000 \cdot}$ (thick dotted line) as reference volume. Both highlights that a size effect is not present. (C) displays a classical Weibull plot with $V_i = V_0$ (for key data see Table 3), where the regression line proves a good approximation of the data ($R^2 = 0.973$).

Table 3
Overview of the scaling analysis of spines of *H. mamillatus*. For some specimen the Young's Modulus determination failed, therefore the number of specimen *n* used, differ. Abbreviations same as in Table 2.

n	Volume [mm^3]		Porosity [/]		σ_0 [MPa]	*m*	Young's Modulus [GPa]	
	Median	IQR	Median	IQR			Median	IQR
72	688	300–898	0.63	0.62–0.65	66	5.0	8.4 ($n = 62$)	7.6–9.5

large volume is used as reference volume, the calculated strengths lie outside or in the whiskers of the populations (dotted lines in Fig. 5B). Again, this highlights that a size effect was not found for the sea urchin spines.

In general, porosity has a significant effect on the critical strength of samples (e.g. [41,42]). In Fig. 6A and B the expected negative correlation between porosity and strength is clearly visible. The dotted line (B) represents the well-known power law relation between strength and porosity modified by [42] underlining that the strengths lie in the expected range. The compressive strength of fully dense calcite was assumed with 440 MPa and the pores were approximated as spherical. Statistically significant differences are present between samples with a porosity of '0.57–0.59' and '0.66–0.68' and between samples with a porosity of '0.60–0.62' and '0.66–0.68' (One-way Analysis of Variance, $F(3,62) = 6.1$, p-value <0.01, Tukey HSD post-hoc test) (Fig. 6B). Volume and porosity are mutually independent ($R^2 = 0.008$) and therefore cannot be biased by a size effect.

The influence of porosity and volume on the strength of the segments might be overprinted by the internal stereom characteristics. It is reasonable to assume, that the densest and thus stiffest parts of the spines, the growth layers, have a large influence on the strength. Fig. 7A shows that growth layers finishing in the segment and forming a cap affect the Weibull distribution. The data are separated in 3 groups according to the presence and number of finishing growth layers (Table 4). The characteristic strength of these groups does not deviate considerably from 66 MPa, the characteristic strength of all samples. However, the Weibull modulus of those samples without finishing growth layers is much higher and strength decreases with increasing number of growth layers finishing in a segment.

Fig. 7B shows the Weibull plots of segments with growth layers being permanently present close to the rim of the spine. Again, data were separated in 3 groups according to the number of permanent growth layers per segment (Table 5). Groups with one and two permanent growth layers show no distinction in Young's modulus and characteristic strength, while group 3, with multiple permanent growth layers, stands out by a comparably high characteristic strength and Young's modulus despite a porosity level similar to group 1 and 2. The difference in strength between group 1

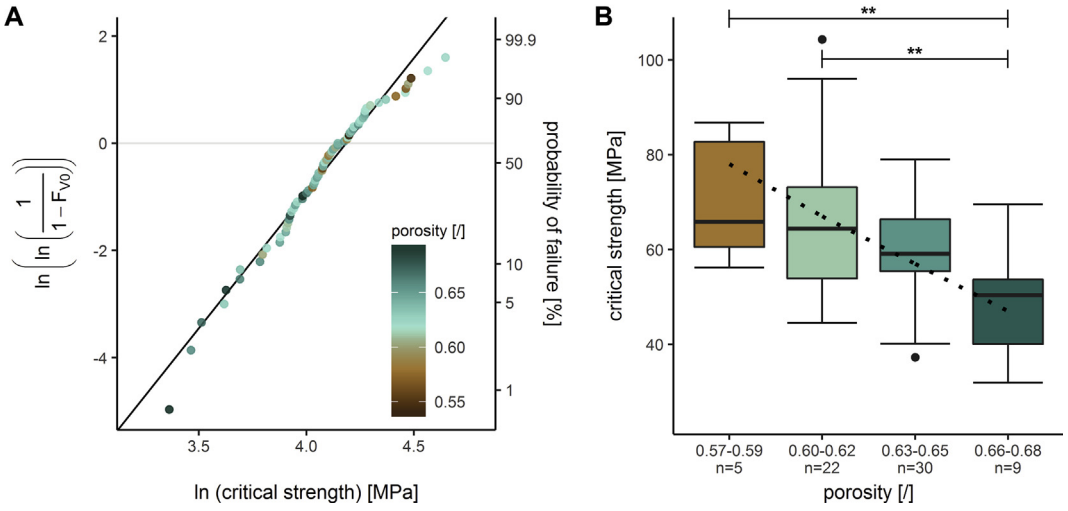

Fig. 6. From the visual impression in (A) porous samples tend to plot at lower strength than denser samples. (B) confirms this impression with groups formed using porosity intervals of 0.02 (0.57–0.59, 0.60–0.62, etc.) and a minimum number of specimens of $n = 5$ per group. A one-way Analysis of Variance with Tukey HSD post-hoc test revealed significant differences between the groups '0.57–0.59' and '0.66–0.68' (**: $p < 0.001$) and '0.60–0.62' and '0.66–0.68' (**: $p < 0.001$). The dotted line models the porosity as a function of strength and pore shape after the model of Pabst and Gregorová [33]. The strength of dense sea urchin spine calcite was assumed with 440 MPa and the pores as spherical.

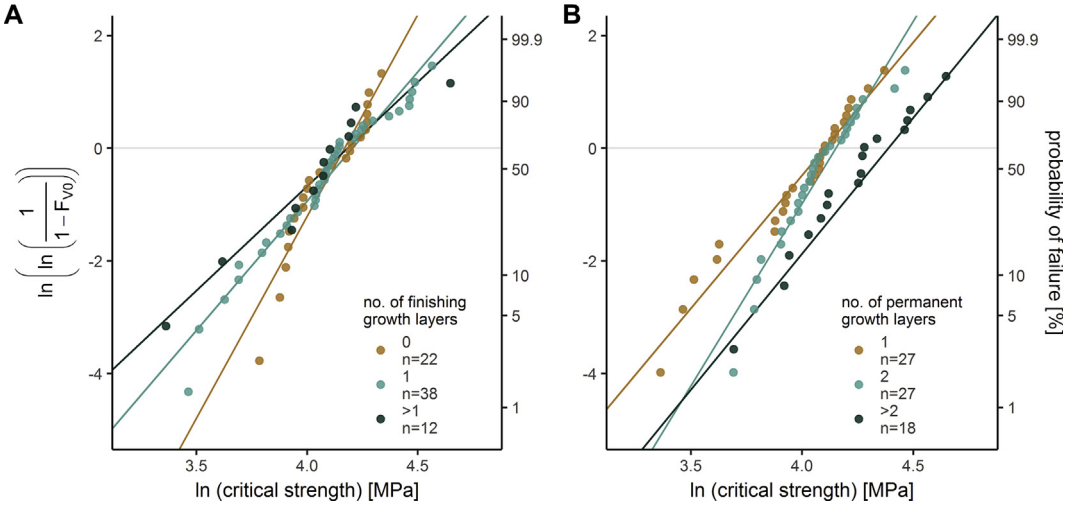

Fig. 7. Weibull plots of critical strength vs. failure probability distinguishing groups with different numbers of finishing growth layers per segment (A) and permanent growth layers per segment (B). No volume correction was applied (Eq. (5)) as a size effect was not found (Fig. 5). Corresponding data are listed in Table 4 and 5.

Table 4
Influence of growth layers finishing in the segments on mechanical key data and porosity. Abbreviations as in Tables 2 and 3, GL: growth layer, No.: number.

Group (n)	No. of GL finishing	σ_0 [MPa]	m	Young's modulus [GPa]		Porosity [/]	
				Median	IQR	Median	IQR
1 (22)	0	65	7.2	8.9 (n = 20)	8.1–9.8	0.64	0.62–0.66
2 (38)	1	67	4.6	7.8 (n = 32)	6.9–9.4	0.63	0.62–0.65
3 (12)	>1	66	3.7	8.3 (n = 10)	8.3–9.4	0.61	0.58–0.63

Table 5
Influence of permanent growth layers on mechanical key data. Abbreviations as in Tables 2–4.

Group (n)	No. of GL permanent	σ_0 [MPa]	m	Young's modulus [GPa]		Porosity [/]	
				Median	IQR	Median	IQR
1 (27)	1	60	4.7	8.1 (n = 24)	7.0–8.4	0.64	0.61–0.65
2 (27)	2	64	6.4	8.1 (n = 24)	7.4–9.4	0.65	0.62–0.65
3 (18)	>2	81	4.8	10.5 (n = 14)	9.6–10.9	0.62	0.62–0.64

and 3 and group 2 and 3 is statistically significant (see also Fig. S6) (One-way Analysis of Variance, F(2,69) = 7.65, p-value <0.001, Tukey HSD post-hoc test).

This is supported by the finding that the four segments with the highest strengths (Figs. 5A and 6A) all have >2 permanent growth layers, and from the 16 samples with highest strengths 12 have >2 permanent growth layers.

4. Discussion

4.1. Coconut endocarp

The critical strength values for small and large coconut endocarp samples, respectively, did not scatter much, which is reflected by the high Weibull modulus, even though the volumes of the samples varied up to 20% from the median. The median critical strength in compression of 222 MPa and 196 MPa for small and large specimen (Fig. 3A) is significantly higher compared to the values reported for macadamia shell cubes of 80 MPa [43]. The occurrence of water pressed out of the specimens prior to failure was unexpected because the samples were at equilibrium with the surrounding moisture conditions. We hypothesize that this was water bound by hydrogen bonds inside the thick sclereid cell walls, and got pressed out during the test due to the high stresses applied to the material. Furthermore, this bound water inside the cell wall is hypothesized to be responsible for the high Weibull moduli found for the coconut endocarp. When the cell wall is saturated with water, the material is less brittle (as known for wood [44]) and therefore less prone to defects caused during sample preparation (e.g. to not entirely coplanar surfaces), resulting in a more homogeneous critical stress within the sample groups. Łysiak et al. [24] investigated a similar effect for pea seeds. They measured significantly higher Weibull moduli for hydrated pea seeds than for dried ones, so water increases the reliability of the seed material. The moisture content of lignified materials such as wood or lignified fruit shell layers has a marked effect on the mechanical properties, which increase with decreasing moisture content below the fiber saturation point (e.g. [44–46]). However, as our samples were stored and tested at the same conditions only a negligible moisture effect on the test results with regard to the size effect can be assumed.

Our results prove a size effect for the coconut endocarp, which is shown by the significantly higher critical strength of the small samples (Fig. 3B). Eq. (2) derived from Weibull theory is already a reasonable fit to the coconut data. However, the slight overestimation of the scaling effect for the coconut endocarp (dotted lines in Fig. 3C) can be minimized applying the model of [20]. The data of the two groups are best described by one master curve with β = 0.84, which is a numerical expression of the finding that the data indicate a size effect slightly less pronounced as under the Weibull assumption. Due to the larger vascular bundles, the overall porosity in the large samples is higher than in the small ones (Table 2), which is expected to reduce the strength [41,42] additionally to the influence of volume increase. Therefore, it could be expected that – if the large and small samples would have the same porosity – the calculations would result in a β value even smaller than 0.84. This consideration points towards an even more diminished size effect for the coconut endocarp.

The question arises which structural element could be responsible for the scaling effect or in other terms which structural element can be seen as the flaw causing failure which is the basis for the weakest link theory used in the Weibull and Lei models. As hypothesized by Schmier et al. [13] the vascular bundles are crucial for the failure mechanism of coconut endocarp. The CT analysis proves that the maximum diameter range of the vascular bundles is larger for large samples than for small ones and that it scatters more for large samples (Fig. S5). If the vascular bundles were responsible for the failure of the samples, the critical strength of the large samples would scatter more than those of the small samples, which would lead to a greatly reduced Weibull modulus. This was not observed. We therefore assume that the structural element causing the failure of the entire sample lies in the cellular structure of the sclereid cell matrix or its intercellular spaces. However, in order to be able to make a well-founded statement about this and in how far differences in stiffness and hardness of the various endocarp elements (sclereids, vascular bundles and connective zones between them) play an important role for fracture initiation and propagation, the structure needs to be investigated in more detail including the various hierarchical levels, which goes beyond the scope of this study.

4.2. Spines of H. mamillatus

The spines of *H. mamillatus* are a good example for the heterogeneity of natural samples. Besides the size of the segments, the porosity and the internal stereom distribution vary considerably. There is no doubt that well-known negative correlation between porosity and strength (e.g. [41,42]) is valid for the spines as well. However, the scatter in strength values is high that a statistically satisfying modelling is not possible from the sea urchin strength data alone. This is a clear indication that the details of the sea urchin structure are a major parameter, which has to be taken into account, as hypothesized by [32].

Samples with more permanent growth layers are stiffer and stronger than their counterparts with only one or two permanent growth layers at comparable porosities (Fig. 7B). We interpret this

phenomenon as reflecting an approach to build up a stiff, dense outer shell, which makes the spine structure stronger than the stereom. This core-shell principle is quite common in nature e.g. in plant stems or animal quills [47].

In case of finishing growth layers forming the characteristic cap, it was found that the Weibull modulus m decreases with increasing number of these layers per segment (Fig. 7A, Tables 5 and 6). The dome shaped ends of such layers do certainly influence the stress distribution in spines. The depth, at which these caps end, varies in each segment and this gives rise to a change in the stress distribution, particularly above those caps. Already with the latter the scatter in strength data has to increase. Consequently segments lacking finishing growth layers have a higher Weibull modulus (m = 7.2) compared to those with these layers, where the Weibull modulus is considerably reduced (Fig. 7A, Table 5). The heterogeneity induced by finishing growth layers may also account for the much lower Weibull modulus reported in the data set by Presser et al. [1].

Our data do not show a size effect in spines of *H. mamillatus* as it would be expected from Weibull theory for brittle materials or other scaling theories for quasi-brittle materials [16]. Calculating the expected characteristic strength with Eq. (2) for the group with smallest volume shown in Fig. 6B yields a characteristic strength of nearly 90 MPa, which deviates markedly from the observed 65 MPa. This absence of any scaling effect is very surprising considering the many results from other biological materials with proven or likely size effects, such as the coconut endocarp or the biological materials listed in Table 1.

In the light of the theory of Lei [20] we therefore are confronted with a value of $\beta = 0$ (no volume effect at all) or at least $\beta \ll 1$, as the natural heterogeneity is pronounced and a size effect cannot be ruled out completely. Furthermore, it is important to highlight that these results are only valid for the here reported sample sizes spanning a magnitude. Future studies aim to enlarge the size differences. Nevertheless, according to our findings, the structural design of spines of *H. mamillatus* is an effective way to diminish or even overcome the size effect being so disadvantageous for brittle materials. Grossmann and Nebelsick [9] could show that the strut size diameter constituting the stereom of the radiating layer for small (juvenile) and large (fully grown) spines of *H. mamillatus* does not differ significantly (16.8 ± 9.2 μm and 19.6 ± 6.0 μm, respectively). Calculating the critical crack length a_c for the spines with the fracture toughness $K_{Ic} = 0.39$ MPa*m$^{1/2}$ [48], the characteristic strength σ_0 identified here (66 MPa) and as geometrical factor $Y = \pi$, we yield $a_c \sim 11$ μm (for whole stress range observed a_c = 5–50 μm). Thus, we hypothesize the high porosity made up by small pores and struts with nearly constant size in the order of the critical crack length could restrict the (critical) flaw size occurring in the structure no matter which size the spines display.

This finding is similar to Lu et al. [22]. In the ZnO ceramics the homogenization of critical crack size was achieved by the interplay of pore/grain size interactions and the overall high porosity, in the case of *H. mamillatus* homogenization is achieved by the constant strut size limiting the crack size, which is of the same order as the struts constituting the structure. As the strut size and the flaw size are of very similar size and the spines show a Weibull distribution of strength, it might be possible that the strut size itself is also Weibull distributed.

5. Conclusions

For biological materials, the volume term in Eq. (5) needs to be taken into account, since precise manufacturing is difficult due to constraints of the sample shapes and the hierarchical structuring. It was demonstrated, that the volume can be set to 1, when a ±25% constant volume is achieved (coconut endocarp) and no size effect is present in the observed size range (sea urchin spines).

Both materials tested, although being strictly speaking quasi-brittle in uniaxial compression, show a Weibull distribution of critical strength, but on a completely different level of reliability. The coconut endocarp has a high Weibull modulus (m = 15) comparable to technical ceramics [49]. This fits to the finding that the material of sclereid cells with embedded vascular bundles is comparably homogeneous on the sub-mm scale. Furthermore, as it is known for seeds, water has a profound impact on the mechanical properties and failure.

In contrast the modulus of the spines of *H. mamillatus* (m = 5) is markedly lower and in the range of other tested biological materials (Table 1). The reasons for this difference may be found in the failure mechanism and in the heterogeneity of the material. The spines feature additionally to the twofold porosity gradient from bottom to tip and exterior to interior [32] a variable number of finishing and permanent growth layers. Presser et al. [1] demonstrated their importance for the failure behavior itself and this study highlights their influence on the failure reliability. The simplest setup with dense growth layers only at the rim and not finishing in the structure comes close to a core shell principle common in many natural materials [47] and *H. mamillatus* spines with this simple layout have the highest Weibull modulus (Fig. 7B).

In terms of the size effect, both materials found a way to at least mitigate the size effect. The coconut endocarp shows the expected volume strength relation for brittle materials, although less pronounced than predicted by Eq. (2). The structural element responsible for the reduced size effect is not found yet and needs further investigations. The spines of *H. mamillatus* do not show any size effect at all in our data set covering a magnitude of size. However, the heterogeneity in the sample population is considerable, so a size effect with $\beta \ll 1$ [20] cannot be ruled out. We hypothesize the reason for this remarkable property lies in the structure: (1) The strut diameters in small and large spines are of the same size, (2) the critical crack size being of similar size as the struts and (3) an overall high porosity homogenizes the crack size occurring in the material.

These results from biological materials lay a first foundation for manufacturing materials with a decreased size effect. Even for nearly dense materials like the coconut endocarp nature could find a way to mitigate the usually so disadvantageous relation between increasing size and decreasing strength. Based on the results from spines of *H. mamillatus,* a first approach for the design for elements out of concrete would need to have a high overall porosity made out of an interconnected pore network with a constant strut size to tackle the size effect in a similar way. The authors are aware of the technical difficulties arising from this design principle.

Acknowledgements

The authors kindly thank the German Research Foundation (DFG-Deutsche Forschungsgemeinschaft) for funding this work within the framework of the Collaborative Research Center (SFB/Transregio) 141 “Biological Design and Integrative Structures”, project B01. The authors thank Stefan Bierer und Mathias Siegel (workshop of the Institute of Biology II/III, University Freiburg) for their support in the rapid manufacturing, as well as Barbara Maier and Simone Schafflick (workshop of the University Tübingen). We are also grateful to four anonymous reviewers for their valuable and thoughtful remarks.

Author’s contribution

CL performed the experiments and analysis of the sea urchin spines, SS performed the experiments and analysis of the coconut

endocarp, CL, SS, TS and KGN wrote the manuscript, TS and KGN supervised the experiments.

Conflicts of interests

The authors declare that they have no conflict of interest.

Animal rights

The sea urchins were not killed for the purpose of this study and were purchased dead from a fossils collector. *Heterocentrotus mamillatus* is not listed as endangered species.

Appendix A. Supplementary data

Supplementary data associated with this article can be found, in the online version, at https://doi.org/10.1016/j.actbio.2018.07.010.

References

[1] V. Presser, S. Schultheiß, C. Berthold, K.G. Nickel, Sea urchin spines as a model-system for permeable, light-weight ceramics with graceful failure behavior. Part I. Mechanical behavior of sea urchin spines under Compression, J. Bionic Eng. 6 (3) (2009) 203–213.

[2] K. Klang, G. Bauer, N. Toader, C. Lauer, K. Termin, S. Schmier, D. Kovaleva, W. Haase, C. Berthold, K.G. Nickel, T. Speck, W. Sobek, Plants and Animals as Source of Inspiration for Energy Dissipation in Load Bearing Systems and Facades, in: J. Knippers, K.G. Nickel, T. Speck (Eds.), Biomimetic research for architecture and building construction: biological design and integrative structures, Biologically-Inspired Systems, Springer, Heidelberg, Berlin, 2016, pp. 109–133.

[3] K.S. Vecchio, X. Zhang, J.B. Massie, M. Wang, C.W. Kim, Conversion of sea urchin spines to Mg-substituted tricalcium phosphate for bone implants, Acta Biomater. 3 (5) (2007) 785–793.

[4] L. Cao, X. Li, X. Zhou, Y. Li, K.S. Vecchio, L. Yang, W. Cui, R. Yang, Y. Zhu, Z. Guo, X. Zhang, Lightweight open-cell scaffolds from sea urchin spines with superior material properties for bone defect repair, ACS Appl. Mater. Interfaces 9 (11) (2017) 9862–9870.

[5] N. Toader, W. Sobek, K.G. Nickel, Energy absorption in functionally graded concrete bioinspired by sea urchin spines, J. Bionic Eng. 14 (2017) 369–378.

[6] R. Seidel, A. Bührig-Polaczek, C. Fleck, T. Speck, Impact resistance of hierarchically structured fruit walls and nut shells in view of biomimetic applications Guyana, ECOFOG, Cayenne, France, 2009, pp. 406–411.

[7] V. Presser, C. Kohler, Z. Zivcova, C. Berthold, K.G. Nickel, S. Schultheiß, E. Gregorova, W. Pabst, Sea urchin spines as a model-system for permeable, light-weight ceramics with graceful failure behavior. Part II. Mechanical behavior of sea urchin spine inspired porous aluminum oxide ceramics under Compression, J. Bionic Eng. 6 (4) (2009) 357–364.

[8] N. Grossmann, Stereom differentiation in sea urchin spines under special consideration as a model for a new impact protective system, Paleontology, Institute for Geosciences, University Tübingen, Tübingen, 2010, p. 160.

[9] J.N. Grossmann, J.H. Nebelsick, Comparative morphological and structural analysis of selected cidaroid and camarodont sea urchin spines, Zoomorphology 132 (3) (2013) 301–315.

[10] F.W. Clarke, W.C. Wheeler, The inorganic constituents of echinoderms, U.S. Geol. Surv. Prof. Pap. 90 (L) (1915) 191–196.

[11] D.M. Raup, Crystallography of echinoid calcite, J. Geol. 67 (6) (1959) 661–674.

[12] J.N. Weber, The incorporation of magnesium into the skeletal calcites of echinoderms, Am. J. Sci. 267 (5) (1969) 537–566.

[13] S. Schmier, C. Lauer, I. Schäfer, K. Klang, G. Bauer, M. Thielen, K. Termin, C. Berthold, S. Schmauder, T. Speck, K.G. Nickel, Developing the Experimental Basis for an Evaluation of Scaling Properties of Brittle and 'Quasi-Brittle'Biological Materials, in: J. Knippers, K.G. Nickel, T. Speck (Eds.), Biomimetic research for architecture and building construction: biological design and integrative structures, Biologically-inspired systems, Springer, Heidelberg, Berlin, 2016, pp. 277–294.

[14] A.L. Winton, Anatomy of the fruit of *Cocos nucifera*, Am. J. Sci 70 (1901) 265–280.

[15] Z.P. Bažant, Size effect, Int. J. Solids Struct. 37 (2000).

[16] Z.P. Bažant, Scaling theory for quasibrittle structural failure, PANAS 101 (2004) 13400–13407.

[17] M. Genet, G. Couégnat, A.P. Tomsia, R.O. Ritchie, Scaling strength distributions in quasi-brittle materials from micro- to macro-scales: a computational approach to modeling Nature-inspired structural ceramics, J. Mech. Phys. Solids 68 (2014) 93–106.

[18] W. Weibull, A statistical distribution function of wide applicability, J. Appl. Mech. 18 (3) (1951) 293–297.

[19] R. Danzer, P. Supancic, J. Pascual, T. Lube, Fracture statistics of ceramics-Weibull statistics and deviations from Weibull statistics, Eng. Fract. Mech. 74 (18) (2007) 2919–2932.

[20] W.-S. Lei, A generalized weakest-link model for size effect on strength of quasi-brittle materials, J. Mater. Sci. 53 (2) (2018) 1227–1245.

[21] G. Dill-Langer, R.C. Hidalgo, F. Kun, Y. Moreno, S. Aicher, H.J. Herrmann, Size dependency of tension strength in natural fiber composites, Physica A 325 (3-4) (2003) 547–560.

[22] C. Lu, R. Danzer, F.D. Fischer, Scaling of fracture strength in ZnO: effects of pore/grain-size interaction and porosity, J. Eur. Ceram. Soc. 24 (14) (2004) 3643–3651.

[23] R. Menig, M.H. Meyers, M.A. Meyers, K.S. Vecchio, Quasi-static and dynamic mechanical response of *Haliotis rufescens* (abalone) shells, Acta Mater. 48 (9) (2000) 2383–2398.

[24] G. Łysiak, Fracture toughness of pea: Weibull analysis, J. Food Eng. 83 (3) (2007) 436–443.

[25] Y.L. Chan, A.H. Ngan, N.M. King, Use of focused ion beam milling for investigating the mechanical properties of biological tissues: a study of human primary molars, J. Mech. Behav. Biomed. Mater. 2 (4) (2009) 375–383.

[26] E. Trujillo, M. Moesen, L. Osorio, A.W. Van Vuure, J. Ivens, I. Verpoest, Bamboo fibres for reinforcement in composite materials: strength Weibull analysis, Compos. Part A-Appl. S. 61 (2014) 115–125.

[27] M.U. Pedersen, C.O. Clorius, L. Damkilde, P. Hoffmeyer, A simple size effect model for tension perpendicular to the grain, Wood Sci. Technol. 37 (2) (2003) 125–140.

[28] A.F. Moshtaghin, S. Franke, T. Keller, A.P. Vassilopoulos, Experimental characterization of longitudinal mechanical properties of clear timber: random spatial variability and size effects, Constr. Build. Mater. 120 (2016) 432–441.

[29] B. Gludovatz, F. Walsh, E.A. Zimmermann, S.E. Naleway, R.O. Ritchie, J.J. Kruzic, Multiscale structure and damage tolerance of coconut shells, J. Mech. Behav. Biomed. 76 (2017) 76–84.

[30] L. Fishelson Dotan, Morphology of spines of *Heterocentrotus mammillatus* (Echinodermata, Echinoidae) and its ecological significance, Echinodermata, Balkema Rotterdam (1985) 253–260.

[31] Stereom Smith, microstructures of the echinoid test, Spec. Pap. Palaeontol. 25 (1980) 1–81.

[32] T.B. Lauer, I. Grun, R. Zutterkirch, G. Jemmali, J.H. Buck, K.G. Nickel Nebelsick, Morphology and porosity of the spines of the sea urchin *Heterocentrotus mamilllatus* and their implications on the mechanical performance, Zoomorphology (2017) 1–16.

[33] G.C. Braga, S.M. Couto, T. Hara, J.T.A. Neto, Mechanical behaviour of macadamia nut under compression loading, J. Agr. Eng. Res. 72 (3) (1999) 239–245.

[34] J. Seto, Y. Ma, S.A. Davis, F. Meldrum, A. Gourrier, Y.Y. Kim, U. Schilde, M. Sztucki, M. Burghammer, S. Maltsev, C. Jager, H. Colfen, Structure-property relationships of a biological mesocrystal in the adult sea urchin spine, PANAS 109 (10) (2012) 3699–3704.

[35] M. Albéric, E.N. Caspi, M. Bennet, W. Ajili, N. Nassif, T. Azaïs, A. Berner, P. Fratzl, E. Zolotoyabko, L. Bertinetti, Y. Politi, Interplay between Calcite, amorphous calcium carbonate, and intracrystalline organics in sea urchin skeletal elements, Cryst. Growth Des. (2018).

[36] H.J. Bargel, G. Schulze, Werkstoffkunde, Tenth ed., Springer, Heidelberg, 2008.

[37] O.K. DeFoe, A.H. Compton, The density of rock salt and calcite, Phys. Rev. 25 (5) (1925) 618–620.

[38] H. Wickham, ggplot2: Elegant Graphics for Data Analysis, Springer, New York, 2009.

[39] J. Fox, S. Weisberg, An R Companion to Applied Regression, second ed., Sage, Thousand Oaks, CA, 2011.

[40] R. Core Team, R: A language and environment for statistical computing, R Foundation for Statistical Computing, Vienna, Austria, 2017.

[41] L.J. Gibson, M.F. Ashby, The mechanics of three-dimensional cellular materials, P. Roy. Soc. Lon. A Mat. 382 (1982) 43–59.

[42] W. Pabst, E. Gregorová, Young's modulus of isotropic porous materials with spheroidal pores, J. Eur. Ceram. Soc. 34 (13) (2014) 3195–3207.

[43] C.-H. Wang, Y.-W. Mai, Deformation and fracture of Macadamia nuts, Int. J. Fracture 69 (1) (1994) 67–85.

[44] J. Bodig, B.A. Jayne, Mechanics of Wood and Wood Composites, Krieger, Malabar Fla, 1993.

[45] C. Skaar, Wood-water relations, Springer, Berlin, 1988.

[46] C. Aydin, Physical properties of hazel nuts, Biosyst. Eng. 82 (3) (2002) 297–303.

[47] M.A. Dawson, L.J. Gibson, Optimization of cylindrical shells with compliant cores, Int. J. Solids Struct. 44 (3–4) (2007) 1145–1160.

[48] B.E. Broz, R.F. Cook, D.L. Whitney, Microhardness toughness, and modulus of Mohs scale minerals, Am. Miner. 91 (2006) 135–142.

[49] R. Danzer, On the relationship between ceramic strength and the requirements for mechanical design, J. Eur. Ceram. Soc. 34 (15) (2014) 3435–3460.

Strength-size relationships in two porous brittle biological materials

Christoph Lauer, Stefanie Schmier, Thomas Speck, Klaus G. Nickel

Supplementary 1. Error determination of volume and porosity for spines of *H. mamillatus*

Error bars for porosity and volume were calculated as follows: As the volume of the segments is never an ideal cylinder it was determined by averaging the area of the lower (A1) and upper cross section (A2) and by multiplying it with the height of the segment (h). This way, a linear increase or decrease of the cross section over the segment's height is assumed (Fig. S1a). This is a simplification and may not hold true for all segments as they vary in their shape. Two boundary scenarios for maximal and minimal volume were assumed and are shown in Fig. S1b, c. Error bars for volume are given on this basis and are a conservative estimate as the segment shape rarely tends to these schematic extremes. Since the volume influences the porosity, error bars are given accordingly. The height of the coplanar segment the mass have been determined accurately and changes of a few μm and mg are irrelevant for the error in porosity determination and are outbid by the volume changes and were therefore not taken into account.

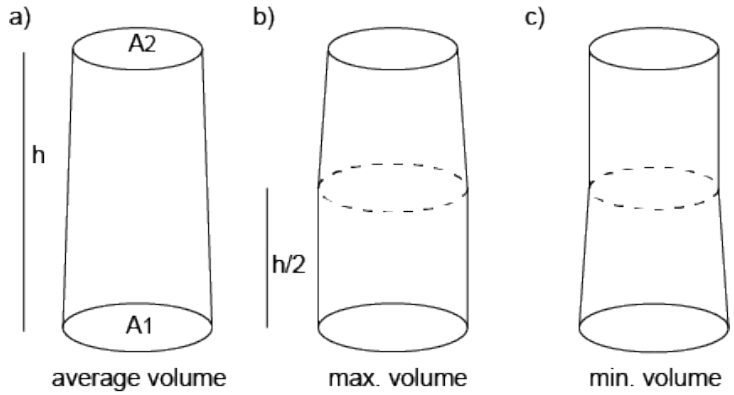

Fig. S1. Schematic representation of the error calculation for volume of segments: A1 = lower cross section, A2 = upper cross section and h = height. (a) shows how the volume was approximated, (b) represents the maximal volume and (c) the minimal volume.

Supplementary 2. Additional Information on the failure behaviour of spines of *H. mamillatus*

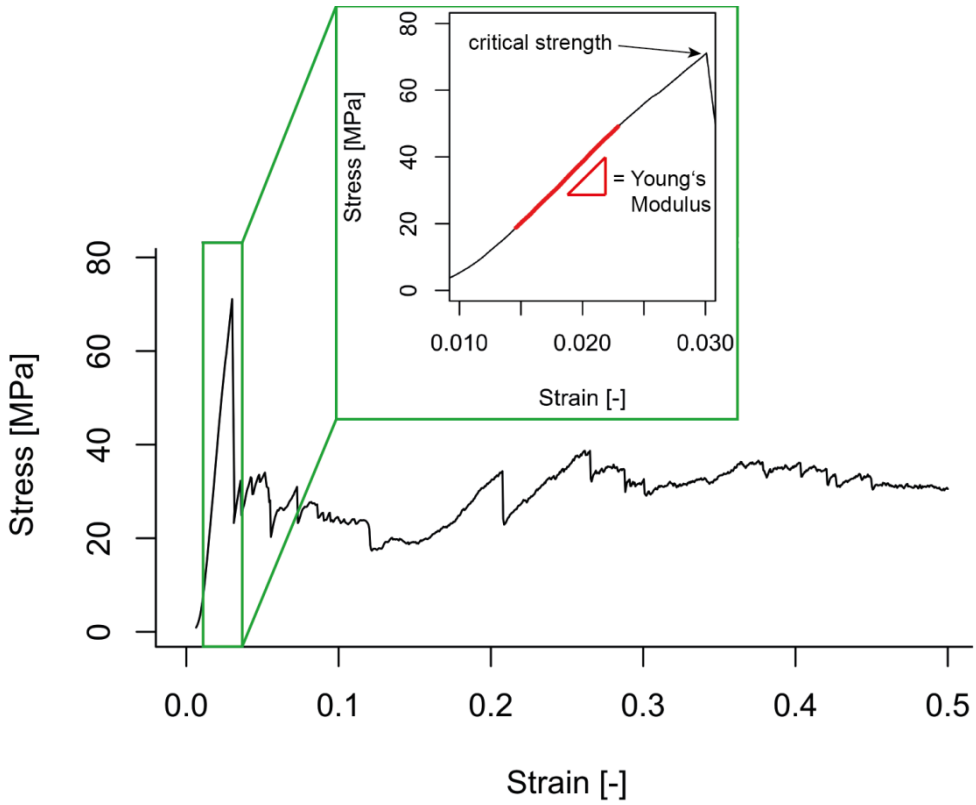

Fig. S2. Representative stress-strain curve of a segment from *H. mamillatus*. For the determination of the Young's Modulus only the steepest part of the stress strain curve was used (red line, enlarged part of the stress strain curve). The strength terminating the initial linear elastic increase is the critical strength used for Weibull analysis. The non-catastrophic failure behaviour is highlighted by the load bearing capacities even after high strain which makes this material very energy dissipating effective. For more information on the failure of spines of *H. mamillatus* see Presser et al. 2009 [1].

Supplementary 3. Conversion of Eq. (1) in Eq. (5)

$$P = 1 - \exp\left(-\left(\frac{V_i}{V_0}\right) \cdot \left(\frac{\sigma_i}{\sigma_0}\right)^m\right)$$

$$\Leftrightarrow 1 - P = \exp\left(-\left(\frac{V_i}{V_0}\right) \cdot \left(\frac{\sigma_i}{\sigma_0}\right)^m\right) \quad |\ln$$

$$\Leftrightarrow \ln(1 - P) = -\left(\frac{V_i}{V_0}\right) \cdot \left(\frac{\sigma_i}{\sigma_0}\right)^m \quad |\cdot(-1)\left(\frac{V_0}{V_i}\right)$$

$$\Leftrightarrow \ln(1 - P)^{-\left(\frac{V_0}{V_i}\right)} = \left(\frac{\sigma_i}{\sigma_0}\right)^m$$

$$\Leftrightarrow \ln\left(\frac{1}{(1-P)^{\left(\frac{V_0}{V_i}\right)}}\right) = \left(\frac{\sigma_i}{\sigma_0}\right)^m \quad |\ln$$

$$\Leftrightarrow \ln\left(\ln\left(\frac{1}{(1-P)^{\left(\frac{V_0}{V_i}\right)}}\right)\right) = m \cdot \ln\left(\frac{\sigma_i}{\sigma_0}\right)$$

$$\Leftrightarrow \ln\left(\ln\left(\frac{1}{(1-P)^{\left(\frac{V_0}{V_i}\right)}}\right)\right) = m \cdot \ln(\sigma_i) - m \cdot \ln(\sigma_0))$$

Supplementary 4. Analysis of the diameter range of vascular bundles gained from the CT-data with CT-Analyser

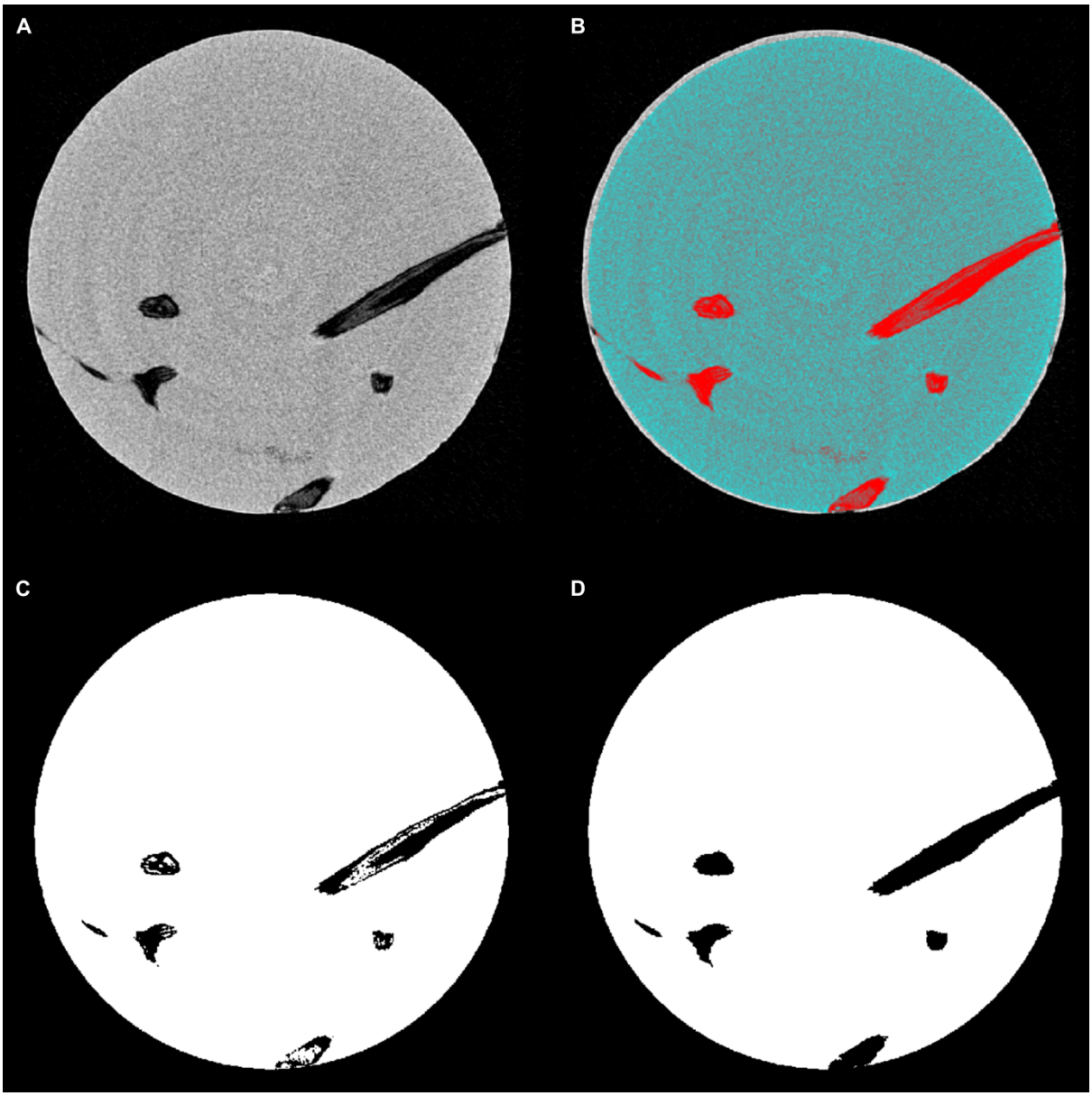

Fig. S3. Analysis of the µCT-data with CT-Analyser, exemplarily shown on a cross section of a big coconut endocarp sample with a diameter of 8 mm. The volume of the raw data (A) was approximated from the inside with a cylindrical region of interest (B). Afterwards a threshold value was used to differentiate between air and lignified material within the region of interest (C). The threshold value was determined manually on one data set so that all tissues are mapped and kept constant for the remaining samples. This data set was used to determine the porosity of the sample for which the volume of the lignified material was divided by the volume of the region of interest. The cell walls of the tracheids were removed from the vascular bundles using the "Despeckle"-function of CT-Analyser to determine the vascular bundle diameter with the structure separation distribution for each point in the pore space (D). The “Structure separation distribution”-function is based on the local thickness for a point defined as the diameter of the largest sphere fulfilling two conditions: (i) the sphere encloses the point (but the point is not necessarily the centre of the sphere) and (ii) the sphere is entirely bounded within the pores surfaces.

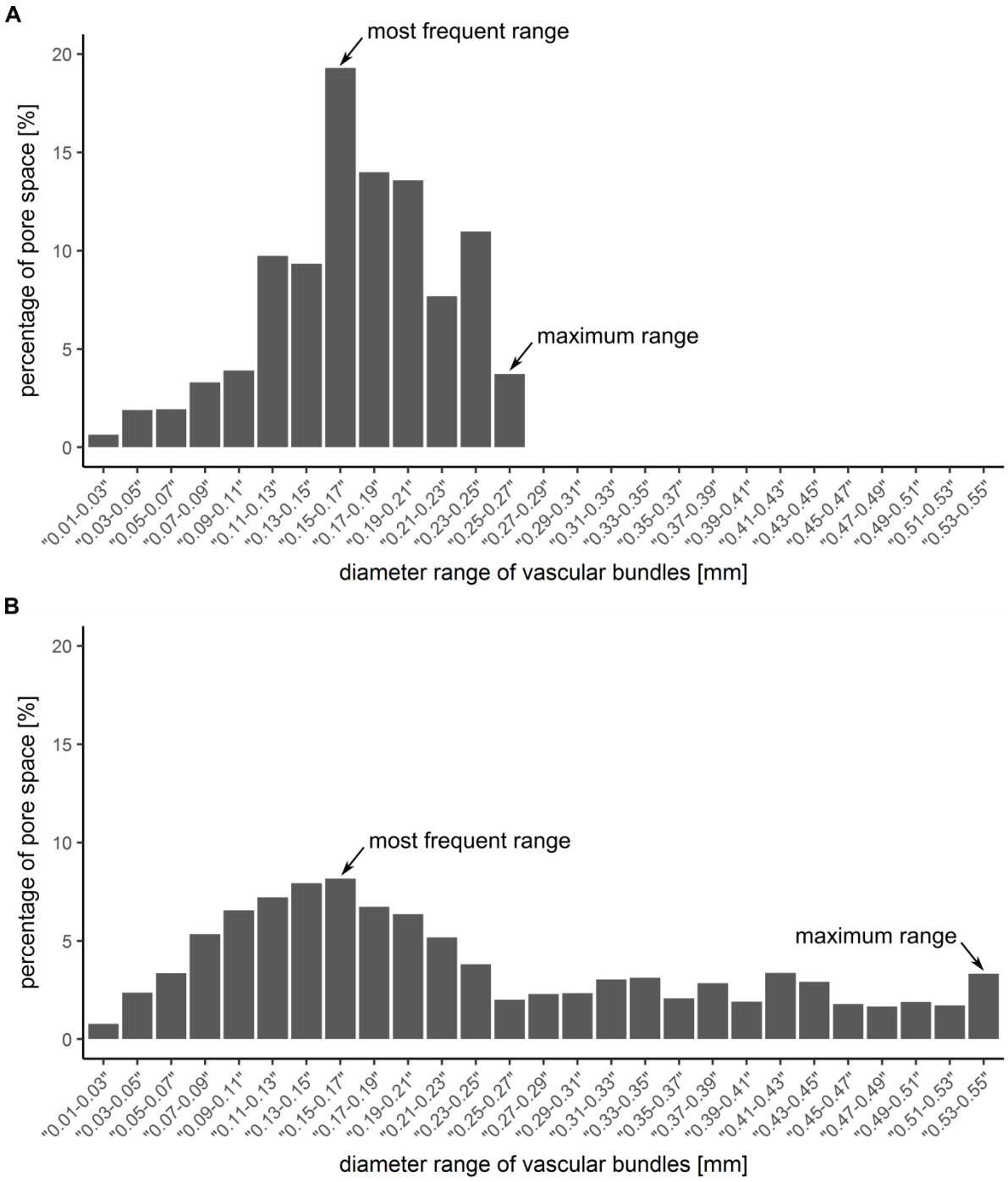

Fig. S4. Resulting diameter ranges of the vascular bundles for a representative small (A) and large (B) specimen from the analyses of CT-Analyser. To compare the diameter distribution between small and large specimen the two parameters most frequent diameter range and maximum diameter range are listed (Table S1).

Table S1. Comparison of the diameter distribution of the vascular bundles of small and large coconut endocarp specimen. The most frequently found diameter ranges are "13-15" and "15-17", as well for small specimen as for large ones. A trend is visible for the maximum diameter range, that in large samples larger maximum diameters occur. Abbreviations: mfr: most frequent range, mr: maximum range.

group	porosity [/]	mfr [mm]	mr [mm]
small	0.021	"0.11-0.13"	"0.23-0.25"
small	0.009	"0.15-0.17"	"0.17-0.19"
small	0.020	"0.09-0.11"	"0.27-0.29"
small	0.011	"0.07-0.09"	"0.15-0.17"
small	0.011	"0.15-0.17"	"0.25-0.27"
small	0.018	"0.13-0.15"	"0.27-0.29"
small	0.009	"0.19-0.21"	"0.25-0.27"
small	0.013	"0.13-0.15"	"0.23-0.25"
small	0.037	"0.27-0.29"	"0.27-0.29"
small	0.019	"0.19-0.21"	"0.21-0.23"
large	0.040	"0.13-0.15"	"0.75-0.77"
large	0.026	"0.13-0.15"	"0.59-0.61"
large	0.027	"0.17-0.19"	"0.35-0.37"
large	0.045	"0.33-0.35"	"0.47-0.49"
large	0.025	"0.15-0.17"	"0.57-0.59"
large	0.031	"0.15-0.17"	"0.53-0.55"
large	0.013	"0.13-0.15"	"0.27-0.29"
large	0.018	"0.13-0.15"	"0.31-0.33"
large	0.021	"0.25-0.27"	"0.31-0.33"
large	0.027	"0.13-0.15"	"0.35-0.37"

Supplementary 5. Weibull analysis of the coconut data considering the volume factor

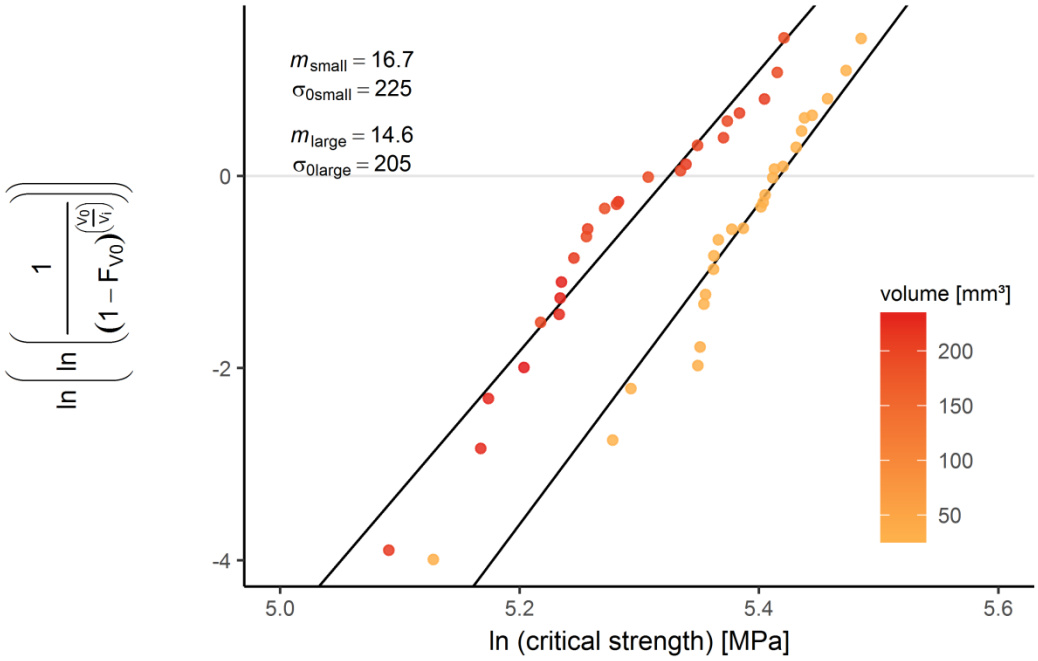

Fig. S5. Weibull plot according to Eq. (5) taking the volume factor (V_0/V_i) into account with the respecting Weibull moduli and characteristic strengths for small and large coconut samples. Do not confuse with Fig. 3C, where the volume factor is not taken into account with $V_0/V_i = 1$ and therefore another y-axis was applied.

Supplementary 6. Additional Information for the influence of the growth layers on the critical strength

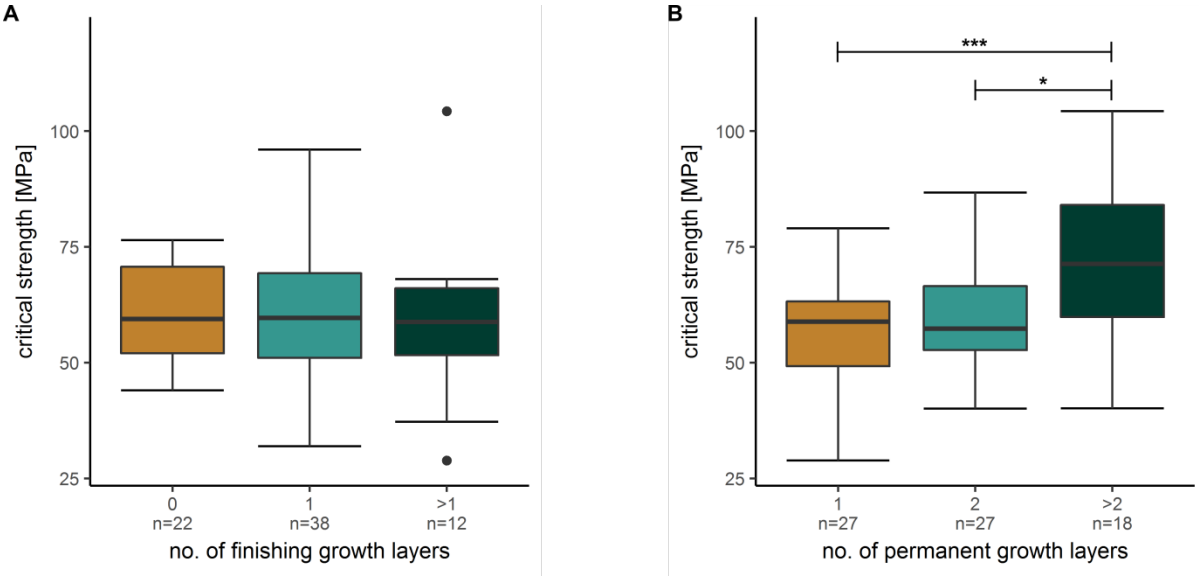

Fig. S6. Box plots of Groups listed in Table 4 (A) and 6 (B). Significant difference in strength only between groups with 1 and >2 permanent growth layers ($p<0.001$) and 2 and >2 permanent growth layers ($p<0.05$) (One-way Analysis of Variance, $F(2,69) = 7.65$, p-value < 0.001, Tukey HSD post-hoc test) (B).

Manuscript 4 with Supplementary Material

Strength, elasticity and the limits of energy dissipation in two related sea urchin spines with biomimetic potential

(15+5 pages)

Bioinspiration & Biomimetics

PAPER

Strength, elasticity and the limits of energy dissipation in two related sea urchin spines with biomimetic potential

Christoph Lauer[1], Kilian Sillmann, Sebastian Haußmann and Klaus G Nickel

Division of Applied Mineralogy, Department of Geosciences, University of Tübingen, Wilhelmstraße 56, D-72074 Tübingen, Germany
[1] Author to whom any correspondence should be addressed.

E-mail: christoph.lauer@uni-tuebingen.de

RECEIVED
15 August 2018

REVISED
7 November 2018

ACCEPTED FOR PUBLICATION
30 November 2018

PUBLISHED
19 December 2018

Keywords: biogenic calcite, sea urchin spines, *Heterocentrotus*, mechanical testing, Young's Modulus, energy dissipation

Supplementary material for this article is available online

Abstract

The calcitic spines of the sea urchins *Heterocentrotus mamillatus* and *H. trigonarius* are promising role models for lightweight applications, bone tissue scaffolds and energy dissipating processes due to their highly porous and organized structure. Therefore, mechanical properties including Young's Modulus, strength, failure behaviour and energy dissipation efficiency have been investigated in depth with uniaxial compression experiments, 3-point bending tests and resonance frequency damping analysis. It was found that despite a very similar structure, *H. trigonarius* has a significantly lower porosity than *H. mamillatus* leading to a higher strength and Young's Moduli, but limited ability to dissipate energy. In order to show reliable energy dissipation during failure in uniaxial compression, a transition porosity of 0.55–0.6 needs to be exceeded. The most effective structure for this purpose is a homogeneous, foam-like structure confined by a thin and dense shell that increases initial strength and was found in numerous spines of *H. mamillatus*. Sharp porosity changes induced by dense growth layers or prominent wedges of the spines' radiating building principle act as structural weaknesses, along which large flakes can be spalled, reducing the energy dissipation efficiency considerably.

The high strength and Young's Modulus at the biologically necessary high porosity levels of the spines is useful for *Heterocentrotus* and their construction therefore remains to be a good example of biomimetics. However, the energy dissipative failure behaviour may be regarded as a mere side effect of the structure.

1. Introduction

Sea urchin spines attracted scientific attention early on due to their apparent single-crystallinity [1–3], their well-organized, highly porous and elaborate calcite meshwork [4, 5], called stereom [6], and the incorporation of considerable amounts of Mg into the biogenic calcite, which is thermodynamically metastable at room temperatures [7–9]. More recently, the scientific interest shifted towards the role of amorphous calcium carbonate (ACC) in the formation and growth of echinoderm calcite by the example of sea urchin spines [10–15] and bionic research [16–22]. A biomimetic potential of sea urchin spines was recognized first by Weber for bone tissue replacement [23] and for energy dissipating processes (e.g. impact protection) [24].

This study focuses on the outstanding mechanical properties of sea urchin spines and addresses the question of energy dissipation and the spines' potential as biological concept generator for lightweight ceramics [25] and lightweight concrete [19]. The spines of the Indo-Pacific sea urchins *Heterocentrotus mamillatus* and its closest relative *H. trigonarius* have been chosen for this purpose as their spines belong to the largest among echinoids. This permits manufacturing of samples for mechanical testing in manageable size.

Spines of both species share a common building principle, which can be seen well in cross or longitudinal sections. In the centre is the most porous part, the Medulla, surrounded by radiating layers, which alternate with conspicuous growth layers (GLs) [26–28], which are the densest part of the spine [29] (figure 1(a)). Those are fairly thin (usually $<100\ \mu$m) and can

be seen by the naked eye due to their brown to red colouration caused by naphtaquiones [30] (figure 1(b)).

The whole spine is structured in a radiating manner (figure 1(a)) out of a large number of thin 'wedges' consisting out of radiating trabeculae and radial septa of the GLs, bordered by a porous zone. A detailed description is given elsewhere [29]. The characteristic GLs represent outlines of the spine at earlier stages of growth. The time resolved in one growth cycle is still a matter of debate [26, 31–34]. Despite these uncertainties it is clear that the dense GLs are beneficial for the mechanical performance of the spines of *H. mamillatus*.

The concentration of the GLs on the spine's rim and the highly porous core in the interior resembles a core–shell construction [29]. This building principle is common in natural materials and has a superior stiffness compared to materials with the same but uniform porosity [35, 36]. It was found that spine segments with more GLs close to the spine's rim (permanent GLs (figure 1(b))) have a significantly higher strength than spines with fewer of those GLs [37]. On the other hand, due to the highly porous structure of the spines they behave similar to brittle foams in uniaxial compression (UC) experiments and have no catastrophic failure and can withstand loads even after considerable strain ($\gg$0.2). This failure behaviour is even improved by the dome shaped GLs ending in the tested segment (finishing GLs (figure 1(b))). They can withstand more load than the regular radiating layer, which can be seen in the corresponding stress–strain curves by repeated stress increases and drops as soon as such a GL is reached and overcome [17, 38]. This behaviour has been termed 'graceful cascading failure' [17] and was conceptually transferred to porous ceramics, where it was shown that the alternation of more porous and denser layers mimicking *H. mamillatus*' building principle dissipates more energy than ceramics of same but uniform porosity [18]. *H. trigonarius* has more GLs than *H. mamillatus* [26, 34] so this failure principle should be observed in *H. trigonarius* spines as well. It is expected to find it in an improved way as more GLs are present and the porosity alternates more often. This one of the question addressed in this study.

In order to quantify the 'graceful failure behaviour' the concept of energy dissipation efficiency has been adapted from foam literature [39, 40]. The energy dissipation efficiency (η) is the energy dissipated (or absorbed) during the UC experiment (area under stress (σ)-strain (ε) curve (figure 2) and is divided by the maximum of energy that could have been dissipated by an ideal foam with the same maximal strength (σ_{max}) [40, 41]:

$$\eta(\varepsilon) = \frac{\int_0^{\varepsilon} \sigma d\varepsilon}{\sigma_{max}\varepsilon}. \quad (1)$$

Aluminium foams can reach η of above 0.8 and even 0.9 and are thus very close to an ideal absorber [42]. However, (equation (1)) treats the material to have

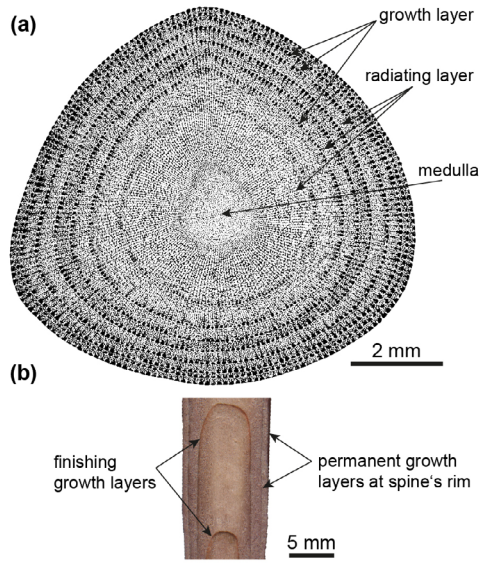

Figure 1. (a) Displays the dense stereom of a cross section from a GL rich spine of *H. mamillatus*. The radiating building principle is well visible. A UC segment is cut longitudinally to reveal the two mechanically relevant GL types: finishing GLs and permanent GLs at the spine's rim (b).

an infinite Young's Modulus (E) (figure 2). This can be corrected using the strain at the high elastic limit (HEL) as the lower boundary

$$\eta(\varepsilon) = \frac{\int_{\varepsilon_{HEL}}^{\varepsilon} \sigma d\varepsilon}{\sigma_{max}(\varepsilon - \varepsilon_{HEL})}. \quad (2)$$

The elastic energy stored in the material is in this equation removed to look only at the dissipated energy part. Equation (2) can then be simplified to the ratio out of the average plateau strength, σ_{pl} (figure 2) divided by the maximum stress of the linear elastic increase (σ_{max}):

$$\gamma = \frac{\sigma_{pl}}{\sigma_{max}}. \quad (3)$$

Mechanical properties of sea urchin spines are widely reported without relating them to porosity [17, 20, 43, 44], although it is well known, that porosity directly influences elastic properties [45–47]. Usually the open-cell porosity model by Gibson and Ashby [46] (which is equal to the Coble Kingery approach [45]) obtained by dimensional analysis is used for porous ceramics as what sea urchin spines can be considered, with E_ϕ the Young's Modulus of the porous material, E_0 the Young's Modulus of the dense (pore wall) material and the porosity ϕ.

$$E_\phi = E_0 * (1-\phi)^2. \quad (4)$$

Pabst and Gregorová [47] incorporated the influence of the aspect ratio of spherical pores into the model with the Eshelby–Wu coefficient (EW), a constant depending on the Poisson's ratio ν of the cell wall material and the aspect ratio of the pores.

$$E_\phi = E_0 * (1-\phi)^{EW}. \quad (5)$$

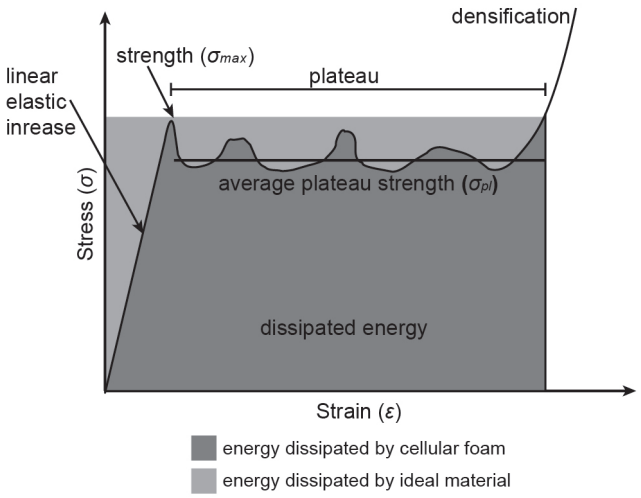

Figure 2. Ideal cellular materials display three distinct regions in UC: the linear elastic increase, the plateau and the densification. The energy dissipated is the area under the stress strain curve and the energy dissipation efficiency is the ratio of the energy dissipated by the sample (dark grey) and the energy dissipated by an ideal material (light grey). Instead of this definition the present study uses simply the ratio of strength and average plateau strength, which discards the elastic stored energy.

With $\nu = 0.322$, which can be considered for calcite [48], the EW ranges from 2 to ∞ for oblate pores and 2–2.3 for prolate pores in loading direction. So intuitively, columnar pores have roughly the same effect as spherical pores on E, whereas sheet like pores can reduce E almost to zero at any given porosity [47]. The porosity of the sea urchin spines investigated spans from 0.41 to 0.78 so we are able to examine whether the spines follow the predictions by (equations (4) and (5) and we can evaluate the mechanically relevant pore shape. E is determined by three methods in this study: 3-point-bending, UC (both static E) and resonance frequency damping analysis (RFDA, dynamic E). These methods are compared and the most suitable method for biological samples is identified.

2. Materials and methods

Sea urchins were not killed for the purpose of this study. Spines were purchased from a fossils collector (Fossilienhandlung Peter Gensel, Weimar, Germany) and from Fischhaus Zepkow (Zepkow, Germany). For UC experiments the spines were cut coplanar ($\pm$15 μm) with a Buehler med 3000 saw to a length diameter ratio not exceeding 2($\pm$0.3):1 to avoid buckling under uniaxial loading [49]. Length was measured with a micrometre gage (Mitutoyo IP65, Mitutoyo Deutschland GmbH, Germany) with an accuracy of 1 μm and the mass was determined with a Sartorius scale BP 211D (AG, Göttingen, Germany) with a precision of 0.01 mg. The area of top and bottom cross section of each segment was measured using the ImageJ software environment Fiji 2.0.0. The volume of the segments was obtained by taking the mean of the two cross sections and multiplying it by the length of the segment. This way the gravimetrical porosity was determined for each segment tested.

2.1. 2d porosity determination and optical microscopy

The detailed 2d porosity determination was carried out as described by [29]. The Micrographs were obtained with a Hitachi TM 3030 (Hitachi High-Technologies Europe GmbH, Krefeld, Germany) scanning electron microscope (SEM). For measuring the cross-sectional area and counting GLs on segments for mechanical testing, it was sufficient to scan the segment with a commercial scanner at 600–1200 dpi. For more detailed investigations an optical microscope (Hirox MXB 2016Z, Hirox Europe, Limonest, France) was used.

2.2. Uniaxial compression

UC experiments were conducted with a 10 kN Instron 4502 universal testing machine (Instron Deutschland GmbH, Pfungstadt, Germany). The displacement was recorded with a videoextensometer (Limess RTSS_C02, Limess Software und Messtechnik GmbH, Krefeld, Germany) for calculating E from the slope of the linear elastic increase in the stress–strain diagrams (cp. [37]). For UC only spine segments >260 mm^3 were used. In total 41 experiments with *H. trigonarius* and 103 with *H. mamillatus* were conducted. The cross-head speed was 0.5 mm min^{-1}.

2.3. 3-point bending

The 3-point bending module was mounted in the same universal testing machine used for UC tests. The experiments were also recorded with the videoextensometer and the cross-head speed was 0.5 mm min^{-1}. A pre-load of 20N was applied.

The span width of the outer loading points in the 3-point bending module was 40 mm and the inner loading point was calibrated to apply load exactly in the center of the span. The three cylindrical loading rollers (ø = 5 mm) were supported in such a way

that they could adapt to the partly irregular sea urchin spine shape and distribute load evenly. 10 segments from exceptional circular *H. mamillatus* spines were prepared for 3-point bending experiments. Still, the cross section was only approximately circular as the samples are of biological nature. The 3-point bending strength (σ_{3pb}) can be calculated with [50]:

$$\sigma_{3pb} = \frac{16Pa}{\pi d^3} \tag{6}$$

with the applied load P, the diameter of the specimen d, and the moment arm a, which is half of the span width. As the diameter changes over the segment length, for calculations the diameter of the fracture surface was used. The strain ε was obtained by:

$$\varepsilon = \frac{6ds}{(2a)^2} \tag{7}$$

with the deflection s, recorded by the videoextensometer.

2.4. Resonance frequency damping analysis

The RFDA (also: impulse excitation) was used to determine E in flexural (perpendicular to crystallographic c-axis) and longitudinal (parallel to crystallographic c-axis) modes. The method exploits the mechanical resonant frequencies f_i of the material, which are functions of the sample geometry, the density and the elastic properties of the material. By measuring the damping of the oscillation, the resonant frequency can be calculated. Therefore, a sample of known geometry and density is gently excited with a tapping device. It is supported in such a way that it can oscillate freely according to ASTM E1876-15 [51]. For flexural measurement the sample is fixated at the two nodes of the oscillation and excited in the middle of length L. For longitudinal measurements it is fixated at the only node in the middle of L and excited in the centre of the cross section. E is calculated after [51] in flexural mode by:

$$E = 1.6067\left(\frac{L^3}{d^4}\right)\left(mf_f^2\right)K_1 \tag{8}$$

and in longitudinal mode after [52] by:

$$E = \left(\frac{4L^2f_l^2\rho}{10^9}\right)K_2 \tag{9}$$

where a specimen is used with diameter d, mass m, density ρ and the resonant frequency f, in flexural (f_f) and longitudinal (f_l) mode and correction factors K_1 and K_2 for flexural and longitudinal mode, respectively. The correction factor is based on the sample geometry and the Poisson's ratio and its calculation is given in the corresponding norm.

The measurements were carried out with an IMCE RFDA Professional 23 system (IMCE N.V., Genk, Belgium). The properties of the sea urchin spines (ρ: 1–1.5 g cm^{-3}, E: 5–20 GPa (depending on ϕ) and a Poisson's ratio of calcite of 0.322 [48]) restricted the sample geometry for RFDA testing to a minimum L/d ratio of ~4 (*H. mamillatus*)–8 (*H. trigonarius*). This limitation arises from the experimental setup, as the microphone cannot record frequencies above 50 kHz. Therefore, for UC segments the Young's Modulus could not be determined by RFDA prior to testing. All 3-point bending specimen were tested in the RFDA beforehand and additional segments were prepared ($n = 8$ for *H. mamillatus* and *H. trigonarius* respectively). From those segments cores were extracted afterwards with a core drill ($d = 5$ mm) and also measured. Core samples are advantageous because the geometry is well-defined and the measurement error becomes smaller (equations (8) and (9)). All samples were measured repeatedly ten times and the average of these measurements is reported here. Scatter of these ten measurements was, if present at all, negligible and lay well in the measurement error.

2.5. Statistical analysis

Data processing was carried out with the free software GNU R (V. 1.1.442) [53] with the additional packages *ggplot2* [54] for plotting, *car* [55], *psych* [56] and *rsq* [57] for statistical evaluation. Data were checked for normal distribution (Shapiro–Wilk test) and variance homogeneity (Levene test). For two groups with parametric data and no variance homogeneity a Welch t-test was carried out and for two groups with non-parametric data and no variance homogeneity Wilcoxon rank sum test was performed to test for statistically significant difference. For multiple groups with non-parametric data and no variance homogeneity a Kruskal–Wallis followed by pairwise Benjamini, Hochberg and Yekutieli p-adjusted Wilcoxon post hoc test was used.

3. Results

3.1. Structure of *H. mamillatus* and *H. trigonarius*

H. mamillatus and *H. trigonarius* are closely related and their spines share a common construction principle. Both are composed out of the porous, randomly ordered medulla (figures 3(g) and (h)) in the centre and followed by a succession of more ordered, radiating layers alternating with the characteristic, comparably dense GLs (figure 3). Their outer appearance is similar as well, the spines of *H. trigonarius* tend to be pointier than the blunt spines of *H. mamillatus* (figures 3(b) and (e)). The name *H. trigonarius* might be a bit misleading as it suggests a triangular cross section of the spines. This could not be verified by our observations. In contrast, the spines of *H. mamillatus* exhibited in many cases a more trigonal cross section than *H. trigonarius* (as for example in figures 3(a) and (d)). However, *H. trigonarius* spines always have a characteristic ridge running from base to tip, which was present on all spines (figure 3(b)).

From the typical cross sections in figures 3(a) and (d) it is evident, that *H. trigonarius* possesses more GLs than *H. mamillatus*. This is also underlined in

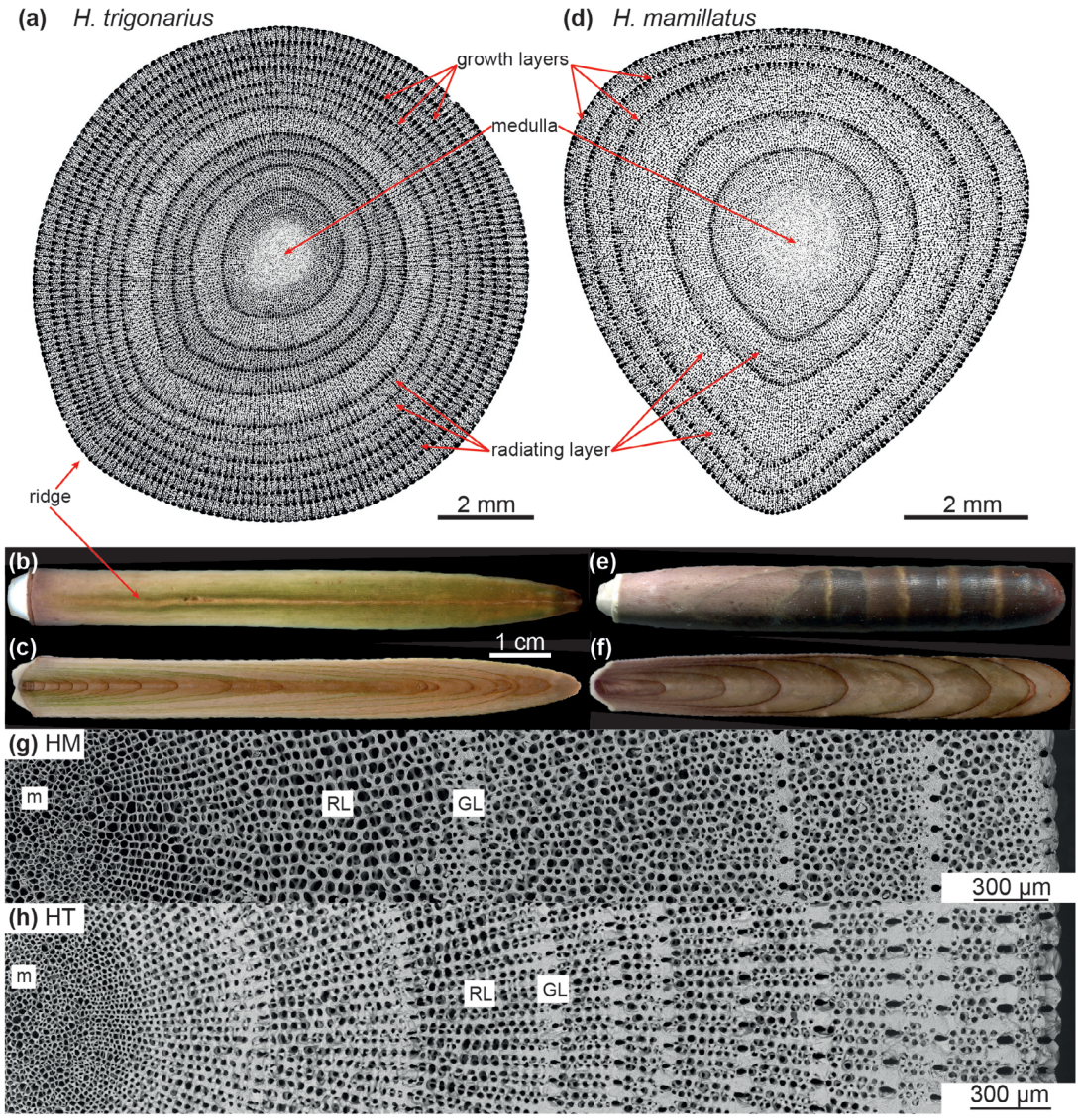

Figure 3. The spine structure of *H. trigonarius* (HT) (a)–(c) and *H. mamillatus* (HM) (d)–(f). (a) and (d) Are typical cross sections from 10% of the spine length (measured from base, dense stereom shown only). (b) and (e) Are representative spines of both species and (c) and (f) show longitudinal sections of these spines with the GLs well visible. *H. trigonarius* has a characteristic ridge on the spine surface (a) and (b). GLs are more abundant in *H. trigonarius* and spaced more tightly (a) and (c). (g) and (h) Are SEM pictures of *H. mamillatus* and *H. trigonarius* respectively, with the three stereom types medulla (m), radiating layers (RL) and GL from the centre of the spine (left) to the rim (right).

figure 4(a), where the number of all GLs from the bottom side of the segments tested in UC are shown (*H. mamillatus*: median = 3, IQR = 1.75, $n = 103$, *H. trigonarius*: median = 6, IQR = 3.75, $n = 41$) This difference is statistically significant (Wilcoxon rank-sum test, $W = 264$, $^{***}p \ll 0.001$). In longitudinal sections *H. trigonarius* reveals the same GL types as for *H. mamillatus* (cp. [29], figure S1 (stacks.iop.org/BB/14/016018/mmedia) (S = supplementary)). Besides the higher number of GLs, the more ordered, radiating building principle of *H. trigonarius* compared to *H. mamillatus* is discernible in figures 3(a), (b), (g) and (h). Both are composed out of the radial septa of the GLs and the radial trabeculae connecting these radial septa. In *H. trigonarius* this is more clearly expressed by the higher number of GLs and thicker radial septa compared to *H. mamillatus* (figures 3(a) and (d)) and it is especially well resolved in SEM pictures (figures 3(h) and (g)). This structure can be seen throughout the whole spine length of *H. trigonarius*, whereas it becomes very vague in spines of *H. mamillatus* close to the tip (figure S2).

The porosity of *H. trigonarius* spines is considerably lower than of *H. mamillatus*. The gravimetric characterization of all segments for the UC tests reveals a median porosity for *H. trigonarius* of 0.49 (interquartile range, IQR = 0.05, sample size, $n = 41$) and for *H. mamillatus* of 0.62 (IQR = 0.07, $n = 103$) (figure 4(b)). This is statistically significant (Welch t-test, $t = 19.919$, $df = 106.4$ $^{***}p \ll 0.001$). A representative *H. trigonarius* spine was selected for a detailed 2d porosity investigation and compared to the results of Lauer *et al* [29] for *H. mamillatus* (figure 4(c)). The overall lower porosity is firstly caused by a lower porosity in the radi-

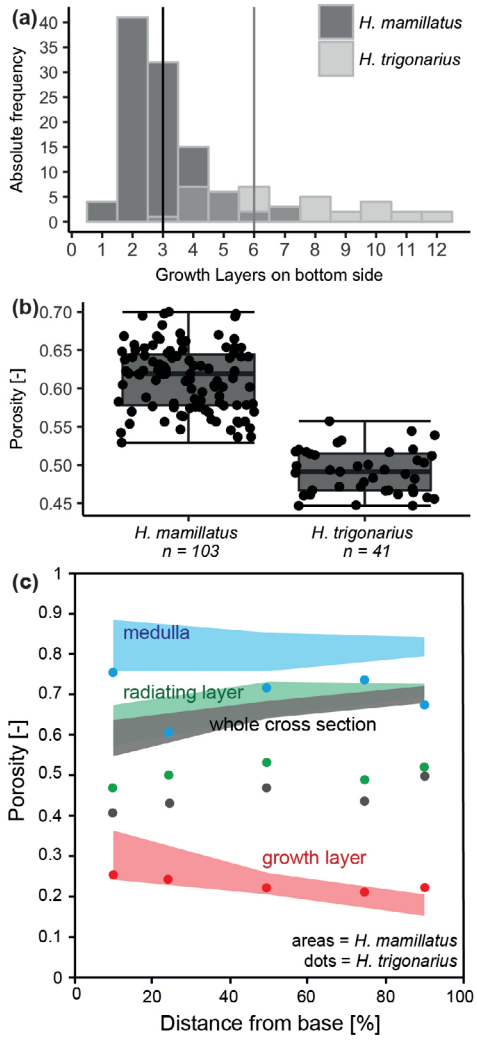

Figure 4. *H. trigonarius* has considerably more GLs than *H. mamillatus* (a). Lines indicate the median for each species. The segments of *H. mamillatus* have a significantly higher porosity than *H. trigonarius* (b). The lower porosity of *H. trigonarius* is caused by more dense GLs and by a generally lower porosity in the radiating layer and medulla (c) as the detailed 2d analysis of five cross sections extracted from a representative *H. trigonarius* spine shows (*H. mamillatus* data from [29]).

ating layer constituting the largest part of the spine. Secondly, the dense GLs, which have a comparable porosity as in *H. mamillatus*, are more abundant and make up a larger proportion of the spine's volume. And thirdly, the Medulla is less porous (figure 4(c)).

The following paragraphs will show how the lower porosity and slightly different structure influence the mechanical properties in comparison to *H. mamillatus*.

3.2. UC experiments

Figure 5 displays representative stress–strain curves of both species, showing that there are samples from both species, which fracture almost catastrophically or with graceful failure. However, the behaviours are by no means equally distributed.

H. trigonarius exhibits a significantly higher strength compared to *H. mamillatus* (Welch *t*-test, $t = -7.56$, $df = 60.74$, $^{***}p \ll 0.001$, see also figure 6(a)) but the graceful failure behaviour is, if present at all, very weak (figure 5(a)). Most segments of *H. trigonarius* show a ceramic like failure behaviour with an almost catastrophic failure (black curve, figure 5(a)). The pictures of the experiment show that the at point 3 the segment is internally completely destroyed and is fallen apart in point 4. The red curve (figure 5(a)) is one of the two *H. trigonarius'* curves from the total 41 experiments that showed a 'graceful-like' failure behaviour. Here, the segment stays intact to a strain of 0.2 (c). Then vertical fractures appear and the segment loses its capability to bear load (d).

H. mamillatus often shows a graceful failure behaviour. The red curve in figure 5(b) depicts an extraordinary segment (see also S6 and supporting videos), where the stress of the linear elastic increase was even surpassed during later stages of the experiment. This was observed rarely (4/103 experiments). All segments with an exceptional graceful failure behaviour shared the characteristics showed by the corresponding pictures of the red curve (figure 5(b)). Initial damage is localized at the top region (a) and is gradually spreading with the progress of the experiment, but the whole segment is never damaged (b) and (c). Stress drops occur because the cross section is reduced by spallation and not due to vertical cracks (c). Technically, the segments exhibit a much higher stress at these stages (c), however, it is difficult to assess the true extend of the cross section during the experiments (see also: 4.1). Vertical cracks occur at a late stage of these experiments (d). Not all segments of *H. mamillatus* show a graceful failure behaviour. The black curve (figure 5(b)) is representative for ceramic-like failure. As for *H. trigonarius*, the occurrence of vertical cracks leads to a rapid drop in load bearing abilities (2–3) and the segment becomes destroyed by displacement along these vertical cracks (3, 4).

3.3. Energy dissipation efficiency

To quantify the graceful failure behaviour γ (equation (3)) was calculated for all experiments with $\varepsilon \geqslant 0.37$. Figure 6(b) shows that the ability of dissipating energy is clearly a function of the porosity. For the comparably dense *H. trigonarius* only 24% of the experiments could be evaluated, as in all others the stress fell to zero before reaching $\varepsilon = 0.37$. For *H. mamillatus*, 71% of the experiments reached $\varepsilon = 0.37$ without complete failure. The maximum γ of *H. trigonarius*' segments is 0.18 with the majority well below 0.1 (figure 6(b)). In stark contrast the more porous *H. mamillatus*' segments have a maximum γ of 0.72 and many above 0.4. This considerable difference in γ is partly attributed to the way of calculating this measure (equation (3)). As the plateau strength is divided by the maximum strength, the stronger *H. trigonarius* will have automatically a lower γ when having the same plateau strength as *H. mamillatus*. As can be seen in figure 6(b), the higher the strength of the segment, the

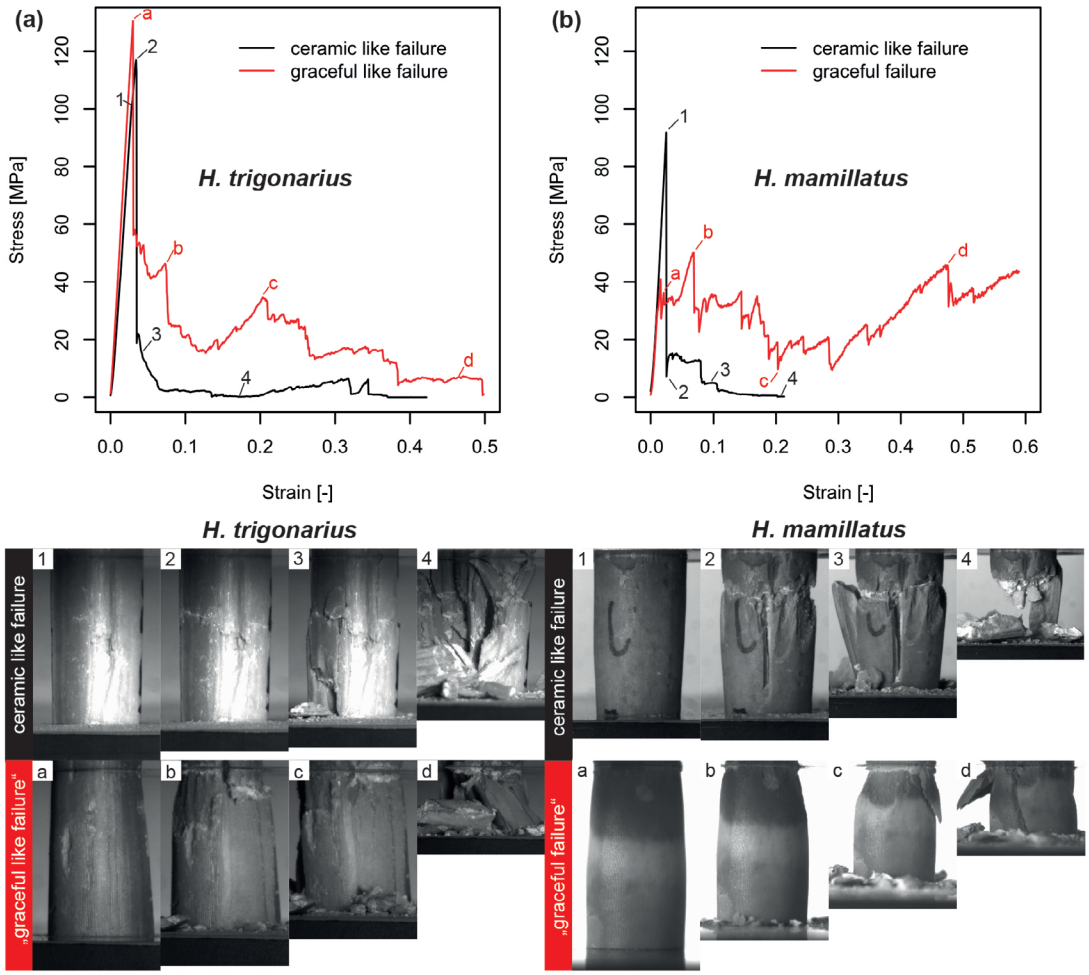

Figure 5. Representative stress–strain curves of UC experiments of *H. trigonarius* (a) and *H. mamillatus* (b). For both species a ceramic like failure (black) and the desirable graceful failure (red) is shown. Important points of the stress strain curves are shown by the pictures below (numbers: ceramic like failure, letters: graceful failure). For videos of UC experiments the reader is referred to the electronic supplementary material.

higher the likelihood of a low γ. However, as figure 6(c) shows, *H. mamillatus* has also a significantly higher plateau strength (Wilcoxon rank-sum test $W = 264$, $^{***}p \ll 0.001$) than *H. trigonarius*. So the lower γ has two reasons.

As reported by [37] the permanent GLs have a significant impact on the strength of *H. mamillatus* segments. Figure S3(A) highlights that samples with comparable porosity but with more permanent GLs are more likely to have a higher strength than their counterpart with only one permanent GL. No such correlation could be found for the segments of *H. trigonarius* (supplementary: figure S3(B)). Figures 6(d) and (e) investigate the relation between γ and the number of finishing GLs (figure 6(d)) and permanent GLs (figure 6(e)). There is no benefit from more GLs finishing in a segment in terms of γ as it remains unchanged (Kruskal–Wallis rank sum test, $\chi^2 = 1.39$, $df = 3$, $p > 0.05$) (figure 6(d)). Permanent GLs do influence γ (figure 6(e)), however, not significantly (Kruskal–Wallis rank sum test followed by Pairwise Benjamini, Hochberg and Yekutieli p-adjusted Wilcoxon post hoc test, $p = 0.056$). This changes when all experiments (not only those with $\varepsilon \geqslant 0.37$) are considered (figure S4(b)), with significant differences between groups with 1 permanent GL and 2 permanent GLs (**), 1 permanent GL and 3 permanent GLs (*), 1 permanent GL and 4 permanent GLs (***), 2 permanent GLs and 4 permanent GLs (*) and 3 permanent GLs and 4 permanent GLs (*) (Kruskal–Wallis rank sum test followed by pairwise Benjamini, Hochberg and Yekutieli p-adjusted Wilcoxon post hoc test). Segments with only 1 permanent GL exhibit the highest occurring γ and there is a decrease towards those with many permanent GLs. Within a single group, segments with a higher porosity are more likely to have a higher γ than segments with a low porosity (figures 6(e) and S4(b)).

3.4. 3-point bending tests

No displacement was visible by the naked eye in all 10 3-point bending experiments, although the recorded cross head movement was in the order of 200–500 μm. Examination of the bending specimen revealed considerable imprint marks of the loading rollers in the stereom of the spine segments. The dense outer GL was pressed by the loading roller into the

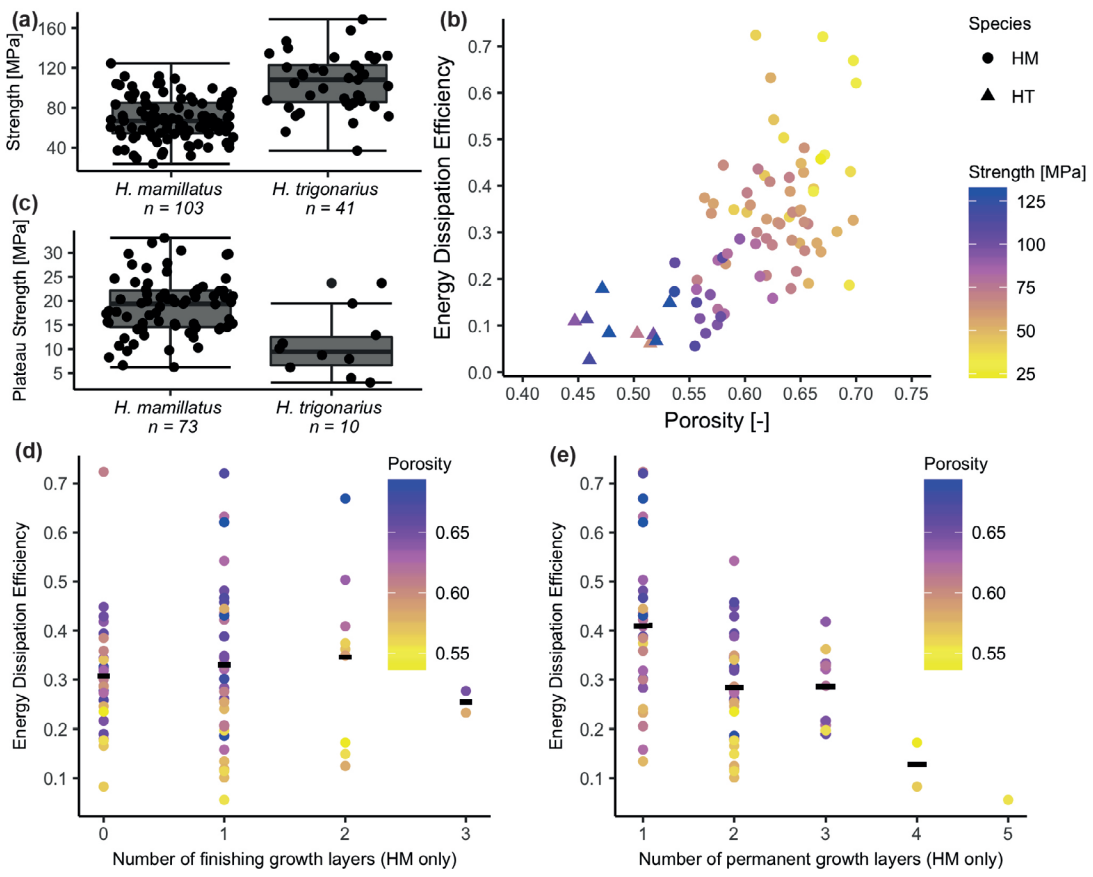

Figure 6. *H. trigonarius* has a significantly higher strength than *H. mamillatus* (a) but also a significantly lower plateau strength than *H. mamillatus* (c). Samples with a high energy dissipation efficiency (γ) tend to have a lower strength (b). (b) and (c) show that *H. trigonarius* lacks the ability for dissipating energy effectively (only 10 samples withstood load until $\varepsilon > 0.37$). No relationship between finishing GLs and γ (d) was found for *H. mamillatus*. On the contrary: the more permanent GLs, the lower γ (e). Black lines in (d) and (e) represent the average of each group. Error bars are not displayed in plots as all γ values represent minima (4.1). Abbreviations: HM: *H. mamillatus*, HT: *H. trigonarius*.

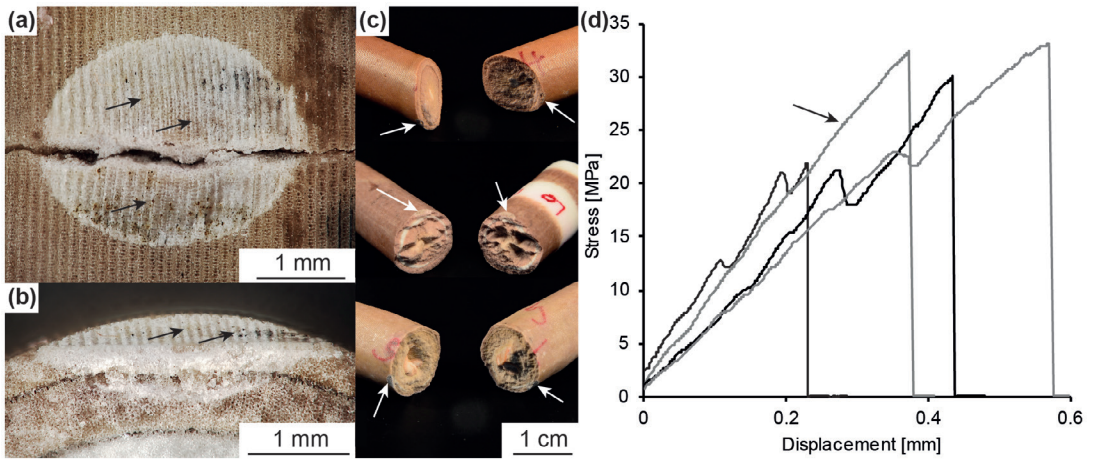

Figure 7. Deepest central imprint of all 3-point bending specimen (top view: (a), side view: (b)), representative fracture surfaces of 3-point bending specimen (c) and representative stress displacement curves of 3-point bending experiments (d). The structure of the GL ribs is even preserved in the imprint (arrows, (a) and (b)). The arrows in (c) indicate the imprint of the central loading roller. Only the stress-displacement curve indicated by arrow has a linear increase until fracture (d). Other samples experienced minor drops in the stress level by different magnitudes and their recovery.

compliant stereom underneath (figures 7(a) and (b)). The imprint below the inner loading roller was the deepest with 95–300 μm compared to the two outer rollers (30–140 μm). For strength calculations, all displacement measurements were corrected for the depth of the imprint by subtracting the imprint of the inner roller and the average of the two imprints of the outer rollers from the recorded displacement. The

Table 1. Young's Modulus determination with different methods. For RFDA flexural (regular font) and longitudinal (italics) measurements are listed. All specimen measured longitudinally could also be measured flexurally. Abbreviations: as in figure 6, IQR = interquartile range, PI = *Phyllacanthus imperialis*.

			Young's Modulus [GPa]		
Method	Species (*n*)	Porosity [−] range	Range	Median	IQR
UC	HT (41)	0.45–0.56	6.4–18.8	14.1	3.2
	HM (94)	0.53–0.70	5.1–14.2	9.3	2.7
3-point bending	HM (7)	0.58–0.65	6.6–16.5	10.6	—
RFDA (whole segments)	HT (8, *2*)	0.45–0.53	15.9–24.4	19.2	3.6
		0.46	*19.0–19.1*	*19.05*	—
	HM (18, *14*)	0.55–0.65	10.5–15.9	12.9	2.8
		0.55–0.65	*9.4–13.5*	*10.8*	*2.6*
RFDA (drilled cores)	HT (8, *1*)	0.41–0.53	15–23.3	17	3.0
		0.45	*19.6*	—	—
	HM (6, *6*)	0.6–0.73	5.3–8.6	6.9	1.4
		0.6–0.73	*5.6–8.1*	*6.8*	*1.2*
	PI (11, *11*)	0.64–0.77	3.8–9.8	5.1	1.5
		0.64–0.77	*3.6–9.3*	*4.9*	*1.6*

depth of the imprints was determined geometrically by using Pythagoras theorem (figure S5) as direct optical measurement of the imprint's depth was difficult.

In all 10 experiments the fracture ran through the central loading point and in 6 experiments the crack ran directly vertical through the segment. Only in 1 experiment the crack path deviated considerably from the vertical and was curved (figure 7(c)). The fracture surface was often rough (figure 7(c)). Maximum load ranged from 234 to 602 N (median = 353 N) and the 3-point bending stress was 22 to 33 MPa (median = 30 MPa). In 7 of 10 experiments sudden small stress drops are visible during the linear elastic increase (figure 7(d)). These drops might be attributed to pronounced imprinting of the loading rollers. Three experiments showed a linear elastic increase without a pressure drop (figure 7(d), highlighted by arrow).

3.5. Young's Modulus determination

E was determined by three methods in this study: UC, 3-point bending and RFDA. A summary alongside with the porosity range of the samples is given in table 1. From table 1 alone it is obvious that the *E* obtained by 3-point bending scatters considerably, although the porosity range is comparably narrow indicating difficulties with this method. RFDA measurements give consistently higher Young's Moduli than the UC at a similar porosity range.

The restricted sample sizes for RFDA measurements, especially for the longitudinal ones, arise from the difficulty to obtain long enough samples that were still reasonably round. *H. trigonarius* cores were more difficult to obtain by core drilling, because the higher density of the samples made them more prone to fracture during the drilling process. To enlarge the sample size range, cores of *Phyllacanthus imperialis* were also measured. These spines are fairly round and have a high overall internal porosity, which makes them easy to process. Details are given elsewhere [17, 38]. Representative RFDA samples (segments and cores) are displayed in figure 8(b).

Figure 8(a) (UC) and figure 8(c) (RFDA) show the Young's Moduli compared to variants of the model of Pabst and Gregorová (2014) (equation (5)). As all spines of the three different species investigated consist of biogenic Mg-Calcite, it is reasonable to assume that they have a very similar *E* and thus they are all displayed together. Two different Young's Moduli have been considered as calcite is an anisotropic material (72 GPa || c, 88 GPa ⊥ c [58]) and Eshelby–Wu coefficients (EW) of 2 and 2.3, which reflect well the dominant pore shapes from spherical to columnar. Young's Moduli obtained by UC follow the predictions of the model (E_0 = 72 GPa and EW = 2, 2.3, black lines) well at lower and intermediate porosities (~0.7–0.55), but especially *H. trigonarius* deviates from the model considerably towards lower Young's Moduli. The model with a higher *E* (grey lines) seems only to apply, if at all, at low porosities (>0.6). Young's moduli measured by RFDA (flexural, ⊥ c) all lie in the expected range of the models, although *E* of 88 GPa seems also a bit too high for satisfactorily fitting. Examination of the anisotropy of biogenic sea urchin calcite was done by comparing flexural (⊥c) and longitudinal (||c) RFDA measurements of the same specimen (figure 8(d)). Full segments seem to exhibit an anisotropy as described for geological calcite with the flexural *E* being ~15% higher than the longitudinal Modulus. This could not be found for cores obtained by drilling out of the same segments. Their ratio of flexural and longitudinal *E* is close to 1 (m = 0.96). It becomes obvious from figures 8(c) and (d) that a well-defined geometry such as cylinders (obtained by core drilling) reduce the error of RFDA measurements considerably.

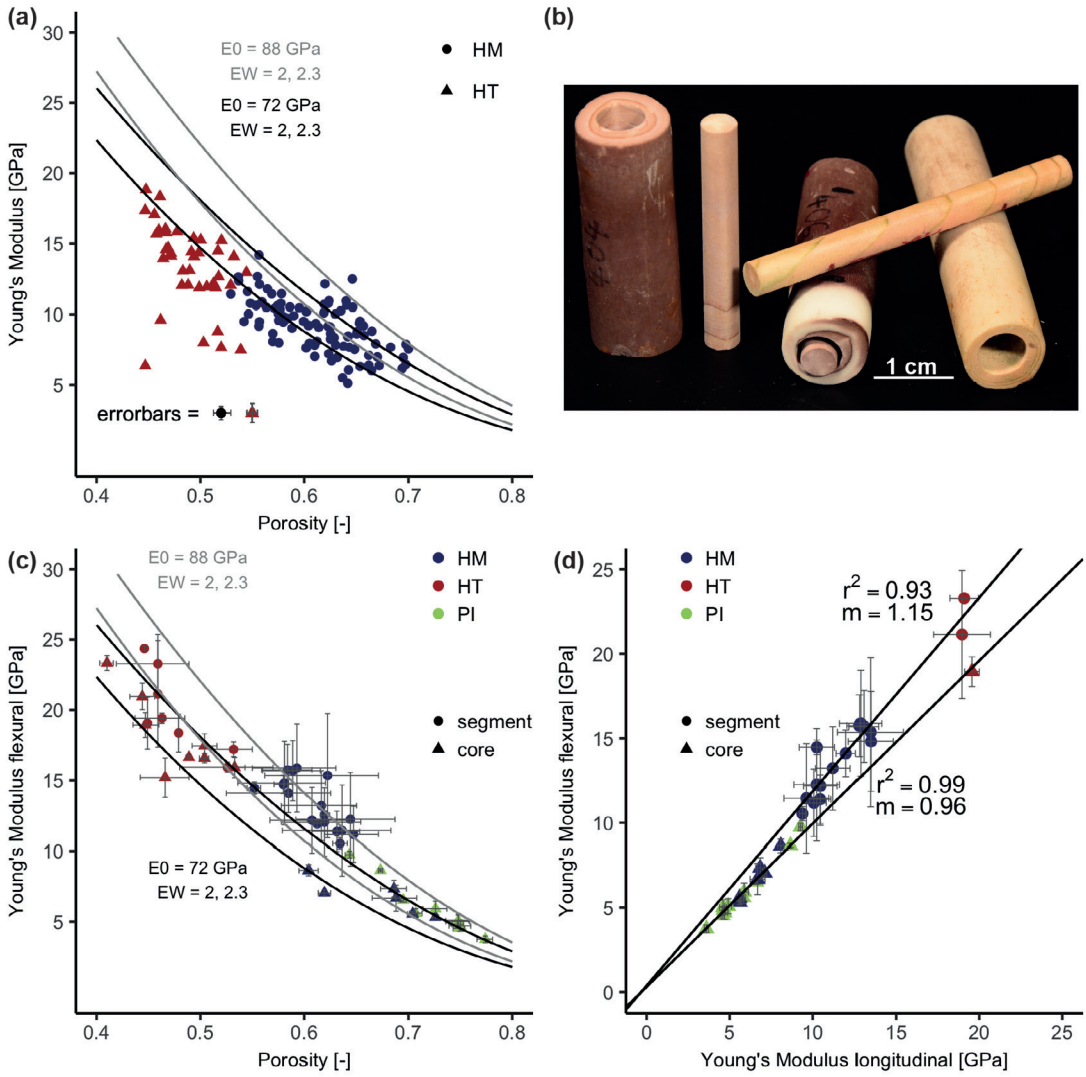

Figure 8. Young's Modulus (E) measurements with UC (a), resonance frequency damping analysis (RFDA) flexural (c) and RFDA comparison between flexural and longitudinal mode (d) of full segments and drilled cores. (b) shows representative specimen used for RFDA measurements. Cores were obtained after segments were measured. Data in (a) and (c) are compared to (equation (5)) with Eshelby–Wu coefficient (EW) of 2 and 2.3 and Young's moduli of 72 GPa (black curves) and 88 GPa (grey curves) for Young's moduli parallel and perpendicular (c), respectively. The lower of each two curves corresponds to EW = 2.3. The circled data dot in (a) is referencing to figure 10.

4. Discussion

4.1. Interplay of mechanical properties and structure

The Young's Modulus can be successfully modelled with the Papst–Gregorová formalism [47], which is a modification of the open cell model by [46] incorporating a model for pore shape. However, difficulties in the E determination with each method arose and they are discussed in 4.2.

Strength is clearly a function of porosity, as the less porous spines of *H. trigonarius* have a significantly higher strength than more porous *H. mamillatus* spines (figure 6(a)). With the increase in strength, the ability to dissipate energy effectively is gradually lost. In most cases spines of *H. trigonarius* showed a catastrophic failure behaviour with a very low plateau strength, if present at all. This results in a low energy dissipation efficiency with only 2 of 41 segments exceeding $\gamma = 0.1$ considerably.

Consequently, there seems to be a transition porosity of 0.55–0.6 (figure 6(b)), which needs to be exceeded for exhibiting 'graceful failure behaviour' (=showing a plateau strength) and thus the ability to dissipate energy after the linear elastic increase. This value is close but slightly lower than the definition of cellular materials with $\phi = 0.7$ [59, 60], which generally exhibit a plateau strength and are effective in dissipating energy [39, 61], but is in accordance with [62–64]. Therefore, *H. trigonarius* spines are not suitable for this purpose, although they share the same building principle with *H. mamillatus* (figure 3) and have

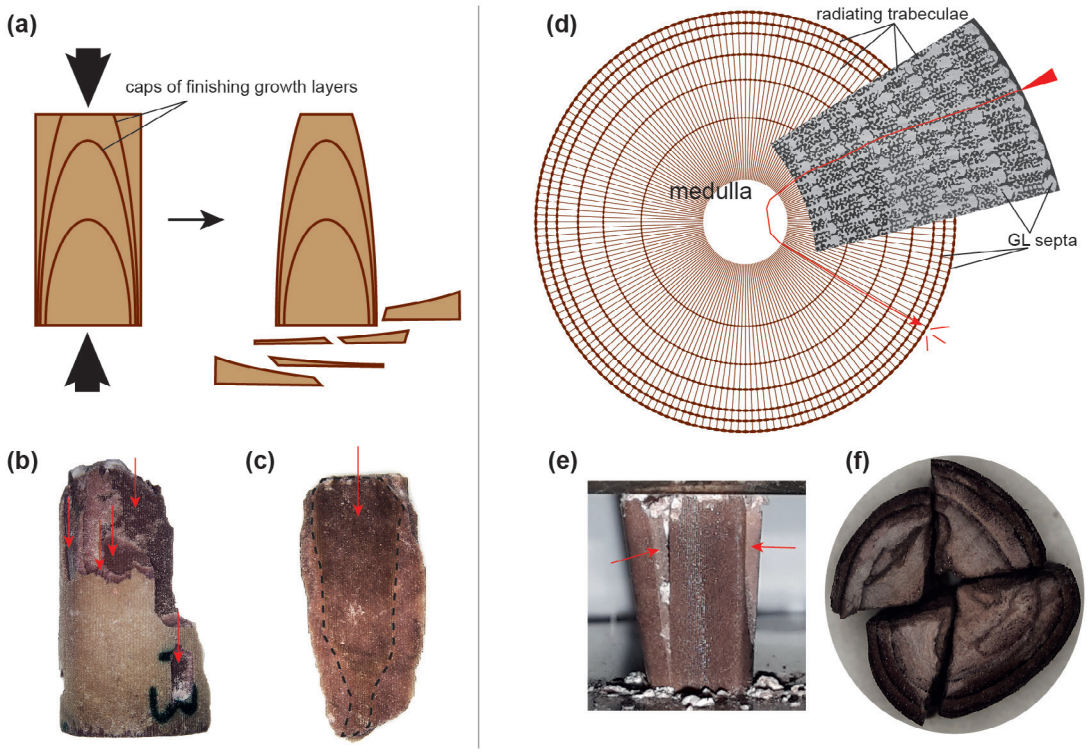

Figure 9. Fracture mechanisms along structural weaknesses: GL caps in schematic longitudinal section (a) and with corresponding flakes (b) and (c). Weak zones between two wedges of a schematic segment in cross section (d) and the resulting flakes (e) and (f). In both cases, cracks are guided by the structural weakness from the large density contrasts. Arrows in (c) and (d) highlight the fracture surface along internal GLs and the dotted line outlines the fracture surface exactly along a GL (d). Resulting crack patterns along wedges are shown during (e) and after the experiment (f) (not the same segment).

even more GLs (alternating porosity), that were identified as crucial for 'graceful failure' [17, 18]. Spines of *H. trigonarius* are simply too dense.

On the other hand not all of the more porous *H. mamillatus* (usually $\phi > 0.58$) spines can dissipate energy as good as described in [17]. This is attributed to the large differences in structure and porosity present in spines of this species. It could be shown that segments with only one permanent GL and high porosity are the most likely ones to dissipate energy effectively (figures 6(b) and (e)). All segments with $\gamma > 0.6$ share this building principle. In contrast to the findings of [17] a beneficial effect of finishing GLs on the failure behaviour in terms of γ could not be found (figure 6(d)).

A high γ can only be reached, when large parts of the segment stay intact over the whole compression test and spallation of large flakes does not occur. Besides exceeding the transition porosity of approx. 0.55–0.6, it is important that no predominant structural weaknesses are located in the spine structure that enable large parts of the segment to be spalled easily. If so, only remnants of the segment continue to carry on load and dissipate energy, leading to a drop in the calculated engineering stress and thus γ.

Such predominant weak spots are large porosity contrasts in the structure as GL caps [17, 38], but also the porous meshwork between two 'wedges' of the radiating building [29]. Figure 9 highlights schematically the cracking mechanism likely to be induced by GL caps (figures 9(a)–(c)) and by wedges (figures 9(d)–(f)) alongside with representative micrographs of spalled flakes. It is clear that both mechanisms are likely to induce longitudinal cracks. They are fatal in terms of γ as the segment falls apart easily (figures 5(a)4, (b)2–4 and 9(e), see also supporting videos and S6). In contrast, a sea urchin spine is optimised for dissipating energy when it has a foam like internal stereom structure combined with a high porosity. Spines with fewer GLs are of this type [29] and typically occur in regions close to the tip of *H. mamillatus* spines (figure S1). The five segments with $\gamma > 0.6$ are all from this region, where the internal structure becomes foam like underlining this hypothesis.

However, not all spine segments with a high porosity, only one permanent GL and a foam like stereom structure yielded good energy dissipation levels. In those cases rather random cracks with no obvious microstructural cause were observed. This is often attributed to non-uniform loading of irregular sample geometries. For example, a segment that is loaded at non-coplanar faces will have local excess stresses near the contact region and these are likely to give rise to the spallation of flakes (figure 10(a)). This makes clear, that all γ for *Heterocentrotus* are only minima as the true energy dissipation potential can only be reached when no spallation occurs and leads directly to the question whether unconfined UC testing is the

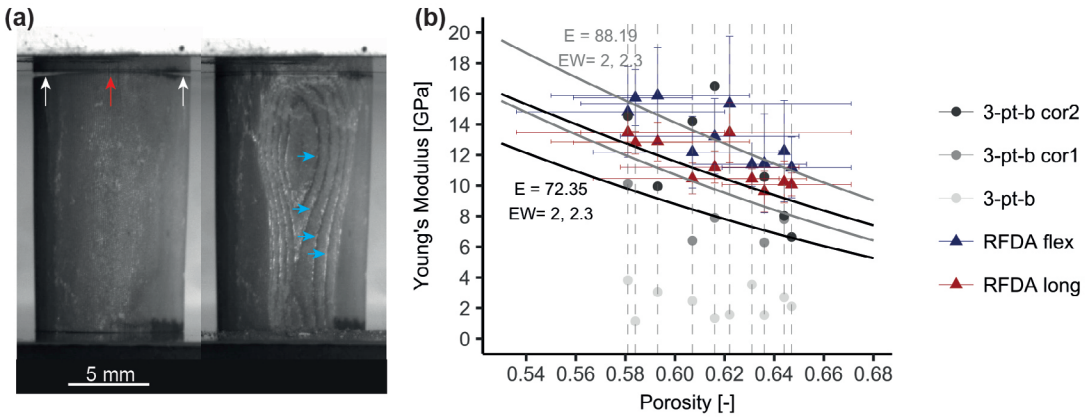

Figure 10. Segment with non-parallel surfaces (deviation $> 50\ \mu$m) experiences load (a). Red arrow indicates contact of segment with compression die, whereas other parts of the segment are not in contact with the die (white arrows). The resulting fracture pattern is strongly influenced by the inclination underlining that fracture is no longer controlled by structural weaknesses, such as GLs (blue arrows). The computed Young's Modulus (E) of this segment is too low (encircled in figure 8(a)). (b) shows how different corrections affect the E obtained by 3-point bending (3-pt-b: as measured, 3-pt-b cor1: imprints were subtracted from deflection, 3-pt-b cor2: imprints and stress drops subtracted from deflection) and is compared to the more reliable resonance frequency damping analysis (RFDA) measurements of the same samples. Dotted lines connect measurements of the same samples. Solid lines are computed with (equation (5)).

ideal method to assess the γ of brittle materials. Spallation of flakes occurs rarely for plastic materials such as metal or polymeric foams. This is why brittle materials perform poorly when compared to metal or polymeric foams, which often exceed $\gamma = 0.8$ [42]. We will discuss the details elsewhere (Lauer *et al*, in prep).

4.2. The determination of Young's Modulus

Difficulties arising for E determination are common for most natural materials. They rarely come in a well-defined geometry and the preparation of specimens for mechanical testing according to standard testing procedures is often not possible or not reasonable as sectioning to the required geometry may destroy the hierarchical organization of the natural material, which is responsible for the mechanical properties. In our case the spines of *H. trigonarius* and *H. mamillatus* are round in first approximation, which is an advantage for testing. However, the standards for bending, UC and RFDA require a much better perfection in geometry.

The three methods used for E determination yielded a considerable scatter in E that cannot be explained by fluctuating porosity alone (table 1). RFDA proved to be a simple and effective method to determine E. Although the sample geometry should be as precise as possible as (length enters cubed and diameter even to the forth (equation (8)) for flexural mode and both are squared in longitudinal mode (in K_2 in (equation (9))) all measurements lie in the expected range by the model of Pabst and Gregorová [47], even if sample geometry was comparably unprecise. Core drilling of the segments yields minimized measurement error (figure 8(c)). The tested samples spanned porosities from 0.41 to 0.78 and all measurements are in accordance with (equation (5)) with EW of 2–2.3, highlighting that a spherical to columnar pore shape is predominant [47]. Besides simple and fast measurement RFDA measurements are non-destructive and results reproducible.

E obtained by UC scatter noticeably (figure 8(a)). However, for $\phi = 0.6$–0.7 the results are reasonable and only few deviate considerably from (equation (5)) with EW 2–2.3. At lower porosities, especially for *H. trigonarius*, a deviation of EW > 2.3 can be seen in the data. This is also attributed to unprecise sample geometry. The local stresses of non-coplanar cross sections differ from the engineering stresses calculated and hence may cause systematic errors in the determination of E [49, 65, 66]. Furthermore, if only a fraction of the whole segment carries the load, the slope of the linear elastic increase is not as steep as if the whole cross section would bear the load, which leads to additional errors in E determination [66]. Figure 10(a) shows a non-coplanar segment (deviation $> 50\ \mu$m) of *H. trigonarius* and how this affects load bearing capacity and fracture behavior. The calculated E is encircled in figure 8(a) with its considerable deviation from the expected range. This underlines that only near-perfect to coplanar segments should be taken for E determination by UC.

3-point bending proved to be the least suitable method for determining E. The main shortcoming here is the imprinting of the loading rollers in the compliant sea urchin stereom. In order to obtain the correct deflection, the imprints need to be subtracted from the recorded displacement. Additionally, as figure 7(d) shows, most stress-displacement curves show stress drops that need to be corrected as well. Exact correlation of stress and strain is thus not possible anymore. Figure 10(b) depicts the E obtained after each correction step alongside with the Young's Moduli obtained by RFDA measurements prior to 3-point bending. The so obtained values for E scatter substantially. For the

same segment that measured 2 GPa without any correction of the stress–strain curve, 18 GPa were reached after correction of stress drops and imprints, well exceeding predictions by (equation (5)) and RFDA measurements of the same segment (figure 10(b)). The Young's Moduli obtained by Großmann and Nebelsick [28] for *H. mamillatus* in 3-point bending tests were probably not corrected for imprints and are thus much too low with 2–4 GPa. Although after correction some values are in reasonable agreement with (equation (5)) and RFDA measurements, uncertainties remain high and 3-point bending tests surely provide no reliable Young's Moduli for sea urchin spines.

4.3. Young's Modulus and strength of biogenic calcite

Gibson *et al* [67] give an E of 77–79 GPa for biogenic calcite, Broz *et al* [68] give 78.1 ± 5.2 GPa for geological calcite and Presser *et al* [69] gives 76.6 ± 1.9 GPa. All values are in broad agreement with our measurements when using them as E_0.

Compressive strength for the sea urchin spines ranges from 24 to 169 MPa, depending on porosity ($\phi = 0.44$–0.7) and flaw size distribution [70, 71]. It is possible to extrapolate our strength data obtained from porous spines to dense material with (equation (5)) by substituting E and E_0 by σ and σ_0 (strength of dense material). However, a fit for both dense material property and Eshelby–Wu factor is very sensitive to small changes and creates large error margins. Compressive strength for dense calcite is unknown due to the perfect cleavage of geological calcite. As biogenic calcite lacks the cleavage [2], EW was assumed to range in between 2–2.3, as found for E. This gives a σ_0 of 440–570 MPa for biogenic calcite. It should be noted that it is not clear, whether the critical stress to be used for the modelling with (equation (5)) should be a compressive stress, because in pores shearing or tensile stressing could be the real stress for fracturing. The bending strength of *H. mamillatus* is not 1/10 as expected from dense brittle materials [59] but closer to 1/2, underlining this hypothesis.

4.4. Biological implications

The high porosity of the spines of *Heterocentrotus* is advantageous, as this way the unusual large and heavy spines of this echinoid in relation to body size [72] are comparable to the density of water and are not a burden to carry [29]. However, the porosity of echinoderm calcite may not only serve weight reduction but has also other functional reasons such as muscle insertion or the interaction with collagen fibres [6]. Whether this is the case for *Heterocentrotus* is unknown. The porosity in the first place also arises from the formation of this biological material. It is laid down as ACC (e.g. [12, 13] and then subsequently crystallises to calcite. As hydrous ACC has a significantly lower density than calcite [73] volume is freed in this transformation [14].

The high porosity of the spines of *Heterocentrotus* is combined with a core–shell construction, which provides more stiffness than a uniformly distributed porosity [35, 36]. This core–shell construction can be very pronounced when many GLs are present close to the spine's rim making breaking and fracturing spines more difficult for e.g. predators.

The ability to dissipate energy effectively is likely a side effect from the porous, foam-like structure as *H. mamillatus* does not exploit this ability in its habitat. There, spines are unlikely loaded in pure compressive mode and even if, before the spines would fail gracefully, the sea urchin test would probably fracture under the transferred load, as it is much thinner than the thick spines. The large spines are mainly used for keeping predators at distance and wedging into reef cavities for protection.

5. Conclusions

(1) The spines of the closely related species *H. trigonarius* and *H. mamillatus* show a common building principle with GLs, radiating layers and medulla. The spines of *H. trigonarius* have a more evolved radiating structure.
(2) Resonance frequency damping analysis seems is the most suitable method for measuring the Young's modulus of the spines and is a promising method for other biological materials. UC and 3-point bending were in case of the sea urchin spines more susceptible to inaccurate sample geometries and measurement constraints.
(3) Spines of *H. trigonarius* are significantly denser than spines of *H. mamillatus* and thus have a higher Young's Modulus, a higher compressive strength and a lower energy dissipation efficiency.
(4) The model of Pabst and Gregorová [47] is well suited to model the Young's Modulus in dependence of the porosity of these two sea urchin spines. The Eshelby–Wu coefficient of 2–2.3 indicates that the predominant pore shape is a spherical to columnar, which is in accordance with the pore shape found in SEM micrographs and with literature [28].
(5) In terms of energy dissipation efficiency of the sea urchin spines, a threshold porosity of ~0.55–0.6 needs to be exceeded to show a foam like failure behaviour. This is why most of the denser spines of *H. trigonarius* show no foam-like or graceful failure.
(6) Spines with simple core–shell structure and an overall porosity of 0.65–0.7 proved to be the most effective energy dissipaters in this study. Spines with many permanent GLs

pronouncing the shell are not suitable for this purpose.

(7) Spines predominantly crack along two structural weaknesses: the GLs [17] and even more so, the porous meshwork between two wedges of the radiating building principle.

(8) The ability to dissipate energy is a side effect from the porous structure and it is very likely irrelevant to *Heterocentrotus*' life style.

Acknowledgments

The authors thank the German Research Foundation (DFG-Deutsche Forschungsgemeinschaft) for funding this work within the framework of the Collaborative Research Centre (SFB/Transregio) 141 'Biological Design and Integrative Structures', project B01. We also thank Barbara Maier and Simone Schafflick in the workshop for their support with sample preparation. We are grateful for Willi Pabst's advice for longitudinal RFDA measurements and Tobias B Grun's help for statistical testing. We thank two anonymous reviewers for their valuable remarks and comments, which helped to improve the quality of the manuscript.

Ethical statements

Potential conflict of interests

The authors declare that they have no conflict of interest.

Statements on the welfare of animals

The sea urchins were purchased dead from a fossils collector, were not killed for the purpose of this study and are not on listed as endangered species.

ORCID iDs

Christoph Lauer https://orcid.org/0000-0002-3283-7759

References

[1] Raup D M 1959 Crystallography of echinoid calcite *J. Geol.* **67** 661–74
[2] Towe K M 1967 Echinoderm calcite: single crystal or polycrystalline aggregate *Science* **157** 1048–50
[3] Nissen H U 1969 Crystal orientation and plate structure in echinoid skeletal units *Science* **166** 1150–2
[4] Hesse E 1900 *Die Mikrostruktur der fossilen Echinoidenstacheln und deren systematische Bedeutung* (Suttgart: E. Schweizertbart'sche Verlagshandlung)
[5] Deutler F 1926 *Das Wachstum des Seeigelskeletts* (Jena: Verlag von Gustav Fischer)
[6] Smith A 1980 Stereom microstructures of the echinoid test *Spec. Pap. Palaeontol.* **25** 1–81
[7] Clarke F W and Wheeler W C 1915 The inorganic constituents of echinoderms *United States Geological Survey Professional Paper* **90** 191–6
[8] Goldsmith J R, Graf D L and Joensuu O I 1955 The occurence of magnesian calcies in nature *Geochim. Cosmochim. Acta* **7** 212–30
[9] Weber J N 1969 The incorporation of magnesium into the skeletal calcites of echinoderms *Am. J. Sci.* **267** 537–66
[10] Beniash E, Aizenberg J, Addadi L and Weiner S 1997 Amorphous calcium carbonate transforms into calcite during sea urchin larval spicule growth *Proc. R. Soc.* B **264** 461–5
[11] Levi-Kalisman Y, Raz S, Weiner S, Addadi L and Sagi I 2002 Structural differences between biogenic amorphous calcium carbonate phases using x-ray *Absorpt. Spectrosc. Adv. Funct. Mater.* **12** 43–8
[12] Aizenberg J, Lambert G, Weiner S and Addadi L 2002 Factors involved in the formation of amorphous and crystalline calcium carbonate: a study of an ascidian skeleton *J. Am. Chem. Soc.* **124** 32–9
[13] Politi Y, Arad T, Klein E, Weiner S and Addadi L 2004 Sea urchin spine calcite forms via a transient amorphous calcium carbonate phase *Science* **306** 1161–4
[14] Seto J *et al* 2012 Structure-property relationships of a biological mesocrystal in the adult sea urchin spine *Proc. Natl Acad. Sci. USA* **109** 3699–704
[15] Albéric M *et al* 2018 Interplay between calcite, amorphous calcium carbonate, and intracrystalline organics in sea urchin skeletal elements *Cryst. Growth Des.* **18** 2189–201
[16] Vecchio K S, Zhang X, Massie J B, Wang M and Kim C W 2007 Conversion of sea urchin spines to Mg-substituted tricalcium phosphate for bone implants *Acta Biomater.* **3** 785–93
[17] Presser V, Schultheiß S, Berthold C and Nickel K G 2009 Sea urchin spines as a model-system for permeable, light-weight ceramics with graceful failure behavior. Part I. Mechanical behavior of sea urchin spines under compression *J. Bionic Eng.* **6** 203–13
[18] Presser V, Kohler C, Zivcova Z, Berthold C, Nickel K G, Schultheiß S, Gregorova E and Pabst W 2009 Sea urchin spines as a model-system for permeable, light-weight ceramics with graceful failure behavior. Part II. Mechanical behavior of sea urchin spine inspired porous aluminum oxide ceramics under compression *J. Bionic Eng.* **6** 357–64
[19] Toader N, Sobek W and Nickel K G 2017 Energy absorption in functionally graded concrete bioinspired by sea urchin spines *J. Bionic Eng.* **14** 369–78
[20] Cao L *et al* 2017 Lightweight open-cell scaffolds from sea urchin spines with superior material properties for bone defect repair *ACS Appl. Mater. Interfaces* **9** 9862–70
[21] Grun T B and Nebelsick J H 2018 Structural design of the minute clypeasteroid echinoid Echinocyamus pusillus *R. Soc. Open Sci.* **5** 171323
[22] Grun T B, von Scheven M, Bischoff M and Nebelsick J H 2018 Structural stress response of segmented natural shells: a numerical case study on the clypeasteroid echinoid Echinocyamus pusillus *J. R. Soc. Interface* **15** 20180164
[23] Weber J N, White E W and Lebiedzik J 1971 New porous biomaterials by replication of echinoderm skeletal microstructures *Nature* **233** 337–9
[24] Weber J, Greer R, Voight B, White E and Roy R 1969 Unusual strength properties of echinoderm calcite related to structure *J. Ultrastruct. Res.* **26** 355–66
[25] Nickel K G, Klang K, Lauer C and Buck G 2017 *Sea Urchin Spines as Role Models for Biological Design and Integrative Structures* (Berlin: De Gruyter)
[26] Weber J N 1969 Origin of concentric banding in the spines of the tropical echinoid *Heterocentrotus Pac. Sci.* **23** 452–66
[27] Ebert T A 1988 Growth, regeneration, and damage repair of spines of the slate-pencil sea urchin *Heterocentrotus Mammillatus Pac. Sci.* **42** 160–72
[28] Grossmann J N and Nebelsick J H 2013 Comparative morphological and structural analysis of selected cidaroid and camarodont sea urchin spines *Zoomorphology* **132** 301–15
[29] Lauer C, Grun T B, Zutterkirch I, Jemmali R, Nebelsick J H and Nickel K G 2017 Morphology and porosity of the spines of the sea urchin *Heterocentrotus mamillatus* and their implications on the mechanical performance *Zoomorphology* **137** 137–54
[30] Vevers H G 1966 *Pigmentation* (New York: Interscience)

[31] Pearse J S and Pearse V B 1975 Grwoth zones in the echinoid skeleton *Am. Zool.* **15** 731–53
[32] Ebert T A 1986 A new theory to explain the origin of growth lines in sea urchin spines *Marine Ecol.* **34** 197–9
[33] Dotan A and Fishelson L 1984 Morphology of spines of *Heterocentrotus mammillatus* (Echinodermata, Echinoidae) and its ecological significance *5th Int. Echinoderm Conf.*
[34] Dotan A 1990 Population structure of the echinoid *Heterocentrotus mammillatus* (L.) along the littoral zone of the South-Estern Sinai *Coral Reefs* **9** 75–80
[35] Gibson L J 2005 Biomechanics of cellular solids *J. Biomech.* **38** 377–99
[36] Dawson M A and Gibson L J 2007 Optimization of cylindrical shells with compliant cores *Int. J. Solids Struct.* **44** 1145–60
[37] Lauer C, Schmier S, Speck T and Nickel K G 2018 Strength-size relationships in two porous biological materials *Acta. Biomater.* **77** 322–32
[38] Klang K *et al* 2016 *Plants and Animals as Source of Inspiration for Energy Dissipation in Load Bearing Systems and Facades* (Switzerland: Springer)
[39] Ashby M F, Evans A G, Fleck N A, Gibson L J, Hutchinson J W and Wadley H N G 2000 *Metal Foams—a Design Guide* (Woburn: Butterworth-Heinemann)
[40] Ghosh D, Wiest A and Conner R D 2016 Uniaxial quasistatic and dynamic compressive response of foams made from hollow glass microspheres *J. Eur. Ceram. Soc.* **36** 781–9
[41] Alizadeh M and Mirzaei-Aliabadi M 2012 Compressive properties and energy absorption behavior of Al–Al_2O_3 composite foam synthesized by space-holder technique *Mater. Des.* **35** 419–24
[42] Xia X C, Chen X W, Zhang Z, Chen X, Zhao W M, Liao B and Hur B 2013 Effects of porosity and pore size on the compressive properties of closed-cell Mg alloy foam *J. Magnesium Alloys* **1** 330–5
[43] Burkhardt A, Hansmann W, Märkel K and Nieman H-J 1983 Mechanical design in spines of diadematoid echinoids (Echinodermata, Echinoidea) *Zoomorphology* **102** 189–203
[44] Su X, Kamat S and Heuer A H 2000 The structure of sea urchin spines, large biogenic single crystals of calcite *J. Mater. Sci.* **35** 5545–51
[45] Coble R and Kingery W 1956 Effect of porosity on physical properties of sintered alumina *J. Am. Ceram. Soc.* **39** 377–85
[46] Gibson L J and Ashby M F 1982 The mechanics of three-dimensional cellular materials *Proc. R. Soc.* A **382** 43–59
[47] Pabst W and Gregorová E 2014 Young's modulus of isotropic porous materials with spheroidal pores *J. Eur. Ceram. Soc.* **34** 3195–207
[48] Ito J, Matsushima Y, Unuma H, Horiuchi N, Yamashita K and Tajika M 2017 Preparation and properties of pressureless-sintered dense calcite ceramics *Mater. Chem. Phys.* **192** 304–10
[49] Zhang H, Schuster B E, Wei Q and Ramesh K T 2006 The design of accurate micro-compression experiments *Scr. Mater.* **54** 181–6
[50] Quinn G D, Sparenberg B T, Kosky P, Ives J K, Jahanmir S and Arola D D 2009 Flexural strength of ceramic and glass rods *J. Test. Eval.* **37** 1–23
[51] ASTM International 2016 Standard test method for dynamic Young's modulus, Shear modulus, and Poisson's ration by impulse excitation of vibration E1876-15
[52] ASTM International 2003 Standard test method for fundamental transverse, longitudinal, and torsional resonant frequencies of concrete specimens C 215-02
[53] R Core Team 2017 *R: a Language and Environment for Statistical Computing* R (Vienna: Foundation for Statistical Computing)
[54] Wickham H 2009 *ggplot2: Elegant Graphics for Data Analysis* (New York: Springer)
[55] Fox J and Weisberg S 2011 *An {R} Companion to Applied Regression* (Thousand Oaks, CA: Sage) http://socserv.socsci.mcmaster.ca/jfox/Books/Companion
[56] Revelle W 2018 *psych: Procedures for Personality and Psychological Research* (Evanston, IL: Northwestern University) (https://CRAN.R-project.org/package=psych Version=1.8.3)
[57] Zhang D 2018 rsq: R-squared and related measures R package version 1.0.1 https://CRAN.R-project.org/package=rsq
[58] Korth Kristalle GmbH 2018 Calcite product sheet www.korth.de/index.php/162/items/11.html
[59] Ashby M F 1983 The mechanical properties of cellular solids *Metall. Trans.* A **14** 1755–69
[60] Brezny R and Green D J 1990 Characterization of edge effects in cellular materials *J. Mater. Sci.* **25** 4571–8
[61] Scheffler M and Colombo P 2005 *Cellular Ceramics: Structure, Manufacturing, Properties and Applications* (Weinheim: Wiley)
[62] Seuba J, Deville S, Guizard C and Stevenson A J 2016 Mechanical properties and failure behavior of unidirectional porous ceramics *Sci. Rep.* **6** 24326
[63] Meille S, Lombardi M, Chevalier J and Montanaro L 2012 Mechanical properties of porous ceramics in compression: on the transition between elastic, brittle, and cellular behavior *J. Eur. Ceram. Soc.* **32** 3959–67
[64] Jiang G, Li Q, Wang C, Dong J and He G 2016 Characterization and investigation of the deformation behavior of porous magnesium scaffolds with entangled architectured pore channels *J. Mech. Behav. Biomed. Mater.* **64** 139–50
[65] Brezny R and Green D J 1993 Uniaxial strength behavior of birttle cellular materials *J. Am. Ceram. Soc.* **76** 2185–92
[66] Dam C Q, Brezny R and Green D J 1990 Compressive behavior and deformation-mode map of an open cell alumina *J. Mater. Res.* **5** 163–71
[67] Gibson L J, Ashby M F and Harley B A 2010 *Cellular Materials in Nature and Medicine* (Cambridge: Cambridge University Press)
[68] Broz B E, Cook R F and Whitney D L 2006 Microhardness, toughness, and modulus of Mohs scale minerals *Am. Mineral.* **91** 135–42
[69] Presser V, Gerlach K, Vohrer A, Nickel K and Dreher W 2010 Determination of the elastic modulus of highly porous samples by nanoindentation: a case study on sea urchin spines *J. Mater. Sci.* **45** 2408–18
[70] Weibull W 1951 A statistical distribution of wide applicability *ASME J. Appl. Mech.* **18** 293–7
[71] Danzer R, Supancic P, Pascual J and Lube T 2007 Fracture statistics of ceramics—Weibull statistics and deviations from Weibull statistics *Eng. Fract. Mech.* **74** 2919–32
[72] Lewis L S, Smith J E and Eynaud Y 2018 Comparative metabolic ecology of tropical herbivorous echinoids on a coral reef *PLoS One* **13** e0190470
[73] Bolze J, Peng B, Dingenouts N, Panine P, Narayanan T and Ballauff M 2002 Formation and growth of amorphous colloidal $CaCO_3$ precursor particles as detected by time-resolved SAXS *Langmuir* **18** 8364–9

Supplementary to "Strength, elasticity and the limits of energy dissipation in two related sea urchin spines with biomimetic potential"

Supplementary 1

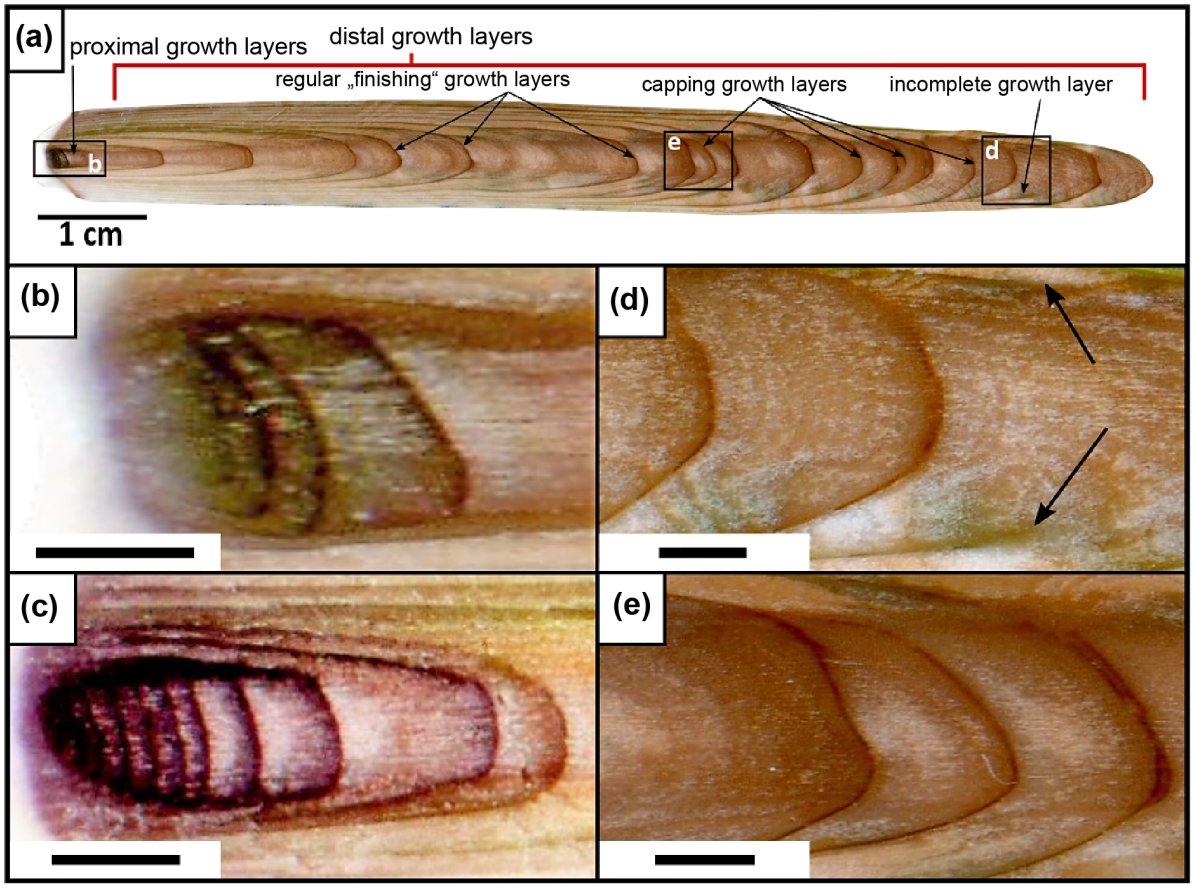

Fig. S1: Growth layer types of H. trigonarius are the same as in H. mamillatus (cp. Lauer et al. [29]) with proximal and distal growth layers ((a)-(c)). The latter can be subdivided in incomplete (d) and capping growth layers (e).

Supplementary 2

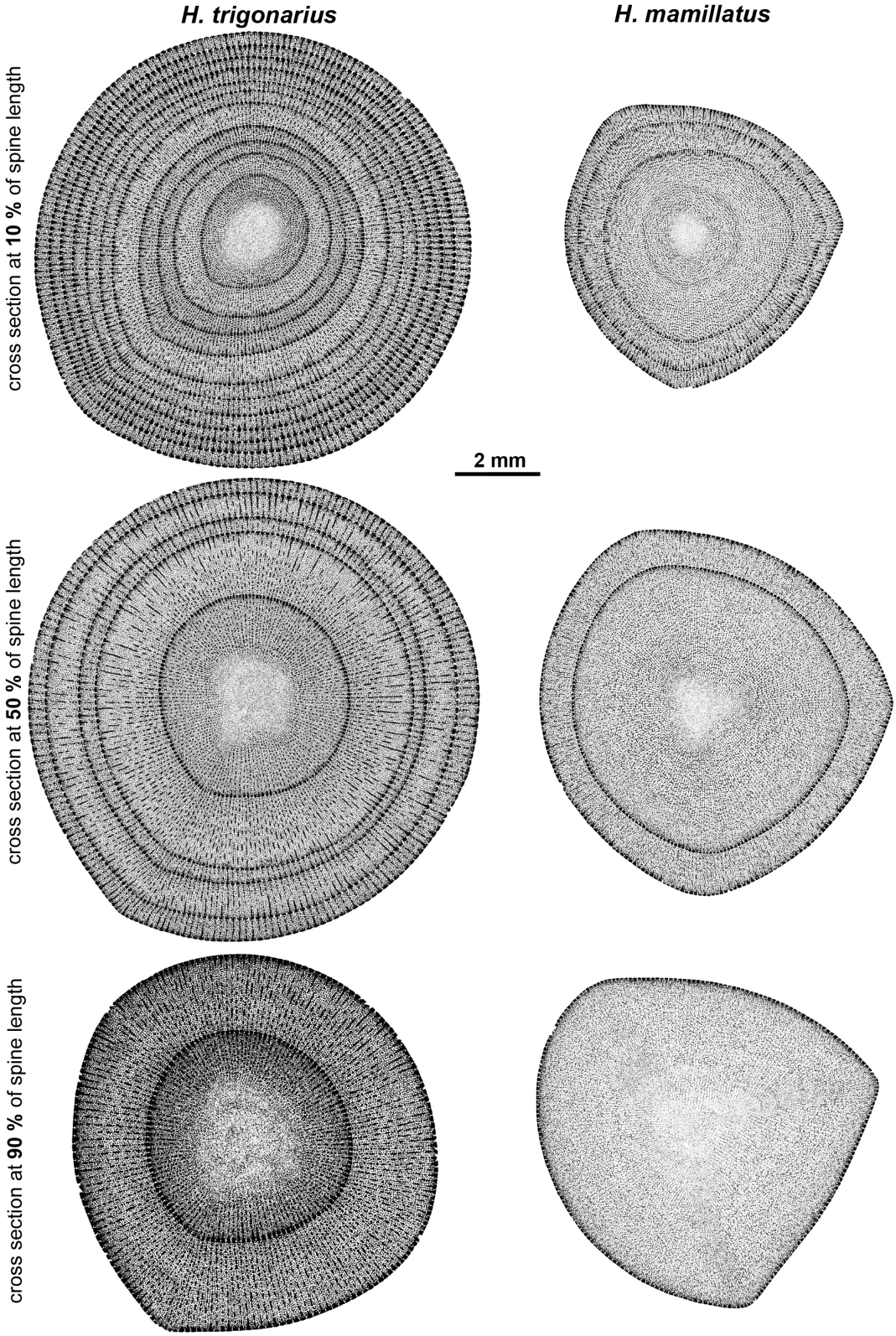

Figure S2: Structure of H. trigonarius and H. mamillatus in different cross sections at 10 %, 50 % and 90 % of spine length measured from the base. It is well visible that H. trigonarius has more growth layers than H. mamillatus. Furthermore the radiating building principle is much more obvious in H. trigonarius than in H. mamillatus. Whereas the stereom orientation of H. mamillatus appears nearly isotropic in the sections extracted at 50 and 90 %, for H. trigonarius the radiating septa originating from the Medulla and organising the whole spine are still apparent.

Supplementary 3

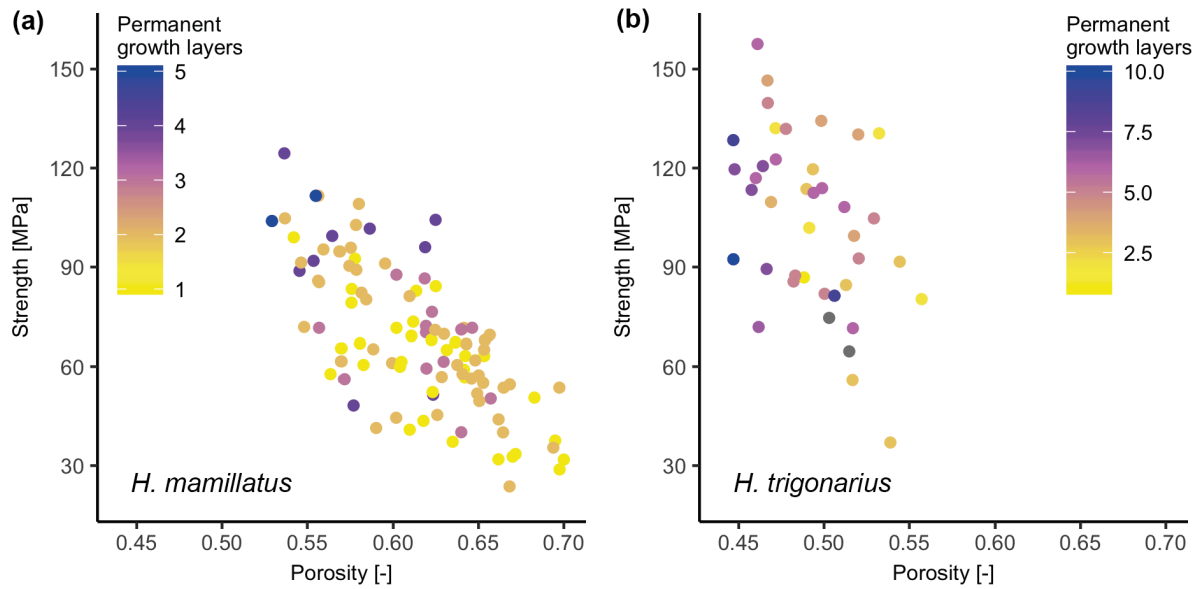

Figure S3: Influence of permanent growth layers on strength of H. mamillatus (a) and H. trigonarius (b). For H. mamillatus segments with more growth layers tend to have a higher strength than segments with fewer growth layers but a comparable porosity. For H. trigonarius this trend was not found. The two grey data dots (b) represent segments with uncounted growth layers.

Supplementary 4

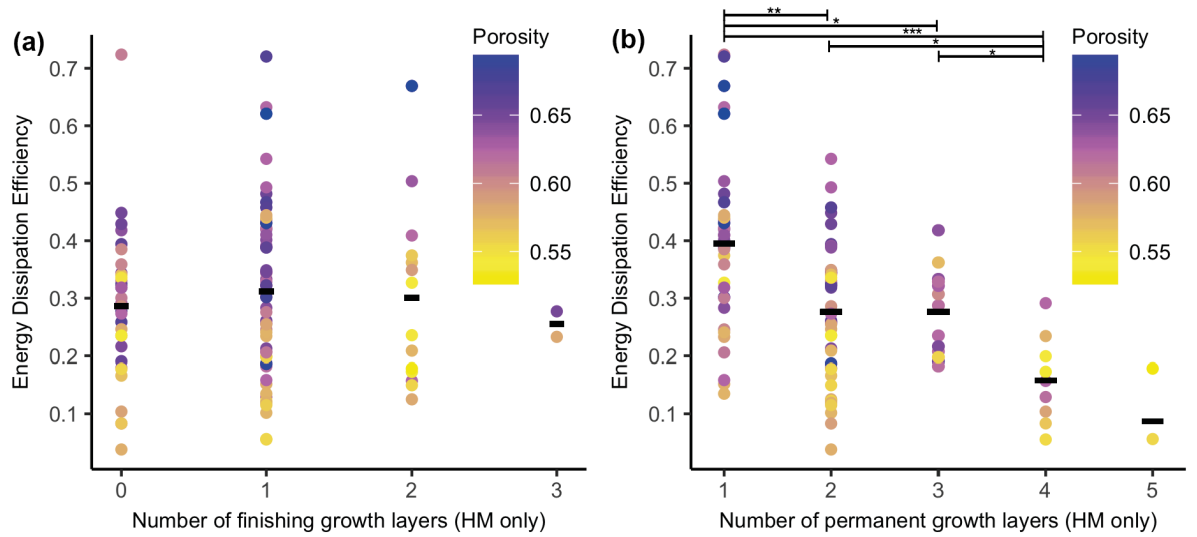

Figure S4: Influence of growth layers on Energy Dissipation Efficiency (finishing growth layers with cap (a), permanent growth layers (b)) when all experiments are considered, not only those with $\varepsilon > 0.37$ (see Fig. 6(d), (e)). The trend observed in Fig. 6(d), (e) is clarified by incorporating those segments that failed prior to $\varepsilon = 0.37$: Finishing growth layers with cap do not seem to influence the energy dissipation efficiency, whereas more permanent growth layers generally result in a lower energy dissipation efficiency. Black vertical lines in both diagrams represent the average energy dissipation efficiency per group. Significance levels indicated as described in 3.3.

Supplementary 5

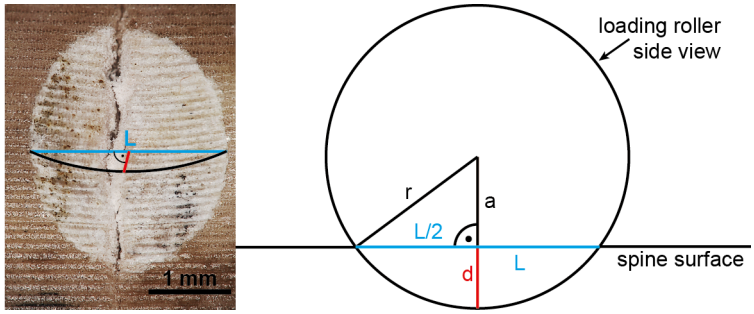

Figure S5: Determination of depth of imprints by loading rollers (3-point bending). Radius of a loading roller was 2.5 mm. L was determined on microscope images of the imprint. With these two measures "a" could be determined. The depth of the imprint (d) was calculated by r-a.

9. Appendix II: Prepared manuscripts for submission

Manuscript 5 with Supplementary Material

Individual growth of the spines of *Heterocentrotus mamillatus*

(19+7 pages)

Individual growth and morphology of the spines of *Heterocentrotus mamillatus*

Christoph Lauer[1*], Stefan Mück[1], Tobias B. Grun[2], Isabel Zutterkirch[1] and Klaus G. Nickel[1]

[1]University of Tübingen, Department of Geosciences, Division of Applied Mineralogy, Wilhelmstraße 56, 72074 Tübingen, Germany,

[2]University of Tübingen, Department of Geosciences, Division of Invertebrate Palaeontology and Paleoclimatology, Hölderlinstraße 12, 72074 Tübingen, Germany

[*]corresponding author: Christoph Lauer, christoph.lauer@uni-tuebingen.de, +49 7071 29 73142

ABSTRACT

Spines of the pencil urchin *Heterocentrotus mamillatus,* Linnaeus, 1758, were analysed in order to obtain insight into the morphology of these large primary spines, recently used as biomimetic role-models for the development of lightweight structures. This research provides an easy conductible and low-cost approach for detailed analyses on spine morphology, which, in this specific case, allows the interpretation of spine growth patterns. Spines of *H. mamillatus* were detached from the complete individuals and sectioned in their longitudinal plane to expose growth layers for analysis. Results of the comparative morphological examination indicate that early stages of the large pencil-shaped primary spines are morphologically indistinguishable from secondary spines. Morphologies of oral and aboral primary spines were quantified with the aspect ratio at the maximum thickness of the primary spine. An aspect ratio ≥ 2 indicates oral primary spines. Oral primary spines have in average more distal growth layers than the younger aboral primary spines, however, growth layers cannot be used for absolute age determination. Growth of primary spines occurs highly localized and irregularly across the spines. Primary spines of the same age (same relative position between the oral and aboral side) have often dissimilar amounts of growth layers meaning they experienced different amounts of growth cycles. This result indicates that the spacing of growth layers is unique for each spine. Regeneration of a large primary spine can take place in a single growth stage indicating an effective way to provide large quantities of calcium carbonate and that spine length is conserved.

Keywords: *Heterocentrotus*, sea urchin spine, growth, morphology, stereom, lightweight design

1 INTRODUCTION

Echinoid spines have been the subject of numerous analysis with respect to their morphology (Régis and Thomassin 1983, Mooi 1986, Coppard and Campbell 2004, Moureaux et al. 2010, Tsafnat et al. 2012, Grossmann and Nebelsick 2013, Schlüter et al. 2015), function (Randall et al. 1964, Strathmann 1981, Telford 1982, Mooi 1986), growth (Ebert 1967, 1986, 1988, Weber 1969a, Dubois et al. 2001), and regeneration (Ebert 1967, 1988, Heatfield 1971, Dubois 2001). The echinoid spines, as the entire echinoid skeleton, is made up of a lattice-like, porous meshwork, the stereom (e.g. Smith 1980), which organizes the lightweight material in an elaborate fashion (Hesse 1900, Deutler 1926, Smith 1980). Besides the exploration of their morphology, function and regeneration potential, spines have attracted interest due to their (1) apparent construction out of a calcite, optically behaving as single crystals, which lacks cleavage planes (Raup 1959, Towe 1967, Nissen 1969), (2) construction out of thermodynamically metastable Magnesium calcite (Clarke and Wheeler 1915, Goldsmith et al. 1955, Weber 1969b, Hozmann 1983, Magdans and Gies 2004, Gorzelak et al. 2014), (3) formation via amorphous calcium carbonate (Beniash et al. 1997, Aizenberg et al. 2002, Politi et al. 306, Radha et al. 2010, Seto et al. 2012, Albéric et al. 2018), and (4) biomimetic potential for lightweight materials (Weber 1969b, Presser et al. 2009a,b, Toader et al. 2017, Lauer et al. 2018a,b) and bone tissue scaffolding (Vecchio et al. 2007, Cao et al. 2017).

The multi-plated echinoid skeleton grows by two mechanisms. First, the addition of new plates at the ocular ring results in an increase of the number of plates and thus an increase of the test diameter. In this case, the youngest plates are at the ocular ring, becoming older in the course towards the peristome (e.g. Pearse and Pearse 1975, David et al. 1995, Simth 2005, Zachos 2009). Second, the increase of plate size by addition of new material to the plate's edges. This incremental additive process can be detected as growth lines within the plates (Pearse and Pearse 1975, Russel and Meredith 2000). Plate growth in echinoids has been widely analysed and controversially discussed with respect to their use as chronometers for absolute age determination of sea urchins (Pearse and Pearse 1975, Gage 1991, Russel and Meredith 2000). Although growth lines are interpreted to reflect periodical echinoid growth, they are unreliable characters for absolute age determination of an individual (Ebert 1986, Gage 1991, Russel and Meredith 2000), as these growth lines rather reflect ecological conditions such as temperature and nutrient availability (Weber 1969a, Gage 1991) than annual cycles.

In contrast to the echinoid test, spines possess only a single growth mechanism: the addition of calcite to the present spine resulting in an extension of length and girth. Spines of the echinometrid echinoid *Heterocentrotus mamillatus* (Fig. 1a) have attracted specific interest as growth lines are readily recognisable in spine sections due to their dark coloration (Fig. 1b,c) (Weber 1969a, Ebert 1988, Dotan and Fishelson 1985, Lauer et al. 2017a) which is a great advantage as usually growth lines become only visible

under further chemical treatment, e.g. tetracycline tagging (Pearse and Pearse 1975, Ebert 1988, Gage 1991). Furthermore, the spines are unusually large for echinoids, which facilitates ecological and mechanical investigations. The distinct growth layers of *H. mamillatus* are visible in horizontal section as roughly circular rings (Fig. 1c), or as downscaled versions of the spine in longitudinal sections (Fig. 1b). Two types of growth layers can be distinguished: the proximal growth layers (PGLs) close to the spine's base, and the distal growth layers (DGLs) which expand from above the spine's base to its tip resembling the shape of the spine (e.g. Lauer et al. 2017). While primary spines feature both PGLs and DGLs (Fig. 1), secondary spines only possess PGLs (Lauer et al. 2017). The growth layers in *H. mamillatus* spines represent outer surfaces of past growth cycles (Weber 1969a, Ebert 1988). Several growth parameters, however, still remain unclear, such as the (1) elapsed time between two growth layers (= one growth cycle), which is reported to range between lunar cycles (Weber 1969a) and a full year (Dotan and Fishelson 1985). (2) Reasons for the cycles interpreted to rely on seasonal supply of nutrients, or, can be due to differential growth trajectories of the test size and spine length (Ebert 1988). (3) Growth rates were also discussed to follow a linear function (Dotan 1990), or, behaving irregularly (Ebert 1986). The dense, imperforate stereom type of growth layers is reported to indicate slow growth (e.g., Smith 1980).

The overall morphology of *H. mamillatus* spines change gradually from the aboral to the oral side of the test (Fig. 1a,c). Aboral spines are typically bulky with a nearly circular outline in horizontal section. Towards the peristome, the spines become distinctively smaller with a blade-shaped horizontal section (Dotan and Fishelson 1985, Hasenpusch 2000, Lauer et al. 2017). The largest spines are usually located at, or just above the ambitus (Dotan and Fishelson 1985) (Fig. 1a).

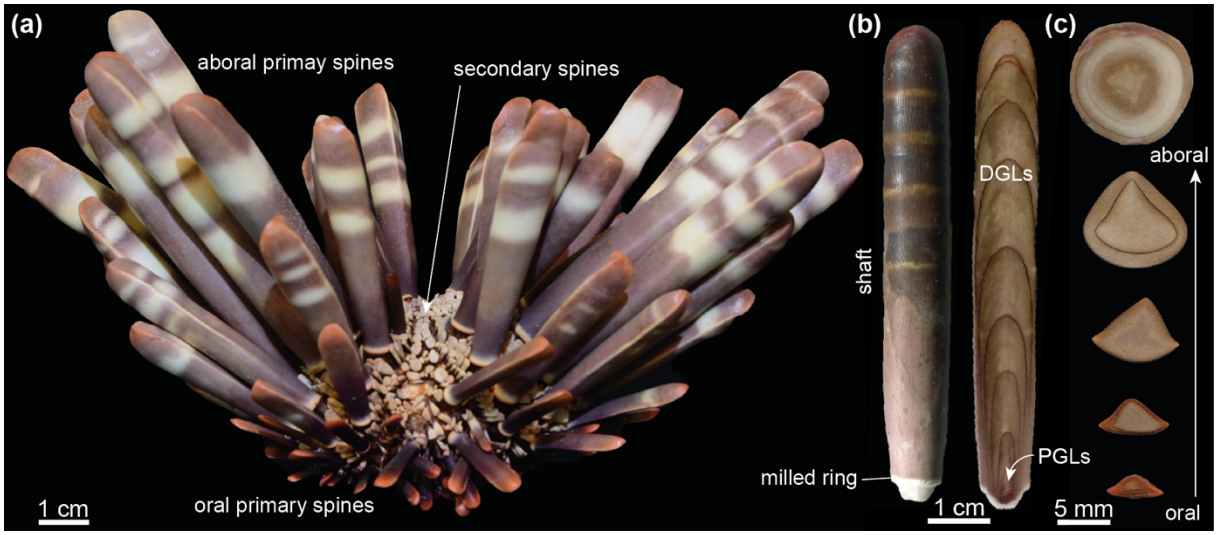

Fig. 1 *(a) Heterocentrotus mamillatus with primary and secondary spines and their distribution on the test. (b) Aboral primary spine in longitudinal section revealing the distal growth layers (DGLs) along the shaft and the proximal*

growth layers (PGLs) close to the milled ring. (c) A series of horizontal sections from oral to aboral spines showing the change in shape and the growth layers

In the following study the spine morphology of *H. mamillatus* is analysed in depth in order to interpret growth patterns and spine ontogeny based on an easy-conductible and low-cost methods. Therefore, various parameters have been investigated, including (1) spine mass, (2) spine length, (3) spine shape, (4) number of growth layers, (5) growth layer distribution, and (6) growth layer spacing.

2 MATERIAL AND METHODS

2.1 Material

In total, eight specimens of *Heterocentrotus mamillatus* (HM1-HM8) were obtained from a professional distributor (Fossilienhandlung Peter Gensel, Weimar, Germany). At this time, the dry specimens were stored for at least three years. All specimens originate from Pacific Ocean (Philippines), were dried and remained untreated after removal from the ocean. Material is stored at the University of Tübingen under repository GPIT/00897 – 904. The test diameter was determined at the maximum diameter of the ellipsoid structure with a calliper (precision: 0.05mm).

2.2.1 Spine differentiation

Primary spines were systematically detached from the tests and numbered according to their position (=relative age) on the test: Primary spine position (PSP) 1 refers to the first circlet of mature primary spines closest to the periproct. PSP increases towards the peristome. I. e. PSP 2 includes the ten interambulacral spines (two per plate column of five interambulacral plate columns) from the second interambulacral plates with primary spines counted from the periproct. Primary spines of the ambulacral plates occur later (in aboral view) at the 3rd PSP onwards relatively to interambulacral plates. Therefore, PSP 3 firstly includes all 20 primary spines. For length and mass determination, 406 spines were used. Growth layer analyses were performed on a subset of 330 spines where 195 spines originate from interambulacral areas and 135 from ambulacral areas. The spine length was measured using the aforementioned calliper. The spines' aspect ratios were determined at two positions in order to assess spine shape. Position 1 is at the maximum thickness of the spine (d_1), position 2 just above the milled ring (d_2) (Fig. 2a). Spines were weighed using a Sartorius scale BP 211D (Sartorius AG, Göttingen, Germany) with a precision of 0.01 mg.

Secondary spines were detached around the apical system from both ambulacral and interambulacral plates from PSP 0, the plate circle before the first primary spines occur. Other secondary spines surrounding primary spines on plates with higher primary spine positions were randomly chosen for comparison to those on PSP 0. Spine morphologies were also compared between primary and secondary spines.

2.2.2 Growth layer identification and measuring

To access growth layers, longitudinal sections of the spines were made. Therefore, spines were ground using carborundum abrasive paper (grain size 10 µm) longitudinally to the point where the small proximal growth layers were seen best. Large spines were sawn with a low speed saw (Buehler Isomet 11-1180, Buehler, Lake Bluff, USA) longitudinally prior to grinding. Sections were scanned with an Epson V370 Photo scanner to a resolution of 1200 - 2400 dpi. Secondary spines were analysed with a digital microscope (Hirox MXB 216Z, Hirox Europe, Limonest, France). Resulting images were used for growth layer quantification and inter-layer distance measuring between distal growth layers (DGLs) using Fiji 2.0.0 (ImageJ software environment). PGLs numbers are to be understood as minima owing to cutting effects: The slice where all PGLs can be seen is << 1 mm and thus difficult to reach by grinding. DGLs were numbered in ascending order from the innermost (= oldest) to the outermost (= youngest) layer. Distances were measured between the maximal extend of two layers (Fig. 2b). When incomplete DGLs without the characteristic cap were encountered, the cap was interpolated. Interpolation was carried out with Adobe Photoshop Elements 11 (Adobe Systems, San José, California). Interpolation was performed by using the shape of the next younger complete DGL and downscaling its dimension until it matches the overlapping shape of the incomplete and older growth layer (Fig. 2b). The precision of this procedure was determined by interpolating the shape of 23 growth layers in spines also possessing complete growth layers and comparing length of the interpolated growth layer to their real length (Fig. 2b). The precision is ±1.1 mm (standard deviation, STD) and the overall replication of the growth layers is accurate underlining the impression of larger layers being a scaled version of the smaller ones.

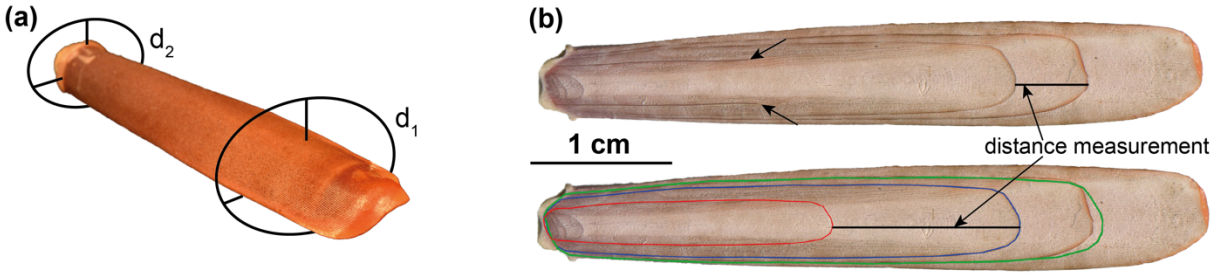

Fig. 2 *(a) Determination of the aspect ratio at the maximum thickness of the spine (d_1) and just above the milled ring (d_2). (b) The interpolation of an incomplete DGL (ending points marked by arrows). Therefore, the next complete DGL was outlined (blue) in interpolated in such a way, that it fits the remnants of the incomplete layer (red). It was checked with the next complete DGL whether the interpolation yields agreeable results (green)*

2.2.3 Statistical testing

The free software GNU R (V. 1.1.442) (R Core Team 2018) was used for data processing and statistical analysis with the additional packages *ggplot 2* (Wickham 2009) for plotting, *car* (Fox 2011) and *psych*

(Revelle 2018) for statistical evaluation of the measurements. The data was analysed for normal distribution with a Shapiro-Wilk test and for homoscedasticity with a Levene test. A Wilcoxon test was applied for testing statistical differences between the quantity of PGLs in ambulacral and interambulacral spines.

3 RESULTS

3.1 Primary and secondary spines

Spines of *H. mamillatus* are differentiated into primary and secondary spines. The large primary spines are attached to the large primary tubercles on the sea urchin's test, where the small secondary spines are attached to small tubercles. Young primary spines around the apical system are morphologically similar to secondary spines. Older primary spines are characterized by their large and typical pencil-shape.

Secondary spines are as morphologically differentiated as primary spines. Secondary spines around the apical disc (where no primary spines are present yet) are knobbly spines with a flat upper surface (Fig. 3c). Together they cover the whole apical disc (Fig. 3). All of these small secondary spines grow on the primary tubercle. The GLs of these secondary spines are closely stacked as PGLs in primary spines (Fig. 3a) and occur in large abundance. Before the first mature primary spine on PSP 1 occurs, an often slightly enlarged secondary spine appears (Fig. 3b). In this spine, the youngest GLs is the first not closely stacked layer (Fig. 3b). Large primary spines are surrounded of a circlet of thin and flat secondary spines situated on the same plate (Fig. 3d), well distinguishable from those in Fig. 3b,c. At the oral side of the animal, secondary spines become subsequently thinner and their overall shape resembles oral primary spines, only as a down scaled version.

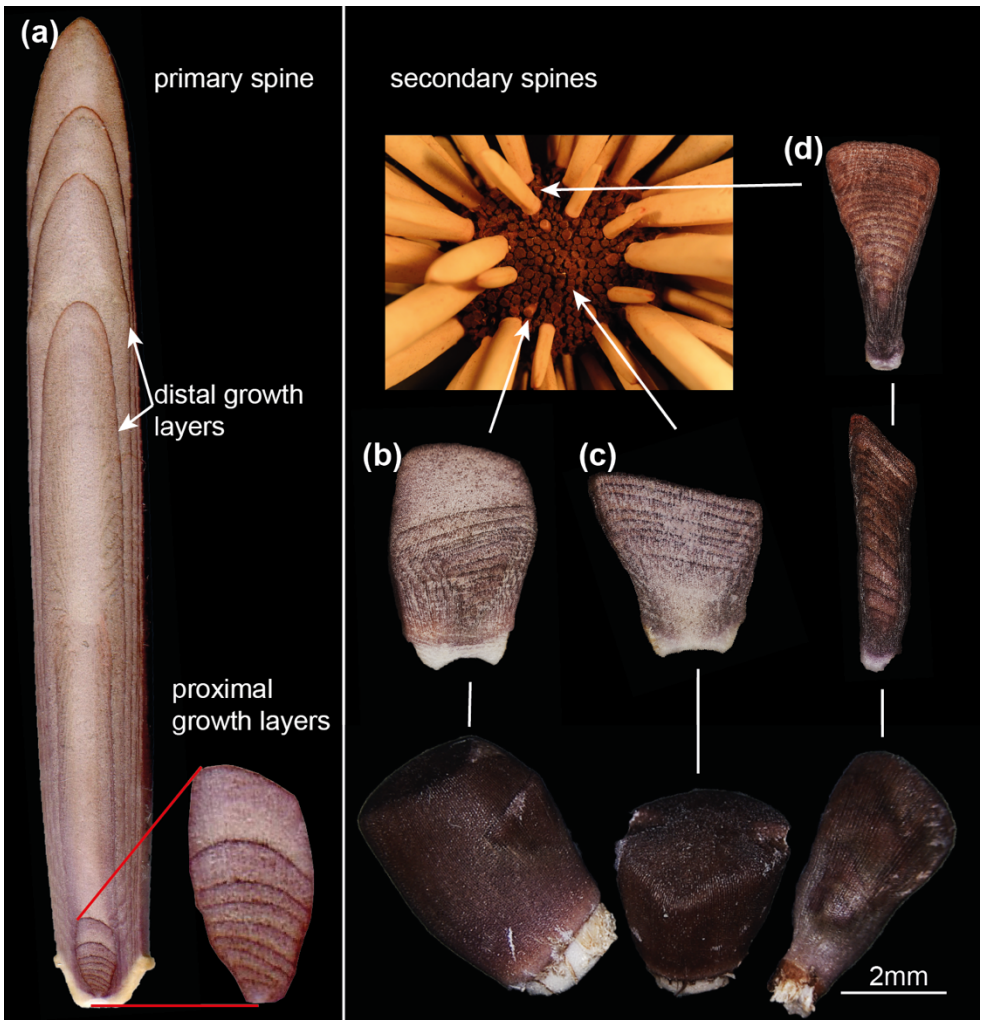

Fig. 3 *A Primary spine and its proximal growth layers (PGLs) (a) compared to secondary spines (b-d). Morphologically different secondary spines were identified in respect to their position on the test (b-d). All secondary spines possess many closely stacked PGLs*

The number of PGLs was evaluated in secondary spines on the plate position just prior to the first primary spine (interambulacral spines: prior to PSP 1, ambulacral spines: PSP 2) (Fig. 4). Ambulacral secondary spines possess generally more PGLs than their interambulacral counterparts across all animals investigated.

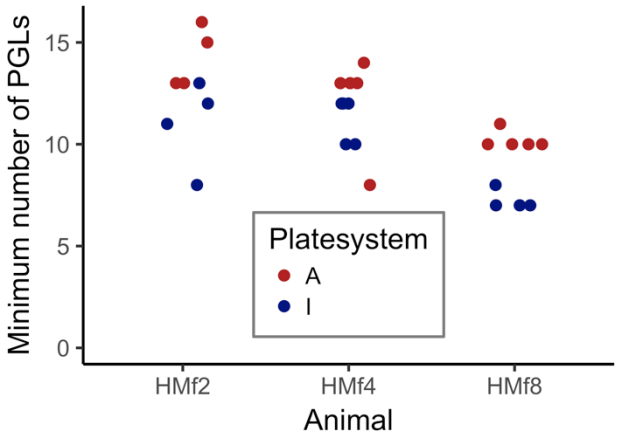

Fig. 4 *Minimum number of proximal growth layers (PGLs) on secondary spines situated on plates prior to the plate with the first primary spine. A = ambulacral plate, I = interambulacral plate*

3.2 Primary spine differentiation

In total, 406 mature primary spines of *Heterocentrotus mamillatus* were analysed for length and weight (Table 1). Slight differences in spine length are detectable between individuals, although tests are of comparable diameters (Table 1). The length of the spines increases until the ambitus of the test and then gradually decreases towards the peristome (Fig. 5a, colour code). Spines of the oral side (PSP 5-9) are small, rarely longer than 2.5 cm, and light, clustering well below 1 g (Fig. 5a). There is no notable difference between interambulacral (n = 260) and ambulacral spines (n = 146) following power law fits (interambulacral spines (black fitting line): $y = 0.000045\ x^{2.66}$, $R^2 = 0.966$, N = 260 and ambulacral spines (grey fitting line): $y = 0.00005\ x^{2.62}$, $R^2 = 0.952$, n = 146*)*. Moderate deviations arise from animal specific characteristics of the spines (supplementary material: Fig. S1). Specimen HM4 possesses the thickest and densest spines, deviating to higher masses. Specimen HM6 features comparably porous and thin spines and thus deviates towards lower masses (Fig. S1). Spine masses do not follow a cubed power law (red dotted line, Fig. 5a), which one would expect from a mass-size (volume) relation (see 4.3).

Table 1 *Measurements of test diameter and spine mass and length of mature primary spines used in this study*

			Length (mm)		Mass (g)	
specimen	max test diameter (mm)	*n* (spines)	min	max	min	max
HM1	-	67	11.86	85.8	0.0796	6.295
HM2	59	45	5	68	0.0016	3.684
HM3	58	51	7.8	64.1	0.0086	2.517
HM4	55	52	6.3	68.2	0.0043	5.228
HM5	54	47	8.8	66	0.0076	3.643
HM6	57	55	7.7	76.9	0.0045	3.548

HM7	49	46	7.5	72.7	0.0046	3.440
HM8	53	47	6.3	76.9	0.0028	4.599

Two aspect ratios were selected to evaluate how the spine shape changes from the aboral (PSP 1-3) to the oral side (PSP 5-9) (Fig. 5b). The aspect ratio at maximum thickness of the spine (d_1) is close to 1 for the aboral side, indicating approximately round cross sections of the spines. Aspect ratio d_1 increases significantly at PSP 4 to d_1 = 2-3 and stays constantly at this level until PSP 9 resulting in an oblate cross section, typically for the blade shaped oral spines (PSPs 5-9). The aspect ratio d_2 measured just above the milled ring stays below 1.5 over the whole test. The maximum d_2 is observed for PSPs 5 and 6, with slightly lower ratios for the spines located at the oral and aboral poles. Overall, d_2 seems not to be affected by the transition from oral to aboral spine shape. Differences between ambulacral and interambulacral spines are negligible (Fig. 5b). It was observed that primary spines on the ambulacral plates occur later than those attached to interambulacral plates. In all observed specimens, the first primary spine on ambulacral fields occur on higher primary spine positions (PSP3) compared to those of the interambulacral plates (i.e. Fig. 5b).

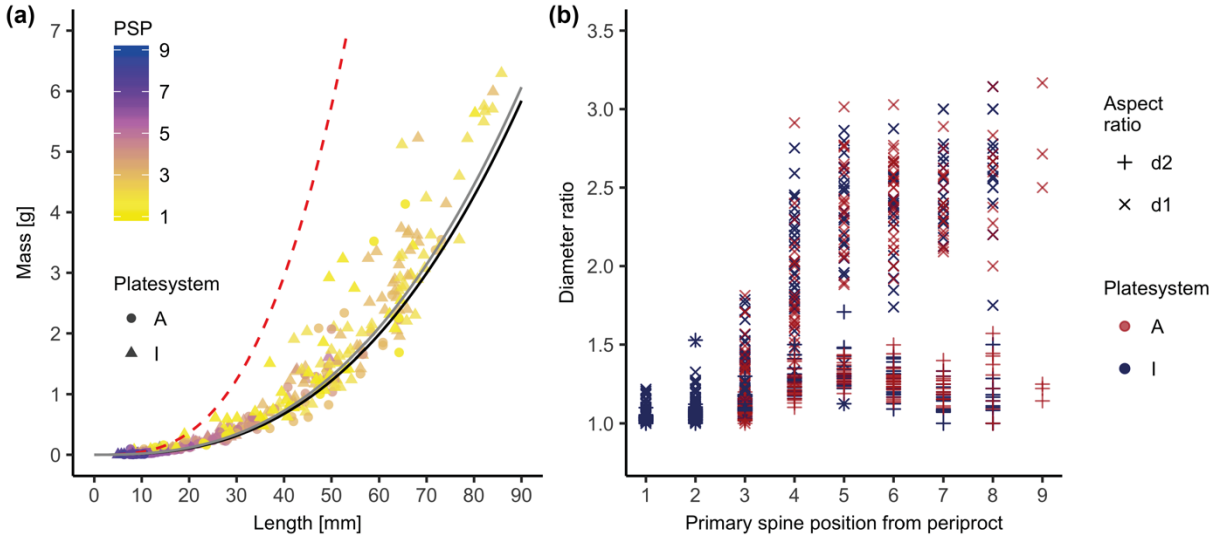

Fig. 5 *(a) Mass-length correlation of spines (n = 406) with respect to primary spine position (PSP). Black line = fit of interambulacral spines (I) ($y = 4.56*10^{-5}\ x^{2.67}$, $R^2 = 0.966$, n = 260), grey line = fit of ambulacral spines (A) ($y = 5.09*\ 10^{-5}\ x^{2.62}$, $R^2 = 0.952$, n = 146) revealing no difference between spines of the two fields. Red dotted line is a cubed power law fit representing the expected increase in mass when becoming larger. (b) Aspect ratios at the maximum thickness (d_1) and just above the milled ring (d_2) of spines (A = ambulacral, n = 144; I. = interambulacral, n = 254) describing the spines shape in the course from the aboral (~ PSPs 1-3) to oral side (~ PSPs 5-9)*

3.3 Growth layers

The number of distal growth layers (DGLs) correlates to the PSP on the test (R^2 = 0.42, *n* = 39) (Fig. 6a (for HM6, other animals see Fig. S2). Spines close to the periproct generally possess lower numbers of DGLs, where the quantity of these layers increases in the course to the peristome. The number of DGLs in a single PSP can deviate considerably from the fitting line (i.e. PSP6, Fig 4a): the median number of DGLs ranges between 4-6, specimen HM2 shows the maximum range (2-11) and the spine with the most DGLs in this study (oral spine on PSP 7 with 11 DGLs) (Fig. S3). The minimum DGL range was observed in specimen HM7 with 2-6 DGLs. The number of DGLs are not normal distributed in the analysed individuals (Fig. 6b, S3, Shapiro-Silk test, $p < 0.05$).

The test sizes of these echinoids are similar, with only specimen HM7 being notably smaller (table 1). A correlation exists between the maximum number of DGLs and the maximum diameter of the ellipsoid test (Fig. 6c). Other parameters such as the median number of DGLs, the length of the longest spines or the mass of the heaviest spines did not correlate with the maximum test diameter (Fig. S4).

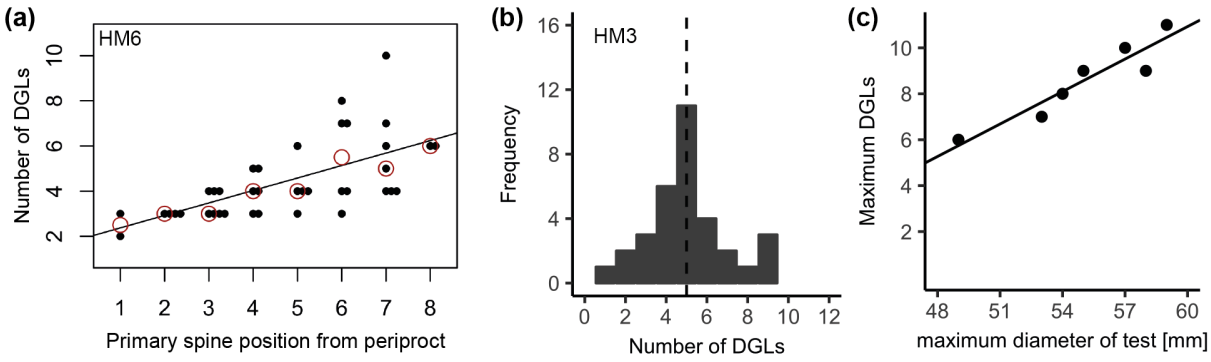

Fig. 6 *(a) Scatterplot showing the correlation between DGLs and the position of primary spines for specimen HM6. Black line is a linear fit (R^2=0.42, n = 39). Red circles are the median at each primary spine position. Histogram of DGL distribution in the spines of HM3 (b); dotted line = median. (c) Maximum DGL quantity correlates with the maximum diameter of the test (R^2 = 0.878, n = 7)*

For the comparison between PGLs and DGLs (Fig. 7), spines were subdivided by their origin from ambulacral (*n* = 106) and interambulacral plates (*n* = 141). For both ambulacral and interambulacral spines, the ratio of proximal by distal growth layers (PGLs/DGLs) decreases from above 1 on the first PSP of their occurrence (interambulacral spines: PSP 1, ambulacral spines: PSP 3) towards 0 for the oral PSPs. Ambulacral spines tend to have a higher ratio than interambulacral spines at the same relative position. Furthermore, ambulacral spines feature more PGLs (median ambulacral: 5, median interambulacral: 2), which is statistically significant (Wilcoxon rank sum test: $W = 10352$, $p < 0.001$, $n = 247$).

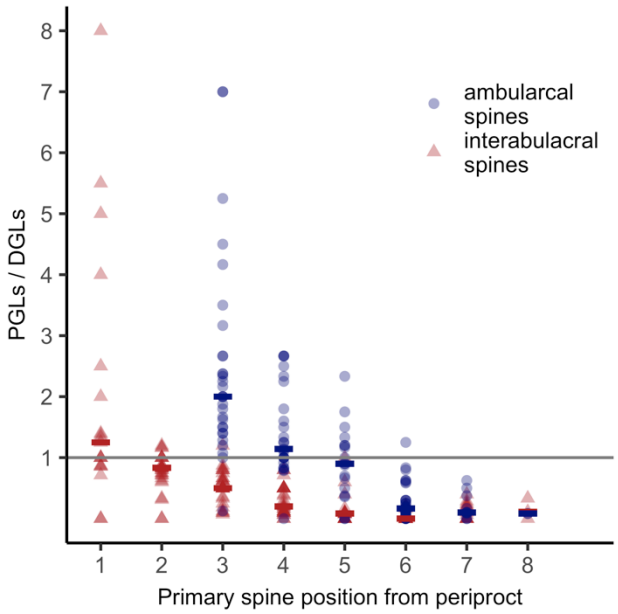

Fig. 7 *Ratio of proximal and distal growth layers (PGLs/ DGLs) of ambulacral and interambulacral spines. Blue and red bars correspond to the median for ambulacral or interambulacral spines, respectively. Ambulacral spines have a higher ratio than interambulacral spines of the same relative position*

The distance between the first DGL and the last PGL (P-DGL1, blue), which represents the earliest growth cycle of the primary spine, is always largest compared to the later growth cycles (Fig. 6, other animals: Fig. S5). Only spines from the aboral test area deviate from this pattern. Later growth cycles of the spines differ in their extent, with each spine possessing a unique distribution of growth layers even when they are of the same age and from the same PSP (Fig. 8).

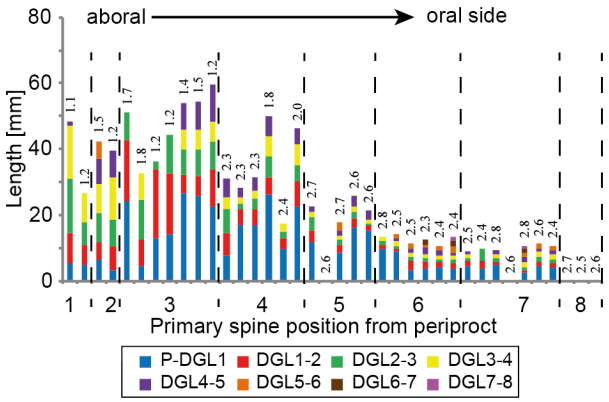

Fig. 8 *Extent of distal growth layers (DGLs) in HM5. For all spines except for those on 1st, 2nd and partly 3rd PSP the first growth layer (blue) has the largest extend relative to all others. Numbers above the bars give the aspect ratio d_1 of the corresponding spine (Fig 2a)*

4 DISUSSION

4.1 Primary and secondary spines

Our findings indicate that the hitherto termed "secondary spines" (Dotan and Fishelson 1985, Lauer et al. 2017) on the central tubercle of a plate are actually small primary spines and develop into mature primary spines with growth, likely when the plate becomes large enough. Following observations underline this hypothesis: (1) Proximal growth layers of primary spines strongly resemble PGLs of these "secondary spines" (Fig. 3, see also Dotan and Fishelson 1985, Lauer et al. 2017). (2) The number of PGLs in primary spines decreases from PSP 1 towards the ambitus. Older primary spines that grew in times of earlier and thus faster test growth (e.g. Ebert and Russel 1993, Lamare and Mladenov 2000) have fewer PGLs. (3) The number of PGLs in secondary spines on the central tubercle on a plate prior to PSP1 and in primary spines on PSP1 are similar taking into account the difficulties with grinding (Fig. 4, 7). (4) Ambulacral mature primary spines, that developed at later stages (in this study first occurrence at PSP 3) have generally more PGLs than interambulacral spines (Fig. 7). The same was observed for ambulacral and interambulacral small primary spines that were hitherto termed "secondary spines" (Fig. 4). Ambulacral spines grow thus longer at the small primary spine stage (more PGLs) before the plate becomes large enough to feature a mature primary spine.

This primary spine development is in contrast to the findings of Hasenpusch (2000), who claimed without further evidence that secondary spines would develop into oral and finally aboral spines. This hypothesis also neglects the well-known principles of test growth with new plates added at the apical disc and that oral spines are thus the oldest of the animal. We state that primary spines start as a small knobbly spine and develop into full-grown primary with time.

4.2 Primary spine differentiation

As often described qualitatively, oral spines are blade-shaped and aboral spines in first approximation round (Dotan and Fishelson 1985, Grossmann and Nebelsick 2013, Lauer et al. 2017). The here introduced aspect ratio d_1 at maximum spine thickness describes this observation quantitatively: $d_1 > 2$ is a clear indicator for the oral, oblate spine shape. In this study, the shape transition from round aboral to blade-shaped oral spines takes place for most primary spines at PSP4, but this might be dependent on the size and age of the animal. As the blade shaped aboral spines need to attach to the round tubercle, aspect ratio d_2 just above the milled ring is unaffected by the transition from aboral to oral spine shape.

Oral spines are generally lighter and smaller than aboral spines (Fig. 5a) and exhibit in average a higher number of DGLs than their aboral counterparts (Fig. 6a, S3) due to their higher relative age. This

relation was hitherto hypothesised, but not quantitatively tested (e.g. Dotan and Fishelson 1985). Oral spines show less PGLs than aboral spines, or even lack them (Fig. 7).

Oral spines have a lower porosity and a more distinct core-shell construction (the dense growth layers concentrating on the spine's rim and the porous medulla in the centre) than the aboral spines (Fig. S6). This overall lower porosity is interpreted due to slower growth combined with higher relative age, resulting in more growth layers per area. Whether the low porosity (thus higher strength) has also functional reasons remains speculative. However, the blade-like, spatula shape of the oral spines is likely beneficial for locomotion as these slender spines can attach more effectively to rocky substrate than the thick spines at the ambitus (Dotan and Fishelson 1985, Schlüter et al. 2015).

4.3 Directed and localized growth in spines of *H. mamillatus*

Spine growth of *H. mamillatus* is highly localized and directed as highlighted by the following observations:

(1) The distribution of primary spines on the test: The size of primary spines increases from the aboral and oral side towards the ambitus where the largest spines are present (see also Dotan and Fishelson 1985, Dotan 1990). Furthermore, there is a distinct bilateral distribution of primary spine length in *H. mamillatus* reflecting the laterally elongated shape of this echinometrid echinoid. Two spots with the largest aboral spines are located directly opposite to each other (Fig. 1) not reflecting the pentamerous symmetry.

(2) Spines of the same PSP on the five differing plate columns (= indicating similar relative age) often have a different amount of DGLs (Fig. 6a, 8, S2, S5) which means they experienced not the same amount of growth cycles. Additionally, when spines possess the same quantity of growth layers the extend of the growth layers on each spine is different from one another (Fig. 8, S5). The growth layer sequence is thus unique for each spine.

(3) Spine length seems conserved and regulated by growth layers. After partial spine loss (e.g. by predatory attacks, autotomy, disturbed growth, etc.) the spine can regenerate within a single growth cycle (Fig. 9b). These spines show considerably less DGLs than spines of the same size and PSP from the same individual (Fig. 9a, b). This finding is in accordance with Weber (1969a), who studied spines of *H. trigonarius*, which are congeneric to *H. mamillatus*. Although Ebert (1988) noted that regeneration in *H. mamillatus* is slow compared to other echinoids, the large quantities of calcium carbonate supplied (>g) to regenerate such large spines of *Heterocentrotus* is probably unparalleled.

(4) In order not to become too heavy spine growth does not follow the cubed volumetric growth: when the size of a growing structure is doubled, its volume and thus mass triples (see deviation from red dotted line in Fig. 5a). The experimentally determined function in primary spines of H. mamillatus

possesses an exponent of ~2.67, which deviates from the theoretical cubical function by ~11 %. Three reasons for the deviation have been identified: (1) the spine shape changes from oral to aboral side (Dotan and Fishelson 1985, Hasenpusch 2000, Lauer et al. 2017), (2) the porosity decreases from oral to aboral spines (Fig. S6), and (3) within aboral spines, the porosity decreases from the bottom part (early growth cycles) to the tip region (later growth cycles). Together this reduces the theoretical mass of a 80 mm long primary from 23.3g to 5.5g. This considerable reduction reflects the lightweight construction of H. mamillatus.

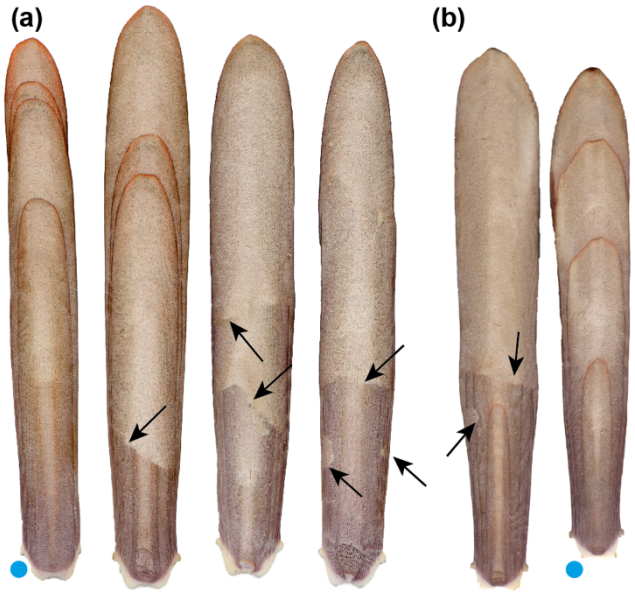

Fig. 9 *Regeneration after damage (interpreted fracture highlighted by black arrows) in spines of specimen HM2 (a) and HM3 (b). Blue dots identify unbroken spines from the same animal and a comparable PSP*

4.4 Age resolution between different growth layers

Previous research has shown that growth layers of *H. mamillatus* cannot be used as age markers (Weber 1969, Ebert 1988). Our results emphasize this conclusion as the number of DGLs varies widely in spines of a single individual and even in spines of the same PSP (= similar age). Previous studies only focused on the time resolution provided by DGLs (Weber 1969, Ebert 1988, Dotan and Fishelson 1985, Dotan 1990), but neglecting the information of PGLs as growth cycles. However, it is unclear whether the time resolved in PGLs and DGLs is comparable, as the quantity of PGLs in young primary spines even exceeds the quantity of DGLs in the oldest oral spines. These results indicate that more emphasis should be granted to the PGLs when conducting further experimental analysis on the spine growth of *H. mamillatus*.

4.5 Growth layers are laid down in phases of no or reduced growth?

It is proposed that the dense imperforate stereom type of the growth layers might be the result of slow growth (Simth 1980). The results of this study lead to some thoughts of the origin of growth layers. Of the 406 spines investigated not a single spine had no growth layer on its surface exposing the rough and porous radiating layer underneath. This means all spines had terminated growth cycles when the animals died. A rather odd coincidence given the individual and localized growth of the spines of *H. mamillatus*. Ebert (1988) therefore concluded that these spines usually do not grow. He also stated that growth in *H. mamillatus* is slow compared to other sea urchins. Since these large spines need large amounts of calcium carbonate to grow, a slow growth would likely result in a permanent growth. Régis and Thomassin (1983) observed in vivo experiments with *H. mamillatus* in sea water aquarium that the loss of epidermis and underlying growth layer only occurs when calcification malfunctions.

The lack of spines without growth layer on the spine surface can be also interpreted as the dense growth layer is a prerequisite for growth as it protects the porous stereom and the mesodermal syncytium. This would also explain the occurrence of capping growth layers and other frequently found growth layers not covering the whole spine (Lauer et al. 2017). Following this interpretation, the formation of a growth layer would not provide insight into the growth speed.

5 CONCLUSIONS

1) The aspect ratio at maximum spine thickness can be used to differentiate between oral and aboral spines quantitatively. Oral spines have a ratio of ≥2.
2) Oral spines have in average more distal growth layers (DGLs) than aboral spines as they are generally older and thus experienced more growth cycles. As growth patterns are irregularly distributed over the test and spine damage and regeneration occurs frequently this DGL increase can only be found statistically.
3) The small spines on the plates surrounding the apical disc were identified as primary spines due to their growth layer signature, their location on the central tubercle and their shape. These spines were wrongly termed secondary spines so far.
4) *H. mamillatus* is able to regenerate damaged primary spines in a single growth cycle indicating that spine length is conserved.
5) Growth occurs irregularly and highly localised across the spines of *H. mamillatus*. Even undamaged spines on the same primary spine position (=same age) possess differing numbers of distal growth layers and therefore experienced not the same amount of growth cycles. Each spine thus has a unique growth layer spacing.
6) Neither distal, nor proximal growth layers can be used for reliable age determination.

ACKNOWLEDGEMENTS

The authors kindly thank the German Research Foundation (DFG – Deutsche Forschungsgemeinschaft) for funding this work within the framework of the Collaborative Research Centre (SFB/Transregio) 141 "Biological Design and Integrative Structures", project B01. The authors thank Barbara Maier and Simone Schafflick (workshop of the University Tübingen) and Ingmar Werneburg in the repository of the University Tübingen. We are also grateful to James Nebelsick for proofreading.

COMPLIANCE WITH ETHICAL STANDARDS

Conflict of Interest

The authors declare that they have no conflict of interest.

Statements on the welfare of animals

This research was conducted on dried material obtained from a material distributor. A statement on animal welfare is not applicable.

Data accessibility

Raw data and the supplementary data is accessible via the supplementary material repository.

Author's contributions

CL developed techniques (shape, growth layer and porosity analysis) for lab work, carried out statistical analysis, produced figures and wrote the manuscript. SM carried out the majority of the lab work (shape and growth layer analysis). TBG contributed in theoretical background and wrote the manuscript. IS helped with porosity determination. KGN supervised the experiments, provided infrastructure, acquired funding and improved the quality of manuscript. All authors gave their final approval for publication.

REFERENCES

Aizenberg J, Lambert G, Weiner S, Addadi L (2002) Factors involved in the formation of amorphous and crystalline calcium carbonate: A study of an ascidian skeleton. J Am Chem Soc 124(1):32-9

Albéric M, Caspi EN, Bennet M, Ajili W, Nassif N, Azaïs T, Berner A, Fratzl P, Zolotoyabko E, Bertinetti L, et al (2018) Interplay between Calcite, Amorphous Calcium Carbonate, and Intracrystalline Organics in Sea Urchin Skeletal Elements. Cryst Growth Des 18(4):2189-201

Beniash E, Aizenberg J, Addadi L, Weiner S (1997) Amorphous calcium carbonate transforms into calcite during sea urchin larval spicule growth. Proc R Soc Lon B 264:461-5

Cao L, Li X, Zhou X, Li Y, Vecchio KS, Yang L, Cui W, Yang R, Zhu Y, Guo Z, et al (2017) Lightweight Open-Cell Scaffolds from Sea Urchin Spines with Superior Material Properties for Bone Defect Repair. ACS Appl Mater Interfaces 9(11):9862-70

Clarke FW, Wheeler WC (1915) The inorganic constituents of echinoderms. United States Geological Survey Professional paper 90(L):191-6

Coppard SE, Campbell AC (2004) Taxonomic significance of spine morphology in the echinoid genera diadema and echinothrix. Invertebr Biol 123(4):357-71.

David B, Mooi R, Telford M (1995) The ontogenetic basis of Lovén's Rule clarifies homologies of the echinoid peristome. In Emson R, Smith AB, & Campbell A (eds) Echinoderm Research – Proceedings of the Fourth European Echinoderms Colloquium, London, United Kingdom, 10-13 April 1995 A. A. Balkema, Rotterdam, pp 155-164

Deutler F (1926) Das Wachstum des Seeigelskeletts. Verlag von Gustav Fischer, Jena

Dotan A (1990) Population structure of the echinoid Heterocentrotus mammillatus (L.) along the littoral zone of the south-estern Sinai. Coral Reefs 9:75-80

Dotan A, Fishelson L (1985) Morphology of spines of Heterocentrotus mammillatus (Echinodermata, Echinoidae) and its ecological significance. In: Keegan BF, O'Connor BDS (eds) Fifth International Echinoderm Conference, A.A.Balkema, Galway, pp 253-260

Dubois P, Ameye L (2001) Regeneration of Spines and Pedicellaria in Echinoderms: A Review. Microsc Res Techniq 55:427-37

Ebert TA (1967) Growth and repair of spines in the sea urchin strongylocentrotus purpuratus (stimpson). Biol Bull 133(1):141-9

Ebert TA (1986) A new theory to explain the origin of growth lines in sea urchin spines. Mar Ecol 34(1):197-199

Ebert TA (1988) Growth, Regeneration, and Damage Repair of Spines of the Slate-Pencil Sea Urchin Heterocentrotus mammillatus. Pac Sci 42(3 - 4):160-72

Ebert TA, Russell MP (1993) Growth and mortality of subtidal red sea urchins (Strongylocentrotusfranciscanus)at San Nicolas Island, California, USA: problems with models. Mar Biol. 117:79-89

Fox J, Weisberg S 2011 An {R} Companion to Applied Regression. Thousand Oaks CA: Sage http://socserv.socsci.mcmaster.ca/jfox/Books/Companion

Gage JD (1991) Skeletal growth zones as age-markers in the sea urchin Psammechinus miliaris. Mar Biol 110 217-28

Goldsmith JR, Graf DL, Joensuu OI (1955) The occurence of magnesian calcies in nature. Geochim Cosmochim Ac 7:212-30

Gorzelak P, Stolarski J, Dery A, Dubois P, Escrig S, Meibom A (2014) Ultrascale and microscale growth dynamics of the cidaroid spine of Phyllacanthus imperialis revealed by 26Mg labeling and NanoSIMS isotopic imaging. J Morphol 275(7):788-96

Grossmann JN, Nebelsick JH (2013) Comparative morphological and structural analysis of selected cidaroid and camarodont sea urchin spines. Zoomorphology 132(3) 301-15

H. Wickham (2009) ggplot2: Elegant Graphics for Data Analysis. Springer-Verlag New York.

Hasenpusch W (2000) Die Stachel der Griffelseeigel Mikrokosmos 89(1):23-7

Heatfield B M (1971) Growth of the Calcareous Skeleton during Regeneration of Spines of Sea Urchin, Strongylocentrotus purpuratus (Spimson): A Light and Electron Microscopic Study Journal of Morphology.

Hesse E (1900) Die Mikrostruktur der fossilen Echinoidenstacheln und deren systematische Bedeutung. E. Schweizertbart'sche Verlagshandlung, Stuttgart

Hozmann P (1983) Das unterschiedliche Härteverhalten biogener und anorganischer Calcitkristalle Bochumer geologische und geotechnische Arbeiten 10:100

Lamare MD, Mladenov PV (2000) Modelling somatic growth in the sea urchin Evechinus chloroticus (Echinoidea: Echinometridae). J Exp Mar Biol Ecol 243:17-43.

Lauer C, Grun TB, Zutterkirch I, Jemmali R, Nebelsick JH, Nickel KG (2017) Morphology and porosity of the spines of the sea urchin Heterocentrotus mamillatus and their implications on the mechanical performance. Zoomorphology 137:139-154

Lauer C, Schmier S, Speck T, Nickel KG (2018) Strength-size relationships in two porous biological materials. Acta Biomater 77:322-32

Lauer C, Sillmann K, Haußmann S, Nickel KG (2018) Strength, elasticity and the limits of energy dissipation in two related sea urchin spines with biomimetic potential. Bioinspir Biomim 14(1):016018

Magdans U, Gies H (2004) Single crystal structure analysis of sea urchin spine calcites: Systematic investigations of the Ca/Mg distribution as a function of habitat of the sea urchin and the sample location in the spine Eur J Mineral 16(2):261-8

Mooi R 1986 Structure and function of clypeasteroid miliary spines (Echinodermata, Echinoides). Zoomorphology 106(4):212-23

Moureaux C, Perez-Huerta A, Compere P, Zhu W, Leloup T, Cusack M, Dubois P (2010) Structure, composition and mechanical relations to function in sea urchin spine. J Struct Biol 170(1):41-9

Nissen HU (1969) Crystal Orientation and Plate Structure in Echinoid Skeletal Units. Science 166:1150-2

Pearse JS, Pearse VB (1975) Growth Zones in the Echinoid Skeleton. Amer Zool 15:731-53.

Politi Y, Arad T, Klein E, Weiner S, Addadi L (2004) Sea Urchin Spine Calcite Forms via a Transient Amorphous Calcium Carbonate Phase. Science 306:1161-4

Presser V, Kohler C, Zivcova Z, Berthold C, Nickel KG, Schultheiß S, Gregorova E, Pabst W (2009) Sea Urchin Spines as a Model-System for Permeable, Light-Weight Ceramics with Graceful Failure Behavior. Part II. Mechanical Behavior of Sea Urchin Spine Inspired Porous Aluminum Oxide Ceramics under Compression. J Bionic Eng 6(4):357-64

Presser V, Schultheiß S, Berthold C, Nickel KG (2009) Sea Urchin Spines as a Model-System for Permeable, Light-Weight Ceramics with Graceful Failure Behavior. Part I. Mechanical Behavior of Sea Urchin Spines under Compression. J Bionic Eng 6(3):203-13

R Core Team (2018) R: A language and environment for statistical computing. R Foundation for Statistical Computing, Vienna, Austria

Radha AV, Forbes TZ, Killian CE, Gilbert PU, Navrotsky A (2010) Transformation and crystallization energetics of synthetic and biogenic amorphous calcium carbonate. Proc Natl Acad Sci USA 107(38):16438-43

Randall JE, Schroeder RE, Starck WA (1964) Notes on the biology of the echinoid Diadema antillarum. Caribb J Sci 4:421-33

Raup DM (1959) Crystallography of echinoid calcite. J Geol 67(1):661-74

Régis MB, Thomassin BA (1983) Anomalies de structure des radioles de Heterocentrotus mammillatus (Echinodermata: Echinoidea) en microcosme in vitro. Mar Biol 75(1):89-98

Revelle, W (2018) psych: Procedures for Personality and Psychological Research. Northwestern University, Evanston, Illinois, USA, https://CRAN.R-project.org/package=psych Version = 1.8.3.

Russell MP, Meredith RW (2000) Natural growth lines in echinoid ossicles are not reliable indicators of age: a test using Strongylocentrotus droebachiensis. Invertebr Biol 199(4):410-20

Schlüter N, Wiese F, Reich M (2015) Systematic assessment of the Atelostomata (Spatangoida and Holasteroida; irregular echinoids) based on spine microstructure. Zool J Lin Soc-Lon 175(3):510-24

Sethmann I, Putnis A, Grassmann O, Löbmann (2005) Observation of nano-clustered calcite growth via a transient phase mediated by organic polyanions: A close match for biomineralization Am Mineral 90(7):1213-7

Seto J, Ma Y, Davis SA, Meldrum F, Gourrier A, Kim YY, Schilde U, Sztucki M, Burghammer M, Maltsev S, et al (2012) Structure-property relationships of a biological mesocrystal in the adult sea urchin spine. Proc Natl Acad Sci USA 109(10):3699-704

Smith A (1980) Stereom microstructures of the echinoid test. Spec Pap Palaeontol 25:1-81

Smith A (2005) Growth and Form in Echinoids: The Evolutionary Interplay of Plate Accretion and Plate Addition. In: Briggs DEG (ed) Evolving Form and Function: Fossils and Development, Peabody Museum of Natural History, New Haven, pp 181-193

Strathmann RR (1981) The role of spines in preventing structural damage to echinoid tests. Paleobiol 7(3):400-6

Telford M (1982) Echinoderm spine structure, feeding and host relationships of four species of dissodactylus (Brachyura: Pinnotheridae). Bull Mar Sci 32(2):584-94.

Toader N, Sobek W, Nickel KG (2017) Energy Absorption in Functionally Graded Concrete Bioinspired by Sea Urchin Spines. J Bionic Eng 14(2):369-78

Towe K M (1967) Echinoderm calcite: single crystal or polycrystalline aggregate. Science 157:1048-50

Tsafnat N, Fitz Gerald JD, Le HN, Stachurski ZH (2012) Micromechanics of Sea Urchin spines. PLoS One 7(9) e44140

Vecchio KS, Zhang X, Massie JB, Wang M, Kim CW (2007) Conversion of sea urchin spines to Mg-substituted tricalcium phosphate for bone implants. Acta Biomater 3(5) 785-93

Weber J., Greer R., Voight B., White E., Roy R (1969) Unusual strength properties of echinoderm calcite related to structure. J Ultras Mol R 26:355-366

Weber JN (1969a) Origin of Concentric Banding in the Spines of the Tropical Echinoid Heterocentrotus. Pac Sci 23:452-66

Weber JN (1969b) The incorporation of magnesium into the skeletal calcites of echinoderms. Am J Sci 267(5):537-66

Zachos L G (2009) A new computational growth model for sea urchin skeletons. J Theor Biol 259(3):646-57

Supplementary to
Individual growth and morphology of the spines of *Heterocentrotus mamillatus*

Supplementary 1 (Fig. S1):	Mass length relations in animals HM1-HM8
Supplementary 2 (Fig. S2):	Distal growth layer occurrence in relation to primary spine positionfor HM1- HM8
Supplementary 3 (Fig. S3):	Histograms of distal growth layer frequency in HM1-HM8
Supplementary 4 (Fig. S4):	Test diameter of animals correlated with different spine parameters
Supplementary 5 (Fig. S5):	Growth stages of spines broken down for all distal growth layers
Supplementary 6 (Fig. S6):	Porosity comparison of aboral and oral spines

Raw Data files can be found alongside with this supplementary information on the same server. The following files are provided:

SecondarySpines.xlsx:	Data of Secondary Spines (Fig. 4)
SpineEvaluation_for_R.xlsx:	Data of Primary Spines
TestDiameter.xlsx:	Diameters of *H.mamillatus*' tests
DiameterPlot_Fig8.xlsx:	Data for Fig 8 only

Supplementary 1

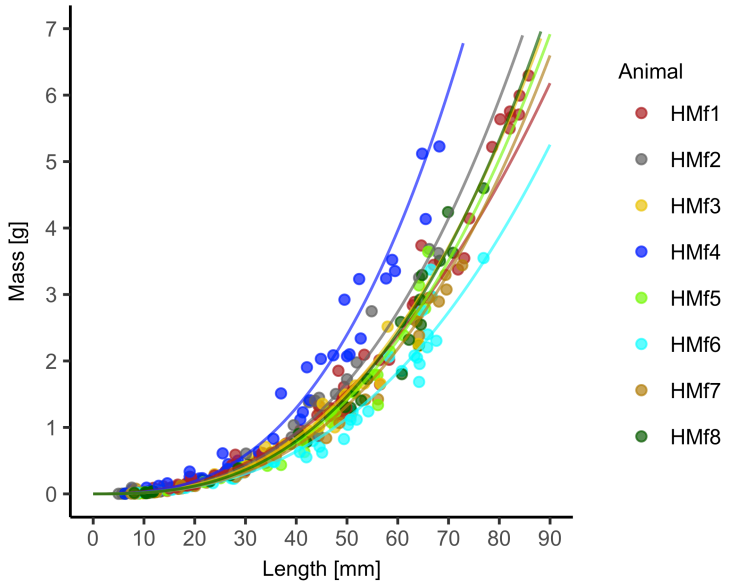

Fig. S1: It is evident that each animal has a slightly different relation between length and mass. Notably different are HM4 and HM6. MH4 tends to have heavier spines (=lower porosity) at the same length than all other animals, HM6 has lighter spines (higher porosity). Fits are in the same colours as animals and details are given in table S1.

Table S1: Details to the power law fits $y=ax^b$ in Fig S1 obtained by Excel. n = sample size

Animal	***n***	***a***	***b***	r^2
HM1	70	1.51E-04	2.36	0.948
HM2	45	4.51E-05	2.69	0.950
HM3	51	4.79E-05	2.65	0.963
HM4	52	4.90E-05	2.76	0.961
HM5	47	3.66E-05	2.70	0.989
HM6	55	4.36E-05	2.60	0.989
HM7	46	3.05E-05	2.73	0.970
HM8	47	3.25E-05	2.74	0.984

Supplementary 2

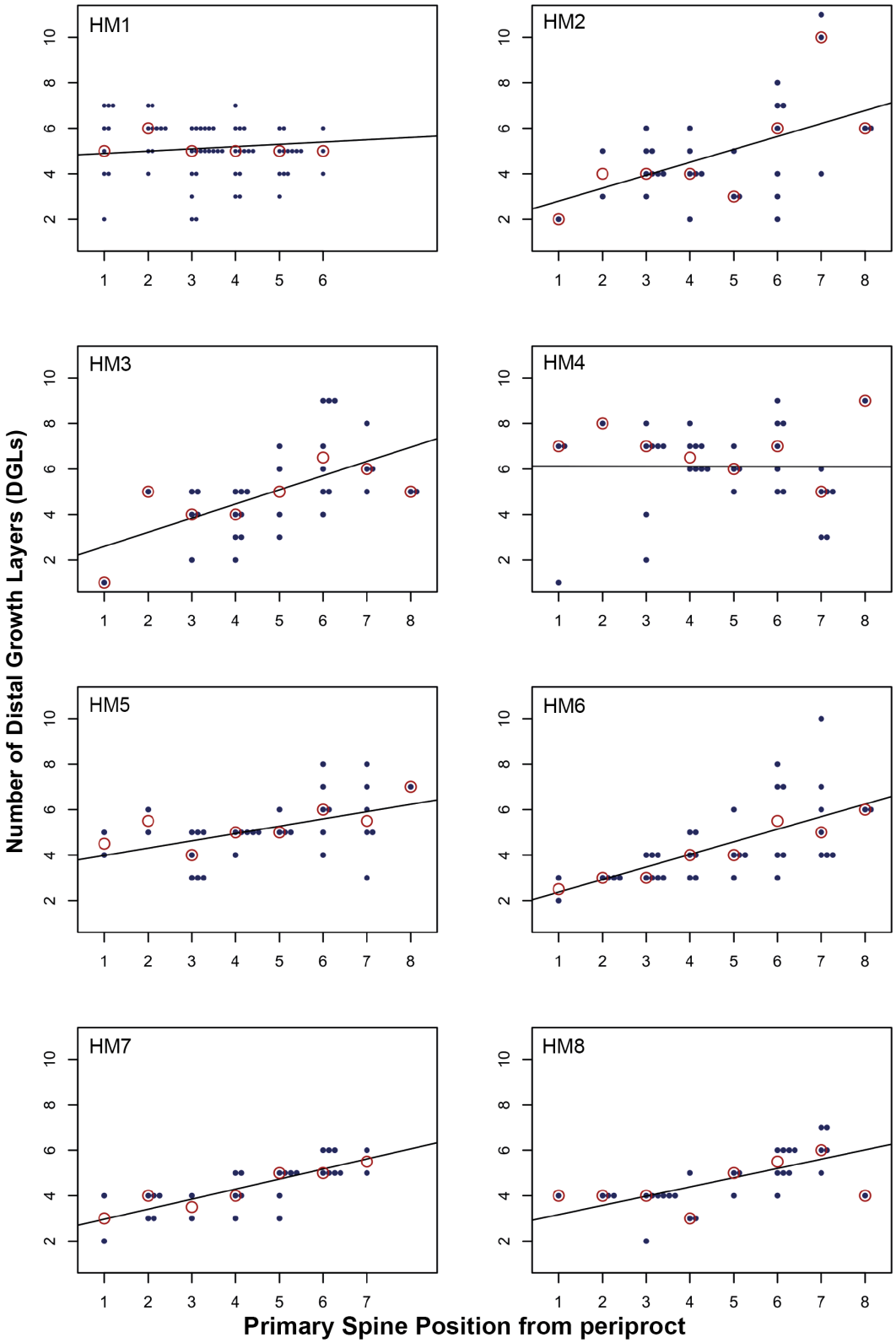

Figure S3: The average number of distal growth layers increases for each animal except HM4 from the aboral to the oral side. Red circles indicate the median. For HM1 data from the most oral plates were not collected, thus the trend here can be omitted. All in all, the scatter for a single spine position can be considerable, reducing the goodness of fit. r^2 values are as follows: HM1: 0.038, HM2: 0.246, HM3: 0.305, HM4 <0.001, HM5: 0.224, HM6: 0.417, HM7: 0.565, HM8: 0.44

Supplementary 3

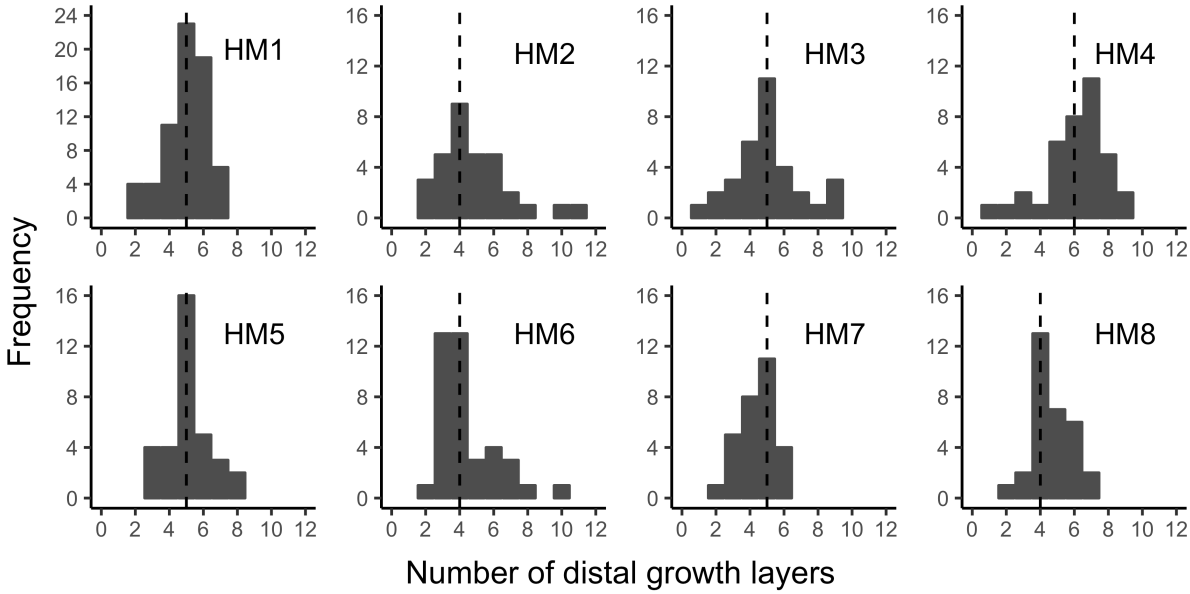

Figure S2: Distribution of distal growth layers in HM1-HM8. For HM1 oral plate positions 7,8 are lacking, explaining why growth layer rich spines are missing in this distribution. For all other animals primary spines until the peristome were analysed. A Shapiro test for each animal revealed that these distributions are non-parametric (p-value < 0.05). Not that scale of y-axis of HM1 is different from all other plots.

Supplementary 4

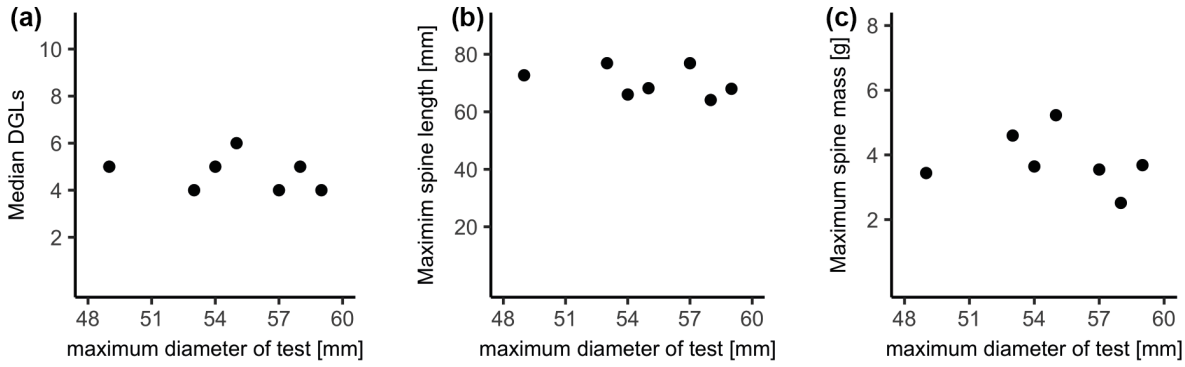

Figure S4: No relations were found for maximum diameter of the test and median of distal growth layers (dGLs) (a, $R^2 = 0.07$), length of the longest spine (b, $R^2 = 0.05$) and mass of the heaviest spine (c, $R^2 = 0.08$). All R^2 values correspond to linear models.

Supplementary 5

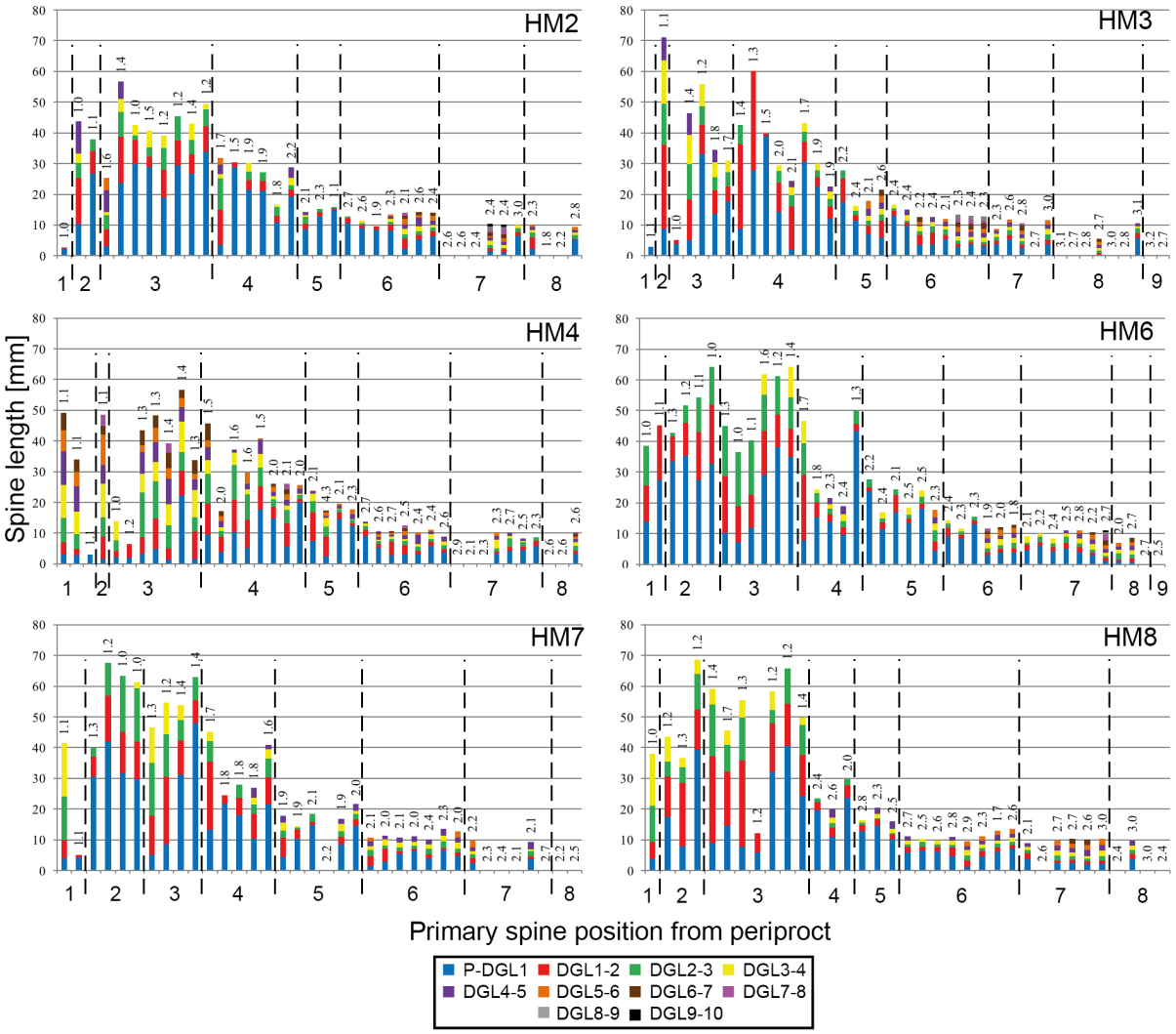

Figure S5: Extent of distal growth layers (DGLs) in all animals except of HM1 (not measured). As for HM5 (see Results), the extent of the first growth stage (distance between last proximal and first distal growth layer (P-DGL1), blue) is for most spines the larger than later growth stages, especially for those from primary spine positions 4-9. Notable exceptions are often the aboral primary spine positions 1-3. Only for HM4 the first growth stage is less predominant.

Supplementary 6

The porosity of three aboral spines from the first PSP, and from four oral spines was determined and compared to results of Lauer et al. (2017) from large aboral spines from 2-3 PSP. Porosity was analysed as described in Lauer et al. (2017). Therefore, SEM analyses of infiltrated cross sections of the spines (extracted in intervals of 10 %, 25 %, 50 %, 75% and 90 % of the spine length from the base) were carried out with a Hitachi TM 3030 scanning electron microscope (Hitachi High-Technologies Europe GmbH, Krefeld, Germany).

Porosity signatures could be identified for aboral and oral spines (figure S6a). Oral spines tend to be denser than aboral spines showing average porosities between 0.5 and 0.6, whereas aboral spines range between 0.6 and 0.7 over the spine length. The trend of lower porosity of the oral spines is caused by the higher number of growth layers, which are the densest part of the spine and thus make up a larger share of the cross section (figure S6b-d). For both, small spines of PSP 1 and larger spines of PSP 2-3, the porosity increases towards the tip of the spine (Fig. S6a). In oral spines, the highest porosity is found in its middle decreasing towards the base and the tip. Variations in oral spine porosities are larger than in aboral spines. Differences in porosity of youngest primary spines (PSP 1) and the largest primary spines (PSP 2 and 3) were minor, although the youngest spines tend to be denser than larger older spines and their porosity covers a larger range (figure S6a).

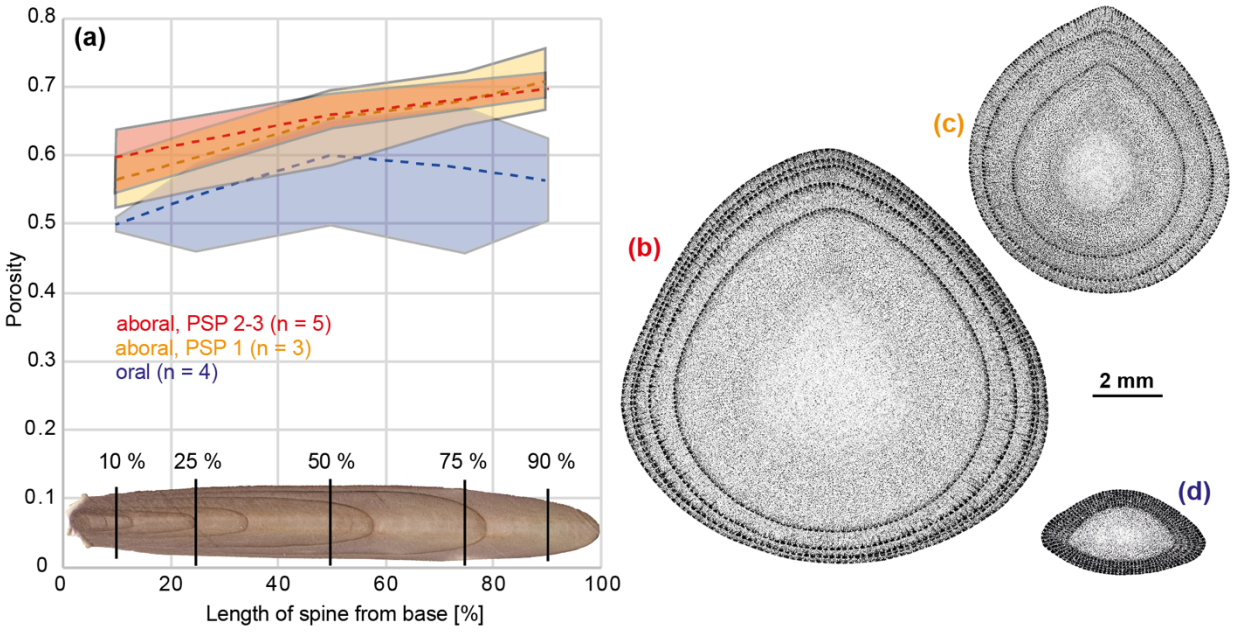

Figure S6: Porosity of oral and aboral spines measured on cross sections extracted from 10 %, 25 %, 50 %, 75 % and 90 % of the spine length as described in Lauer et al. 2017. Colours indicate the range of porosity for the spine types and dotted line is the average porosity, respectively. Representative horizontal sections at 50 % of the spine length of (b) a large aboral spine (PSP 2), (c) a small aboral spine (PSP 1) and (d) an oral spine are given (all from HM4).

Manuscript 6 with Supplementary Material

On the relationship of amorphous calcium carbonate and the macromechanical properties of sea urchin spines

(20+10 pages)

ON THE RELATION OF AMORPHOUS CALCIUM CARBONATE AND THE MACROMECHANICAL PROPERTIES OF SEA URCHIN SPINES

Christoph Lauer[1,*], Sebastian Haußmann[1], Patrick Schmidt[1,2], Carolin Fischer[3], Doreen Rapp[3], Christoph Berthold[1], Klaus G. Nickel[1]

[1]Department of Geosciences, Division of Applied Mineralogy, Eberhard Karls University of Tübingen, Wilhelmstraße 56, 72074 Tübingen, Germany

[2]Department of Prehistory and Quaternary Ecology, Eberhard Karls University of Tübingen, Schloss Hohentübingen, 72070 Tübingen, Germany

[3]NETZSCH-Gerätebau GmbH, Applications Laboratory, Wittelsbacherstraße 42, 95100 Selb, Germany

*corresponding author:
Christoph Lauer
Department of Geosciences - Division of Applied Mineralogy
Wilhelmstraße 56
D-72074 Tübingen
Germany
Tel.: +49 7071 29 76810
Fax: +49 7071 29 3060
E-mail address: christoph.lauer@uni-tuebingen.de

Key words: amorphous calcium carbonate, mechanical properties, Echinoderm calcite, inra-red spectroscopy, thermogravimetry

Amorphous calcium carbonate (ACC) plays a crucial role in the formation of biogenic carbonates. It is widely accepted that ACC and organic macromolecules alter the fracture properties of Echinoderm calcite from the well-defined cleavage planes of the raw material to conchoidal. However, the influence of ACC on the outstanding macromechanical properties of Echinoderm calcite is unknown. To address this question full grown spines of the slate pencil urchin are shortly heated to 250 °C. At this temperature all ACC is crystallized indicated by differential scanning calorimetry. Other processes, such as the decomposition of organics, Mg calcite transformation, loss of water, formation of considerable cracks and micropores do not take place, as found by X-ray diffraction, infra-red spectroscopy, thermogravimetry coupled with mass spectroscopy and secondary electron scanning microscopy. By these analyses an ACC content of 5.5 wt.%, a water content of 2.5 wt.% and an organic content of << 1wt.% of full grown spines is determined. Heated spines are compared to an untreated control group and no significant differences in compressive strength, bending strength, damage tolerance and Young's modulus are detected. This highlights the low influence of ACC on the macromechanical properties of Echinoderm calcite, which are likely established by their intricate microstructure.

Introduction

The formation of carbonate shells of marine organisms has been enigmatic for a long time. Nature achieves crystallization of carbonate minerals at ambient conditions, where human technology requires high pressures and temperatures. The key in formation of biogenic calcite is the involvement of a more soluble [1], energetically favorable [2] transient phase: amorphous calcium carbonate (ACC) [2a, 3]. This thermodynamically unstable phase [4] is stabilized by its Mg content [5] and ion impurities [6], as well as organic macromolecules [4, 7], which induce and guide the crystallization of ACC [8].

ACC contains structurally bonded water [9] and has the general formula $CaCO_3 \bullet nH_2O$. The amount of molecular water is highly variable and depends on the size of ACC nanoparticles [10] and includes completely dehydrated forms in crystallization sequence (e.g. [2b]). Many authors give a value of n = 1 for stabilized biogenic calcite (e.g. [7, 11]), but also forms with less water have been found (spines of *P. lividus* [12]. In any case ACC is not a single phase but a polyamorph and variable in its water content [13].

As the formation of biogenic calcite was enigmatic for decades, so were its mechanical properties, especially those of sea urchin spines. Optically and in X-ray diffraction (XRD) they appear as perfect calcite single crystal, but they lack the calcite characteristic cleavage planes along {104} and even show glass-like, conchoidal fracture surfaces (e.g. [14]). Berman et al. [15] found that proteins are oriented obliquely to the cleavage planes and thus a "composite material at the molecular level" impedes the calcite typical fracture. A more recent study [16] treated sea urchin spines with UV light for

degradation of organic content and detected a more "calcite-like" fracture along cleavage planes in treated samples than in untreated ones.

Seto et al. [7] found evidence for the long held assumption [14b] that calcite is a mesocrystal of numerous calcite nanocrystals (~100 nm) aligned along the crystallographic c-axis. These nanocrystals are embedded in a matrix made out of ACC and macromolecules. The whole mesocrystal might be described in a "brick and mortar" fashion altering the fracture properties from well-defined along cleavage planes to conchoidal [7]. This mesocrystal structure contains between 8-10 wt.% ACC in mature spines [7, 12].

Although the influence of the organic macromolecules on the fracture and micromechanical properties of sea urchin spines is well studied, it was not investigated yet, how their macromechanical properties, such as compressive strength, bending strength and Young's Modulus, are affected by the ACC content. This study sets out to fill this gap.

Spines of the slate pencil urchin *Heterocentrotus mamillatus* were chosen for this purpose as their structural composition [17] and the interplay with mechanical properties [18] is covered in literature. Spines of this species are unusually large for echinoids [19] (Figure 1a,b) and feature striking growth layers in sections, which are outlines of past growth stages of the spines [20] (Figure 1c). These dense growth layers (porosity, ϕ = 0.2-0.3) are mechanically beneficial, as they increase bulk stiffness of the highly porous spines (porosity of 0.58-0.7) [17b] by giving them a kind of core shell structure.

Spine segments fail in uniaxial compression like a brittle foam, with no catastrophic failure and a plateau-like strength level after linear elastic increase [21]. Repeated strength recovery and drops in this plateau are also attributed to the dome shaped end of growth layers [18c] (Figure 1c). Lauer et al. [18a] demonstrated, that these peculiar spines reduce or even lack the size effect predicted by Weibull fracture statistics [22] for brittle materials.

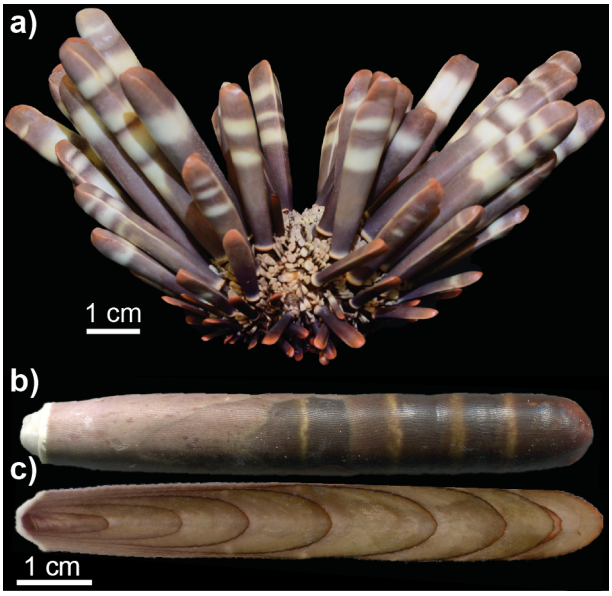

Figure 1: Heterocentrotus mamillatus and its large primary spines (a). b) shows the comparably bulky appearance of these spines and in longitudinal sections (c) the growth layers are well visible as smaller versions of the same spine at earlier growth stages.

In this paper we attempt to identify the influence of ACC on the macromechanical properties of *H. mamillatus* spines by heating them above the crystallization temperature of ACC and comparing the compressive strength, the bending strength and the Young's Modulus to unheated samples. This is not trivial, because besides the crystallization of ACC, heat induces many changes in biogenic calcite. (1) Organic matter will decompose (e.g. [12]). (2) Thermodynamically metastable Mg calcite will transform into energetically more favorable low Mg calcite phases (e.g. [23]). (3) Furthermore, as ACC contains water, this phase will also be present in the system and escape at elevated temperatures [24].

Therefore, all processes and their respective temperature dependence need to be characterized in order to find a suitable temperature for inducing ACC crystallization only, or, if not possible, separate the influences of the processes (1-3) on the mechanical properties of heated *H. mamillatus* spines. Hence we had to employ a number of techniques to separate individual processes.

Results and Discussion

Analytical determination of relevant temperatures

A weak mass loss in thermal gravimetry (TG) experiments with a ramp of 5 °C/min is visible from ~250 °C in Figure 2. Mass spectroscopy (MS) simultaneously records first water emissions at 220 °C, so this temperature is likely the onset of mass loss. (Figure 2). Long-time heat treatments (Figure S1, S = supplementary material) showed that a very low mass loss indeed is detectable already at 150 °C. Thus a process leading to water loss is active from about 150 °C, even though the kinetics are slow. From temperatures exceeding ~250 °C the MS recording (Figure 2) indicates the additional emission of CO_2.

For the determination of the maximum relative mass loss we performed a number of experiments at long dwelling times at different temperatures (Figure S1). The results indicate losses well below 1 % at 150 °C, in the order of 2.5 % for 250 °C and 350 °C, and approx. 5 % at 500 °C. These values are given as dots in Figure 2 against the low mass loss in TG at these temperatures.

The most pronounced mass loss in TG occurs above 500 °C and approaches a maximum at 770 °C, which coincides with the maximum CO_2 gas emission, which totals to 44.1 wt.% (Figure 2). The total water loss sums up to 2.5 wt.% being in agreement with [25] who studied water species in echinoids. Water loss shows increased rates between 470 °C and the maximum at 550 °C and a second maximum at 660 °C, which coincides with the onset of the final CO_2 loss from a carbonate decomposition reaction. At roughly 700 °C the water loss is completed, at 800 °C the CO_2 loss.

The total mass loss recorded by TG is 30.27 mg (46.2 wt%) and by MS 30.58 mg (46.6 wt%). The difference of 0.3 mg is well within the measurement error of 1-3%, however it might also account for combusted organic material.

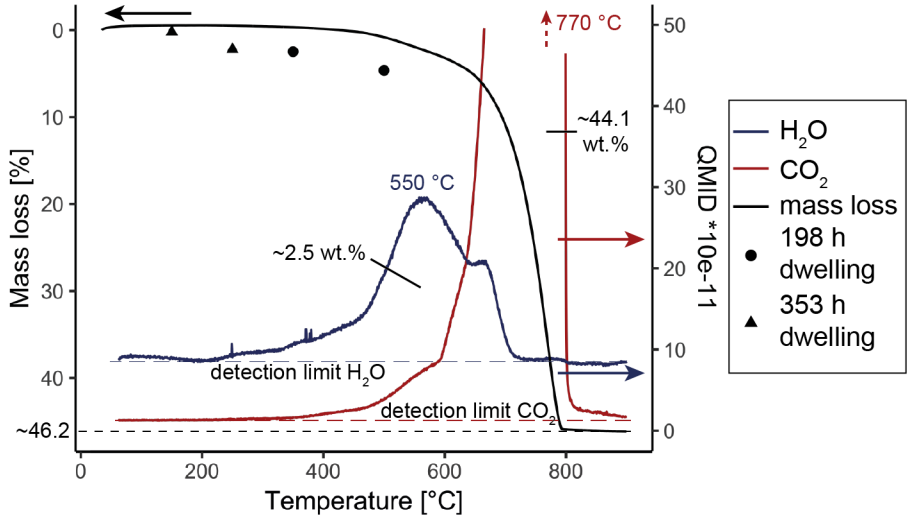

Figure 2: TG-MS measurement (5 °C/min, synthetic air atmosphere) of a 65.59 mg powder sample of H. mamillatus. Data dots show mass loss of segments from long term dwelling experiments (see also Figure S1).

With increasing temperature samples of *H. mamillatus* change their color from the initial brown-red to grey-white (thick sections used for IR spectroscopy, Figure 3a). Strong buckling of the 150 µm thick section becomes apparent at 600 °C (Figure 3b). The loss of water is well documented by ex-situ IR spectroscopy (Figure 3C) with focus on the H_2O combination band at 5200-5000 cm^{-1} and on the sharp fundamental OH^- stretching vibration at 3700 cm^{-1} emerging form 250 °C (Figure 3D) and indicating the presence of brucite [26]. The broad stretching band at 3600-3000 cm^{-1} is caused by H_2O undergoing hydrogen bonding of varying strengths and cannot be used for quantification because of the superposition of H_2O and OH absorption phenomena that cannot be disentangled. For comparison, a spectrum of Iceland spar (water free geological calcite) is also shown (black curve). It is obvious that all observed absorption bands can either be explained by calcite vibrations or water species. CH bands caused by organics bands, which would be expected in the 3000-2000 cm^{-1} region are not present or remain below the detection limit. The intensity of the H_2O combination band is ± constant or even slightly rising until 400 °C and drops to zero before 600°C, at which temperature the brucite vibrations also disappear (Figure 3a) .

The DSC heat flow curve of a powdered sample (Figure 3E) shows an exothermal peak with an enthalpy of ~8.1J/g between 150-250 °C. As no significant amounts of H_2O and CO_2 are released in this temperature interval (Figure 2, figure 3d) this peak is attributed to the crystallization of ACC, which is in good agreement with literature [12]. The IR ν_2/ν_4 band height ratio of the *H. mamillatus* spines' spectrum, an indirect proxy for ACC crystallization [3] also decreases sharply until 250 °C and then plateaus, as the ACC caused lattice disorder is healed [27](Figure S2).

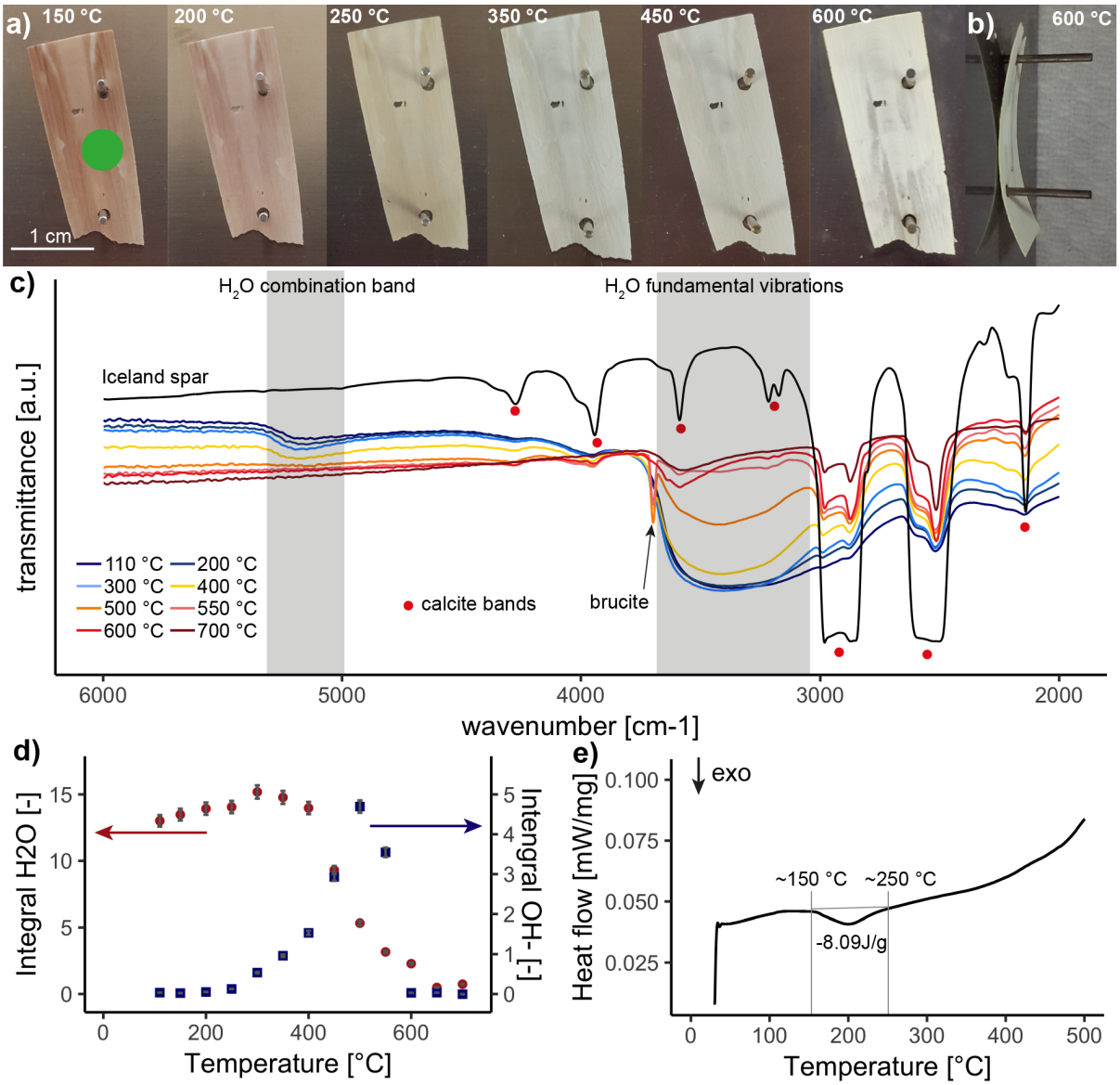

Figure 3: Color changes of the thick section upon heating with green dot representing aperture (a) and buckling of the thick section (b). Spectra and relevant bands are shown in c) and integrals of the 5200 cm^{-1} H_2O vibration and 3700 cm^{-1} isolated OH^- vibration are shown in d). DSC curve of a 62 mg powder sample is displayed in e).

Both stadiums of Mg calcite decomposition (formation and decomposition of dolomite) described by [23a] could be identified in XRD and they are both dependent on temperature and on dwelling time. Formation of dolomite was found already at 250 °C when held for 353 h (Figure 4). At shorter dwelling times (4 h) it could not be identified before 350 °C and was detectable until 500 °C (Figure 4). When held longer at 500 °C the dolomite peak vanishes and after 126 h a clear and Mg free shoulder develops the Mg calcite [104] peak (Figure 4). Peak intensity decreases with temperature and dwelling time and the full width at half maximum (FWHM) of [104] increases significantly (much more than the observed natural variations in a single spine) from 250-350 °C (Figure S3a). 353 h dwelling at 250 °C shifts this increase to lower temperatures (Figure S3a). d-values of [104] peak vary strongly in a single spine (Figure S3b), however, an increase in d is obvious from 200 °C to 300 °C, followed by a

drop to lower d-values (Figure S3b). Alberic et al. [12] found a similar temperature dependence of d-values for skeletal elements of *P. lividus* and argued that the increase is due to ACC crystallization and the decrease to removal of organic phases. Prolonged dwelling times at 150 °C and 250 °C shift the increase in d values to lower temperatures and d-values after 353 h even clearly surpass those from 4 h dwelling at 300 °C (Figure S3b).

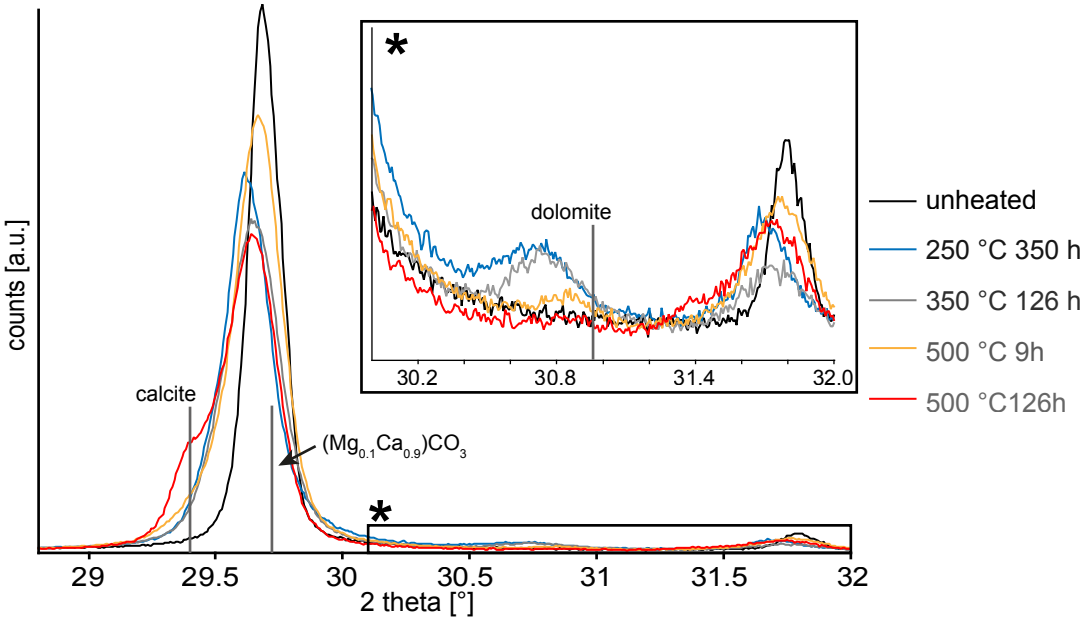

*Figure 4: XRD diffraction patterns from powdered samples of the main Mg calcite peak [104] exposed to different temperatures and for different times. Peak positions are indicated. * denotes magnification to increase visibility of weak dolomite peak.*

Using the peak position of the [104] carbonate main reflection the bulk $MgCO_3$ content of an unheated spine was determined to be ~9.5 mol% well matching literature values [28]. Attempts to measure Mg distribution locally by means of electron microprobe (EMP) failed, as totals were below 90 % (S4). The low totals are explained by a strong interaction of the electron beam and the sample surface, often resulting in vigorous reactions and degassing (Figure S4a, b).

Figure 5 shows how the stereom structure of the spines reacts to heating by forming cracks (a-d) and forming a peculiar microporosity (c,d) also described by [7] and attributed to the crystallization and dewatering of ACC. From dilatometry (Figure S5) we know that *H. mamillatus* spine segments show an irreversible length change on heating, amounting to ~0.1 % at 250 °C (Figure S5a, b) and ~2 % at 500 °C (Figure S5c). This is caused by microcrack or microporosity formation (Figure 5). However, microporosity was not found on samples heated up to 4 h at 250 °C (Figure 5b).

Detailed studies on the microstructure after heating are given in Figure S6,7 and show that only after long dwelling (353 h) considerable microporosity develops at 250 °C (Figure S6d). At 350 °C microporosity arises already after 4 h (Figure S6e). At 500 °C microporosity is well developed after 4 h and prominently visible with strongly widened cracks after 198 h (Figures 5c, d, S6i). Almost all

cracks are aligned roughly perpendicular to the calcite c-axis and are thus best seen in sections parallel to this axis (Figure S6h). Microporosity develops in the center of struts first and only a small proportion of the pore volume reaches the surface. Measurements of the same location with increasing acceleration voltages confirm this impression. At the highest acceleration voltage most micropores are visible indicating that they are located shallowly below the surface Figure S7. Intriguingly, even after decarbonization at 1050 °C the stereom structure persists (Figure 5d) in the form of lime (CaO) grains, including traces of the microporosity (Figure S6j-l).

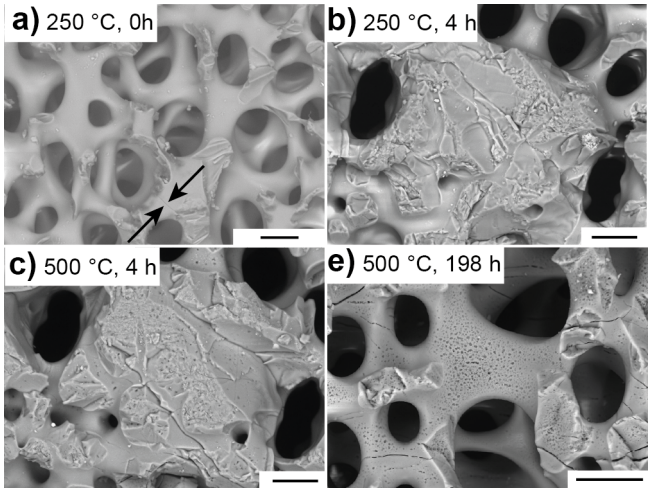

Figure 5: Development of microporosity in H mamillatus' spines upon heat treatment. Microporosity has not evolved at 250 °C (0-4h) (a,b) and emerges from 350 °C onwards when heated for 4 h. Small cracks are already visible at 250 °C, indicated by arrows (a). Pciture c) shows the same strut as in b) after heated to 500 °C with increased microporosity and cracks. A sample heated for nearly 200 h at 500 °C (d) shows much more microporosity than c) and considerable cracking. Scale bars are 20 µm.

Based on these results mechanical testing samples were heated to 250 °C with ramp of 1 °C/min and no dwelling time. This temperature with no dwelling time ensures crystallization of all ACC (DSC measurement, Figure S8) without starting the Mg calcite transformation and the water loss inducing large flaws (Figure 5) to the structure. Hence, this temperature is suitable to crystallize ACC into calcite and water and assess its influence on macromechanical properties. Formation of very small cracks (Figure 5a) is responsible for the irreversible length change recorded in dilatometry (Figure S4) and might alter the mechanical properties of the spines slightly.

Mechanical tests

For uniaxial compression (UC) and 3-point bending (3PB) each, we prepared two sample groups that were statistically similar in average porosity, specimen volume and number of growth layers as these factors can have a profound influence on mechanical properties [18a]. One group was heated as

described above and the other group was the unheated control group. For more information of the statistical similarity of the groups the reader is referred to S9.

Table 1 summarizes the key data from mechanical testing. No difference in compressive strength, σ_{UC} and Young's Modulus, E was found between heated and unheated samples. A drop in bending strength, σ_{3PB} is observed, although not statistically significant (Wilcoxon test: p-value: 0.24).

Table 1: Overview of the data from the mechanical tests. Values for heated samples are reported in italics. UC = uniaxial compression, 3PB = 3 point bending, RFDA = resonance frequency damping analysis

Method	mechanical property measured	median	mean	range	statistical test
UC	compressive strength, σ_{UC} (n = 25, *24*)	55.3 MPa *53.3 MPa*	53.5 MPa *56.1 MPa*	25.7-118.1 MPa *20.8-107.8 MPa*	Wilcoxon test: p = 0.7
3PB	bending strength, σ_{3PB} (n = 16, *16*)	33.4 MPa *28.1 MPa*	34.0 MPa *32.2 MPa*	21.7-53.9 MPa *16.8-64.7 MPa*	Wilcoxon test: p = 0.24
RFDA	Young's Modulus, E (n = 7, *7*)	5.5 GPa *5.3 GPa*	5.5 GPa *5.3 GPa*	2.7-7.3 GPa *2.6-7.0 GPa*	Welch t-test: p = 0.7

Weibull analysis (fitted with maximum likelihood method) supports that both groups, unheated and heated, are undistinguishable in UC. Their Weibull modulus m (unheated: 2.8, heated: 3.1) and characteristic strength σ_0 (unheated: 60 MPa, heated: 63 MPa) are nearly identical (Figure 6a). There was also no difference in failure behavior exceeding the linear elastic limit. Both groups showed the characteristic, foam-like failure in a low plateau with occasional load increases and drops, described as "cascading-graceful failure behavior" by [18c]. The median strength of the "plateau" is 19 % of σ_{UC} for unheated samples and 16 % of σ_{UC} for heated samples. These differences are statistically not significant (t-test: p = 0.33) (Table S9).

Although the median σ_{3PB} of both groups is statistically not significant (Table S9), Weibull analysis reveals differences between groups. Unheated samples fail more reliable (= have a higher m) than heated samples (Figure 6b). This points towards the presence of additional flaws in heated samples, that were absent in the unheated samples. As heating induces an irreversible length increase and accompanying flaws could be identified in SEM pictures (Figure S4a), it is likely that these flaws altered the statistics of bending failure.

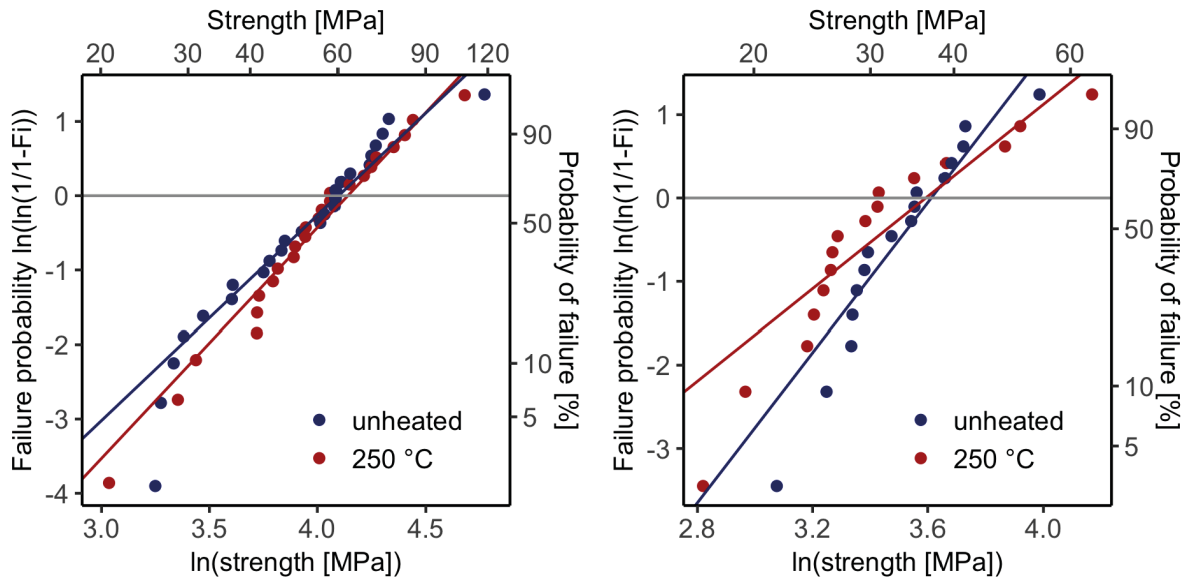

Figure 6: Weibull plots of unheated samples and heated (250°C) in uniaxial compression (UC) (a) and 3 point bending (3PB) (b). In UC both groups are practically identical (m = 2.8, 3.1 and σ_0 = 60 MPa, 63 MPa for unheated and heated, respectively) in bending m is higher for unheated samples (m = 4.5 vs. 2.8), however, σ_0 is comparable (σ_0 = 37 MPa vs. 36MPa).

In contrast to UC and 3PB, resonance frequency damping analysis (RFDA) is a non-destructive testing method and the same samples could be tested before and after heat treatment. Figure 7 shows how *E* and the relative density decrease with heating up to 500 °C due to the development of cracks and microporosity (Figure 5, S3). Changes in *E* up to 250 °C are statistically not significant. However, it is noteworthy that *E* decreases consistently for all seven samples, although in the range of error bars and only by 2-8 %. After exposure to 500 °C *E* dropped by 12-26 %. If we model the loss in *E* from porosity increase (relative density decrease) using the open pore model by [29], which was successfully applied to model *E* of spines of *H. mamillatus* [18b], it accounts for up to 50 % of this decrease. The remaining decrease is surprisingly small and may be attributed to crack formation.

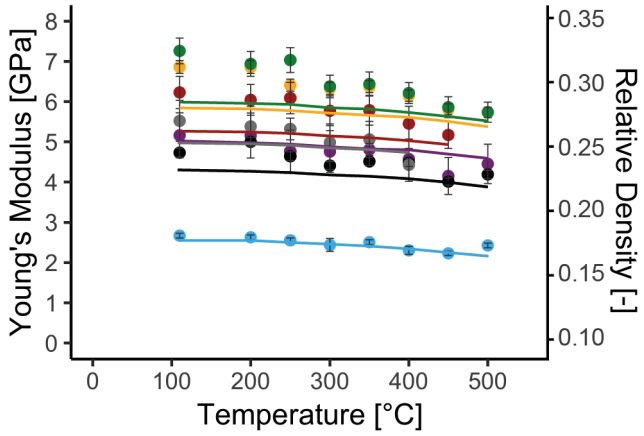

Figure 7: Change in Young's Modulus (data dots) and relative density (lines) upon heat treatment of seven cylindrical rods machined out of H. mamillatus spines. Samples were heated stepwise to 500 °C. Each dwelling time was 4h and the ramp was always 1 °C/min.

Figure 8 summarizes the ongoing processes in the spines of *H. mamillatus* upon heat treatment. All of them except the final decarbonization also take place slowly at low temperatures (light grey shading) and are detectable when holding sample for a longer time at the relevant temperature. In the following paragraphs the interplay of these processes is discussed.

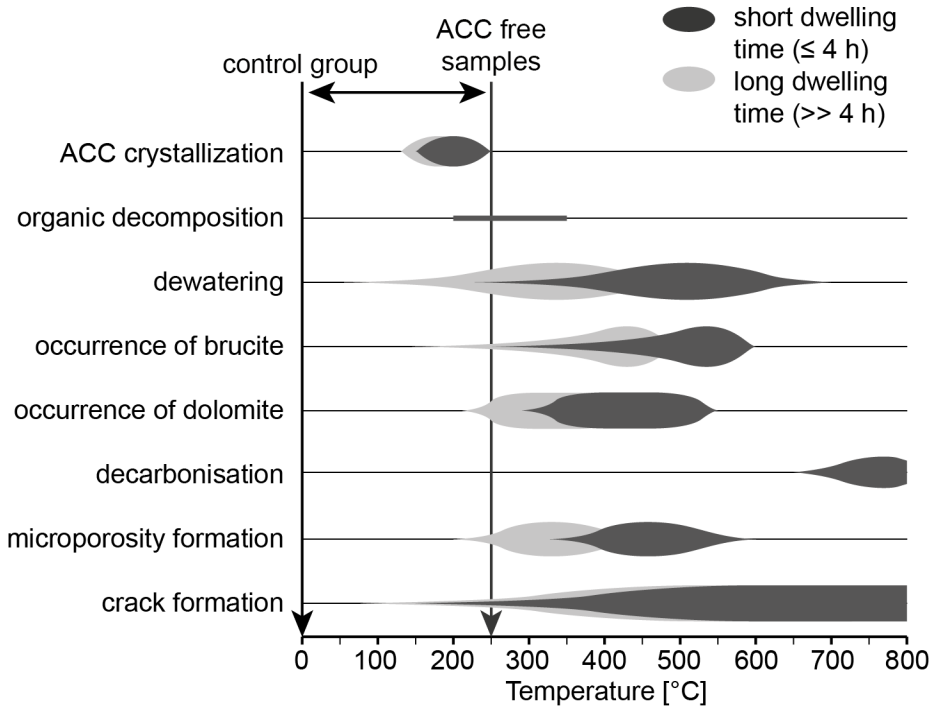

Figure 8: Schematic summary of all processes and their temperature range when heating spines of H. mamillatus. Approximate temperature ranges are given for short dwelling (dark grey) and long dwelling times (pale grey).

Nature of ACC

From our XRD results (Figure 4) we identify Mg calcite as the only crystalline starting phase and assume that all water in the spines originates from ACC. If the stoichiometry of the ACC is known, the ACC content could be estimated by the amount of water measured in TG-MS (Figure 2). Despite the reported findings of polyamorphs of ACC with varying amounts of water (e.g. [11b, 13]), most authors (e.g. [7, 11a, 30]) consider a 1:1 $CaCO_3$:H_2O ratio for ACC. For this ratio ~16 wt.% ACC would be present in the mature spines of *H. mamillatus*, which is considerably more than 8-10 wt.% reported by [7, 12], respectively. However, those authors studied other species (*Paracentrotus lividus* and *Heliocidaris crassispina*, respectively).

In the light of recrystallization and growth studies of sea urchin spines [2a, 31] it is highly likely that all calcite of the spines forms via a ACC crystallization. In respect to the very slow water diffusion

at <400 °C, the total water content may be retained and hence rather derived from an original 100 % ACC. Following this thought a minimum $CaCO_3$:H_2O ratio in ACC calculates to ~1:0.14, close to the one identified for *P. lividus* [12].

Direct evidence for the still present ACC content in the mature spines comes from DSC measurement (Figure 3e). With the formula given by Albéric et al. [12] a fraction of ~5.5±0.4 wt.% ACC is obtained (ΔH_{cr} = -14.3 ±1 kJ/mol [2b, 6], M = $(Mg_x\text{-}Ca_{1-x})CO_3$ = 98.66 g/mol, with x ≈ 0.09 [28], ΔH = -8.09 J/g (Figure 3e)). If all of this water would be found in ACC, it would result in $nH_2O > 3$, which is very unlikely for mature spines and could not be modeled as stable phase [10]. This has two implications: (1) Water from previous ACC crystallization is captured in the structure (if ACC has $n(H_2O) = 1$, ~0.8 wt.% H_2O are bound in ACC and 1.7 wt.% (>60 %!) originate from earlier ACC crystallization) and (2) the considerable ACC content of 5.5 ±0.4 wt.%, which makes the mature spines by definition a composite material (CITATION), has little influence on macro mechanical properties.

Nature of water species

The water found by TG-MS (Figure 2) and indicated by the H_2O combined band in FTIR measurements (Figure 3) may be attributed to both trapped free water inside already crystallized spine parts or the ACC still preserved, because freely vibrating water was reported to be similar to structural bound water of ACC [9]). Our IR data support this, as they show no change in water species and concentration over the temperature of ACC crystallization. Freely vibrating water was also found in other echinoids [25, 32]. During the crystallization of ACC water is expelled from the structure and potentially kept in cavities created. Such cavity formation is feasible as ACC is considerably lighter than calcite. Bolze et al. [33] give 1.62 g/cm^3 for 1:1 hydrated ACC, leaving ~40 % of space behind ($\rho_{calcite}$≈2.7 [34]) for accommodating free water and resulting in fluid inclusions dispersed over the whole structure. The size of these inclusions is potentially very small (nm) due to their formation mechanism. Trapped water of earlier ACC crystallization is thus a likely assumption. An elimination of water from the material may become only effective after the simultaneous decomposition of Mg calcite started and created pathways.

The emergence of isolated OH^- vibrations at 3700 cm^{-1} from 300 °C on at 3700 °C is attributed to brucite. This vibration is known to be unusually strong and sharp and is caused by the fundamental stretching mode of OH^- [26]. Brucite emerges roughly simultaneously (Figure 8) to the dolomite formation which starts at ~350 °C and at lower temperatures (250 °C) when held for longer. Dickson [23b] found that the formation of dolomite depends on the availability of water and is a dissolution/precipitation reaction. Quantities of brucite calculated from the linear absorption coefficient of the OH^- stretching at 3700cm^{-1} following [26] yield as little as 0.2-0.3 wt.%. This low amount of brucite explains why it was not detected in XRD. The brucite breakdown at 500 °C (Figure 3d) takes place at higher temperatures than reported by [35]. The shoulder in TG-MS at 660 °C (Figure 2) is then

probably due to the water loss of brucite breakdown as it shifts towards higher temperatures when faster ramps are used. The formation of brucite can account for CO_2 emissions recorded at low temperatures (Figure 2).

Mg calcite transformation

The above mentioned formation and later decomposition of brucite is one component of the Mg calcite decomposition. Furthermore we observed the formation of dolomite in XRD (Figure 4) as described by [23a] with a simultaneous widening of the FWHM of the [104] Mg calcite peak (Figure S6a) towards Mg free calcite, which indicates Mg poor calcite formation. If held for 126 h at 500 °C, also Mg free calcite was found (Figure 4).

Dolomite formation stops after only a small fraction of Mg calcite is transformed, probably due to the lack of sufficient water for the dissolution/precipitation process of Mg ions as described by [23b]. Pronounced water loss is observed form 400 °C onwards (Figure 2, 3d) and cannot be used as transport medium for the Mg ions anymore. Furthermore, in accordance with [23] the dolomite is enriched in Ca as its peak position is shifted towards calcite (Figure 4).

The dolomite and brucite formation takes place in a very similar temperature range (Figure 8) and from the here presented data we are not able to assess whether brucite formation occurs via direct conversion of Mg calcite or via transient poorly ordered dolomite. The exact nature of the process might depend on the initial Mg and water content of the spines.

However, it is important to point out that significant proportions of the CO_2 emissions below 500 °C (Figure 2) in spines of *H. mamillatus* are caused by decarbonization and are thus unsuitable for evidencing organic matter.

Microporosity formation

The development of microporosity was attributed to the loss of water from ACC [7]. However, the shape of these pores closely resemble structures described by [23b], which are caused by the dissolution/precipitation mechanism of Mg calcite decomposing into dolomite (see above). According to [23b] this process is firstly restricted to areas below the surface. As soon as pathways to the surface are created the water vapor escapes and the formation of dolomite stops. This matches well our observations, which on one hand show that microporosity formation takes place firstly below the surface (Figure S7) and stops at elevated temperatures (Figure 5d, 8), so does dolomite formation (Figure 4, 8) The presence of pressurized water and CO_2 might also explain the “jumping” of particles observed by Albéric et al. in TG [12] and the vigorous reaction under the electron beam in EMP (Figure S6).

Organic phases

Organic phases were not detected in spines of *H. mamillatus* by IR spectroscopy. Their content is thus below the detection limit as also noted by [32]. Also no additional exothermal peak in DSC was identified. If taking the color change as proxy for the combustion of organic phases, their decomposition occurs between 200-350 °C (Figure 3a). Because of the very low CO_2 emissions at those temperatures which can be also attributed to the brucite formation, the organic content is very minor. This agrees well with findings of Currey [36]. The mismatch of ~0.5 wt% in mass loss recorded by MS and TG might also indicate the presence of organics. As this amount is well within the error range of the MS quantification and as organic phases are combusted, quantification is not possible from this measurement, but it also indicates a low organic content.

The difference in water content and organic content in spines of *H. mamillatus* and *P. lividus* [12] is striking. *H. mamillatus* has a more than tenfold higher water content and *P. lividus* a much higher organic content, both measured by TG-MS. The early brucite formation and Mg calcite decomposition was not found/considered in [12] and could therefor account for some of the CO_2 emissions identified as organic phases. These cross-species variations in ACC, water and organic content show that generalizations from one species to another should be avoided.

Implications of mechanical results

Despite an irreversible dilatation of ~0.1 %, the associated crack formation and the crystallization of 5.5 ±0.4 wt.% ACC, the macro mechanical properties of the spines of *H. mamillatus* remain largely unchanged when heated to 250 °C. All this underlines the high damage tolerance of the material. Struts with cracks or even crack systems (Figure S4a,b) cannot carry any load, however, load is redistributed to the numerous other struts of the stereom, a mechanism common for brittle, cellular foam structures [37] and quasi-brittle materials [38]. The main factor controlling the strength is the size of the struts, which limit the size of individual defects, which may be envisaged to act as Griffith defects. These defects (broken struts) cannot grow easily, because the pore space provides a crack stopping by blunting and the direction of the cracks is governed by the morphology of the stereom, in which the thinnest strut parts provide a series of predetermined breaking points with appropriate orientation.

The strength of ideal foams (no flaws) is equal in compression and bending [29]. For the spines this ratio was found to be ~2:1 ([18b], this study), which is close to equality and far from the usual difference between bending and compressive strength in the order of 1:10 for brittle solids [29].

Often the analysis of the Young's modulus measured in RFDA (Figure 7) is physically more meaningful as it is a direct physical parameter, for which the modelling of structural influences is physically more straight forward [39] compared to strength issues. We found this parameter also very robust against structural changes attributed to heat treatment underlining the high damage tolerance of

the material. At 250 °C no significant drop in *E* was found. Even at 500 °C, where considerable microporosity and crack systems have developed, *E* dropped only by ~10 % considering the porosity increase.

Whereas micromechanical properties are governed by the interplay of ACC, organic phase and Mg calcite as could be demonstrated by many authors (e.g. [7, 15-16]), our results highlight that macromechanical properties of spines of *H. mamillatus* seem mainly governed by the porous stereom (foam) structure and its characteristic pore and strut size distribution resulting in a remarkable damage tolerance. Considering the important role organic phases have in nacre [40] their role in constituting the macromechanical properties of sea urchin spines is less important. Instead, crack blunting in the brittle foam composed out of $>10^7$ struts/cm^3 is certainly one key mechanism to keep the strength of partially failed samples on a high level.

Conclusions

1. Unlike mechanical properties of other biogenic ceramic composite materials such as nacre, the interplay of ACC, organic phases and Mg calcite has no or little effect on macromechanical properties of the spines of *H. mamillatus*. They are defined by the foam structure of the highly porous stereom. This structure is strikingly damage tolerant, even to numerous cracks induced by heating to crystallize ACC.
2. Spines of *H. mamillatus* contain up to 2.5 wt.% H_2O finely dispersed in the structure. Water remains in the structure at much higher temperatures (>500 °C) than expected (as hydrothermal fluid or OH^- in brucite). The dewatering process is guided by processes related to Mg calcite demixing and decomposition, which creates pathways for the water vapor to escape from structure.
3. We presume that a large proportion (>60 %) of this water is a remnant of earlier ACC, which crystallized during growth of the spines and was trapped afterwards in the structure. ACC content of mature *H. mamillatus* spines is estimated to be approximately 6 wt.%.
4. Decomposition of Mg calcite into thermodynamically stable phases needs to be taken into account when considering heat treatment of biogenic calcite in order to crystallize ACC or burn organic phases. Mg calcite decomposition starts slowly at temperatures <250 °C.
5. ACC plays an important role in the Mg calcite decomposition as it supplies the water to drive the process, which eventually leads to CO_2 emissions and brucite formation even before 250 °C.
6. Although probably all sea urchin spines contain ACC, organic phases and Mg calcite, the exact proportion varies strongly over species and generalizations are not possible.

Experimental

Material: Sea urchin spines of *H. mamillatus* were purchased from suppliers (Fischhaus Zepkow, Zepkow, Germany and Mineralien und Fossilien Handlung Peter Gensel, Weimar, Germany) and originate from the Philippines. These spines were completely untreated after collection from beaches (pers. comm. with Peter Gensel). Animals were not killed for the purpose of this study and are not listed as endangered species.

Heat treatment: For heat treatment a Nabertherm L3SH furnance (Nabertherm GmbH, Lilienthal, Germany) was used and if not mentioned explicitly otherwise, the heating and cooling rate was always 1 °C/min to avoid thermal shock.

Thermogravimetry (TG): A powdered sample of 65.59 mg was measured with a NETZSCH STA 449 ***F5*** thermogravimetry system (NETZSCH Gerätebau GmbH, Selb, Germany) coupled with mass spectroscopy (NETZSCH QMS 403 Aëolos Quadro) (TG-MS). Synthetic air was chosen as atmosphere in order not to influence the stability field of biogenic calcite. The sample was heated with 5 °C/min to 900 °C in open Al_2O_3 crucibles. The system was calibrated by measuring sodium bicarbonate ($NaHCO_3$) as there the mass loss upon heating is known and these are the same species as in biogenic carbonate (H_2O and CO_2). The measurement error for quantification is < 3 %. The powder sample was pre-dried at 110 °C for at least 24 h. Furthermore, long time dwelling experiments to evaluate the influence of time on the reactions at 150, 250, 350, 500 °C were conducted with powders and segments. The exact setup and more details are reported in S1.

Dilatometry: Two cylindrical machined samples of *H. mamillatus* were measured in a NETZSCH DIL 402C along the crystallographic c-axis and compared to the thermal expansion of geological calcite. Additionally, cylindrical samples used for RFDA measurements were measured after each heating step and the irreversible expansion could be quantified up to 500 °C (S3).

Infrared spectroscopy (IR): Diamond polished plan-parallel sections of *H. mamillatus*' spines and powders (KBr Pelleting) were measured with a Bruker Vertex V80 spectrometer (Bruker Corp. Billerica, USA) with a DTGS MIR detector. Sections were ground to a thickness of 150 µm which was found to provide adequate band hiehgt of the studied water vibrations: a H_2O combination band near 5220 cm^{-1}, a H_2O fundamental vibrations near 3600-3000 cm^{-1} and a fundamental OH^- stretching band that may either indicate brucite ($Mg(OH)_2$, 3700 cm^{-1}) or calcium hydroxide ($Ca(OH)_2$, 3646 cm^{-1}) [41], both products of the decomposition of Mg calcite. However at this thickness, the calcite bands (ν_2 = 876 cm^{-1}, ν_3 = 1435 cm^{-1}, ν_4 = 714 cm^{-1} [42]) are beyond saturation. Organic CH bands would be best to spot in the 3000-2000 cm^{-1} region (CITATION). The fragile sections of this highly porous material were mounted on specially designed stainless steel apertures with a 5 mm pinhole (figure 3a) and were heated and measured on these apertures to avoid damage when mounting into the spectrometer. This also insured that the same spot was measured on the samples after successive heating steps. Samples were held for 4 h at each temperature (110 °C, 200-700 °C in 50 °C steps) and measured in vacuum (≤ 2 mbar) in the 7000 and 400 cm^{-1} range with 1000 repetitions. Baselines of the H_2O combination band (5220 cm^{-1}) and the fundamental OH^- band (3700 cm^{-1}) were straight lines from which the area beneath the curve was integrated. The experimental error of the measurement was determined by measuring one section heated to 350 °C 10 times and integrating the bands of interest in the same manner. KBr pellets with 1 mg sample material and 249 mg KBr were analyzed for the ratio between the calcite ν_2 and ν_4 bands (S2). This ν_2/ν_4 ratio was described to indicates the presence of ACC as it is a proxy for the lattice disorder in carbonates and a decrease of this ratio is interpreted as crystallization of

ACC [3, 27]. All samples were ground and homogenised with KBr for 5 min. As grinding can increase the v_2/v_4 ratio [43], sample preparation was held consistent. Calcite powders were heated to the same temperatures as the plan-parallel sections (additionally: 150 °C, no temperatures above 500 °C) and also kept for 4 h. 32 repetitios were made and spectra were recorded in the range of 4000-400 cm^{-1}.

Differential scanning calorimetry (DSC): Powdered samples were analysed with a NETZSCH DSC 204 ***F1*** *Phoenix* in the temperature range from 30-550 °C (2 °C/min) in Ar atmosphere to document the heat flux in the sample. The crystallization of ACC is exothermic [2b] and the degradation of organic matter would also result in an exothermic deflection [16].

X-Ray diffraction (XRD): Powdered samples were mixed with corundum powder (XXX) as internal standard (1:1 ratio by weight) in order to resolve shifts in peak position in the temperature range from 110-500 °C (same temperatures and dwelling time as for KBr pellets). Samples were measured with a Bruker D8 powder diffractometer (Bruker AXS GmbH, Karlsruhe, Germany) with a Cu Kα source and a rotating sample holder in the 2θ range form 20-45°. Further interest lies in the emergence of Mg-rich phases due to the decomposition of Mg calcite, such as dolomite [23a]. Selected samples of the long term dwelling experiments were also measured (see also S5).

Electron microprobe (EMP): Thin sections were polished for microprobe measurements and coated with graphite. The polishing of the porous and comparably soft calcite is challenging and the procedure is detailed in Schafflick (2019). Samples were measured in vacuum (≤ 0.01mbar) in a Jeol JXA 8900 microprobe (Jeol Germany GmbH, Freising, Germany) in a wave length dispersive mode for the following oxides: CaO, MgO, MnO, SrO, BaO and FeO. C was also measured to improve the applied XXX correction. Natural and synthetic samples were used for calibration. Acceleration voltage and diameter of the electron beam were selected to minimize the impact of the beam on the sample. Peak counting times ranged between 16 and 60 s. Successful measurement of the sea urchin spines (element total of ~100%) was not possible (S6). Still this method gave valuable insight.

Secondary electron microscopy (SEM): Changes of heat treated samples were monitored with a SEM (Hitachi TM 3030, Hitachi High-Technologies Europe GmbH, Krefeld, Germany and Zeiss Gemini Ultra Plus, Zeiss AG, Oberkochen, Germany) Coating of the samples was not needed

Uniaxial compression (UC): Quasi-static UC tests were carried out with a 10 kN Instron 4502 Universal Testing Machine (Instron Deutschland GmbH, Pfungstadt, Germany). The cross head speed was 0.5 mm/min and experiments were stopped after a strain $\varepsilon > 0.5$. Cylindric samples were cut out of the spines with a length diameter ratio of 2(±0.3):1. As coplanarity is crucial for adequate compression testing [18b] only samples a deviation of < 30 µm of the two planes were used. Before testing porosity was determined gravimetrically. Therefore, surface area of planes was obtained with Fiji (version 2.0.0, **F**iji **i**s **j**ust **i**mageJ), length was measured with a micrometer gage (Mitutoyo IP65, Mitutoyo Deutschland GmbH, Germany, error: 1 µm) and the mass was obtained with a Kern ABT 120-5DM scale (Kern & Sohn GmbH, Balingen-Frommern, Germany, error: 0.01 µm).

3-point bending (3PB): A 3 point bending module with a 20/10 mm configuration (Sauter AD 9300, Kern & Sohn GmbH) was mounted in the same universal testing machine as used for UC experiments. The calculation of bending strength was carried out according to [44]. Samples for 3PB were geometrically well defined cores drilled out of spines of *H. mamillatus* with diameters ranging between 4.6 and 4.8 mm.

Resonance frequency damping analysis (RFDA): Young's Modulus of 7 core drilled samples out of *H. mamillatus* spines were measured with non-destructive RFDA (IMCE Professional 23, IMCE N.V., Genk,

Belgium) in flexural mode (⊥ cystallograhic c-axis). Same temperature steps and dwelling times were used as described for powder XRD and KBr pellets. Details of the method are given elsewhere [18b, 45]. Young's Modulus was calculated according to ASTM E1876-15 [46].

Statistical Analysis: Statistical tests were conducted with the free software GNU R with additional packages *psych* [47] and *fitdistrplus* [48]. Groups were checked for normal distribution (Shapiro-Wilk test) and for homoscedasticity (Levene test). For parametric data a Welch t-test was applied and for nonparametric data a Wilcoxon test.

Acknowledgements

The authors thank the German research foundation (Deutsche Forschungsgemeinschaft, DFG) for funding this work in the framework of the collaborative research center (TRR SFB 141), project B01. The authors are indebted to Barbara Maier and Simone Schafflick (workshop of the university of Tübingen) for their advice and support in sample preparation. We are very grateful to NETZSCH Gerätebau GmbH (Selb, Germany) for free measurements. We thank Thomas Wenzel, who helped with EMP measurements, and Markus Ströbele and Manuel Löber, who helped with DSC measurements. We are indebted to Raouf Jemmali (Deutsches Luft und Raumfahrzentrum) for SEM measurements and to Annette Flicker for advising with IR spectroscopy.

REFERENCES

[1] L. Brecevic, A. E. Nielsen, *J Cryst Growth* **1989**, 98, 504.

[2] a) Y. Politi, T. Arad, E. Klein, S. Weiner, L. Addadi, *Science* **2004**, 306, 1161; b) A. V. Radha, T. Z. Forbes, C. E. Killian, P. U. Gilbert, A. Navrotsky, *Proc Natl Acad Sci U S A* **2010**, 107, 16438.

[3] E. Beniash, J. Aizenberg, L. Addadi, S. Weiner, *Proceedings of the Royal Society of London, Series B: Biological Sciences* **1997**, 264, 461

[4] L. Addadi, S. Raz, S. Weiner, *Advanced Materials* **2003**, 15, 959.

[5] E. Loste, R. M. Wilson, R. Seshadri, F. C. Meldrum, *Journal of Crystal Growth* **2003**, 254, 206.

[6] M. Albéric, L. Bertinetti, Z. Zou, P. Fratzl, W. Habraken, Y. Politi, *Adv Sci (Weinh)* **2018**, 5, 1701000.

[7] J. Seto, Y. Ma, S. A. Davis, F. Meldrum, A. Gourrier, Y. Y. Kim, U. Schilde, M. Sztucki, M. Burghammer, S. Maltsev, C. Jager, H. Colfen, *Proceedings of the National Academy of Sciences of the United States of America* **2012**, 109, 3699.

[8] a) I. Sethmann, A. Putnis, O. Grassmann, Löbmann, *American Mineralogist* **2005**, 90, 1213; b) L. Ameye, G. De Becker, C. Killian, F. Wilt, R. Kemps, S. Kuypers, P. Dubois, *Journal of Structural Biology* **2001**, 134, 56.

[9] H. Nebel, M. Neumann, C. Mayer, M. Epple, *Inorganic Chemistry* **2008**, 47, 7874.

[10] P. Raiteri, J. D. Gale, *J. Am. Chem. Soc.* **2010**, 132, 17623.

[11] a) Y. Levi-Kalisman, S. Raz, S. Weiner, L. Addadi, I. Sagi, *Advanced Functional Materials* **2002**, 12, 43; b) S. Weiner, Y. Levi-Kalisman, S. Raz, L. Addadi, *Connective Tissue Research* **2003**, 44, 214
[12] M. Albéric, E. N. Caspi, M. Bennet, W. Ajili, N. Nassif, T. Azaïs, A. Berner, P. Fratzl, E. Zolotoyabko, L. Bertinetti, Y. Politi, *Crystal Growth & Design* **2018**, 18, 2189.
[13] J. H. E. Cartwright, A. G. Checa, J. D. Gale, D. Gebauer, C. I. Sainz-Díaz, *Angewandte Chemie International Edition* **2012**, 51, 11960.
[14] a) H. U. Nissen, *Science* **1969**, 166, 1150; b) K. M. Towe, *Science* **1967**, 157, 1048.
[15] A. Berman, L. Addadi, S. Weiner, *Nature* **1988**, 331, 3.
[16] M. Merino, E. Vicente, K. N. Gonzales, F. G. Torres, *Materials Science and Engineering: C* **2017**, 78, 1086.
[17] a) J. N. Grossmann, J. H. Nebelsick, *Zoomorphology* **2013**, 132, 301; b) C. Lauer, T. B. Grun, I. Zutterkirch, R. Jemmali, J. H. Nebelsick, K. G. Nickel, *Zoomorphology* **2017**, 137, 137.
[18] a) C. Lauer, S. Schmier, T. Speck, K. G. Nickel, *Acta Biomater* **2018**, 77, 322; b) C. Lauer, K. Sillmann, S. Haussmann, K. G. Nickel, *Bioinspir Biomim* **2018**, 14, 016018; c) V. Presser, S. Schultheiß, C. Berthold, K. G. Nickel, *Journal of Bionic Engineering* **2009**, 6, 203.
[19] L. S. Lewis, J. E. Smith, Y. Eynaud, *PLoS One* **2018**, 13, e0190470.
[20] J. N. Weber, *Pacific Science* **1969**, 23, 452.
[21] S. K. Maiti, L. J. Gibson, M. F. Ashby, *Acta Metallurgica* **1984**, 32, 1963.
[22] a) W. Weibull, *Ingeniörsvetenskapsakademiens Handlingar* **1939**, 151, 1; b) R. Danzer, *Journal of the European Ceramic Society* **2014**, 34, 3435.
[23] a) D. L. Graf, J. R. Goldsmith, *Geochimica et Cosmochimica Acta* **1955**, 7, 109; b) J. A. D. Dickson, *Geochimica et Cosmochimica Acta* **2001**, 65, 443.
[24] S. J. Gaffey, J. J. Kolak, C. E. Bronnimann, *Geochimica et Cosmochimica Acta* **1991**, 55, 1627.
[25] S. J. Gaffey, *American Mineralogist* **1995**, 80, 947.
[26] H. A. Benesi, *J Chem Phys* **1959**, 131, 852.
[27] C. Günther, A. Becker, G. Wolf, M. Epple, *Zeitschrift für anorganische und allgemeine Chemie* **2005**, 631, 2830.
[28] a) U. Magdans, H. Gies, *European Journal of Mineralogy* **2004**, 16, 261; b) J. N. Weber, *American Journal of Science* **1969**, 267, 537.
[29] M. F. Ashby, *Metallurgical Transactions A* **1983**, 14, 1755.
[30] Y. U. Gong, C. E. Killian, I. C. Olson, N. P. Appathurai, A. L. Amasino, M. C. Martin, L. J. Holt, F. H. Wilt, P. U. Gilbert, *Proc Natl Acad Sci U S A* **2012**, 109, 6088.
[31] Y. Politi, R. A. Metzler, M. Abrecht, B. Gilbert, F. H. Wilt, I. Sagi, L. Addadi, S. Weiner, P. Gilbert, *Proceedings of the National Academy of Sciences of the United States of America* **2008**, 105, 20045.
[32] S. J. Gaffey, in *Spectroscopic Characterization of Minerals and Their Surfaces* (Ed: L. M. Coyne), Amer. Chem. Soc. **1990**, Ch. 5, p. 94.
[33] J. Bolze, B. Peng, N. Dingenouts, P. Panine, T. Narayanan, M. Ballauff, *Langmuir* **2002**, 18, 8364.
[34] O. K. DeFoe, A. H. Compton, *Physical Review* **1925**, 25, 618.
[35] J. Mu, D. D. Perlmutter, *thermochimica acta* **1981**, 49, 207.
[36] J. D. Currey, D. Nichols, *Nature* **1967**, 214, 81.
[37] a) M. Genet, G. Couégnat, A. P. Tomsia, R. O. Ritchie, *Journal of the Mechanics and Physics of Solids* **2014**, 68, 93; b) S. Meille, M. Lombardi, J. Chevalier, L. Montanaro, *Journal of the European Ceramic Society* **2012**, 32, 3959.
[38] Z. P. Bazant, *International Journal of Solids and Structures* **2000**, 37.
[39] W. Pabst, E. Gregorová, *Journal of the European Ceramic Society* **2014**, 34, 3195.
[40] F. Barthelat, *Bioinspir Biomim* **2010**, 5, 035001.
[41] M. B. Kruger, O. Wiliams, R. Jaeanloz, *J Chem Phys* **1989**, 91, 5910.
[42] J. Aizenberg, G. Lambert, S. Weiner, L. Addadi, *Journal of the American Chemical Society* **2002**, 124, 32.
[43] L. Regev, K. M. Poduska, L. Addadi, S. Weiner, E. Boaretto, *Journal of Archaeological Science* **2010**, 37, 3022.

[44] G. D. Quinn, B. T. Sparenberg, P. Kosky, J. K. Ives, S. Jahanmir, D. D. Arola, *Journal of Testing and Evaluation* **2009**, 37.
[45] W. Pabst, E. Gregoroá, G. Tichá, *Journal of the European Ceramic Society* **2006**, 26, 1085.
[46] in *E1876 - 15*, DOI: 10.1520/e1876-15, ASTM International, 2016.
[47] W. Revelle, https://cran.r-project.org/package=psych *Version = 1.8.3*. **2018**.
[48] M. L. Delignette-Muller, C. Dutang, *Journal of Statistical Software* **2015**, 64, 1.

Supplementary Material

On the relation of amorphous calcium carbonate and the macromechanical properties of sea urchin spines

Table of Contents

S1: Long-time dwelling experiments

Used Times and temperatures of heat treatment of segments and powders are displayed in Table 1 and mass losses are shown in Figure S1. Samples were weighed three times and the average is reported in Figure S1. Note that each dwelling time represents an individual experiment with a different segment/powder sample in order to avoid problems from rehydration. Rehydration occurred quickly after removal from furnace was particularly strong for powders. The natural heterogeneity of the samples causes the "bumps" in the weight loss. They are not caused by rehydration. However, all samples for a given temperature originate from the same spine (i.e. 250 °C 5 different samples from the same spine). The spines were cut vertically into as much segments as needed for the chosen dwelling times. These segments were halved longitudinally and one half was powdered and the other half kept as segment. This way we obtained mass loss data from weighing samples from identical spine section positions at each temperature.

Table S2: Dwelling times at the corresponding temperatures.

Temperature [°C]	Dwelling times [h]
150	$20^{\#+}$, 85, 157, 243, $353^{\#+}$
250	$20^{\#+}$, 85, 157, 243, $353^{\#+}$
350	0.5, $2^{\#*+}$, 4, 6, 9*, 24, 50*, 80, 126^{*+}, 198
500	0.5, $2^{\#}$, 4, 6, 9^{+}, 24, 50^{+}, 80, 126^{+}, 198

* after weighing these samples were heated additionally for 87 h at 500°C

$^{\#}$ powders used also for IR pellets (Figure S2)

$^{+}$ powders used also for XRD (Figure S3), samples with $^{+}$* were measured before and after heating to 500 °C

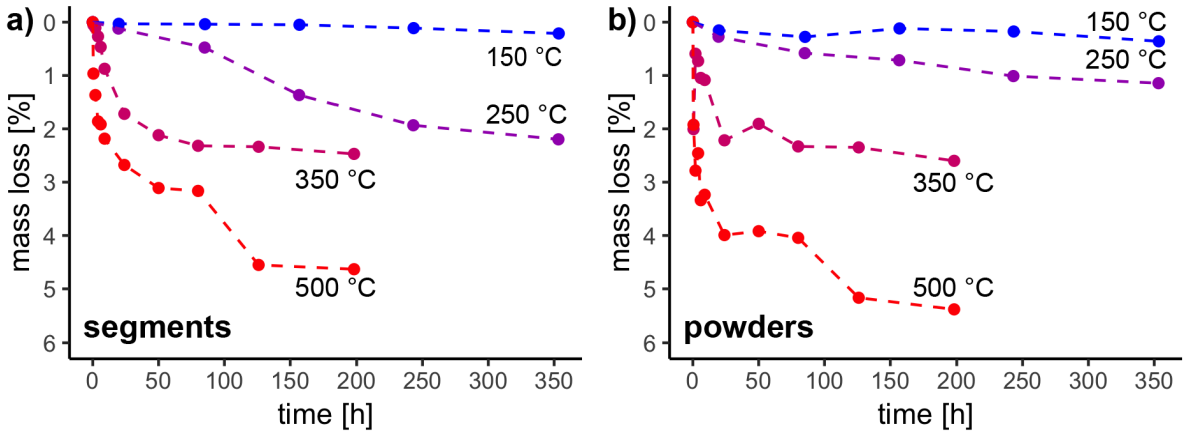

*Figure S1: Mass loss in segments (a) and powders (b). Not that different segments and powders were used for each time step and these sample inhomogeneities account for partly rugged mass decrease, especially for the powders, where also rehydration was an issue. Rehydration induced an error of xx%. Samples of 350 °C denoted with * in Table 1 were reheated to 500 °C for 87 h and their mass loss totaled then to 4-5 % (not shown), well comparable to long-dwelled samples at 500 °C.*

S2: ν_2/ν_4 ratio in KBr pellets (Infrared spectroscopy)

The ν_2/ν_4 ratio is usually determined by utilizing the heights of the corresponding bands. The values reported here (Figure S2) are the integral breadth (i.e. intensity divided by width) of bands fitted to the ν_2 and ν_4 bands. This procedure is more robust than just taking the height and takes more information of the band structure into account. Measurement error of 9 % this procedure was determined by measuring 10 times the KBr pellet of Iceland Spar (also shown in Figure S2). Note that the low ν_2/ν_4 ratio of Iceland spar is not reached, even at the highest temperatures. The Iceland Spar had a high purity (was transparent) which explains the low ratio compared to *H. mamillatus* calcite.

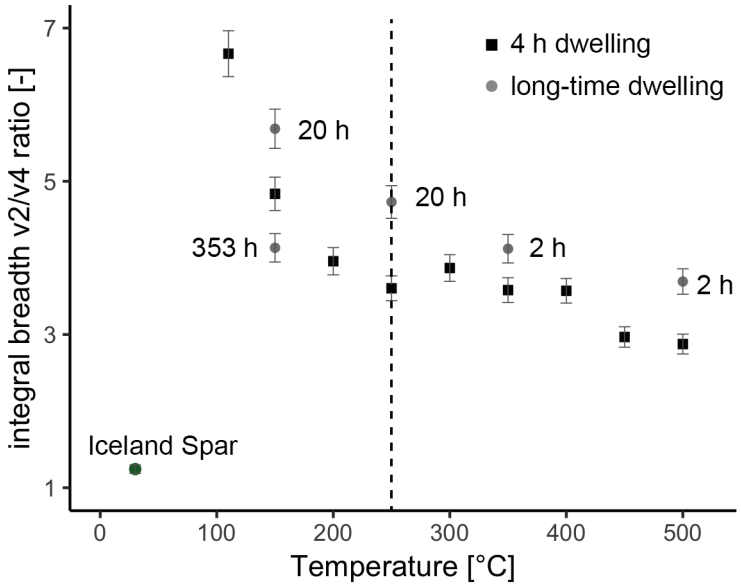

Figure S2: Development of the ν_2/ν_4 ratio with increasing temperature. The temperature at which all ACC is crystallized according to DSC (250 °C) is highlighted by the dotted line. The decrease in ν_2/ν_4 ratio correlates well with DSC data, a further drop in ν_2/ν_4 ratio takes place above 400 °C. Two samples that were held longer (20 h) at the same temperature show a higher ν_2/ν_4 ratio than the 4 h dwelled samples. This observation is intriguing, as all other data of the long time dwelling match well. They might be explained with natural heterogeneities

S3: X-ray diffraction (XRD)

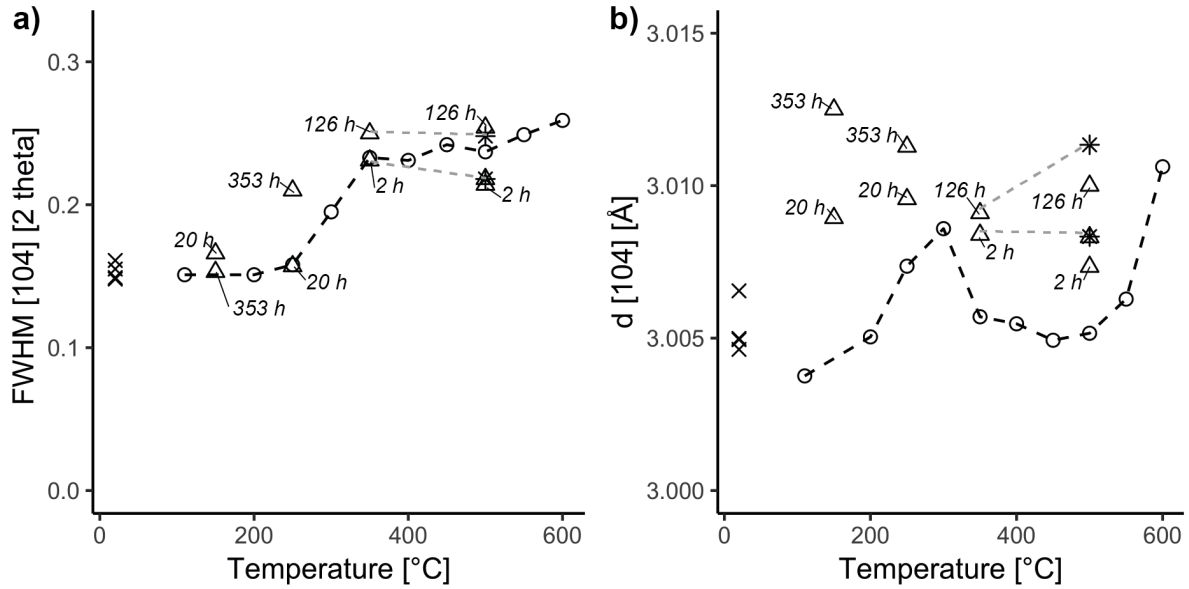

Figure S3: Full width at half maximum (FWHM) of the [104] peak of spine powder of H. mamillatus (a) and the corresponding d values (b). Circles denote homogenised powder from a single spine and heated for 4 h to the corresponding temperatures and are connected by a dotted line. X's represent not homogenised powder from a single spine, to show inter-spine variation. The sample from the tip has a higher d-value than the other 3 samples from bottom and two middle sections. Triangles give values of long time dwelling experiments (see Table S2) with dwelling times annotated. Connected by grey dotted lines are reheated samples at 500 °C for 87 h, originally held at 350 °C (see Table S2).

S4: Electron microprobe measurements (EMP):

Despite smooth and plane surfaces it was not possible to obtain totals of the elementary analysis for spines of *H. mamillatus* exceeding 90 % considerably (n = 96, average total = 84.7 %), even with low acceleration voltage (15 kV), a large probe diameter (20 µm) and low current (~8 nA, all reported values here were obtained with these settings). Surface damage made the trace of the electron beam often visible on the surface. Figure S4 shows two examples with ejecta and relief outlined. In these extreme cases, vigorous degassing was seen in the optical camera. Same observations were made when other sea urchin spines were measured (*Phyllacanthus imperialis:* n = 52, average total = 90.5 %, *Heterocentrotus trigonarius:* n = 98, average total = 86.1 %).

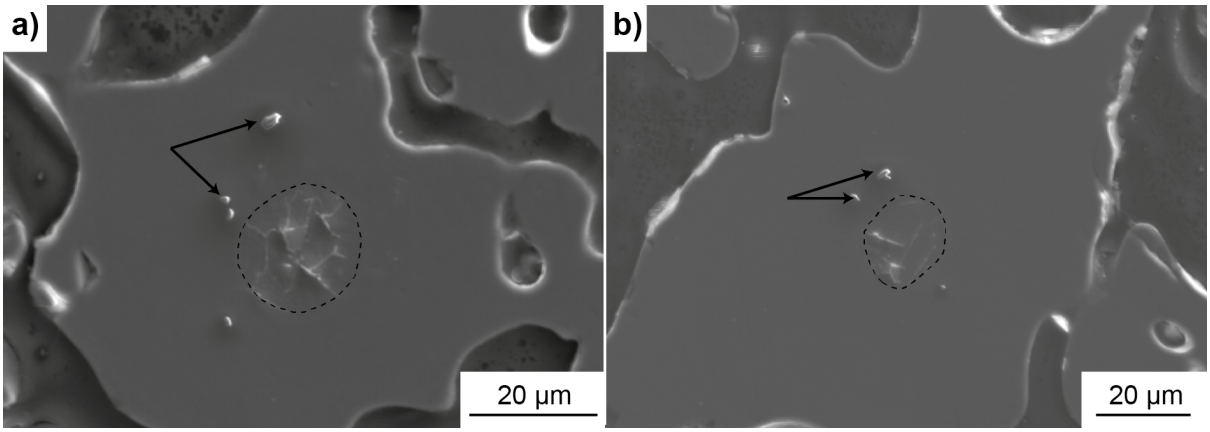

Figure S4. Interaction of electron beam with the biogenic calcite (a-b). Ejecta (marked by arrows) and the extent of damage on the surface are well visible (marked by dotted line). a) shows a comparably strong interaction with electron beam and b) a medium interaction. Dense growth layer struts were selected for measurement to ensure no influence of the surrounding epoxy resin.

S5: Dilatometry

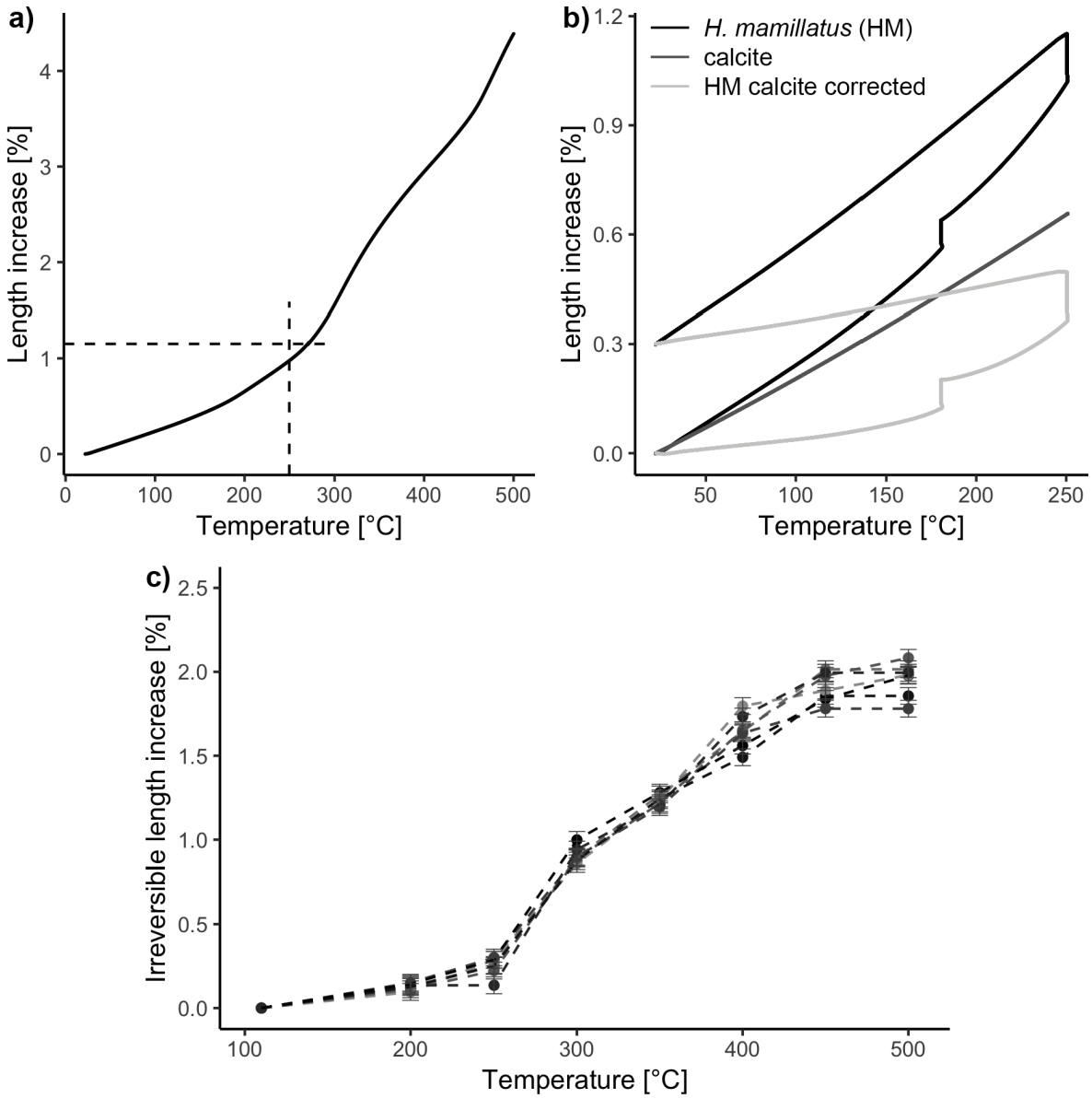

Figure S5: Dilatometric length increase of cylindrical samples machined out of different spines of H. mamillatus measured parallel to crystallographic c-axis heated at a rate of 1 °C/min to 500 °C (a) and 250 °C with two dwelling times at 180 °C and 250 °C for 2 h and subsequent cooling (b). Heating to 500 °C (a) shows a length increase of > 4 % with distinct slope changes at ~180 °C, 270 °C and 460 °C (latter coincides with pronounced water loss from TG-MS, (Figure 2) (dotted lines indicate section of b). Approximately half of this length increase is irreversible (c), as recorded by 7 cylindrical samples used for RFDA experiments show consistently (c). Dilatation until 250 °C during 2h dwelling times at 180° and 250°C in Fig. S5b provides evidence for the isothermal irreversible character of this part of length increase. For comparison, dilatation of geological calcite was calculated with the coefficient of thermal expansion ($\alpha_{||}$) given by Rao et al. [1]:$24.67*10^{-6}+1.742*10^{-8}*T-5.141*10-12*T^2$ (dark grey line in b) and was used to calculate the difference between biogenic and geological calcite. It is obvious, that biogenic calcite differs not only by the irreversible dilatation but also by the reversible. At 250 °C ~0.1% of the dilatation occurred outside of the dwelling times so this value is a good estimation for irreversible length increase of the samples used for mechanical testing.

S6: Development of microporosity and microcracks I

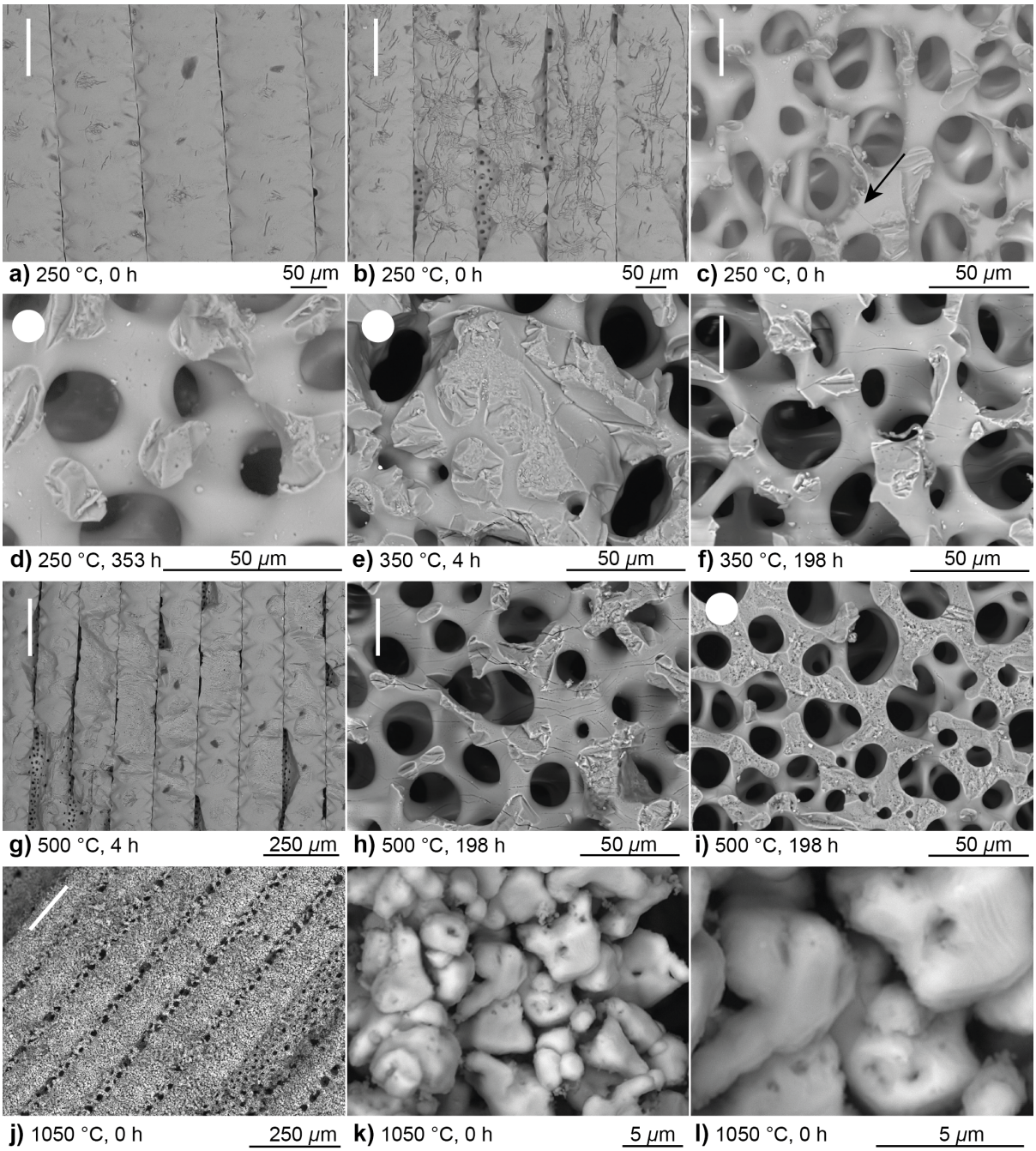

Figure S6: Detailed representation of the microporosity development at different dwelling times at 250 °C (a-d), 350 °C (e-f), 500 °C (g-i) and 1050 °C after decalcification (j-l) parallel the crystallographic c-axis (white line) and perpendicular (white dot). 0 h indicates no dwelling time. In general, cracks are more frequent orthogonal to c, while microporosity is best to find in cross sections of struts. a-c show damage that is to be expected form heating in mechanical tests. While large parts of the growth layers appear completely unaffected (a), in other regions extensive crack systems are visible with spallation of flakes (b). In the radiating layer cracking is rare and only occasionally found (c). Microporosity does not develop with no dwelling time at 250 °C, but is present after 353 h (d). Even at 150 °C few micropores were found (no picture). e) In the growth layer strut of Figure 5a, b some microporosity has developed in the right corner after 4h at 350 °C (e). At 500°C, similar features with higher, but still although irregularly distributed porosity (i) and wider cracks (h) are present. Cracking in growth layers leads to large-scale spallation revealing underlying microporosity (500°C, 4 h, g). Even at 1050 °C (segment out from TG, Fig. S1, pale grey line) stereom structures are clearly visible, it is composed out of interlocking lime granules (k-l), in which microporosity seemed preserved.

S7: Development of microporosity and microcracks II

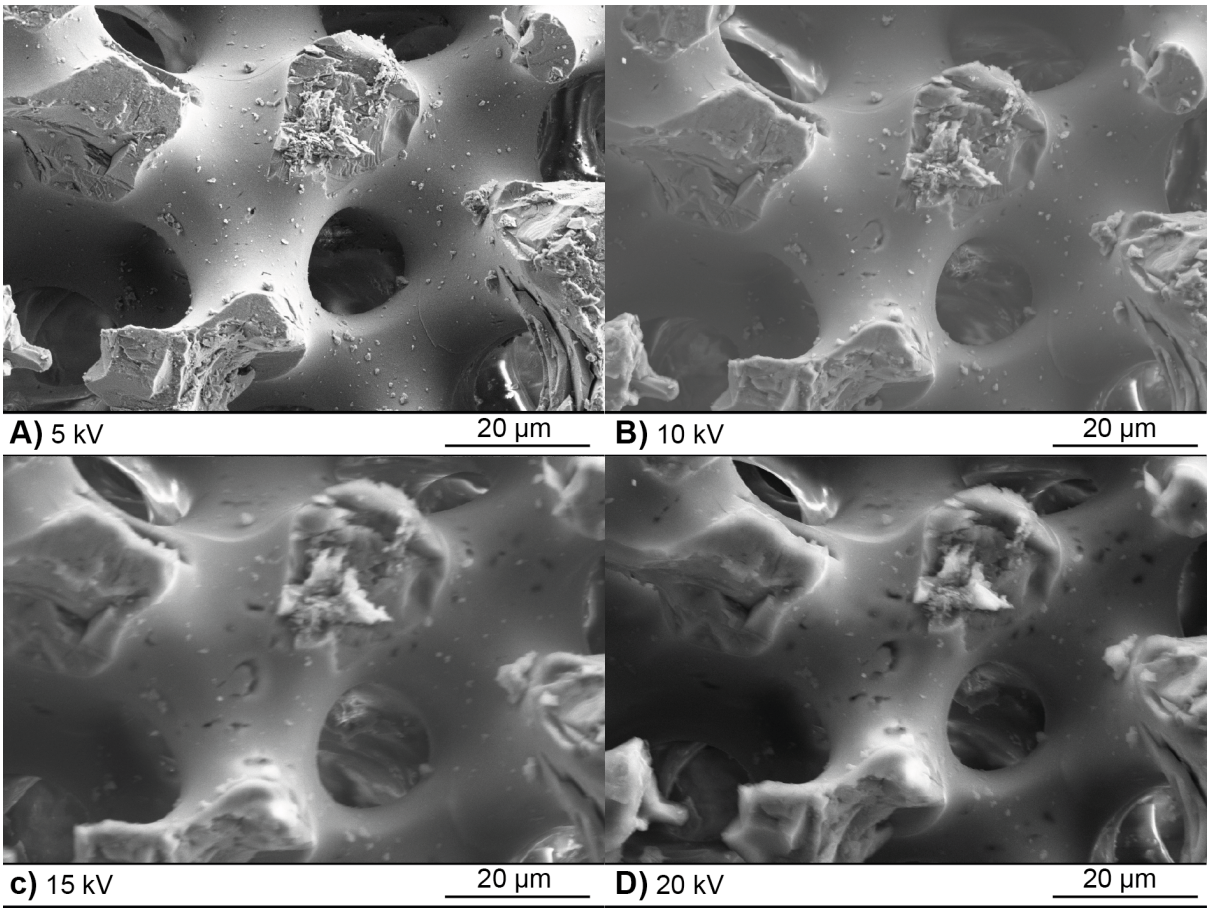

Figure S7: The same location in the stereom structure was exposed to different acceleration voltages. The sample was heated to 250 °C for 353 h. As with higher acceleration voltage the electron beam collects information also from below the surface, this proves that the majority of the microporosity is hidden below the surface.

S8: Differential scanning calorimetry (DSC)

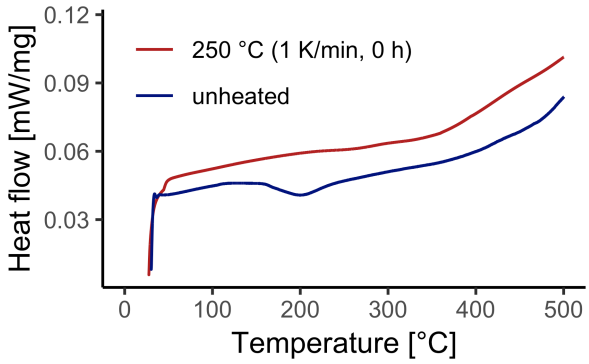

Figure S8: DSC curve of a mechanical test sample (red) heated to 250 °C with 1 °C/min with no holding time compared to the curve of figure 3e (unheated sample). The exothermal peak of ACC crystallization is not detectable anymore, demonstrating that the treatment was capable to yield full ACC crystallization, as desired for mechanical tests.

S9: Group Division for mechanical tests (UC and 3PB)

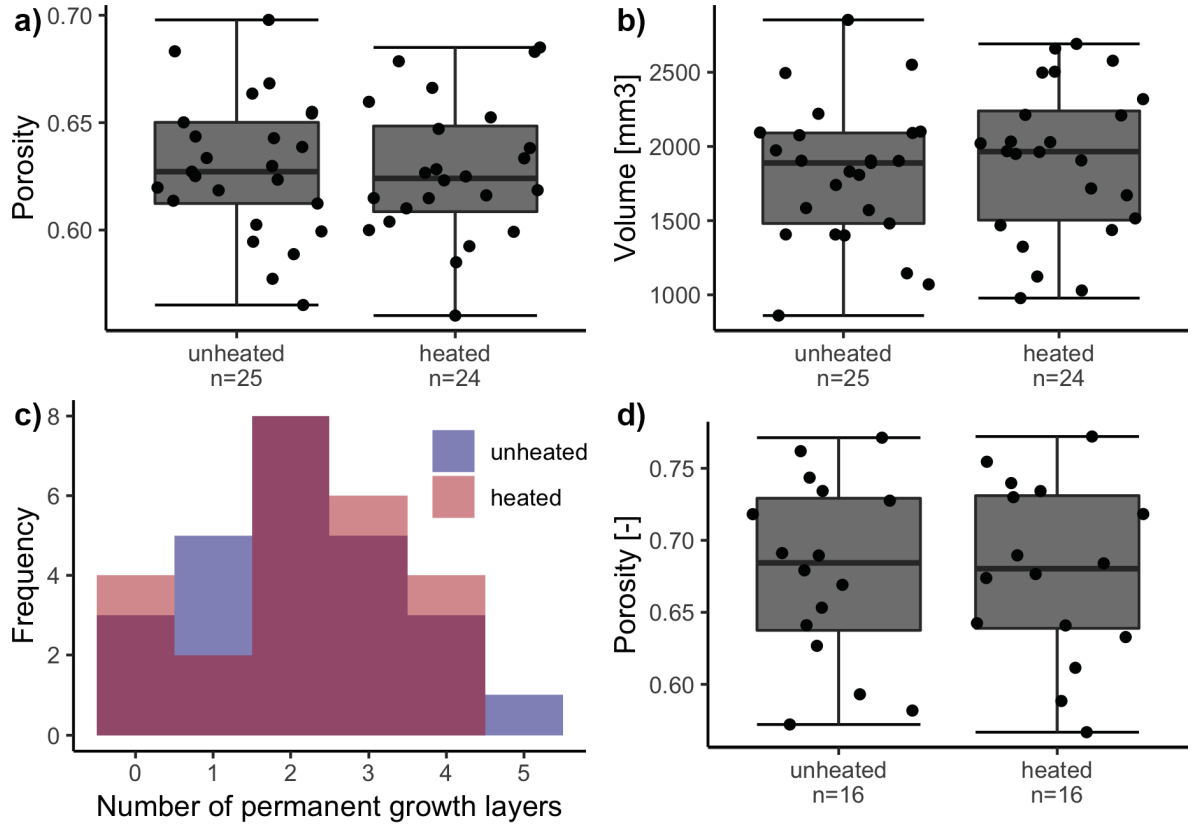

Figure S9: Group division of test samples for uniaxial compression (UC) according to porosity (a), volume (b) and permanent growth layers (c) and for the porosity of the bending samples (3PB) (d). Statistical testing as listed in Table 2 shows the indistinguishability of heated and unheated reference groups. 3PB samples were core drilled out of full spines and thus had a defined, cylindrical geometry with diameters between 4.6-4.8 mm.

Table S9: Statistical testing of the groups for mechanical experiments. UC = uniaxial compression, 3PB = 3 point bending, V = volume, ϕ = porosity, GL_p = permanent growth layers.

Test method	Property	Group	sample size (n)	median	mean	range	statistical testing
UC	ϕ	unheated	25	0.627	0.629	0.565-0.698	Welch t-test:
		heated	24	0.624	0.628	0.560-0.685	p-value = 0.865
	V [mm^3]	unheated	25	1818	1889	860-2853	Welch t-test:
		heated	24	1908	1922	978-2691	p-value = 0.505
	GL_p	unheated	25	2	2.12	0-5	
		heated	24	2	2.17	0-4	
3PB	ϕ	unheated	16	0.678	0.684	0.575-0.771	Welch t-test:
		heated	16	0.678	0.680	0.567-0.772	p-value = 0.995

REFERENCES:

[1] K.V.K. Rao, S.V.N. Naidu, K.S. Murthy, Precision lattice parameters and thermal expansion of calcite, J Phys Chem Solids 29 (1968).

Manuscript 7

Pin indentation: a method for local testing mechanical properties of ceramic foams

(20 pages)

Pin indentation: a method for local testing mechanical properties of ceramic foams

Christoph Lauer [1], Gerald Buck [1], Stefan Mück [1], Raouf Jemmali [2], Christoph Berthold [1], Klaus G. Nickel [1]

[1] University of Tübingen, Department of Geosciences, Division of Applied Mineralogy, Wilhelmstraße 56, D-72074 Tübingen, Germany

[2] German Aerospace Institute (DLR), Institute for Structure and Design, Pfaffenwaldring 38, D-70569 Stuttgart, Germany

Structures in ceramic foam materials (i.e. pore size, shape, orientation) often change on small scales, yet the predominant mechanical testing method is with uniaxial compression a "bulk" testing. This study highlights the benefits of a localized compression test, labelled "pin indentation". A flat-ended, cylindrical-tapered pin, being significantly smaller than the sample, is pushed with constant speed into the material. In direct comparison to uniaxial compression tests it is shown that in pin indentation, depending on the depth of penetration, additional forces occur, so that strength in pin indentation and uniaxial compression differ. This is highlighted with two very different materials: honeycomb-like alumina ceramics and biogenic Mg calcitic foam ceramics from the large spines of the slate pencil urchin *Heterocentrotus mamillatus*. It is also demonstrated that pin indentation is a powerful tool to reveal small scale changes in porosity, pore orientation and other structural changes. Deep pin indentation is able to characterize the energy absorption behavior of a ceramic foam without the shortcomings of spallation or structural collapse in uniaxial compression. Despite the brittleness of the foam, deep pin indentation curves display a smooth plateau between linear elastic increase and densification, highlighting that uniaxial compression is not suitable to characterize energy absorption of brittle foams.

Keywords: Pin indentation, energy dissipation, brittle foam ceramics, mechanical testing, sea urchin spines, ionotropic gelation

1. Introduction

Cellular ceramics are lightweight materials with high temperature, high wear resistance and high corrosive resistance as well as high stiffness and strength. These properties lead to a wide range of applications including filtration of molten metals and hot gases, high temperature insulation, solid oxide fuel cells and scaffolds for bone tissue engineering [1]. In all these applications loads occur, and in bone scaffold engineering, bearing load is the key function besides providing substrate for bone regrowth. Given their widespread use and applicability, it may surprise that there is no norm for mechanical testing of brittle cellular materials [2]. Although a standard or norm for mechanical testing is missing, uniaxial compression is by far the most common method for testing cellular ceramics (applied in e.g. [2-14]) probably due the simple test conduction and the fact that ceramics are generally used in compressive load regimes. However, there are a few issues regarding this wide-spread testing method.

Uniform loading is vital in uniaxial compression testing of any materials and in brittle foams even more so. Small deviations from coplanarity can induce large errors in Young's Modulus and compressive strength determination, because not the whole sample is loaded. Compliant loading pads were used in many studies to make loading more uniform (i.e. [2, 15]). Brezny and Green [16] infiltrated the top and bottom of the ceramic with epoxy resin to obtain uniform loading.

Uniaxial compression only tests the bulk mechanical properties of a sample, yet only small local variations in porosity [17], pore size [18] or pore orientation [19] will lead to an alteration of the mechanical properties and cannot be resolved in uniaxial compression testing. Highly irregular foams are encountered in technical applications (i.e. filter materials, oxide fuel cells, insulation materials) and in biological materials (i.e. bone, wood, echinoderm calcite). The question arises, whether bulk testing like uniaxial compression is an adequate testing method. Moreover, in many loading situations the load is rather punctual than bulk compressive.

Additionally to the issue of homogeneous loading, in uniaxial compression catastrophic failure is often not unambiguously discernible as stress redistribution takes place several times before a major load drop, making calculation of the Young's Modulus difficult as the extent of the true linear elastic increase is difficult to assess. Therefore, Seeber et al. [20] put forward three point bending as the method of choice for testing ceramic foams. Catastrophic failure is well visible and only by this the real influence of porosity and structure can be revealed as no (or considerably less) stress redistribution takes place in 3-point bending [20].

However, three point bending tests cannot measure the energy absorption, which is unquestionably one of the outstanding properties of foams and the reason why they are used in many applications, e.g. in packaging industry [21]. In uniaxial compression all kinds of foams, elastic, flexible and brittle (ceramic), show theoretically three distinct regions in a load displacement diagram: linear elastic

increase, plateau and densification [3]. Within the long plateau on the level of the linear elastic strength, the most energy is absorbed [22]. The absorbed energy is calculated by the integral below the load displacement curve (energy absorbed by specimen) or stress strain cure (energy absorption per volume of material). As ceramic foams are by far the strongest of the three foam types, their potential to absorb energy is large and might find application against severe impacts in extreme environments such as space in e.g. satellites or space ships [23]. Yet, in uniaxial compression testing, the plateau of brittle foams is much lower than the elastic strength and is more rugged than smooth [3, 15] and thus, ceramic foams do not live up to their potential of absorbing energy. The reason for this is obvious: brittle fracture often leads to spallation of large flakes so that the sample geometry and the area intact with the loading plates constantly changes. Hence, engineering stress (σ_{eng}) and the true stress (σ_{true}) deviate largely indicating that the low measured energy absorption of ceramic foams is rather caused by the testing method than by the material.

To overcome spallation, Dam et al. [15] confined samples in a hardened steel die, however, the plateau was still low and rugged. Gosh et al. [10] decreased the sample height to such an extent, that spallation could practically not occur. As the sample is reduced to a thin plate, the influence of the loading plates on the mechanical properties of the foam ceramic might be strong.

With these issues of cellular brittle materials such as scaffolds, foam ceramics or bones in uniaxial compression in mind, we want to put forward a down-scaled compression test, the pin indentation (PI). The principle of this method is that a small loading plate (i.e. a pin), being much smaller than the sample itself, pushes into the material with a constant speed. As the much larger sample confines itself, spallation is inhibited and energy absorption can be measured easily. Local material properties are analysed, variations can be detected and a more detailed structure-property relation can be established.

This principle was already applied to metal foams by [24-28]. It was found that the stresses in pin indentation are higher than in pure uniaxial compression due to additional forces at the rim of the indenter [24, 29]. The pin indentation strength (σ_{PI}) was defined as the peak strength of the linear elastic increase, just before the first major load drop [29]. We refined the method for brittle cellular materials based on the quantitative results of Presser et al. [30] and Schmier et al. [31] and compared it to the "default" testing method, the uniaxial compression (confined and unconfined testing). Two very different cellular materials were chosen to demonstrate the usefulness of this method: honeycomb-like alumina ceramics with porosities of 0.81-0.87 and a biological ceramic, the spines of the sea urchin *Heterocentrotus mamillatus* with porosities of 0.55-0.85. The open foam, scaffold-like structure of these spines has already served as role model for scaffolds in bone tissue engineering [32, 33].

2. Materials and Methods

2.1. Samples

Highly directed, honeycomb-like Al_2O_3 ceramics (IGC) were produced by ionotropic gelation. The synthesis is only briefly outlined here, a detailed manufacturing description is given elsewhere (e.g. [9, 34-37]). A pH-stabilized Al_2O_3 suspension with a solid load of 20 wt.% was mixed with Na-alginate/water solution (sol). This mixed-sol is topped by a crosslinking agent ($CaCl_2$, 0.5M) to start the diffusive gelling process. The divalent metal ion binds to the alginate structure by forming a metal complex. By this, the honeycomb-like structure is created in a gel that is not water soluble ([38]. After freeze drying and sintering the ceramic-gel body (sintering temperature 1350 °C) the final structured ceramic is prepared for mechanical testing. The top and bottom sides of the samples were cut and grinded to obtain coplanarity. Afterwards, cores (diameter = 4.5 to 4.8 mm, height = 7.7 to 12.0 mm, coplanarity = 100-230µm) were drilled out of the ceramic bodies for UC tests (Fig. 3B). Due to their diameters, the cylindrical samples could be directly compared to the 5 mm pin indentations.

A spine assortment of the sea urchin *Heterocentrotus mamillatus* (SUS) was purchased from a supplier (Fischhaus Zepkow, Zepkow, Germany). Spines of these species are roughly round in cross section and were cut in coplanar segments (±15 µm) with a height/diameter ratio of 2 (±0.3):1 for UC experiments (Fig. 3D). Additionally, cylindrical cores were drilled out of the spines. These cores had a diameter of 3.7- 3.9 mm and a height of 4 mm (± 5 µm) and their strength was directly compared to 3 mm pin indentations due to their similar diameter.

Both ceramic materials were also tested in a confined mode in Uniaxial compression. Up to 4 thin strips of fabric tape (“duct tape”) were tied around the specimens (Fig. 8). The intention of testing confined samples was to prevent spallation in uniaxial compression tests to obtain a more meaningful stress-displacement curve to calculate energy dissipation of the material.

2.2. Uniaxial compression

All UC tests were performed with a 10 kN Instron 4502 universal testing machine (Instron Deutschland GmbH, Pfungstadt, Germany). The cross head speed was always 0.5 mm/min and a preload was used in order to align the sample properly in the testing apparatus(IGC = 5 N, SUS = 20 N). Rigid tungsten carbide loading plates were used so that all deformation is constrained into the much more elastic test samples. The loading plates always exceeded the size of the samples. Experiments were recorded with a videoextensometer (Limess RTSS_C02, Limess Software und Messtechnik GmbH, Krefeld, Germany) for documentation.

2.3. Pin indentation

For conducting PI experiments, the setup in the universal testing machine was slightly modified. Instead of a loading plate a tungsten carbide indenter with varying diameter (1, 3, 5 mm) was mounted to the load cell. As for UC experiments, a preload was used (IGC = 5 N, SUS = 20 N). PI experiments were carried out at the same cross head speed as UC experiments (0.5 mm/min). They were stopped either after ~1 mm of displacement (shallow indentation), which was sufficient to determine the PI strength, or at the onset of densification for deep indentations. Afterwards the pin indenter was carefully removed from the sample (Fig.1). The experiments were also recorded with the videoextensiometer to assess the quality of the pin indentations.

The pin indenter diameter was chosen according to the cell size of the materials. Usually more than 50 pores were covered in order to produce representative results [25]. Unless noted otherwise, all PI tests had been performed with a tapered pin in order to reduce friction of the indenter wall with the sample (Fig.1) [24]. Since several measurements were performed on a single sample, the positions of PI tests have been chosen that no mutual influence of the measurements could be observed (e.g. crack formation between two measurements, near-surface spallation, fatal cracks, movement of the sample). All questionable tests in respect to this criterion were excluded from analysis.

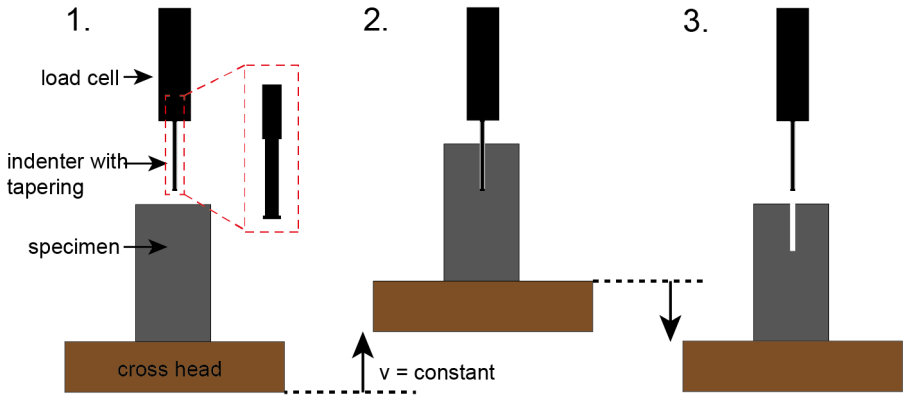

Figure 1: Schematic representation of the pin indentation (PI) method with the tapered indenter magnified in the dashed red box.

2.4. Microscopy

Samples were analysed with a tabletop electron microscope (Hitachi TM 3030, Hitachi High-Technologies Europe GmbH, Krefeld, Germany) to analyse the microstructure and porosity. Furthermore, a digital microscope was used (Hirox MXB 2016Z, Hirox Europe, Limonest, France) to investigate the pin indentations and assess the pore channel inclination of the IGC.

2.5. Determination of porosity and channel inclination

For UC experiments the bulk porosity of all samples was determined gravimetrically prior to testing. The mass of the samples was determined with a precision of 0.01 mg (ABT 120-5DM scale, Kern & Sohn GmbH, Balingen-Frommern, Germany) and length was measured with a calliper (Mahr 16 FN INOXYD, Mahr GmbH, Göttingen, Germany) with a precision of 0.05 mm. For irregular geometries, such as the SUS, the area of the cross sections was determined in micrographs with the open source image analysis software ImageJ. For shallow and deep PIs of the homogeneous IGC, it was assumed that the local porosity at the spot of the PI is very similar to the bulk porosity (porosity variation within a single sample: < 0.02). For shallow PI in SUS, where the bulk porosity is not representative of the local porosity, local porosity determination was done with SEM pictures and requires prior infiltration of the sample with Araldite 2020A. Otherwise information from deeper pore structures will be mistakenly analysed as well, which would decrease porosity (Lauer et al. 2017). Furthermore, infiltration enhances the contrast between pores and calcite and automatic evaluation with ImageJ is possible. The infiltration is, however, permanent and those samples cannot be used for mechanical testing anymore. Therefore, reference sections directly adjacent to those planes which were used for pin indentations were cut beforehand. The reference sections were infiltrated and porosity was determined according to (Lauer et al. 2017) with the default threshold in ImageJ. The exact location of the PI was identified by overlaying the optical image of the section containing the PIs with the corresponding, directly adjacent SEM stich for porosity determination. As these two sections were only separated by the blade width of the saw (1 mm), the error due to local porosity variations is negligible. Furthermore, porosity changes along the spine's width are small compared to radially porosity changes.

The channel inclination of the IGC samples was measured for both tests (UC, PI) from side view images. The given value represents the dip of the pore channels parallel to force transmission.

2.6. Micro computer tomography (μCT)

Raouf Jemmali has agreed to write this paragraph, but the work is still in progress.

3. Results

3.1. Structural characterisation of the ceramic materials

Detailed material characterizations are given elsewhere (IGC: [9, 36, 37]; SUS: [39, 40]). However, we want to point out the most relevant structural aspects for the mechanical response.

The channel size of IGC ranges between 200-500 µm and the overall porosity is 0.81-0.87. These channels often have a honeycomb-like cross section, are not interconnected (Fig. 2A,B) and run approimately straight from top to bottom (Fig. 2B). The cell walls have a thickness of 35 ± 20 µm and are not fully dense (magnifications of Fig. 2A).

The spines of *Heterocentrotus mamillatus* have a very heterogeneous open pore structure (Fig. 3C) with an overall porosity of 0.54-0.7. Densest parts are the growth layers (3) with a local porosity of 0.2-0.3. The centre of a spine can reach porosities of 0.75-0.9 (2), while in between those extrema a porosity of 0.6-0.75 is found in the radiating structure (1) [40]. Generally, the spines can be approximated with a core shell construction (Fig. 2C, D) [40].

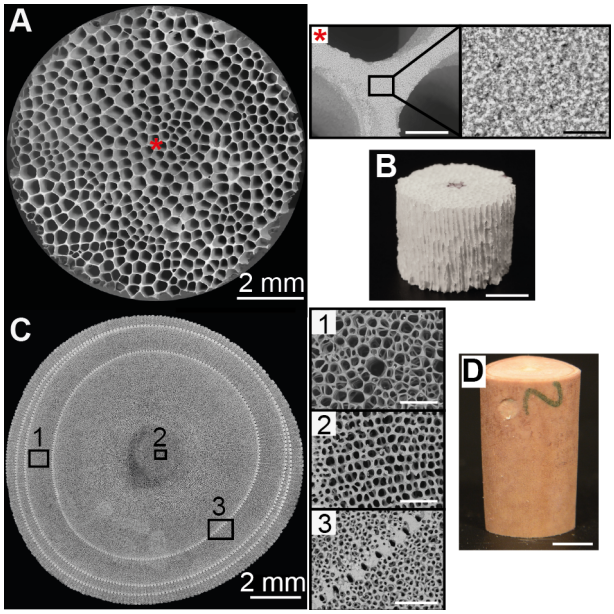

Figure 2: Structure of an Al_2O_3 ionotropic gelation ceramic (IGC) in top view (A) and magnifications of the wall and the wall porosity (A). Samples used in UC were cylindrical (B). Cross section of a sea urchin spine (SUS) of Heterocentrotus mamillatus (C, rings are growth layers) alongside with magnifications of the heterogeneous internal structure (1-3). A typical segment for UC experiments is shown in D. Scale bars: A*: 100 µm and 10 µm, B: 3 mm, C1: 100 µm, C2: 200 µm, C3: 250µm, D: 5 mm.*

3.2. Comparison of uniaxial compression and pin indentation

As outlined in (1), additional forces arise in PI for brittle materials. Based on the results by [24, 29] we identified the following forces influencing PI response, depending on the penetration depth.

1) In the elastic regime, the elastic stress field surpasses pin indenter size considerably (Fig. 3A). Therefore it does not come by surprise, that the measured stress in PI is higher than in UC (Fig. 4). This is, however, only due to the fact that the engineering stress is calculated with the area of the pin and not with the whole area influenced by the stress field. As the exact stress field can only be obtained by modelling [41], this is the most feasible solution.
2) In the moment of the first fracture, directly after reaching the pin indentation strength σ_{PI} (Fig. 3C), the pin cuts into the material. Uniaxial crushing of the material beneath the indenter occurs, as well as bending forces to break the material located at the indenter rim. In comparison to metals, where these forces are high [29], they can be neglected in ceramic materials as they have a much lower bending than compressive strength [17]. If only σ_{PI} is of interest, the measurement can be terminated at this point.
3) For measuring energy absorption or dissipation properties of the ceramic foam, deeper reaching indentations are required (Fig. 3B). In this case, the elastic stress field propagates with the indenter tip into the material. The material adjacent to this area relaxes after the pin penetrates deeper into the material. Damage is usually restricted to the area directly below the indenter, since the peak stresses are located there [41]. Subsequently, a plug of crushed material in front of the indenter develops (Fig. 3B,D). The material is densified by the compressive forces and hence a higher force is needed to penetrate further into the material. Not all of the crushed material is densified beneath the indenter, some of it "flows" around the indenter into the tapering (Fig. 3D). The tapering is required to avoid friction, which would otherwise arise between the pin indenter wall and the material (Fig. 3C, blue dotted line). At some point an equilibrium between the material densifying in front of the indenter and flowing into the tapering is reached and a clear plateau establishes (Fig. 3C). Except for the pin indenter used in Fig. 3D all measurements were conducted with tapered indenters to avoid the issue of friction.

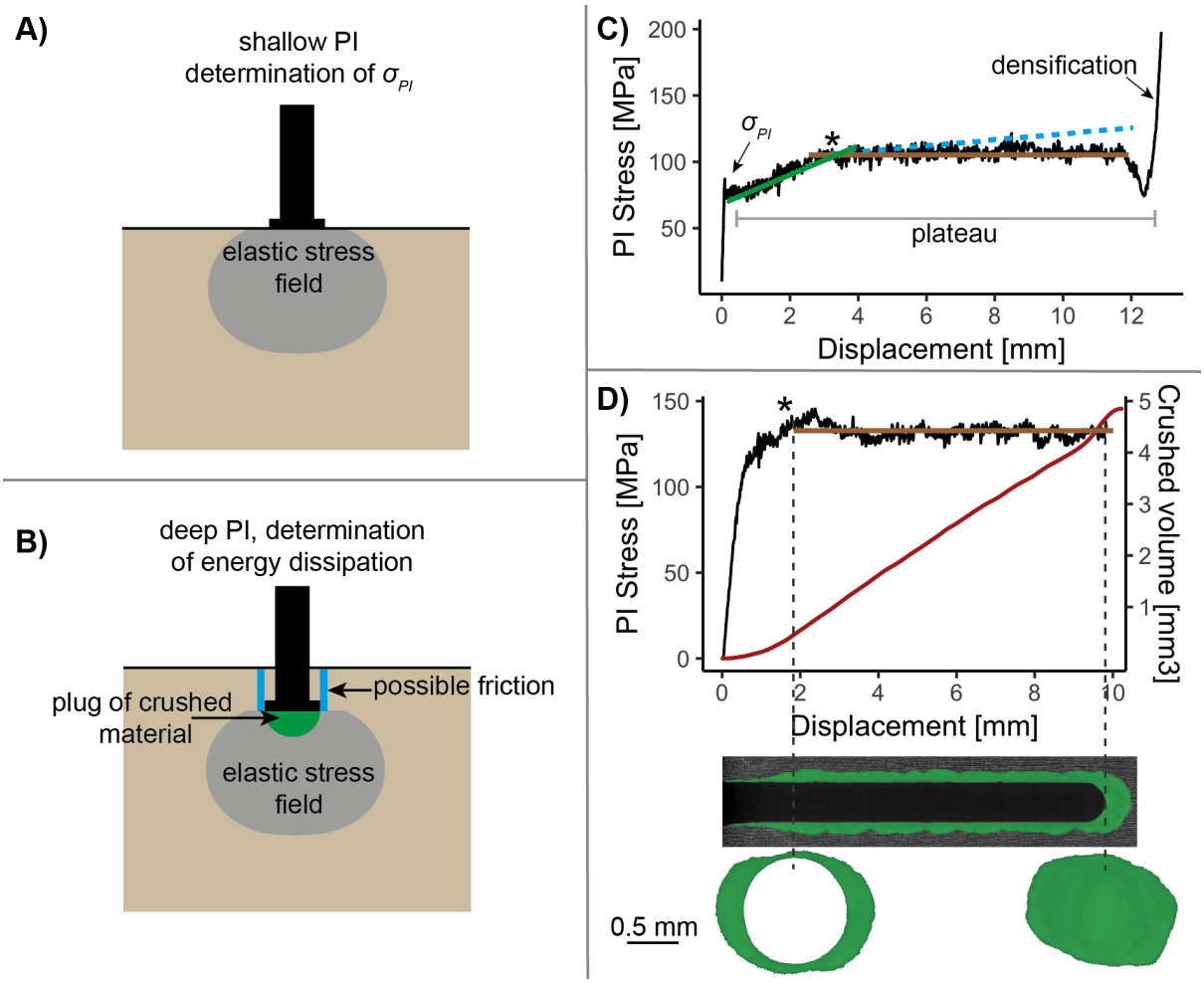

Figure 3: Forces in shallow pin indentation (PI) (A) to determine the pin indentation strength σ_{PI} (C) and in deep indentation (B) to reach a constant plateau and thereby characterizing the energy dissipation of the material (C,D). Due to the elastic force field surpassing the measurement spot of the PI, σ_{PI} is significant higher than σ_{UC} (see Fig. 4). In deep indentation crushed material accumulates beneath the indenter and forms a plug and densifies, which increases the stress (green line, B). It flows also around the indenter and accumulates at the side as can be seen in in the CT scan (D). Usually an equilibrium between these two accumulations establishes (in C and D). If considerable friction between the indenter wall and the material arises, the plateau steadily increases (blue dotted line in C).*

To quantify the difference between σ_{UC} and σ_{PI}, UC tests with samples having a similar diameter as the pin indenter were conducted and compared to PI test. Hence, stresses are directly comparable. Figure 4A, B shows the difference of the strength measured in PI and UC for IGC and SUS. As porosity ϕ is approximately homogeneously distributed in IGC samples (ϕ = 0.81-0.87) it is not displayed in Fig 4A, but for SUS it is taken into account because variations are much larger (ϕ = 0.60-0.76). σ_{PI} is ~90 % higher than σ_{UC} for IGC. Due to the wide range of porosities in SUS, data were fitted with the Gibson and Ashby Model for open cell foams [17] (Eq. 1, dashed lines, Fig. 4B) and the model by Ji et al. [42] (Eq. 2, solid lines, Fig. 4B).

$$\sigma_\phi = \sigma_d * C * (1-\phi)^{1.5} \quad \text{(Eq. 1)}$$

$$\sigma_\phi = \sigma_d * (1 - \phi)^{1/J} \quad \text{(Eq. 2)}$$

σ_ϕ is the strength of the porous material, σ_d the strength of the dense strut wall material, ϕ is the porosity, C a constant given with 0.65 [3, 17] and J a parameter describing the pore shape. For spherical pores J = 0.5 is used, which is in good agreement with the predominant pore shape in spines of *H. mamillatus* [14]. Based on Eq. 1 σ_{PI} is in average 45 % higher for spines of *H. mamillatus* and based on Eq. 2 in average 56 %. In both materials, IGC and SUS, the difference between σ_{UC} and σ_{PI} is caused by the larger extent of the elastic stress field.

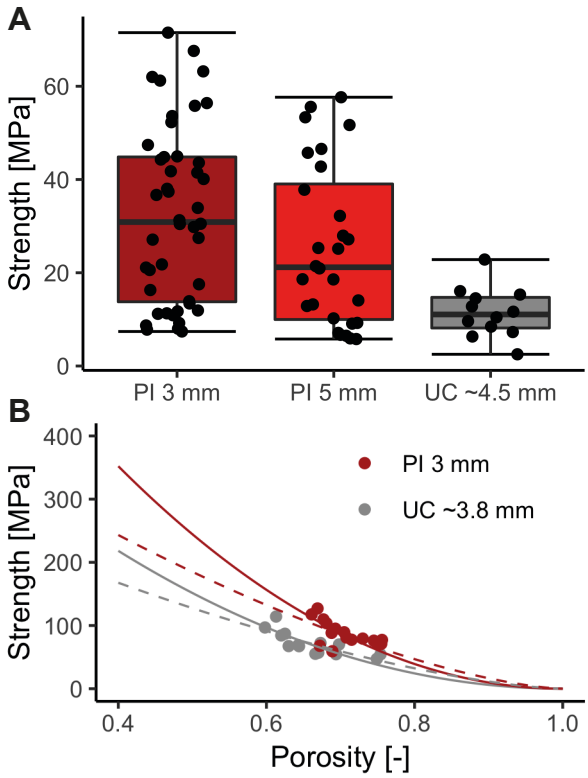

Figure 4: Difference in strength measured by pin indentation (PI) and uniaxial compression (UC) for Ionotropic gelation ceramics (A) and sea urchin spines (B). Diameters of pin indenters and for PI and diameter of samples for UC are given in the figure. Dashed lines correspond to fits with Gibson-Ashby model [17] (σ_d (UC) = 555 MPa, σ_d (PI) = 805 MPa) and solid lines to Ji model [42] (σ_d (UC) = 606 MPa, σ_d (PI) = 946 MPa).

3.3. Local testing with pin indentation

This section reports how different porosities, internal heterogeneities and pore orientation affect the PI response. The porosity dependence can be best seen in the data of SUS, as they have a larger porosity range than IGC. The PI clearly distinguishes the two foam porosities occurring in the spines of *H. mamillatus*. The medulla displays much lower strengths than the radiating layer due to its much higher porosity (Fig. 5A). To measure the narrow medulla, small indenter diameters (0.6 and 1 mm) were

applied (Fig. 5B). For comparison the 3 mm PIs of Fig. 4B are also shown. All data are satisfactorily fitted with by Ji et al. [42].

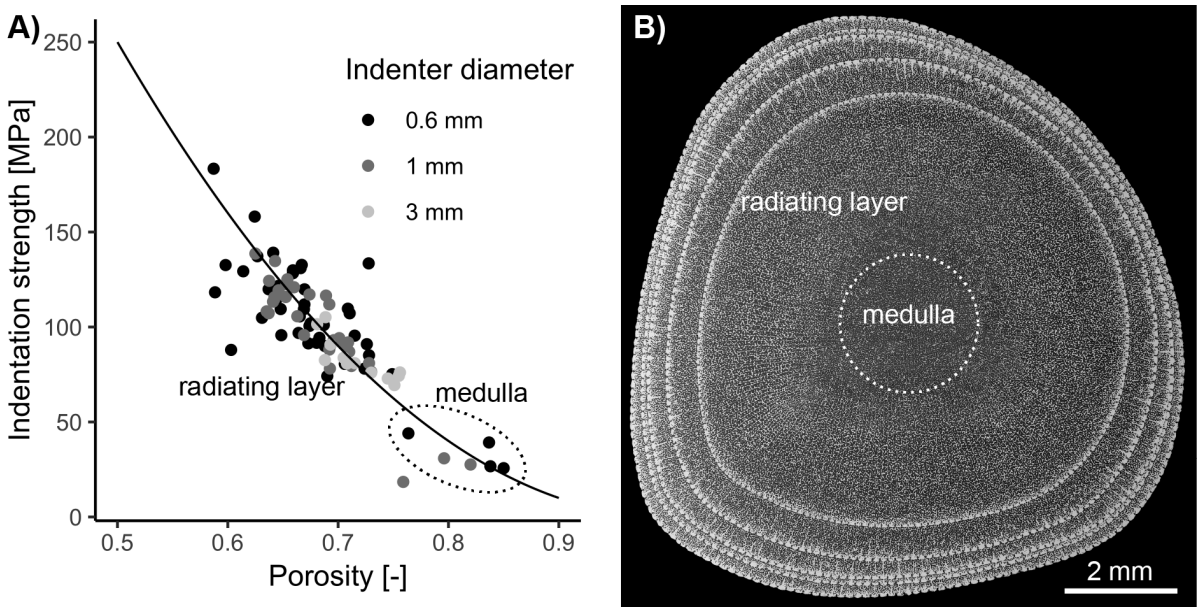

Figure 5: Relation between porosity and PI strength in SUS (A) in radiating layer and medulla (B). The data were fitted with the model by Ji et al. [42] with a value of σ_d = 1002 MPa obtained by fitting for all displayed data.

Within the homogeneous open foam material of the radiating layer, the growth layers represent an internal heterogeneity and are clearly exposed by deep PIs. The location of a growth layer is highlighted by a sudden stress increase (Fig. 6). It is evoked by the large porosity difference between the growth layer and the medulla. Hence, deep indentation can provide a more detailed understanding of the structure than conventional UC tests.

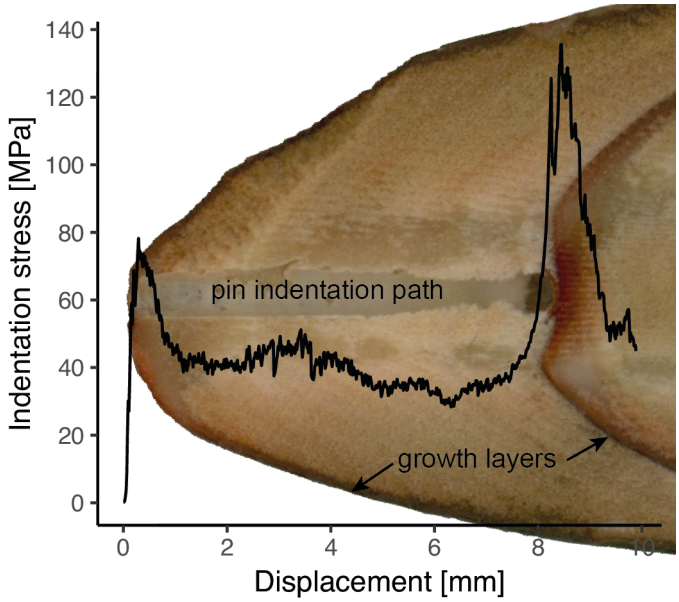

Figure 6: Deep indentation in the structure of a SUS highlighting porosity changes upon pin indentation. The pin cuts through the very porous medulla until it reaches a dense growth layer resulting in a sudden increase and decrease of stress.

Also differences in pore orientation at similar porosities can be revealed in PI tests (Fig. 7). A clear dependence of the pore channel orientation in respect to the loading direction is found. Regions with pore channels almost parallel to the loading direction show a significantly higher σ_{PI} than regions with increasing misalignment. Two examples with corresponding stress strain curves and pore channel orientation are depicted in Fig. 7. In contrast to UC testing the course of the stress displacement diagram contains real structural information, since no spallation can occur as the sample confines itself.

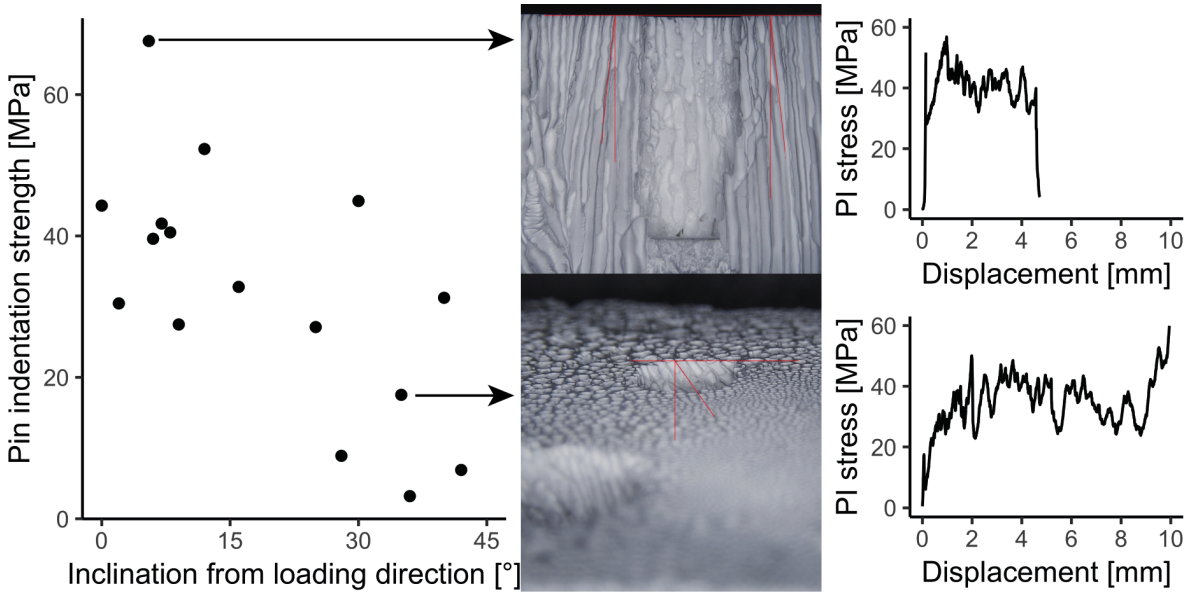

Figure 7: Dependence of pore channel orientation in respect to loading direction. For two pin indentations channel alignment and corresponding stress strain curves are shown. Note that the porosity is 0.04 higher for the low inclined structure. The difference in pin indentation strength is thus attributed to inclination only and would be probably even larger at the same porosity.

3.4. Energy Dissipation

In the following paragraph we compare classical unconfined UC tests, confined UC tests and PI measurements in respect to the characterisation of energy absorption or dissipation in order to highlight the advantages of PI in this respect. As outlined in (1), confined UC tests were conducted to overcome the issues with conventional, unconfined UC tests, which are spallation of flakes resulting in a discrepancy between engineering and true stress and tilting of the sample.

Fig. 8 shows unconfined and confined UC tests of IGC and SUS. All curves show regions with a low level or increasing plateau (shaded area in A, B) caused by brittle crushing [3]. The confinement seems not to influence its occurrence. Unconfined UC testing shows spallation of flakes (Fig. 8A2, B2) and tilting (Fig. 8B4). Confinement of samples prevents spallation. No flakes are visible on the bottom loading plate compared to the unconfined UC tests (Figure 8Ai-v, Bi-iv). However, shearing along structural weaknesses takes place (Fig. 8Aiv), which was also observed on unconfined samples. The

emergence of fatal cracks running through the whole specimen is not prevented by the confinement (Fig. 8Aiv, Biv).

The difference in stress strain curves of unconfined and confined UC tests is small and the benefits of confinement for the determination of energy dissipation or absorption are minor. Confinement generally hinders the widening of large longitudinal cracks (Fig. 8A4, B4) and the subsequent tilting of the sample resulting in spallation of large flakes as in unconfined UC (Fig. 8B4). Densification occurs earlier in confined testing because more material is present to be densified (Fig. 8A). However, the confinement does not lead to the desired plateau formation that is typical for non-brittle foams.

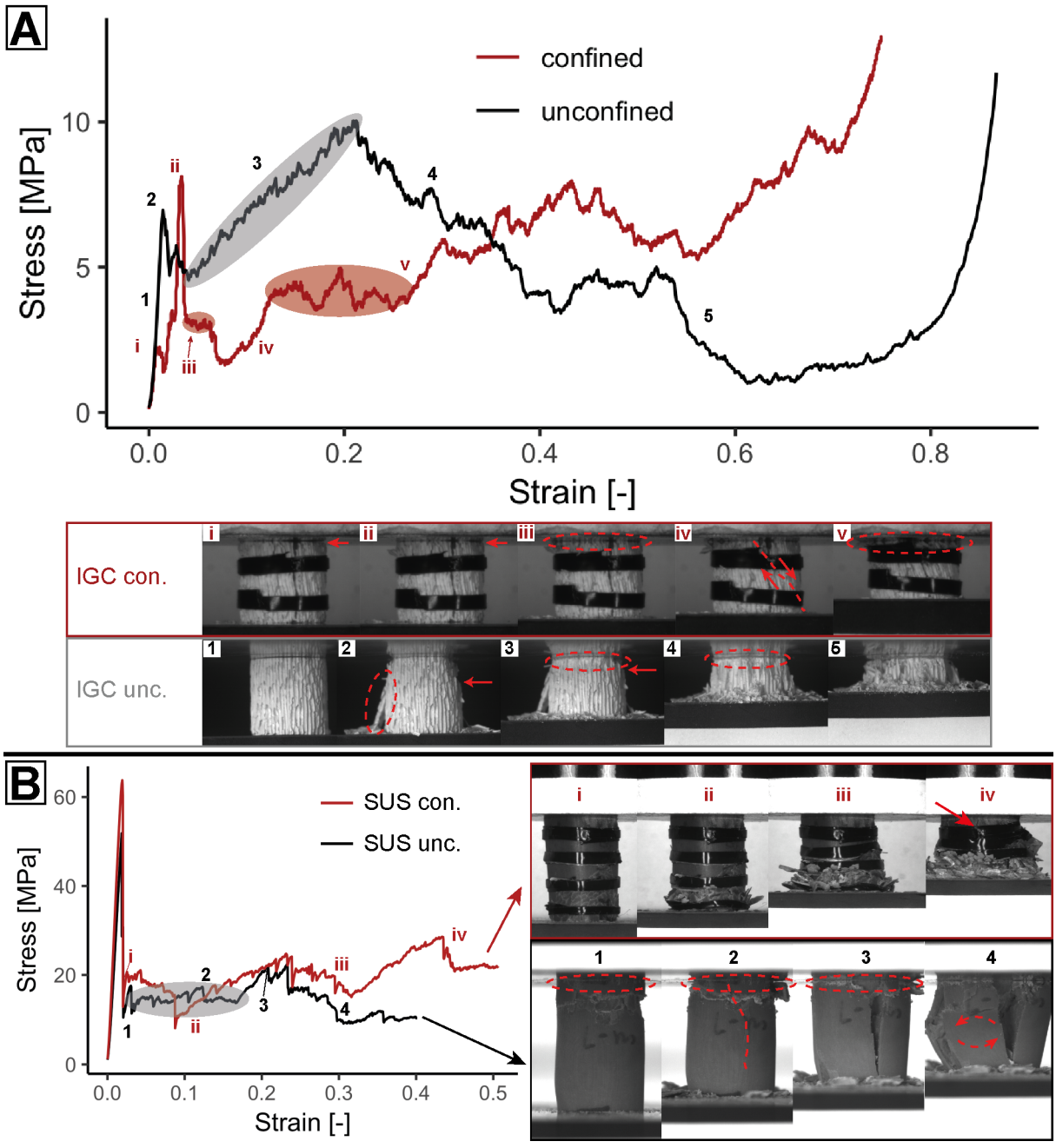

Figure 8: Uniaxial compression experiments of ionotropic gelation ceramics (IGC, A) and sea urchin spines of H. mamillatus (SUS, B) in unconfined and confined testing modes alongside with pictures highlighting relevant fracture events. Brittle crushing is encircled in the pictures and highlighted by shading in stress strain curves.

Longitudinal cracks are underlined by dashed lines, tilting is denoted by turning arrows. Unconfined and confined samples were selected to be as similar as possible in porosity and volume.

In deep PI experiments the stress displacement curves are completely different to UC testing and resemble those of flexible and plastic foams [3]. For IGC there is a load drop after the linear elastic increase, but the load recovers and stays at a constant, plateau-like level until the onset of densification after 6.5 mm of displacement. This plateau develops between 55-90 % of the elastic limit (Fig. 9A). In a sample fractured during PI the accumulation of crushed material forming in front of the pin indenter is visible as a half spherical plug (Fig. 9B). When this plug touches the lower loading plate, after a short drop, densification occurs. This is well visible in Fig. 9C, where two areas of densification of 3 mm PIs are present at the bottom of the IGC. The pin indenter destroys only the material directly beneath it and a thin film of crushed material is smeared to the wall indicating slight friction (Fig. 9C).

PI of SUS is principally comparable to IGC, however, the plateau is fairly constant and surpasses the strength of the linear elastic limit considerably (Fig. 9D). Moreover, in the first 3 mm of displacement a ± linear load increase occurs (3.2). Right before densification the load drops, which is probably due to fracture of the cellular solid by the force that the bulge of crushed material exerts to it. This bulge is pressed out of the structure (Fig. 9E) before densification occurs. Fig. 9F shows the local response of the material to the PI, which was also observed with the IGC (Fig. 9C).

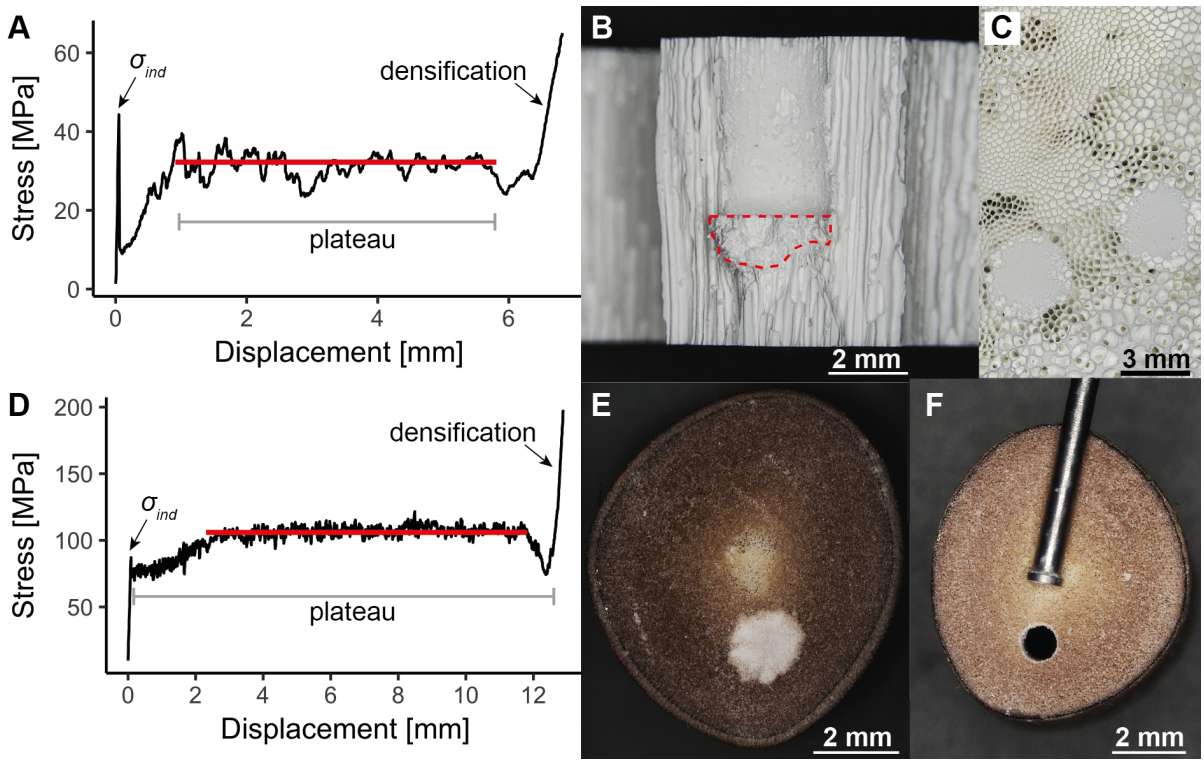

Figure 9: Deep pin indentations of ionotropic gelation ceramic (IGC) and a spine of H. mamillatus. Both stress displacement diagrams show the regions of linear elastic increase, plateau and densification. Indenter diameters used are: 3 mm (IGC), 1 mm (SUS). Please mind the different scales of the diagram axes.

4. Discussion

4.1. Comparison between uniaxial compression and pin indentation

Advantages and disadvantages of UC and PI for testing brittle cellular foams are listed in Table 1. We want to highlight the most relevant aspects, especially for scaffolds and other porous brittle materials. Whereas for UC tests precise coplanar sample preparation is essential, PI can be conducted *in situ* on the samples (i.e. bone scaffold) and preparation is less time consuming. As samples can be tested as received, PI results might be more meaningful in respect to real loading situations of a sample taking its geometry and shape into account (e.g. bone or joint). They are rarely a bulk compressive load as assumed in UC, but are more often a punctual load where the sample is much larger than the tested volume and confines itself, e.g. screws and nails for bone implant fixation.

Since foams often derive their properties from their specific structure and structural variations, PI is well suited to uncover these local property differences (Figs. 5-7), whereas UC measures only bulk properties. These additional information deepens the understanding of the structure-property relationship and can be used for a refined material design.

In contrast to UC, PI shows the classical threefold distinction of stress-displacement curve for porous materials: linear elastic increase, plateau and densification. Hence, energy absorption/dissipation values are more meaningful and display true material properties (Fig. 7-9). The determination of Young's Modulus with PI would require modelling the stress-strain field beneath the indenter. Principally Young's Modulus can be measured with PI.

Table 1: Advantages and disadvantages of uniaxial compression (UC) and pin indentation (PI) for testing of brittle foam materials.

	Uniaxial compression (UC)	Pin indentation (PI)
Advantages	• simple test conduction • "simple" stress field • established method • Young's Modulus determination possible	• simple test conduction • less time consuming sample preparation • few material needed for testing • multiple testing of the same sample • detailed structural characterization possible • determination of energy dissipation/absorption more straight forward (poor coplanarity does not lead to spallation) • more realistic loading situation for many biomedical applications

Disadvantages	• coplanarity essential for adequate testing • after first fracture: $\sigma_{eng} \neq \sigma_{true}$ • more time consuming sample preparation • larger quantities of material needed • no local testing possible	• Young's Modulus determination challenging (strain modelling required) • more complex stress field • additional forces ($\sigma_{PI} \neq \sigma_{UC}$) • no determination of bulk properties

4.2. Forces in pin indentation

The σ_{PI} is in average 90 % and 60 % higher than the σ_{UC} for IGC and SUS respectively (Fig. 3). This difference derives from the elastic deformation of the surrounding porous structure not located beneath the pin and the tear force of the pin cutting into the material. Intuitively these additional forces depend on the structure and the porosity of the material. The IGC has a honeycomb-like structure that reacts differently to load than the open foam of the SUS [43]. The difference in the materials become more obvious in the deep pin indentation. As the IGC is more porous, less material can accumulate below the indenter and the influence of friction at the indenter wall is lower. Furthermore, the material accumulation in comparably large channels requires less force than pushing it into the µm-sized open pore structure of the SUS. To minimize the friction force we used tapered indenters, which were also proposed by [24].

Comparing the plateau of IGC and SUS highlights, that the structure is also reflected in the plateau. For IGC in average ~75 channels are located beneath the 5 mm indenter. The failure of a single, continuous channel wall has a direct effect on the plateau. It results in a considerable stress drop of several percent (Fig. 9). Due to the much smaller pore size of the SUS, more pores are located below the 1 mm indenter (500-1000), so the failure of single struts is not severe and the overall appearance of the plateau is smoother. In order not to test the properties of single walls but of the material, Kumar et al. [25] reported that at least 40 pores need to be located beneath the indenter. This threshold was met in all our tests, however, we want to add that smooth plateaus arise only at much higher pore numbers beneath the indenter. This can be seen well in Schmier et al. [31] where the indenter diameter is varied between 0.6-2 mmm for SUS.

4.3. Energy dissipation

In order to emphasize the difficulty of measuring energy absorption in UC we conducted confined and unconfined UC tests with IGC and SUS. The idea of confining the samples with elastic stripes was to prevent spallation and fracturing of flakes to avoid the divergence between engineering and true

stress. Ideally, the confined UC tests would show a typical stress-displacement curve for foam materials with linear elastic increase, smooth plateau and densification [3]. As Fig. 8 shows confinement prevents spallation but could not lead to the desired result. The fractured flakes are kept by the stripes but do not contribute to strength. The fracture behaviour is still the same as in unconfined UC testing with fatal cracks covering the whole specimen. The crack growth is not impeded by the confinement.

These issues are overcome by PI. Here the sample confines itself to such an extent that fracture only occurs beneath the indenter (Fig. 9). This is, however, just valid as long as the sample is much larger than the indenter. This can be seen in the 3 mm PIs for the SUS, where occasionally the whole sample split when the sample to indenter ration became too small. For IGC the same effect was observed for PIs close to the sample rim (Fig 7). Therefore, the size of the indenter and the location of PI should be chosen accordingly. It is important to highlight that these issues manly arise for deep pin indentations.

When the PI location is suitable, a textbook example of stress-displacement curve for foam materials is obtained (Fig. 9). After the linear elastic increase a high, approximately constant and smooth plateau (smoothness depends on indenter/pore size ratio) develops until densification in agreement with flexible and plastic foams [3]. This highlights that the inferior energy absorption of brittle foams compared to flexible and plastic foams is not only due to the brittleness of the material but also to inadequate testing in UC. In PI brittle foams live up to their high potential of absorbing energy. As they have a much higher strength (= plateau) than flexible and plastic foams, their energy dissipation is also superior. Their high energy dissipation character is of interest in impact protection as i.e. bullet proof vests and in extreme environments such as protection shields of satellites or space ships. However, energy can be dissipated only once in brittle foams, as afterwards the material is destroyed in contrast to flexible and to some extent also plastic foams.

5. Conclusions

1) Pin indentation is a powerful tool to detect small scale heterogeneities in brittle cellular foams such as pore size variations, porosity changes and structural inclination in the sample.

2) Pin indentation is a suitable method to characterize energy dissipation as the full potential of the brittle cellular foams is reached. A long and stable plateau dissipates energy, hence, the stress displacement curve is comparable to those of flexible and plastic foams.

3) Unlike pin indentation, confinement of brittle cellular foams in uniaxial compression with elastic stripes does not lead to a high and steady plateau and has no benefit for testing.

4) Sample preparation for pin indentation is less time consuming, less material is needed and more tests can be done in the same sample.

5) In comparison to uniaxial compression tests, the stress field in pin indentation is more complicated. It exceeds the pin diameter considerably. This way pin indentation strength is higher than the strength measured in uniaxial compression. The difference is structure and material specific.

REFERENCES

1. Studart, Andre R., Urs T. Gonzenbach, Elena Tervoort, and Ludwig J. Gauckler. "Processing Routes to Macroporous Ceramics: A Review." *Journal of the American Ceramic Society* 89, no. 6 (2006): 1771-89.
2. Voigt, Claudia, Johannes Storm, Martin Abendroth, Christos G. Aneziris, Meinhard Kuna, and Jana Hubálková. "The Influence of the Measurement Parameters on the Crushing Strength of Reticulated Ceramic Foams." *Journal of Materials Research* 28, no. 17 (2013): 2288-99.
3. Maiti, S.K., L.J. Gibson, and Michael F Ashby. "Deformation and Energy Absorption Diagrams for Cellular Solids." *Acta Metallurgica* 32, no. 11 (1984): 1963-75.
4. Greil, P., T. Lifka, and A. Kaindl. "Biomorphic Cellular Silicon Carbide Ceramics from Wood: Ii. Mechanical Properties." *J Eur Ceram Soc* 18, no. 14 (1998): 1975-83.
5. Colombo, P., A. Arcaro, A. Francesconi, D. Pavarin, D. Rondini, and S. Debei. "Effect of Hypervelocity Impact on Microcellular Ceramic Foams from a Preceramic Polymer." *Advanced Engineering Materials* 5, no. 11 (2003): 802-05.
6. Fleck, N.A. "An Overview of the Mechanical Properties of Foams and Periodic Lattice Materials." In *Cellular Metals and Polymers*, edited by R.F. Singer, C. Körner and V. Altstädt. Fürth: Fragezeichenverlag, 2004.
7. Yoon, Byung-Ho, Chee-Sung Park, Hyoun-Ee Kim, and Young-Hag Koh. "In-Situ Fabrication of Porous Hydroxyapatite (Ha) Scaffolds with Dense Shells by Freezing Ha/Camphene Slurry." *Materials Letters* 62, no. 10-11 (2008): 1700-03.
8. Meille, S., M. Lombardi, J. Chevalier, and L. Montanaro. "Mechanical Properties of Porous Ceramics in Compression: On the Transition between Elastic, Brittle, and Cellular Behavior." *Journal of the European Ceramic Society* 32, no. 15 (2012): 3959-67.
9. Xue, Weijiang, Yong Huang, Zhipeng Xie, and Wei Liu. "Al2o3 Ceramics with Well-Oriented and Hexagonally Ordered Pores: The Formation of Microstructures and the Control of Properties." *Journal of the European Ceramic Society* 32, no. 12 (2012): 3151-59.
10. Ghosh, Dipankar, Aaron Wiest, and Robert D. Conner. "Uniaxial Quasistatic and Dynamic Compressive Response of Foams Made from Hollow Glass Microspheres." *Journal of the European Ceramic Society* 36, no. 3 (2016): 781-89.
11. Ramavath, P., P. Biswas, N. Ravi, and R. Johnson. "Prediction and Validation of Bukling Stress of the Ceramic Honeycomb Cell Walls under Quasi-Static Copression." *congent engineering* 3 (2016): 1168068.
12. Seuba, J., S. Deville, C. Guizard, and A. J. Stevenson. "Mechanical Properties and Failure Behavior of Unidirectional Porous Ceramics." *Sci Rep* 6 (2016): 24326.
13. Sabree, I., J. E. Gough, and B. Derby. "Mechanical Properties of Porous Ceramic Scaffolds: Influence of Internal Dimensions." *Ceramics International* 41, no. 7 (2015): 8425-32.
14. Lauer, C., K. Sillmann, S. Haussmann, and K. G. Nickel. "Strength, Elasticity and the Limits of Energy Dissipation in Two Related Sea Urchin Spines with Biomimetic Potential." *Bioinspir Biomim* 14, no. 1 (2018): 016018.
15. Dam, C.Q., R. Brezny, and D. J. Green. " Compressive Behavior and Deformation-Mode Map of an Open Cell Alumina." *Journal of Material Research* 5 (1990): 163-71.
16. Brezny, R., and D. J. Green. " Uniaxial Strength Behavior of Birttle Cellular Materials." *J Am Ceram Soc* 76, no. 9 (1993): 2185-92.

17. Ashby, M. F. "The Mechanical Properties of Cellular Solids." *Metallurgical Transactions A* 14, no. A (1983): 1755-69.
18. Brezny, R., and D. J. Green. "The Effect of Cell Size on the Mechanical Behavior of Cellular Materials." *Acta metall. mater.* 38 (1990): 2517-26.
19. Pabst, W., and E. Gregorová. "Young's Modulus of Isotropic Porous Materials with Spheroidal Pores." *Journal of the European Ceramic Society* 34, no. 13 (2014): 3195-207.
20. Seeber, B. S. M., U. T. Gonzenbach, and L. J. Gauckler. "Mechanical Properties of Highly Porous Alumina Foams." *J Mater Res* 28, no. 17 (2013): 2281-87.
21. Ashby, M. F., A.G. Evans, N.A. Fleck, L. J. Gibson, J.W. Hutchinson, and H.N.G Wadley. *Metal Foams - a Design Guide* Woburn: Butterworth-Heinemann, 2000.
22. Gibson, L. J., and M. F. Ashby. *Cellular Solids: Structure and Properties*. 2nd ed. Cambridge, UK: Cambridge University Press, 1997.
23. Scheffler, M., and P. Colombo, eds. *Cellular Ceramics: Structure, Manufacturing, Properties and Applications*. Weinheim: Wiley-VCH 2005.
24. Olurin, O.B., N.A. Fleck, and SAshby M.F. "Indentation Resistance of an Aluminium Foam." *Scripta Materialia* 43 (2000): 7.
25. Kumar, P.S., S. Ramachandra, and U. Ramamurty. "Effect of Displacement-Rate on the Indentation Behaviour of an Aluminium Foam." *Materials Science and Engineering: A* 347 (2003): 8.
26. Ramachandra, S. "Impact Energy Absorption in an Al Foam at Low Velocities." *Scripta Materialia* 49, no. 8 (2003): 741-45.
27. Ramamurty, U., and M.C. Kumaran. "Mechanical Property Extraction through Conical Indentation of a Closed-Cell Aluminium Foam." *Acta Materialia* 52 (2004): 9.
28. Lu, G., J. Shen, W. Hou, D. Ruan, and L. S. Ong. "Dynamic Indentation and Penetration of Aluminium Foams." *International Journal of Mechanical Sciences* 50, no. 5 (2008): 932-43.
29. Andrews, E.W., G. Gioux, P. Onck, and L.J. Gibson. "Size Effects in Ductile Cellular Solids. Part Ii: Experimental Results." *International Journal of Material Sciences* 43 (2001): 13.
30. Presser, V., S. Schultheiß, C. Berthold, and K.G. Nickel. "Sea Urchin Spines as a Model-System for Permeable, Light-Weight Ceramics with Graceful Failure Behavior. Part I. Mechanical Behavior of Sea Urchin Spines under Compression." *Journal of Bionic Engineering* 6, no. 3 (2009): 203-13.
31. Schmier, Stefanie, Christoph Lauer, Immanuel Schäfer, Katharina Klang, Georg Bauer, Marc Thielen, Kathrin Termin, Christoph Berthold, Siegfried Schmauder, Thomas Speck, and Klaus G. Nickel. "Developing the Experimental Basis for an Evaluation of Scaling Properties of Brittle and 'Quasi-Brittle' Biological Materials." In *Biomimetic Research for Architecture and Building Constructions*, edited by Jan Knippers, K.G. Nickel and Thomas Speck, 277-94. Switzerland: Springer International Publishing, 2016.
32. Vecchio, K. S., X. Zhang, J. B. Massie, M. Wang, and C. W. Kim. "Conversion of Sea Urchin Spines to Mg-Substituted Tricalcium Phosphate for Bone Implants." *Acta Biomater* 3, no. 5 (2007): 785-93.
33. Cao, L., X. Li, X. Zhou, Y. Li, K. S. Vecchio, L. Yang, W. Cui, R. Yang, Y. Zhu, Z. Guo, and X. Zhang. "Lightweight Open-Cell Scaffolds from Sea Urchin Spines with Superior Material Properties for Bone Defect Repair." *ACS Appl Mater Interfaces* 9, no. 11 (2017): 9862-70.

34. Eljaouhari, A. A., R. Müller, M. Kellermeier, K. Heckmann, and W. Kunz. "New Anisotropic Ceramic Membranes from Chemically Fixed Dissipative Structures." *Langmuir* 22 (2006): 11353-59.
35. Dittrich, R., G. Tomandl, F. Despang, A. Bernhardt, Th Hanke, W. Pompe, and M. Gelinsky. "Scaffolds for Hard Tissue Engineering by Ionotropic Gelation of Alginate?Influence of Selected Preparation Parameters." *Journal of the American Ceramic Society* 90, no. 6 (2007): 1703-08.
36. Xue, Weijiang, Yang Sun, Yong Huang, Zhipeng Xie, and Jialin Sun. "Preparation and Properties of Porous Alumina with Highly Ordered and Unidirectional Oriented Pores by a Self-Organization Process." *Journal of the American Ceramic Society* 94, no. 7 (2011): 1978-81.
37. Weber, K., G. Tomandl, T. Wenger, and K. Heckmann. "Preparation of Structured Ceramics for Membranes." *Key Engineering Materials* 132-136 (1997): 1754-57.
38. Thiele, H., and K. Hallich. "Kapillarstrukturen in Ionotropen Gelen." *Kolloid-Zeitschrift* 151, no. 1 (1957): 1-12.
39. Grossmann, Jan Nils, and James H Nebelsick. "Comparative Morphological and Structural Analysis of Selected Cidaroid and Camarodont Sea Urchin Spines." *Zoomorphology* 132, no. 3 (2013): 301-15.
40. Lauer, Christoph, Tobias B. Grun, Isabel Zutterkirch, Raouf Jemmali, James H. Nebelsick, and Klaus G. Nickel. "Morphology and Porosity of the Spines of the Sea Urchin Heterocentrotus Mamillatus and Their Implications on the Mechanical Performance." *Zoomorphology* 137 (2017): 137-54.
41. Riccardi, B., and R. Montanari. "Indentation of Metals by a Flat-Ended Cylindrical Punch." *Materials Science and Engineering: A* 381, no. 1-2 (2004): 281-91.
42. Ji, Shaocheng, Qi Gu, and Bin Xia. "Porosity Dependence of Mechanical Properties of Solid Materials." *Journal of Materials Science* 41, no. 6 (2006): 1757-68.
43. Gibson, L. J., M. F. Ashby, and B. A. Harley. *Cellular Materials in Nature and Medicine*. Cambridge: Cambridge University Press, 2010.

Manuscript 8

Hierarchical construction of spines of *Heterocentrotus mamillatus* weakens the size effect on structural strength

(20 pages)

Hierarchical construction of spines of *Heterocentrotus mamillatus* weakens size effect on structural strength

Christoph Lauer[1,+,*], Stefan Mück[1,+], Gerald Buck[1], Klaus G. Nickel[1]

[1] University of Tübingen, Department of Geosciences, Division of Applied Mineralogy, Wilhelmstraße 56, 72074 Tübingen, Germany

[+]shared first author

[*]corresponding author:
Christoph Lauer
Department of Geosciences - Division of Applied Mineralogy
Wilhelmstraße 56
D-72074 Tübingen
Germany
Tel.: +49 7071 29 76810
Fax: +49 7071 29 3060
E-mail address: christoph.lauer@uni-tuebingen.de

Key words: Size effect, hierarchical structure, sea urchin spines, pin indentation, biological materials

Biological materials are usually very heterogeneous because of their hierarchical structuring and porosity, hence, their mechanical performance scatters considerably. This complicates recognizing trends and interpreting data. Recently it was claimed that the strength of the Mg-calcitic spines of the slate pencil urchin *Heterocentrotus mamillatus* have a diminished size effect on structural strength, however, as the scatter in measurements was large, this hypothesis needs more scrutiny. Usually ceramic materials' strength decreases with increasing size and a way to mitigate this disadvantageous relation bears great potential in improving constructions. We address the problem of the large natural heterogeneity by narrowing down the porosity range and excluding the highest hierarchical level, the dense "growth layers" from testing. This is done by a micro-sized compression test, the pin indentation and by removing the highest hierarchical level with core drilling for uniaxial compression testing specimen. Both tests revealed a size effect beyond doubt, however, samples with intact hierarchy do not show a size effect that could stand out of the scatter of strength. We thereby conclude that the hierarchical construction of the spines of *H. mamillatus* weakens the size effect. The mechanism for this is possibly related to the growth of the spines. Large spines contain more growth layers because they experienced more growth cycles than the younger and simultaneously smaller aboral spines and the density of growth layers increases with age. The outermost (youngest) growth layers have the highest density. Both mechanisms provide the spines with additional strength compared to the smaller spines.

1. Introduction

Biological materials, although restricted to a small pool of raw materials [1], often show outstanding mechanical properties and combine contradicting characteristics such as high stiffness and toughness in i.e. nacre or bone [2]. Unlike technical materials, biological materials derive their mechanical properties and multi-functionality from hierarchical structuring from nano to macroscale (e.g. [1, 3]). Therefore, the interdisciplinary field of biomimetics that gains inspiration from nature for improving design of technical materials, is "moving to centre-stage" [3]. Recently Lauer et al. [4] claimed that the spines of the Indo Pacific sea urchin *Heterocentrotus mamillatus* (slate pencil urchin) have a diminished size effect on structural strength. This is a very intriguing finding and is subjected to further scrutiny in this study. Before dealing with the size effect, the composition and structure of the spines of *H. mamillatus* is briefly reviewed.

Spines of *H. mamillatus*

Sea urchin spines in general and the spines of *H. mamillatus* in particular, differ from other ceramic biological materials such as bone, nacre or enamel, as they contain very little organic material [5].

Usually the content is reported to be below or even far below 1 wt.% (e.g. [6-8]), however there are also reports of higher contents (e.g. [9, 10]). This makes sea urchin spines a nearly "all-ceramic" composite material out of Mg calcite nanocrystals (~100 nm [6, 11]) embedded in an amorphous calcium carbonate matrix (~8 wt.%) [6]. Organic macromolecules were found to be occluded in the crystal [7] and the matrix [6]. Weber et al. already noted back in 1971 that sea urchin spines have an "unusual strength" [12], far exceeding the properties of the well-cleaving raw material, which was aptly described as a "rather poor building material" by Weiner and Addadi [13].

The large aboral spines of *H. mamillatus* are a delicately structured lightweight construction and have served as role model for lightweight ceramics [14], for lightweight and functionally graded concrete [15] and for templates for bone tissue replacement [16, 17]. The hierarchical structure of the spines is rather simple with only three clearly distinguishable levels. The lowermost level comprises the mesocrystalline structure described above, which is typical for all sea urchin spines. It is made responsible for the lack of calcite cleavage planes and induces instead conchoidal fracture [6]. This level is followed by the stereom structure, an arrangement of pores and thin struts, which constitutes the lightweight construction. The density of these large and rather clumsy looking spines matches the density of sea water [18] so that the spines are not a burden to carry. Generally, it is distinguished between different stereom types of more ordered and disordered types, which can be related to function e.g. bearing load, filling space or muscle insertion [19]. In the third and highest hierarchical level, the stereom types are interwoven. Thin and dense layers, the growth layers (GL), which mark earlier growth stages and outer surfaces of the spine, are concentrated towards the rim of the spine and provide it with stiffness and strength [4]. The more porous radiating layer (RL) between the GLs and the very porous medulla in the centre of the spine are beneficial for the spine's weight without decreasing its resistance against bending forces. The strength and elastic properties of the spines are highly dependent on the porosity [20]. As the porosity varies considerably, it is important to report the mechanical properties are always linked to porosity, otherwise data might be misinterpreted.

The size effect

The size effect describes the phenomenon that small components of ceramic materials have statistically a higher strength than large components of the same material. It arises since ceramic materials do not fail because their intrinsic strength is surpassed but due to flaws within the material. They can be impurities, little cracks or pores and they usually originate from manufacturing processes [21]. With increasing volume the likelihood of encountering such a large and critical flaw increases. In consequence, failure of ceramic materials is probabilistic, with small samples being more likely to withstand high strengths than large samples of the same material and geometry. This relation was first mathematically described by Weibull [22] and depends on the volume V and the applied stress σ only (Eq. 1):

$$P(V,\sigma) = 1 - \exp\left(-\frac{V_i}{V_0}\left(\frac{\sigma_i}{\sigma_0}\right)^m\right) \quad \text{Eq. 1}$$

with m the shape parameter ("Weibull modulus"), the scale parameter σ_0 ("characteristic strength") the volume V_i of the sample i, the measured strength σ_i of the sample and a referencing volume V_0, for simplicity mostly set equal to the sample volume. m is a measure for the reliability of the material, as a high m indicates a narrow range of failure stresses. σ_0 is the value where ~63.2 % of the samples failed, as the Weibull distribution is usually displayed in double logarithmic expression where y = 0 equals the failure probability of ~63.2 %. By rearranging Eq. 1, the statistical ("Weibullian size effect") can be calculated with (Eq. 2):

$$\left(\frac{\sigma_{01}}{\sigma_{02}}\right) = \left(\frac{V_{02}}{V_{01}}\right)^{\frac{1}{m}}. \quad \text{Eq. 2}$$

σ_{01} and σ_{02} give the characteristic strength of samples with volume V_1 and V_2, respectively. The size effect is not always of statistical cause as it requires that the crack opening leads to an immediate failure, no stable crack growth with stress redistribution occurs [23] and cracks do not interact [24]. Nominally brittle materials with the above mentioned fracture characteristics were named "quasi-brittle" and include most prominently concrete, but also many composite materials and biological materials such as shells or wood [25]. This size effect is labelled "deterministic-energetic". On sufficiently large scales, all quasi-brittle materials behave as purely brittle materials and show statistical (Weibullian) size effect, and vice versa, if selected scales are small enough, all brittle materials behave quasi-brittle [26].

Although being a biological material, the brittle spines of *H. mamillatus* do not behave quasi-brittle in the scales we are concerned with. Bending experiments of [20, 27] show that complete and sudden failure occurs when exceeding the elastic limit, with no stable crack growth or stress redistribution as in e.g. concrete beams. Therefore a size effect according to Eq. 2 is expected. The weakening of the size effect as observed by Lauer et al. [4] cannot be explained with either statistical nor deterministic-energetic size effect models and is therefore investigated in more detail in this study.

The authors hypothesized that the critical Griffith crack size is larger than the strut size constituting the stereom [4]. As the size of these struts does not scale with an increase in spine size [27], a size effect would be eliminated on the second hierarchical level of the spines of *H. mamillatus*. Cracks would not become critical in the material. To verify this hypothesis, two methods were applied to test the second hierarchical level only.

Cores were drilled out of the spines of *H. mamillatus* that lack the highest hierarchical level (growth layers) and tested in uniaxial compression (UC). Moreover, micro compression tests within the spine structure were conducted to reduce porosity variations. The latter method is named "pin indentation" (PI) and originates from testing metallic foams [28-31] and was also applied to the spines of *H. mamillatus* in preliminary tests [32]. First it was checked by systematically varying the area compressed

that PI is able to detect a size effect. This was done on a porous alumina ceramic, a material that is known to have a size effect. Then the method was applied to the spines of *H. mamillatus*.
With these two testing methods, the natural heterogeneities of the spines of *H. mamillatus* could be narrowed down considerably and the uncertainty they induce in assessing the size effect [4] became more controllable.

2. Materials and Methods

Samples

Unidirectional, highly porous alumina ceramics were produced by the ionotropic gelation method. In the manufacturing process, 2 wt% of sodium alginate (Würzteufel GmbH, Nagold, Germany) was solved in deionized water and mixed in a 1:1 ratio with a pH-stabilized ceramic suspension (solid content: 20 wt% alumina, Al2O3, TM-DAR purity 99.99 %, Taimei Chemicals Co. Ltd., Tokyo, Japan). This so-called mixed-sol was then topped by a cross-linking agent (0.5 M $CaCl_2$, Fisher Scientific GmbH, Niddernau, Germany). In a next step, the alginate of the mixed-sol is structured by the cross-linking agent through a diffusive process. In the resulting ceramic-gel body a channel-like porosity is formed. After completion of the structuring process, the samples were solidified using glucono-1,5-lactone (1 M; Sigma-Aldrich Chemie GmbH, München, Germany) and then freeze-dried (Sublimator 2x3x3/5 ZIRBUS technology GmbH, Bad Grund, Germany). The final sintering process produces the ceramics with channel-like porosity (200 – 500 µm channel diameter). For further information on the manufacturing process the reader is directed to refs [33, 34].
Loose aboral primary spines of *Heterocentrotus mamillatus* were purchased from Fischhaus Zepkow (Zepkow, Germany). Despite cutting into appropriate sample sizes, spines were not treated further.

Pin indentation

Pin indentation experiments were carried out with an Instron 4502 universal testing machine (Instron Deutschland GmbH, Pfungstadt, Germany). Cylindrical, flat ended tungsten carbide pins of varying diameter (1.5, 3 and 5 mm for IGC and 0.6, 1 and 3 mm for SUS) were used to investigate the size effect. They were pushed with a constant cross head speed of 0.5 mm/min into the sample. The choice of pin diameters was a trade-off between using the largest range of feasible diameters in order to detect a size effect and to encounter enough pores underneath the smallest pin, so that the measurement is still representative for the material and not for single struts. For SUS these requirements were easy to fulfil, as even below the 0.6 mm pin were >>100 pores, much more than the threshold of 40 pores identified by [29]. However, for IGC, the 1.5 mm pin often covered less than 40 pores. Implications are discussed in XX.

Pin indentations were conducted with their depth not exceeding 1.5 mm in case of IGC and 1 mm for SUS. This was sufficient to yield the pin indentation strength σ_{PI}, which is the strength terminating the linear elastic increase, just prior to the first load drop and the emergence of the plateau [28].

Pin indentation locations were chosen to be as homogeneous as possible, i.e. free of large pores or thick walls in IGC and free of dense growth layers for SUS. IGC used for indentations had dimensions of ~ 35 x 22 x 12 mm and it was ensured that measurements were not conducted close to the rim of the sample in order to avoid spallation or cracking.

Only the largest aboral spines of *H. mamillatus* were selected for analysis, so that ample indentations could be made in a single cross section of the spine (Fig. 3A). Spines were cut in coplanar segments and those sections with a large proportion of homogeneous RL were used for pin indentations.

σ_{PI} differs from strength measured in UC (σ_{UC}), because not solely compressive forces occur [35]. In PI also shearing forces arise on the pin perimeter where it cuts into the material. Although failure occurs in most cases directly beneath the indenter a larger region around the pin is stressed elastically, which also enters the measured force. Therefore σ_{PI} and σ_{UC} are not directly comparable [35]. The same authors found that the strength in PI is 45-60 % higher than in UC of spines of H. mamillatus, however, as this factor depends on porosity and structure it is not attempted here to correlate σ_{PI} and σ_{UC} to evaluate the size effect since uncertainties would be too high.

Uniaxial compression

Uniaxial compression tests were conducted with the same cross head speed and the same universal testing machine as the pin indentation experiments. Small cores had a height of 4 mm (± 0.005 mm) and a diameter of 3.7-3.9 mm. Large cores were approximately 8 times larger with a height of 8 mm (± 0.005 mm) and a diameter of 7.65-7.85 mm. All cores had no confining growth layers at the rim. It was also attempted to have no growth layer within the structure, which was not always possible. A precise coplanarity is vital for reliable UC results [36] and a coplanarity of ± 0.005 mm was achieved by grinding cores from both sides with spacers to the desired height. In a first step cores were stuck with heated wax alongside spacers to a slide and ground after cooling to the height of the spacers. Then cores were detached by gentle heating (< 100 °C) and stuck with the ground face to the slide again. This time slightly shorter spacers were used. Finally, the wax was dissolved out of the porous stereom structure by stirring for 5 h at 40 °C in an acetone bath. Secondary electron microscope (SEM, Hitachi TM 3030, Hitachi High-Technologies Europe GmbH, Krefeld, Germany) revealed only traces of wax remaining in the structure after this cleaning procedure. The groups of large and small cores were chosen to match in average porosity (Table 3).

Porosity determination

Bulk porosity of all IGC samples was determined gravimetrically. For simplicity it was assumed that the local porosity at the spot of the PI is very similar to the bulk porosity of the IGC, as the porosity variation within a single sample was determined to be as little as 0.02. The porosity of the drilled cores of *H. mamillatus* was also determined gravimetrically.

As outlined in (1), porosity is distributed very heterogeneously in the spines of *H. mamillatus*, which made local porosity determination inevitable. It was done with SEM pictures and requires infiltration of the sample to avoid 3d effects in determination, which would decrease porosity systematically [18]. As the infiltration enhances the contrast between pores and calcite, automatic evaluation in image analysis open source ImageJ (version: 1.52h) is possible. Since the infiltration with Araldite 2020A is not easy to remove, porosity was determined at sections directly adjacent to those planes which were used for pin indentations. These sections were cut beforehand and the reference section and pin indentation section were only separated by the blade width of the saw (1 mm). Therefore, the error due to local porosity variations is negligible. Porosity was determined according to [18] with the default threshold in ImageJ. The exact location of the PI was identified by overlaying the optical image of the section containing the PIs (obtained with Hirox MXB 2016Z, Hirox Europe, Limonest, France) with the corresponding, directly adjacent SEM stich for porosity determination. The error due to misalignment in overlapping was determined to be as little as 0.01 in porosity.

Statistical testing

Statistical testing and data processing was done with GNU R (version 1.1.442) with the packages *ggplot*, *car*, *psych* and *fitdistrplus*. Data were checked for normal distribution with Shapiro-Wilk test and for homogeneity of variance with Levene test. All tested data were normal distributed and had a homogeneous variance. A Welch-t-test was applied for two groups and for more than two groups a One-way ANOVA followed by a Tukey HSD post hoc test was used.
Weibull modulus and characteristic strength were obtained by (1) linear regression (LR) and by (2) maximum likelihood estimation (MLE). The expected strength difference by variation of volumes was calculated by Eq. 2. As for pin indentation the extent of the stressed volume is unknown, the areas of the flat-ended pin were used instead. This simplification is discussed in 4.

3. Results

Pin indentation of porous alumina ceramics

Fig 2A-D shows pin indentations of 1.5 and 5 mm diameter in the unidirectional channel structure of the IGC. It is well visible that damage is restricted to the area beneath the indenter. The Weibull analysis (Fig. 2E) highlights that the σ_{PI} for different PI sizes differs systematically. Smallest PIs have the

highest σ_{PI}. The difference to other groups is statistically significant (Table 1). The size effect can be predicted reasonably well with Eq. X (dashed lines, Fig. 2E), especially when taking into account the large uncertainties arising from *m* determination (Table 1). Dotted lines (Fig. 2E) represent the highest *m* covered in the 95 % confidence interval (Table 1). These measurements validate that the size effect can be detected by PI in localized measurements.

Table 1: Data to Fig. 2E. Weibull modulus and characteristic strength in brackets is obtained by maximum likelihood method, as the confidence interval in italics (displayed as dotted lines in Fig. 2E). Weibull modulus in regular font is calculated by LR and displayed by solid lines in Fig. 2E.

pin indenter diameter [mm]	sample size *n*	Weibull modulus *m*	characteristic strength σ_0 [MPa]	Tukey HSD post hoc test	σ_0 [MPa] extrapolated (Eq. X)
1.5	29	5.1 (4.6) *3.4-5.8*	48 (48)	to 3 mm: $^{**}p < 0.01$ to 5 mm: $^{***}p < 0.0001$	71 *51*
3	18	4.6 (4.4) *2.9-6.0*	38 (38)	to 1.5 mm: $^{**}p < 0.01$ to 5mm: $p > 0.1$	-
5	14	2.9 (3.4) *1.9-4.8*	31 (31)	to 1.5 mm: $^{***}p < 0.0001$ to 3 mm: $^{**}p < 0.01$	29 *31*

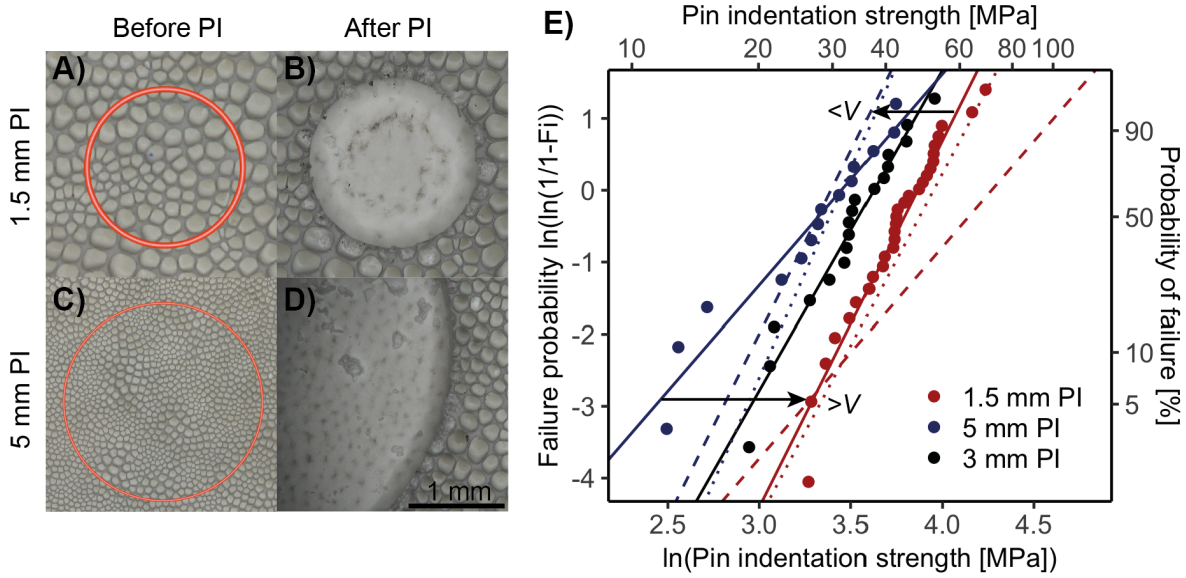

Figure 2: The damage is well restricted to the area of the pin in IGC (A-D). Weibull plot with strength extrapolated after Eq. 2 (dashed lines) and the upper limit of the confidence interval (dotted lines, see Table 1). Predictions (indicated by arrows) and data agree reasonably well.

Pin indentation of spines of *H. mamillatus*

The pin indentations in the spines of *H. mamillatus* could be closely placed without mutual influence on the σ_{PI} as damage was restricted to the area beneath the indenter only (Fig. 3A). It was attempted to place all measurements in the comparably homogeneous RL, a stereom type that can be best seen by its radiating trabeculae accentuated by the densified material (Fig. 3B). However, the 3 mm PIs were often too large for the radiating layer only and included parts of the porous medulla (dotted line, Fig. 3B) or a GL, indicated by arrow (Fig. 3D). As the GLs are the densest part of the spine, they can have a strong

influence on σ_{PI} and on the failure behaviour of the PI (Fig. 3E). Usually the damage is localized in form of a narrow band of crushed material underneath the pin (Fig. 3C). By the involvement of a GL the influence of the PI seems to reach deeper into the material. This is why measurements with GLs were omitted in Fig. 4B.

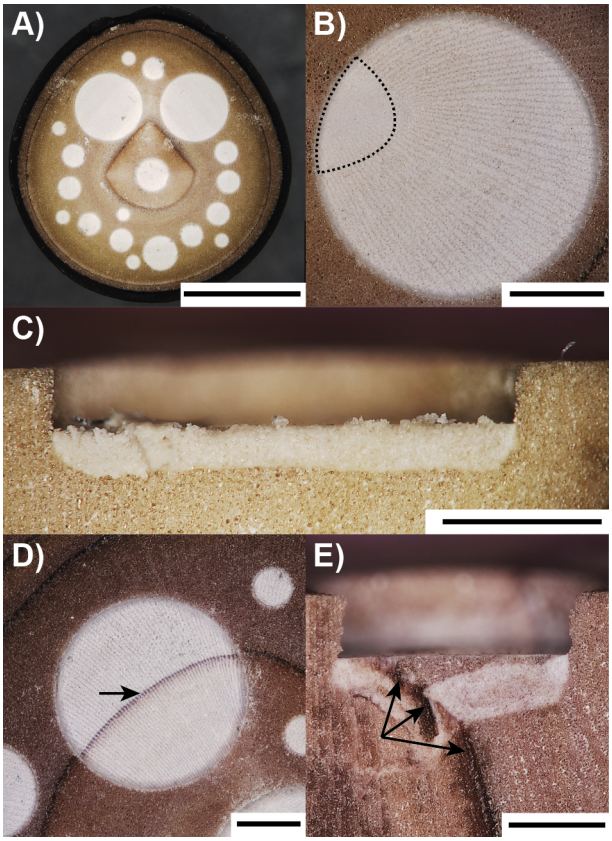

Figure 3: Pin indentations in spines of H. mamillatus (A-E). A) shows that many indentations could be placed in a single spine as damage occurred only locally in a shallow band below the indenter (C). Due to their size it was difficult to place 3 PIs in the radiating layer only (B,D,E). A small proportion in B) is located in the porous medulla (dotted line) and in D) a growth layer was included in the measurement (arrow), which is shown in side view in E). Scale bars: 5 mm (A), 1 mm (B-E).

As porosity varies widely in spines of *H. mamillatus*, it is reported for each measurement by the colour code in Fig. 4. There is a good correlation between porosity and strength, as more porous (red-yellow) locations result in a lower σ_{PI} than PIs in denser areas (blue colours) (Fig. 4). At first it seems that 3 mm σ_{PI} is significantly lower than the σ_{PI} of 0.6 and 1 mm PIs. As 3 mm PIs were usually slightly more porous in average (Table 2), a porosity correction for the strength of the porous bulk material σ_{ϕ} was applied (doubly dashed lines in Fig. 3A-C) with the model given by Ji et al. [37] for spherical pores, which is a good approximation for the open pore shape of *H. mamillatus* [20] (Eq. 3):

$$\sigma_{fc} = \sigma_f(1-\phi)^2 \qquad \text{(Eq. 3)}$$

with the porosity ϕ and strength of the dense material σ_f of 948 MPa, which was obtained by fitting the model to the data. With the applied porosity correction the whole distribution shifts towards the strength of the 0.6 and 1 mm PIs. However, 3 mm PIs are still slightly weaker than the smaller pin indentations (Fig. 4A-C). With the porosity correction applied, the strength prediction (dashed lines) overestimates

the size effect significantly, even when considering the upper limit of the 95 % confidence interval (dotted lines), which results in the lowest size effect (Fig. 4A,B, Table 2). Since the porosity correction underlies uncertainties, a narrower porosity interval was selected (Fig. 4C), where values can be compared without correction. Here, a weak size effect is likely and the predictions by Eq. X come closer to the measured values (Table 2). Nevertheless, it needs to be taken into account, that the sample population, especially of the 3 mm PIs, was small and underlies large uncertainties as the large 95 % confidence interval (Table 2) shows. Please note that *m* increases from Fig. 4A to Fig. 4C with the material becoming more homogeneous and thus reliable in each plot.

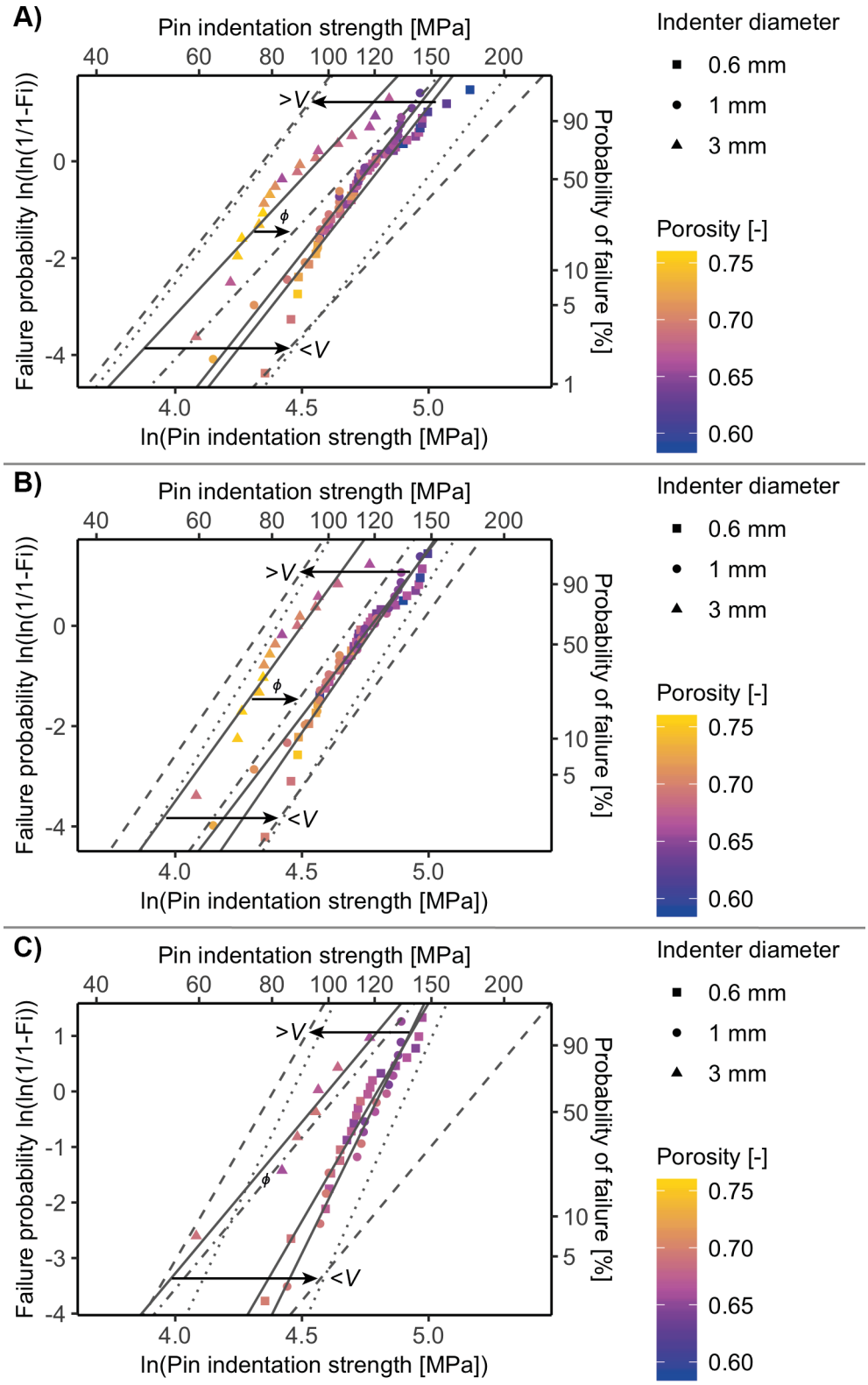

Figure 4: Weibull plots of all pin indentations in spines of H. mamillatus (A), of pin indentations with no growth layer influence (B) and additionally of a narrower porosity interval from 0.64-0.70 (C). Full lines correspond to m obtained by LR, dashed lines to size effect predictions with Eq. 2 and dotted lines to predictions with the upper limit of the confidence interval. Doubly dashed lines represent a porosity correction of the in average more porous 3 mm PIs.

Table 2: Data to Fig. 4. Font coding is as in Table 1. ϕ = porosity.

	pin indenter diameter [mm]	sample size *n*	indenter area [mm^2]	mean porosity [-]	Weibull modulus *m*	characteristic strength σ_0 [MPa]	σ_0 [MPa] porosity corrected	σ_0 [MPa] extrapolated (Eq. 2)
Figure 4A	0.6	40	0.283	0.666	6.7 (5.6) *4.4-6.9*	125 (126)	-	169 (155)
	1	30	0.785	0.674	6.6 (7.1) *5.1-9.2*	120 (120)	-	-
	3	19	7.069	0.698	5.6 (5.0) *3.3-6.7*	96 (97)	113 (at ϕ = 0.67)	77 (79)
Figure 4B	0.6	34	0.283	0.669	7.3 (6.6) *4.9-8.3*	120 (121)	-	143 (133)
	1	27	0.785	0.678	6.6 (7.0) *4.9-9.2*	118 (118)	-	-
	3	15	7.069	0.707	7.0 (6.0) *3.8-8.2*	90 (90)	110 (at ϕ = 0.674)	78 (81)
Figure 4C	0.6	22	0.283	0.669	7.9 (7.3) *5.0-9.6*	121 (121)	-	180 (137)
	1	17	0.785	0.668	9.3 (11.0) *6.6-15.3*	123 (123)	-	-
	3	7	7.069	0.677	5.5 (6.5) *2.7-10.2*	100 (99)	105 (at ϕ = 0.668)	80 (87)

Uniaxial compression of cores of *H. mamillatus*

Small cores had a significantly higher strength than large cores (Figure 5B,C, Table 3). Both sample populations had the same mean porosity (Table 3), so that the porosity influence on strength can be omitted. Size effect predictions agree reasonably well with the measurements and exceed them only slightly. When considering the upper limit of the 95 % confidence interval (Table 3), predictions and measurements agree well in the light of the large natural heterogeneity of the samples.

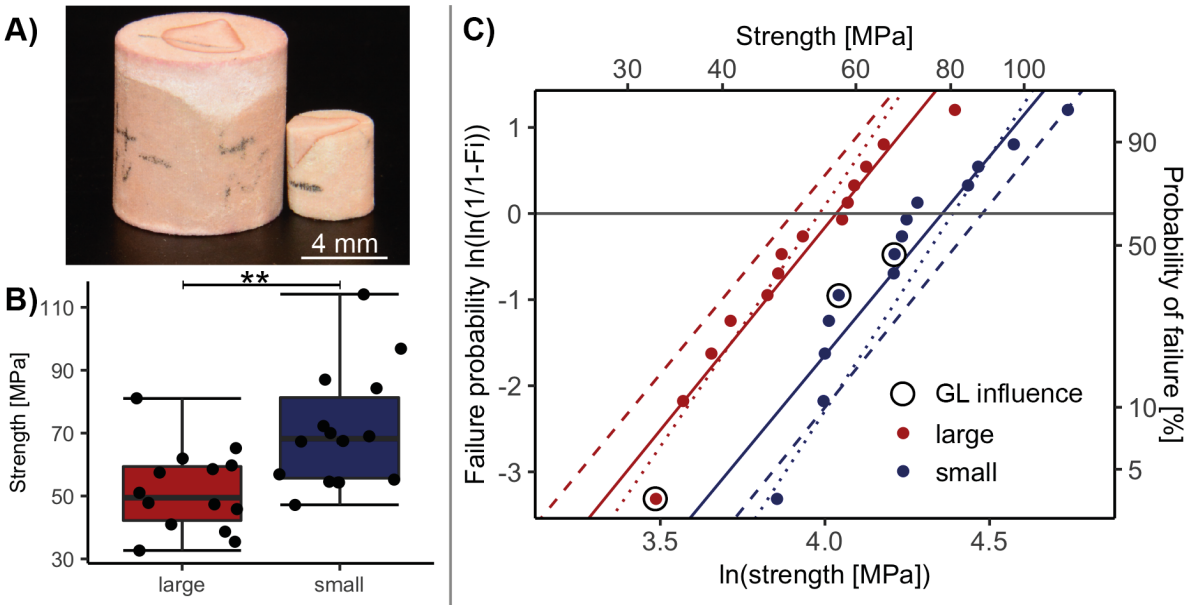

Figure 5: Cores used for uniaxial compression experiments (A). Small cores were significantly stronger than large cores (B) (Welch t-test, $p < 0.01$). This is also reflected in the Weibull plot (C), where the predictions of Eq. 2 (dashed lines) agree reasonably well with the measurements, especially when taking upper limit of 95 % confidence interval as m (dotted lines). Data to C can be found in Table 3.

Table 3: Data to Fig. 5 with the same font coding as in Table 1.

	sample size *n*	mean volume [mm^3] and (range)	mean porosity and (range)	Weibull modulus *m*	characteristic strength σ_0 [MPa]	σ_0 [MPa] extrapolated (Eq. 5)
small	14	46 (41-48)	0.663 (0.598-0.754)	4.6 (4) *2.5-5.6*	78 (78)	88 *81*
large	14	372 (365-379)	0.664 (0.600-0.703)	4.7 (4.3) *2.6-5.9*	56 (57)	50 *53*

Growth layers in small and large aboral spines

Full segments with confining growth layers show no or only a weak size effect [4], while drilled cores lacking this stereom type show a clear size effect (Fig. 5), this section deals with the highest hierarchical level of the spines, the GLs. Large aboral spines are older than small aboral spines. The small spines are located on the youngest plates close to the ambitus of the sea urchin test and the largest spines are usually found close to the ambitus. Hence, large aboral spines have experienced on average more growth cycles, resulting in the formation of a distal growth layer, than their smaller counterparts and therefore have on average more GLs providing them with additional strength.

Porosity data of GLs of Lauer et al. [18, 38] were re-evaluated in respect to differences between large and small aboral spines. Large aboral spines have generally denser GLs than their smaller and younger counterparts (Fig. 6A) which provides large spines with stiffer stereom. As the state of a small aboral spine can still be found in the oldest (smallest) growth layer in large aboral spines, it was investigated how the porosity of the GLs has changed during growth. Fig. 6B shows the how the porosity of the innermost and outermost GL of large aboral spines differs. In all cases the porosity decreases from innermost to outermost GLs, indicating that the densest GL is always located at the spine rim and that

during growth the porosity of growth layers generally decreases, which increases stiffness and strength of larger spines.

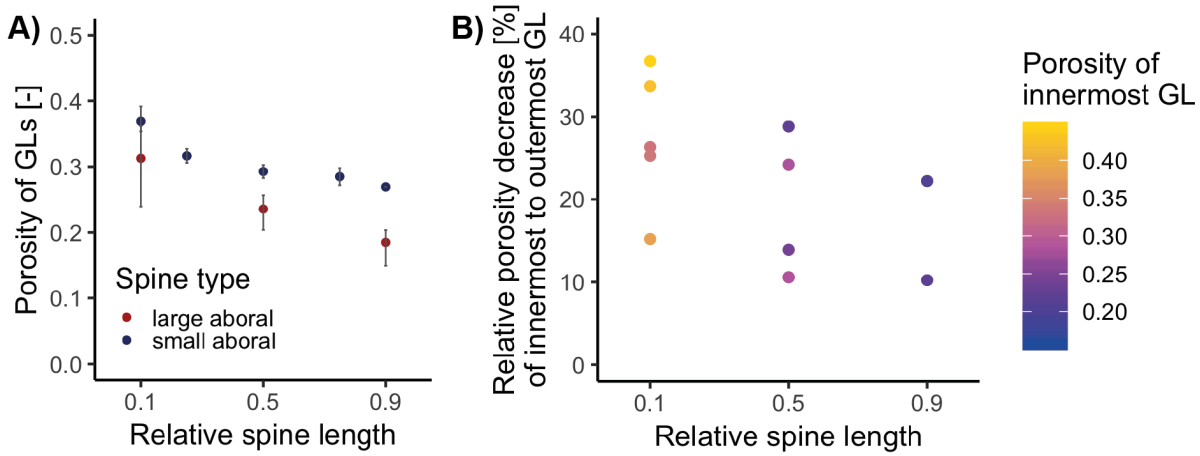

Figure 6: Difference in porosity of growth layers (GLs) of large (n = 5) and small (n = 3) aboral spines over the spine length (A) and relative porosity increase from old (innermost) to the youngest (outermost) GL in large spines.

4. Discussion

Measuring the size effect with pin indentation

IGC shows that a size effect can be measured with pin indentation. Measured σ_{PI} and predictions by Weibull theory coincide well (Figure 2E, Table 1), especially in the light of uncertainties induced by m determination due to small sample populations [39, 40]. To account for these uncertainties, m was calculated by MLE and LR each and the 95 % confidence interval was reported. Furthermore, all size effect calculations were also done with the upper limit of the confidence interval. m differed slightly depending on the method used but no systematic differences were observed. σ_0 was not influenced by method for fitting as it deviated only by 1 MPa.

For extrapolation with Eq. 2, the area of the pin (Fig. 7A) instead of the elastically stressed volume was used, since the exact extent of this volume is unknown. This means that according to the approximation in Fig. 7A all stress fields extend equally deep into the sample, which is probably a simplification. A more realistic elastic stress field after [41] is schematically shown in Fig. 7B, where larger pin sizes produce a deeper stress field. However, the failure was usually located underneath the pin where the peak stresses occur [41], as only 5/61 of IGC and 3/89 of SUS measurements failed outside the PI. Hence, the case in Fig. 7A might be a valid simplification for the purpose of calculating the size effect only, not for modelling the stress field. However, as the elastic stress field extends much beyond the pin (Fig. 7B) and might even surpass sample dimensions (Fig. 7C), weak spots located in this elastic stress field might lead to failure next to the pin, although not experiencing the peak stresses underneath the pin. These measurements need to be excluded for size effect calculations since a different volume

of the sample failed as assumed in calculations. The likelihood for such an event increases with decreasing pin/sample ratio and occurred occasionally for 5 mm in IGC (3) for 3mm pin in SUS (3).

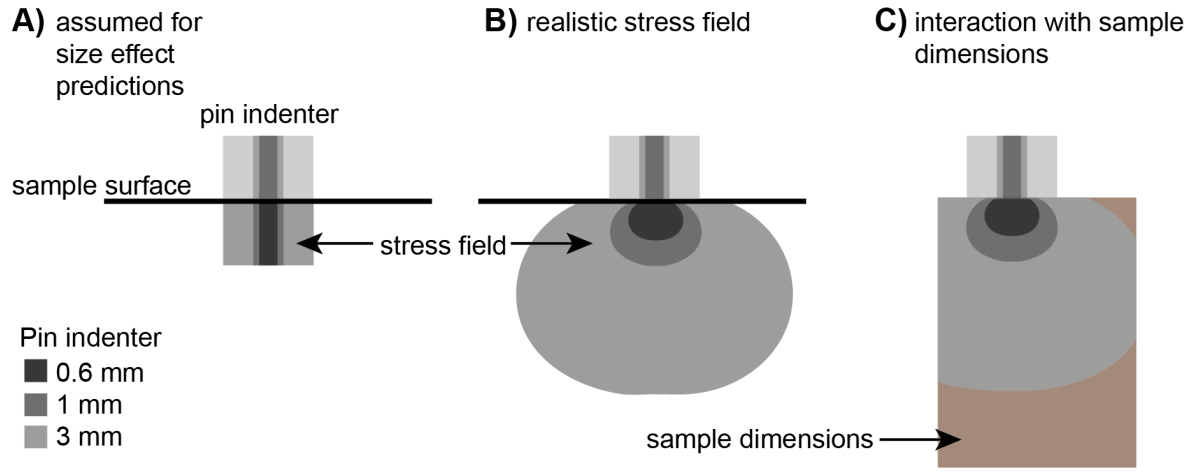

Figure 7: For extrapolations with Eq. 2 it was assumed that the area of the indenter equals the tested volume (A) although the elastic force field is much larger (B) and might surpass sample dimensions (C). If a weak spot is located in the elastic force field, the sample might fail underneath the pin. This was observed rarely.

It is important that the pin covers enough pores in order to yield representative results for the material and not for single struts. Kumar et al. [29] identified 40 pores as this threshold and Andrews et al. [28] found that the pin diameter needs to cover 6 pores (≈ 28 per area). If smaller numbers are measured, tearing and shearing forces at the pin wall cutting into the material become disproportionally large and affect the recorded forces as noted for aluminium foams [28]. However, as shearing strength for ceramic materials is low compared to the compressive strength, this influence might be weaker for ceramic foams as for metal foams. Still it might be that the size effect for the 1.5 PI of the IGC might be slightly overestimated, as the average number of cells beneath the indenter was 34 ± 21 (± SD). These considerations should not weaken the ability of PI to measure the size effect, as the difference in σ_{PI} between 3 mm and 5 mm PI is also statistically significant (Table 1).

Size effect in spines of *H. mamillatus* by pin indentation

Although PI was used to measure the strength of GL free regions, the size effect detected seems weaker than in UC of drilled cores where growth layers were also excluded. The overprinting of the size effect is partly caused by the large porosity intervals in PI (Fig. 4A,B) as it increases heterogeneity. Only in the narrow porosity interval of Fig. 4C, where the sample population of the 3 mm PIs is unfortunately, a size effect is indicated with some certainty, although weaker than predicted by Eq. 2. Whether this deviation is caused by the small sample population or is a real effect cannot be deduced on this data basis. However, there are reasons why the σ_{PI} of 3 mm PI in the spines of *H. mamillatus* might be overestimated.

Firstly, due to their size, it was not possible to place 3 mm PIs far away from the influence of GLs (Fig. 3A). They might have a supporting or confining influence on the 3 PI and by this increasing strength

compared to 0.6 and 1 mm PIs. Probably more important, the porosity in proximity to a GL increases in the RL. This means that each 3 mm PI contains a proportion of dense material that is lacking in 0.6 and 1 mm PIs. This denser material likely increases σ_{PI}. As σ_{PI} is plotted against the average porosity of each PI in Fig. 4A-C and in case of 3 mm PI, σ_{PI} is likely influenced by the denser parts of the RL, the true σ_{PI} of 3 mm PI might derive from a slightly lower porosity. Both effects removed, the proximity to GLs and the local higher density in the RL, would decrease the σ_{PI} of 3 mm PI and thereby increase the size effect measured by PI in the spines of *H. mamillatus*. Hence, despites the uncertainty imposed by the small sample population of 3 mm PIs, a size effect is found in PI.

Size effect in spines of *H. mamillatus* by uniaxial compression

The only difference between the full segments measured in [4] and the drilled cores reported here, lies in the absence of confining GLs in the drilled cores. Without the GL present, cores show no signs of a diminished size effect as Lauer et al. [4] claimed for full segments. Hence, the explanation given by the same authors that the strut size constituting the stereom (its size does not change with increasing spine size [27]) is smaller than the critical crack size a is flawed. The authors used the engineering stress in UC for calculating the critical crack size with the Griffith fracture criterion. Instead, the "true" stress in mode I loading in a single strut is required. This value can only be approximated by extrapolating the strength of 3-point bending measurements by [42] to fully dense conditions, those that are encountered in a strut. This yields σ of ~360 MPa. The fracture toughness K_{IC} of the biogenic calcite of *H. mamillatus* is not known and K_{IC} of biological materials is often very challenging to measure [43]. For calculations in [4] K_{IC} = 0.39 MPa $m^{1/2}$ of geological calcite [44] was assumed, likely a too low estimation. Maiti et al. [45] give a formula for the calculation of K_{IC} of brittle cellular solids, which yields 0.5 MPa $m^{1/2}$ for the biogenic calcite of *H. mamillatus*. By inserting these refined values in the Griffith fracture criterion, a estimates slightly below 1 μm. Even when taking into account the large heterogeneities encountered in this biological material and the uncertainties done by interpolating bending strength, a remains below strut size of ~20 ± 7 µm [27]. Therefore, the reason why a size effect cannot be found lies in the heterogeneity of the samples of *H. mamillatus*. This heterogeneity is primarily caused by the GLs, as cores in UC lacking them show a clear size effect.

How growth layers potentially weaken the size effect

Two mechanisms directly linked to the growth of the spines are potentially able to increase the strength of larger spines against the trend of the size effect (Fig. 6). Whether they are deliberately installed to counteract the size effect is unknown, however they can be both explained by the mechanisms of spine growth. Firstly, as large aboral spines are older than small aboral spines, they usually have more growth layers as they experienced more growth cycles. Only regenerated spines deviate from this rule [46]. By having more growth layers, large aboral spines have a more pronounced core shell construction, with

more growth layers located close to the rim, increasing the strength without a significant overall increase in porosity. The second mechanism of younger GLs located closer to the to be denser than older GLs, located closer to the centre, can also be explained by growth. Growth layers are constituted by comparably large and thick growth layer trabeculae. The number of these trabeculae is approximately constant in a single aboral spine [18]. Therefore it is geometrically given, that the trabeculae need to become larger in size in order to account for the increasing circumference of the spine upon growth. By this, the density of the GLs has to increase, as identified in large aboral spines (Fig. 6B) and due to the same reason, large spines generally have denser GLs than small spines (Fig. 6A). These two mechanisms might explain, why the spines of *H. mamillatus* - simply by the way they grow - work against the size effect. In the light of these results, the highest hierarchical level is able to weaken the size effect by becoming denser and more abundant in larger spines.

Although so far only a few studies on the size effect on structural strength in biological materials were conducted, it seems that nature often implements mechanisms to mitigate the size effect. Spruce wood in longitudinal direction has a four times lower size effect [24, 47] than predicted by Eq. 2 and bamboo fibres' strength decreases only half as much as calculated by Eq. 2 [48]. Unfortunately, the authors of these studies do not give explanations to this specific observation. Taylor found that the fatigue strength of mammalian bone does not increase with animal size and attributed this to the introduction of a new hierarchical level, the secondary osteons, in bones of large mammals. These examples including the aboral spines of *H. mamillatus* highlight that biological materials can provide ample inspiration on how to mitigate the size effect on structural strength, especially considering that only a few materials were investigated in this respect.

Reliability of spines of *H. mamillatus*

Biological materials generally possess a large natural heterogeneity that reduces the reliability of failure of the material, i.e. the Weibull modulus. m of biological (composite) ceramics is usually much lower than of technical ceramics. For the spines of *H. mamillatus* m ranges between 3-5 [4, 49], for nacre of *Haliotis rufescens* m = 2.5-5 [50] and for cortical bone m ~8 [51]. For technical ceramics values of 10-20 are usually reported [21]. However, as the analyses with PI of spines of *H. mamillatus* show, biological ceramics can approach reliability of their technical counterparts. By systematically decreasing the heterogeneity in measurements of PI from Fig. 4A, were all measurements are displayed, to Fig. 4B, where PIs including dense growth layers were omitted to lastly Fig. 4C, where only a porosity interval of 0.06 was analysed, the Weibull modulus increases by 30-60 %, depending on which pin indenter is considered (Table 2). It is important to keep in mind that the porosity range used in Fig. 4C is still large compared to the similarity of technical ceramics, where the scatter in porosity is usually below 0.01. Although the selection of such a narrow porosity interval for the spines of *H. mamillatus* was not feasible in the here presented data, it can be assumed that the reliability further increases,

illustrating how reliable biological materials are when applying the same thresholds for homogeneity as for technical ceramics. The localized testing with PI helps to overcome heterogeneities in the material and reveals how "well-made" the spines of *H. mamillatus* are.

5. Conclusions

1. Localised testing with pin indentation is able to detect a size effect in brittle foam ceramics as demonstrated on alumina ceramics produced by ionotropic gelation method and biological ceramics, the spines of *Heterocentrotus mamillatus*.
2. Spines of *H. mamillatus* only show a clear size effect when removing the highest hierarchical level, the dense growth layers.
3. Upon spine growth two mechanisms might work against the size effect: Growth layers become more abundant (1) and growth layers become denser (2).
4. In the light of these results the earlier hypothesis of Lauer et al. [4] needs to be rejected.
5. Pin indentation reveals that the statistically distributed strength of spines of *H. mamillatus* approaches the reliability technical ceramics when decreasing the natural heterogeneity by localized measurements.

REFERENCES

[1] M.A. Meyers, P.Y. Chen, M.I. Lopez, Y. Seki, A.Y. Lin, Biological materials: a materials science approach, J Mech Behav Biomed Mater 4(5) (2011) 626-57.
[2] R. Wang, H.S. Gupta, Deformation and Fracture Mechanisms of Bone and Nacre, Annual Review of Materials Research 41(1) (2011) 41-73.
[3] J.F. Vincent, Biomimetics--a review, Proc Inst Mech Eng H 223(8) (2009) 919-39.
[4] C. Lauer, S. Schmier, T. Speck, K.G. Nickel, Strength-size relationships in two porous biological materials, Acta Biomater 77 (2018) 322-332.
[5] J.D. Currey, D. Nichols, Absence of Organic Phase in Echinoderm Calcite, Nature 214(4) (1967) 81-83.
[6] J. Seto, Y. Ma, S.A. Davis, F. Meldrum, A. Gourrier, Y.Y. Kim, U. Schilde, M. Sztucki, M. Burghammer, S. Maltsev, C. Jager, H. Colfen, Structure-property relationships of a biological mesocrystal in the adult sea urchin spine, Proceedings of the National Academy of Sciences of the United States of America 109(10) (2012) 3699-704.
[7] A. Berman, L. Addadi, A. Kvick, L. Leiserowitz, M. Nelson, S. Weiner, Intercalation of sea urchin proteins in calcite: study of a crystalline composite material, Science 250(4981) (1990) 664 - 667.
[8] J. Aizenberg, J. Hanson, T.F. Koetzle, S. Weiner, L. Addadi, Control of Macromolecule Distribution within Synthetic and Biogenic Single Calcite Crystals, J Am Chem Soc 119 (1997) 881-886.
[9] M. Albéric, E.N. Caspi, M. Bennet, W. Ajili, N. Nassif, T. Azaïs, A. Berner, P. Fratzl, E. Zolotoyabko, L. Bertinetti, Y. Politi, Interplay between Calcite, Amorphous Calcium Carbonate, and Intracrystalline Organics in Sea Urchin Skeletal Elements, Crystal Growth & Design 18(4) (2018) 2189-2201.
[10] M. Merino, E. Vicente, K.N. Gonzales, F.G. Torres, Ageing and degradation determines failure mode on sea urchin spines, Materials Science and Engineering: C 78 (2017) 1086-1092.
[11] Y. Oaki, H. Imai, Nanoengineering in Echinoderms: The Emergence of Morphology from Nanobricks, Small 2(1) (2006) 66 - 70.

[12] J. Weber, R. Greer, B. Voight, E. White, R. Roy, Unusual strength properties of echinoderm calcite related to structure, Journal of Ultrastructure Research 26 (1969) 355-366.
[13] S. Weiner, L. Addadi, Design strategies in mineralized biological materials, Journal of Materials Chemistry 7(5) (1997) 689-702.
[14] V. Presser, C. Kohler, Z. Zivcova, C. Berthold, K.G. Nickel, S. Schultheiß, E. Gregorova, W. Pabst, Sea Urchin Spines as a Model-System for Permeable, Light-Weight Ceramics with Graceful Failure Behavior. Part II. Mechanical Behavior of Sea Urchin Spine Inspired Porous Aluminum Oxide Ceramics under Compression, Journal of Bionic Engineering 6(4) (2009) 357-364.
[15] N. Toader, W. Sobek, K.G. Nickel, Energy Absorption in Functionally Graded Concrete Bioinspired by Sea Urchin Spines, Journal of Bionic Engineering 14(2) (2017) 369-378.
[16] L. Cao, X. Li, X. Zhou, Y. Li, K.S. Vecchio, L. Yang, W. Cui, R. Yang, Y. Zhu, Z. Guo, X. Zhang, Lightweight Open-Cell Scaffolds from Sea Urchin Spines with Superior Material Properties for Bone Defect Repair, ACS Appl Mater Interfaces 9(11) (2017) 9862-9870.
[17] K.S. Vecchio, X. Zhang, J.B. Massie, M. Wang, C.W. Kim, Conversion of sea urchin spines to Mg-substituted tricalcium phosphate for bone implants, Acta Biomater 3(5) (2007) 785-93.
[18] C. Lauer, T.B. Grun, I. Zutterkirch, R. Jemmali, J.H. Nebelsick, K.G. Nickel, Morphology and porosity of the spines of the sea urchin Heterocentrotus mamillatus and their implications on the mechanical performance, Zoomorphology 137 (2017) 137-154.
[19] A. Smith, Stereom microstructures of the echinoid test, Special Papers in Palaeontology 25 (1980) 1-81.
[20] C. Lauer, K. Sillmann, S. Haussmann, K.G. Nickel, Strength, elasticity and the limits of energy dissipation in two related sea urchin spines with biomimetic potential, Bioinspir Biomim 14(1) (2018) 016018.
[21] R. Danzer, On the relationship between ceramic strength and the requirements for mechanical design, Journal of the European Ceramic Society 34(15) (2014) 3435-3460.
[22] W. Weibull, A Statistical theoroy of the strength of materials, Ingeniörsvetenskapsakademiens Handlingar 151 (1939) 1-45.
[23] Z.P. Bazant, Size effect, International Journal of Solids and Structures 37 (2000).
[24] W.-S. Lei, A generalized weakest-link model for size effect on strength of quasi-brittle materials, Journal of Materials Science 53(2) (2018) 1227-1245.
[25] Z.P. Bažant, S.-D. Pang, Activation energy based extreme value statistics and size effect in brittle and quasibrittle fracture, Journal of the Mechanics and Physics of Solids 55(1) (2007) 91-131.
[26] Z.P. Bazant, Scaling theory for quasibrittle structural failure, Proceedings of the National Academy of Sciences of the United States of America 101 (2004) 13400-13407.
[27] J.N. Grossmann, J.H. Nebelsick, Comparative morphological and structural analysis of selected cidaroid and camarodont sea urchin spines, Zoomorphology 132(3) (2013) 301-315.
[28] E.W. Andrews, G. Gioux, P. Onck, L.J. Gibson, Size effects in ductile cellular solids. Part II: experimental results, International Journal of Material Sciences 43 (2001) 13.
[29] P.S. Kumar, S. Ramachandra, U. Ramamurty, Effect of displacement-rate on the indentation behaviour of an aluminium foam, Materials Science and Engineering: A 347 (2003) 8.
[30] O.B. Olurin, N.A. Fleck, S. M.F., Indentation resistance of an aluminium foam, Scripta Materialia 43 (2000) 7.
[31] S. Ramachandra, Impact energy absorption in an Al foam at low velocities, Scripta Materialia 49(8) (2003) 741-745.
[32] S. Schmier, C. Lauer, I. Schäfer, K. Klang, G. Bauer, M. Thielen, K. Termin, C. Berthold, S. Schmauder, T. Speck, K.G. Nickel, Developing the Experimental Basis for an Evaluation of Scaling Properties of Brittle and 'Quasi-Brittle' Biological Materials, in: J. Knippers, K.G. Nickel, T. Speck (Eds.), Biomimetic Research for Architecture and Building Constructions, Springer International Publishing, Switzerland, 2016, pp. 277-294.
[33] K. Weber, G. Tomandl, T. Wenger, K. Heckmann, Preparation of Structured Ceramics for Membranes, Key Engineering Materials 132-136 (1997) 1754-1757.
[34] W. Xue, Y. Sun, Y. Huang, Z. Xie, J. Sun, Preparation and Properties of Porous Alumina with Highly Ordered and Unidirectional Oriented Pores by a Self-Organization Process, Journal of the American Ceramic Society 94(7) (2011) 1978-1981.

[35] C. Lauer, G. Buck, S. Mück, R. Jemmali, C. Berthold, K.G. Nickel, Pin indentation: a method for local testing mechanical properties of ceramic foams, prepared for submission to: Ceramics.
[36] C.Q. Dam, R. Brezny, D.J. Green, Compressive behavior and deformation-mode map of an open cell alumina, Journal of Material Research 5 (1990) 163-171.
[37] S. Ji, Q. Gu, B. Xia, Porosity dependence of mechanical properties of solid materials, Journal of Materials Science 41(6) (2006) 1757-1768.
[38] C. Lauer, S. Mück, T.B. Grun, I. Zutterkirch, K.G. Nickel, Individual growth and morphology of the spines of Heterocentrotus mamillatus, prepared for submission.
[39] M. Ambrožič, L. Gorjan, Reliability of a Weibull analysis using the maximum-likelihood method, Journal of Materials Science 46(6) (2010) 1862-1869.
[40] A. Khalili, K. Kromp, Statistical properties of Weibull estimators, J Mater Res 26 (1991) 6741-6752.
[41] P. Gondi, R. Montanari, A. Sili, Small-scale nondestructive stress-strain and creep tests feasible during irradiation, journal of nuclear materials (1994) 4.
[42] C. Lauer, S. Haußmann, P. Schmidt, C. Fisher, D. Rapp, C. Berthold, K.G. Nickel, On the relation of amorphous calcium carbonate and the macromechanical properties of sea urchin spines, prepared for submission to: Advanced functional materials.
[43] A.P. Jackson, J.F. Vincent, R.M. Turner, The mechanical design of nacre, Proc R Soc Lond B 234 (1988) 415-440.
[44] B.E. Broz, R.F. Cook, W. D.L., Microhardness, toughness, and modulus of Mohs scale minerals, The American Mineralogist 91 (2006) 135-142.
[45] S.K. Maiti, M.F. Ashby, L.J. Gibson, Fracture toughness of brittle cellular solids, Scripta Metallurgica 18 (1984) 213-217.
[46] J.N. Weber, Origin of Concentric Banding in the Spines of the Tropical Echinoid Heterocentrotus, Pacific Science 23 (1969) 452-466.
[47] G. Dill-Langer, R.C. Hidalgo, F. Kun, Y. Moreno, S. Aicher, H.J. Herrmann, Size dependency of tension strength in natural fiber composites, Physica A: Statistical Mechanics and its Applications 325(3-4) (2003) 547-560.
[48] E. Trujillo, M. Moesen, L. Osorio, A.W. Van Vuure, J. Ivens, I. Verpoest, Bamboo fibres for reinforcement in composite materials: Strength Weibull analysis, Composites Part A: Applied Science and Manufacturing 61 (2014) 115-125.
[49] V. Presser, S. Schultheiß, C. Berthold, K.G. Nickel, Sea Urchin Spines as a Model-System for Permeable, Light-Weight Ceramics with Graceful Failure Behavior. Part I. Mechanical Behavior of Sea Urchin Spines under Compression, Journal of Bionic Engineering 6(3) (2009) 203-213.
[50] R. Menig, M.H. Meyers, M.A. Meyers, K.S. Vecchio, Quasi-static and dynamic mechanical response of Haliotis rufescens (abalone) shells, Acta Materialia 48 (2000) 6.
[51] R.F. Bigley, J.C. Gibeling, S.M. Stover, S.J. Hazelwood, D.P. Fyhrie, R.B. Martin, Volume effects on yield strength of equine cortical bone, J Mech Behav Biomed Mater 1(4) (2008) 295-302.